

# **Investigations of coupled and Kerr non-linear optical resonators**

Von der Fakultät für Mathematik und Physik  
der Gottfried Wilhelm Leibniz Universität Hannover  
zur Erlangung des Grades

**Doktor der Naturwissenschaften**  
– Dr. rer. nat. –

genehmigte Dissertation  
von

**Dipl.-Phys. André Thüring**

geboren am 28. Juni 1978 in Hannover

2009

Referent:	Prof. Dr. Roman Schnabel
Korreferent:	Prof. Dr. Karsten Danzmann
Tag der Promotion:	03.07.2009

# Abstract

Future interferometric gravitational-wave detectors are aimed at a considerable sensitivity increase. This will be achieved by the implementation of high finesse, narrow bandwidth arm cavities and high-power lasers leading to Megawatts of circulating light power. *Coupled optical resonators* are then necessary to improve the sensitivity at frequencies beyond the arm cavities' bandwidth. Additionally, the *injection of squeezed states of light* will be used for shot noise reduction. However, problems will occur due to an increased thermal load in the optical components, strict requirements for laser stabilization and demanding requirements for a broadband squeezed light enhancement.

In this thesis, complex optical resonator configurations were investigated theoretically and proof of principle experiments were conducted accompanied by extensive numerical simulations. A four-mirror cavity enhanced Michelson interferometer with reduced laser power inside the optics was analyzed. In a comprehensive theoretical analysis it is shown that this topology, deemed to be promising for a long time, is not preferable for the reduction of thermal effects at adequate sensitivity levels. Instead, in this thesis, the *Detuned Twin-Signal-Recycling topology* was proposed as advanced detector. Based on the resonance doublet of two coupled resonators, this configuration enables the simultaneous enhancement of upper and lower signal sidebands. As a specific characteristic, the sensitivity in the entire shot noise limited detection band can be improved by the less demanding injection of frequency independent squeezed light. The proposed topology was experimentally demonstrated, and a broadband shot-noise reduction of up to 4 dB was achieved. Another experiment aimed at the passive power noise reduction of a continuous-wave laser beam. A Kerr-type non-linear resonator was set up that yielded a power noise reduction of a reflected laser beam by a great factor of more than a thousand (32dB).

**Keywords:** Gravitational-wave detector, optical resonators, squeezed field injection, optical Kerr effect



# Kurzfassung

Für zukünftige Gravitationswellendetektoren ist eine beträchtliche Sensitivitätssteigerung anvisiert. Dies kann erreicht werden durch die Verwendung optischer Armresonatoren hoher Güte und Hochleistungslasern, wodurch umlaufende Lichtleistungen im Megawattbereich erzielt werden. Gekoppelte optische Resonatoren sind dann nötig, um die Empfindlichkeit bei Frequenzen oberhalb der Bandbreite der Armresonatoren zu steigern. Jedoch werden Schwierigkeiten durch die erhöhte thermische Last in optischen Komponenten, höhere Anforderungen an die Laserstabilisierung sowie an die Realisierung einer breitbandigen Schrotrauschreduzierung durch die Verwendung von gequetschtem Licht auftreten.

In dieser Arbeit wurden komplexe Konfigurationen optischer Resonatoren theoretisch untersucht und Experimente begleitet von umfangreichen numerischen Simulationen durchgeführt. Ein Michelsoninterferometer mit Vier-Spiegel-Resonatoren in den Armen mit reduzierter Leistung innerhalb optischer Komponenten wurde untersucht. In einer umfangreichen theoretischen Analyse wird gezeigt, dass diese Topologie, die lange Zeit als vielversprechend erachtet wurde, nicht geeignet ist für eine Reduzierung thermischer Effekte bei einer gleichzeitig adequaten Empfindlichkeit. Stattdessen wurde in dieser Arbeit die *Detuned Twin-Signal-Recycling* Topologie als fortschrittlicher Detektor vorgeschlagen. Aufgrund einer Doppelresonanz gekoppelter Resonatoren ermöglicht diese Konfiguration die gleichzeitige Überhöhung oberer und unterer Signalseitenbänder. Diese Besonderheit erlaubt die Verwendung von *frequenzunabhängig gequetschtem* Licht für eine breitbandige Steigerung der schrotrauschlimitierten Empfindlichkeit. Die vorgeschlagene Topologie wurde experimentell demonstriert, und eine breitbandige Schrotrauschreduzierung um bis zu 4 dB konnte gezeigt werden. Ein zweites Experiment zielte auf die passive Unterdrückung des Leistungsrauschen eines Dauerstrichlasers ab. Die Verwendung eines auf dem optischen Kerreffekt basierenden Resonators erlaubte eine starke Reduzierung des Laserleistungsrauschens um einen großen Faktor von mehr als 1000 (32 dB).

**Stichworte:** Gravitationswellendetektor, gequetschtes Licht, optischer Kerreffekt



# Contents

<b>Abstract</b>	<b>i</b>
<b>Kurzfassung</b>	<b>iii</b>
<b>Contents</b>	<b>v</b>
<b>Glossary</b>	<b>ix</b>
<b>List of Figures</b>	<b>xiii</b>
<b>List of Tables</b>	<b>xvii</b>
<b>1 Introduction</b>	<b>1</b>
1.1 Detection of gravitational-waves . . . . .	1
1.2 Interferometric gravitational-wave detectors . . . . .	2
1.2.1 Noise sources in interferometric gravitational-wave detectors . . . . .	4
1.2.1.1 Seismic noise . . . . .	4
1.2.1.2 Thermal noise . . . . .	4
1.2.1.3 Quantum noise . . . . .	5
1.3 The next generation of interferometric gravitational-wave detectors . . . . .	5
1.3.1 Realization of high circulating powers . . . . .	5
1.3.2 High power laser noise reduction . . . . .	6
1.3.3 The RSE topology . . . . .	7
1.3.4 Injection of squeezed states of light . . . . .	7
1.4 Structure of the thesis . . . . .	8
<b>2 Optical resonators</b>	<b>11</b>
2.1 Analytical description of a two-mirror cavity . . . . .	11

2.1.1	Carrier fields . . . . .	12
2.1.2	Characteristic quantities . . . . .	14
2.1.3	Description of a lossy two-mirror cavity . . . . .	15
2.1.4	Coupling to a two-mirror cavity . . . . .	17
2.1.5	Resonator dynamics . . . . .	21
2.1.6	Transfer function . . . . .	26
2.2	Coupled optical resonators . . . . .	29
2.2.1	Carrier field in a three-mirror cavity . . . . .	29
2.2.2	Explaining the resonance feature . . . . .	31
2.2.3	Coupling of a three-mirror cavity . . . . .	36
2.2.3.1	Coupling of the impinging carrier light to the three-mirror cavity . . . . .	36
2.2.3.2	Coupling of both resonators in a three-mirror cavity . . . . .	39
2.2.4	Transfer function of a three-mirror cavity . . . . .	43
2.2.5	Determination of characteristic quantities . . . . .	45
2.2.5.1	Periodicity of frequency response . . . . .	46
2.2.5.2	Resonance frequencies and frequency splitting . . . . .	47
2.3	Summary . . . . .	52
<b>3</b>	<b>Analysis of a four-mirror cavity enhanced Michelson interferometer</b>	<b>53</b>
3.1	Introduction . . . . .	54
3.2	Analytical description . . . . .	57
3.2.1	Carrier fields . . . . .	57
3.2.2	Signal sidebands . . . . .	58
3.3	Reduction of parameter space . . . . .	61
3.3.1	Basic assumptions . . . . .	61
3.3.2	Resonance feature . . . . .	62
3.3.3	Power in substrates . . . . .	62
3.3.4	Frequency response . . . . .	64
3.4	Parameter studies . . . . .	65
3.4.1	Special cases . . . . .	65
3.4.2	Exemplary configuration . . . . .	68
3.5	Conclusion . . . . .	70
<b>4</b>	<b>Detuned Twin-Signal-Recycling</b>	<b>71</b>
4.1	Introduction . . . . .	71

4.1.1	History of squeezed field injection for gravitational-wave detectors . . . . .	72
4.2	The Twin-Signal-Recycling topology . . . . .	74
4.3	Comparison of TSR with GEO 600 . . . . .	76
4.3.1	The quantum noise limited sensitivities . . . . .	76
4.3.2	Broadband shot noise reduction by squeezed field injection . . . . .	81
4.4	Further possibilities of shaping the sensitivity curve . . . . .	83
4.4.1	Combination of tuned and detuned SR . . . . .	84
4.4.2	Tunable bandwidth . . . . .	86
4.4.3	Tunable frequency splitting . . . . .	89
4.5	Parameters for a possible application in GEO-HF . . . . .	89
4.6	Application in Advanced LIGO: Conversion of RSE to TRSE . . . . .	91
<b>5</b>	<b>Experimental realization of Twin-Signal-Recycling</b>	<b>93</b>
5.1	Parameter choice . . . . .	93
5.1.1	TSR resonator length . . . . .	94
5.1.2	Simulation of error signals . . . . .	96
5.1.3	The final choice of parameters . . . . .	98
5.2	The experimental setup . . . . .	99
5.3	Alignment procedure . . . . .	101
5.3.1	Interferometer alignment . . . . .	101
5.3.2	Coupling of the squeezed light source to the interferometer . . . . .	104
5.3.3	Alignment of the homodyne detector . . . . .	104
5.4	Hierarchic stabilization of the TSR interferometer . . . . .	105
5.5	Broadband squeezing of quantum noise . . . . .	107
5.5.1	Characterization of the injected squeezed field . . . . .	107
5.5.2	Quantum noise spectra of the TSR interferometer . . . . .	109
5.6	Summary . . . . .	112
<b>6</b>	<b>Analysis of a Kerr non-linear resonator</b>	<b>113</b>
6.1	Introduction . . . . .	113
6.2	Cascaded Kerr effect in second order non-linear materials . . . . .	115
6.3	The experimental methods . . . . .	116
6.3.1	Preparation of the laser source . . . . .	116
6.3.2	The Kerr non-linear resonator . . . . .	119
6.3.2.1	Optical and mechanical layout . . . . .	119
6.3.2.2	Alignment of the non-linear cavity . . . . .	120

6.3.2.3	Control schemes for length stabilization . . .	121
6.3.3	Detection schemes . . . . .	123
6.3.3.1	Self-homodyning of the carrier light's amplitude quadrature . . . . .	123
6.3.3.2	Balanced homodyne readout with external local oscillator beam . . . . .	124
6.4	Prove of the Kerr effect . . . . .	125
6.4.1	Dependence on phase matching temperature . . . . .	125
6.4.2	Hysteresis measurements of the dynamic resonator . .	128
6.5	Enhancement of phase modulation signals . . . . .	131
6.5.1	Strong modulation of the geometrical length . . . . .	132
6.5.2	Transfer function of phase modulation signals . . . . .	135
6.6	Laser power noise reduction . . . . .	137
6.6.1	Introduction . . . . .	138
6.6.2	Measurements . . . . .	139
6.7	Tomographic analysis of the noise transformation . . . . .	140
6.7.1	Motivation . . . . .	140
6.7.2	Measurements . . . . .	141
6.7.3	Evaluation of the measured data . . . . .	143
6.7.4	Discussion of the results . . . . .	146
6.8	Conclusions . . . . .	147
<b>7</b>	<b>Summary and Outlook</b>	<b>149</b>
<b>A</b>	<b>Matlab scripts</b>	<b>153</b>
A.1	Noise spectral densities for GEO 600 with squeezed input . . .	153
A.2	Noise spectral densities for TSR . . . . .	158
<b>B</b>	<b>FINESSE simulation for the TSR experiment</b>	<b>163</b>
<b>C</b>	<b>Investigation of a scanned 3rd-order non-linear resonator</b>	<b>169</b>
	<b>Bibliography</b>	<b>175</b>
	<b>Acknowledgments</b>	<b>185</b>
	<b>Curriculum vitae</b>	<b>187</b>
	<b>Publications</b>	<b>189</b>

# Glossary

## Abbreviations

cw	Continuous-wave
FSR	Free spectral range
FWHM	Full width at half maximum
HOM	Higher order mode
HV	High voltage
KNLR	Kerr non-linear resonator
LO	Local oscillator
M	Mirror
MC	Mode cleaner
NSD	Noise spectral density
OMC	Output mode cleaner
OP	Operating point
PDH	Pound-Drever-Hall
PBS	Polarizing beam splitter
PD	Photo detector
PR	Power-recycling
PRM	Power-recycling mirror

x GLOSSARY

PZT	Piezo electric transducer
RBW	Resolution bandwidth
ROC	Radius of curvature
RSE	Resonant-Sideband-Extraction
SR	Signal-recycling
SRM	Signal-recycling mirror
TSR	Twin-Signal-Recycling
VBW	Video bandwidth

**Symbols**

$\mathcal{F}$	Finesse
$f$	Frequency
$f_{\text{sp}}$	Frequency splitting
$\gamma$	Bandwidth (FWHM) of a cavities resonance
$\lambda$	Wavelength
$L$	Macroscopic cavity length
$N$	Integer number
$n_2^{\text{eff}}$	Effective non-linear refraction index
$\Phi$	Tuning of a cavity
$P$	Power
$\rho$	Amplitude reflectance
$\tau$	Amplitude transmittance
$R$	Power reflectance
$T$	Power transmittance
$\Omega$	Angular sideband frequency

$CF$	Carrier field
$SF$	Sideband field
$t_s$	Storage time of a cavity
$t_{rt}$	Round-trip time
$\omega_0$	Angular carrier frequency
$w_0$	Beam waist



# List of Figures

1.1	Interferometer topologies of current gravitational-wave detectors	3
1.2	Illustration of the Resonant-Sideband-Extraction topology . . . . .	7
2.1	Notation of a two-mirror cavity . . . . .	12
2.2	Free spectral range of a two-mirror cavity . . . . .	15
2.3	Airy peak for various values of the internal loss . . . . .	16
2.4	Reflectance and transmittance of a two-mirror cavity depending on the coupling. . . . .	17
2.5	Phasor diagram of an over-coupled cavity . . . . .	19
2.6	Phasor diagram of an under-coupled cavity . . . . .	20
2.7	Phasor diagram of an impedance-matched cavity . . . . .	20
2.8	Phase shift in reflection of a two-mirror cavity . . . . .	21
2.9	Ringling effect of a two-mirror cavity . . . . .	23
2.10	Field build-up in a static two-mirror cavity . . . . .	24
2.11	Phasor diagram of the field build-up for static tunings . . . . .	25
2.12	Frequency dependent power transmittance of a two-mirror cavity	27
2.13	Transfer function of phase modulation induced sidebands . . . . .	28
2.14	Notation of a three-mirror cavity. . . . .	29
2.15	Carrier light enhancement in a three-mirror cavity . . . . .	32
2.16	Resonance doublet of a three-mirror cavity . . . . .	33
2.17	Resonance pattern of a three-mirror cavity . . . . .	35
2.18	Coupling to a three-mirror cavity . . . . .	37
2.19	Comparison of the coupling to a three-mirror cavity and a two-mirror cavity . . . . .	39
2.20	Resonance branches depending on the mirror reflectance factors .	40
2.21	Maximum power build-up in a three-mirror cavity . . . . .	42
2.22	Exemplary transfer function of a three-mirror cavity . . . . .	44
2.23	Frequency dependent coupling of three-mirror cavity . . . . .	46
2.24	Periodicity of the frequency response . . . . .	47

2.25	Exemplary transfer functions of the Advanced LIGO optical configuration . . . . .	50
2.26	Exemplary resonance doublets of a three-mirror cavity. . . . .	51
2.27	Bandwidth of the resonances in a three-mirror cavity with equal resonator length . . . . .	52
3.1	Two configurations of a four-mirror cavity enhanced Michelson interferometer . . . . .	56
3.2	Notation of the four-mirror cavity . . . . .	57
3.3	Resonance pattern of a four-mirror cavity . . . . .	62
3.4	Sensitivity curves of a four-mirror cavity for various frequency splittings . . . . .	66
3.5	Sensitivity of the four-mirror cavity in dependence of $R_1$ . . . . .	67
3.6	Sensitivity of the four-mirror cavity for various ratios of $L_1/L_3$ . . . . .	68
3.7	Envelope of the four-mirror cavity sensitivity . . . . .	69
4.1	Schematic of TSR and GEO 600 . . . . .	74
4.2	The resonance doublet of TSR for technical design parameters . . . . .	76
4.3	Sensitivity of TSR and GEO 600 for different target frequencies . . . . .	78
4.4	Sensitivities of TSR and GEO 600 tuned to 1 kHz . . . . .	79
4.5	Optimal squeezing and detection angles of GEO 600 and TSR . . . . .	80
4.6	Squeezed light enhanced sensitivities of GEO 600 and TSR. . . . .	82
4.7	Resonance pattern of the TSR resonators . . . . .	84
4.8	Junction of tuned and detuned SR in TSR . . . . .	86
4.9	Tunable bandwidth of TSR . . . . .	88
4.10	Comparison of tuned SR and detuned TSR applicable in GEOHF . . . . .	90
4.11	Comparison of RSE and TRSE . . . . .	91
5.1	Possible frequency splittings in the TSR experiment . . . . .	95
5.2	Simulated error signals (control matrix) . . . . .	97
5.3	Simplified schematic of the TSR experimental setup . . . . .	99
5.4	Mode spectrum of the PRC . . . . .	101
5.5	Pre-alignment of the SRC . . . . .	103
5.6	Mode spectrum of the SRC at the final stage of alignment . . . . .	103
5.7	Mode spectra of the TSRC. . . . .	105
5.8	Hierarchic stabilization of the TSR interferometer . . . . .	106
5.9	Sampled feed back signals during the lock acquisition . . . . .	107
5.10	Squeezing spectra for several detunings of the TSRC . . . . .	108
5.11	Locking of the TSR interferometer . . . . .	110

5.12	Locking of the TSR interferometer . . . . .	111
6.1	Resonance peaks of a Kerr non-linear resonator . . . . .	113
6.2	Illustration of the mode cleaner (laser) stabilization . . . . .	117
6.3	Open-loop gain of the laser frequency control loop . . . . .	118
6.4	Illustration of the oven housing embedding the non-linear crystal	119
6.5	Detection ports used during the alignment of the KNLR and the reference mirror. . . . .	120
6.6	Monitor signals for the alignment . . . . .	121
6.7	Mode spectrum of the Kerr non-linear resonator . . . . .	122
6.8	Open-loop transfer function of the Kerr non-linear resonator length stabilization . . . . .	122
6.9	Homodyne readout schemes . . . . .	124
6.10	Mode spectrum of the output mode cleaner . . . . .	126
6.11	Linearity of the homodyne detector . . . . .	126
6.12	Conversion efficiency of the non-linear resonator . . . . .	127
6.13	Airy peaks of the KNLR in dependence of the phase matching condition . . . . .	128
6.14	Illustration of the hysteresis effect in a multi-stable resonator . . .	129
6.15	Comparison of the hysteresis for different strengths of the Kerr effect	130
6.16	Comparison of simulated and measured hysteresis curves . . . . .	131
6.17	Best fit to measured phase modulation signals . . . . .	133
6.18	Non-optimal fitting . . . . .	134
6.19	Non-optimal fitting . . . . .	135
6.20	Bandwidth of the KNLR depending on the SHG . . . . .	136
6.21	Normalized transfer function of the KNLR . . . . .	137
6.22	Measured laser power noise reduction . . . . .	140
6.23	Mode spectrum of the output mode cleaner . . . . .	141
6.24	Sampled signals of the homodyne detector . . . . .	144
6.25	Histograms of the sampled homodyne detector signal . . . . .	144
6.26	Wigner function for the reference beam and the beam reflected off the KNLR. . . . .	145
6.27	Comparison of the Wigner functions obtained at different operat- ing points of the KNLR . . . . .	145
6.28	Quadrature dependent power noise of the KNLR affected beam . .	146



# List of Tables

4.1	The parameters for the comparison of GEO 600 and TSR. . . . .	77
5.1	Normalized control matrix of the TSR locking scheme . . . . .	97
5.2	Final set of the TSR interferometer parameters. . . . .	98
5.3	Parameters of the developed control scheme. . . . .	98



---

# Introduction

## 1.1 Detection of gravitational-waves

The existence of gravitational-waves was predicted by Albert Einstein [1] as a direct consequence of his theory of general relativity [2]. Gravitational waves are perturbations of space-time which are caused by accelerated massive objects. Exemplary astrophysical sources are supernovae, coalescing binary systems (e.g. black hole – black hole, neutron star – neutron star) and pulsars. The direct detection of their emitted gravitational wave signals will give elementary new information about the nature of these objects. Furthermore, the observation of the gravitational-waves stochastic background provides a deep insight into the early Universe.

The expected gravitational wave amplitudes which are defined as a relative length change

$$h = \frac{2\delta L}{L} \quad (1.1)$$

are in the order of  $10^{-21}$ . Thus, the *direct* detection of gravitational-waves is one of the most challenging tasks of todays experimental physics.

The first *indirect* observation of gravitational-waves was accomplished by Russel Hulse [3] and Joseph Taylor [4]. Their longtime study of the binary pulsar system PSR 1913+16 revealed that the observed orbit decay accords precisely to the decay predicted by energy loss due to gravitational wave emission. For this discovery, Hulse and Taylor were awarded the Nobel price in 1993 .

The first attempt of a direct detection was made by Joseph Weber in the 1960's. He pioneered the use of large metal cylinders – so-called *resonant bar*

*detectors*. These cylinders have a high mechanical Q-factor corresponding to narrowband resonance frequencies. It is expected, that gravitational-waves excite the bars at their eigenmodes. The resulting oscillation of the bar is detected with a transducer converting displacement into an electronic signal. Whereas the first bar detectors were operated at room temperature, today's resonant bar detectors are cooled down to cryogenic temperatures to suppress the internal thermal noise. An overview of today's bar detectors is given in [5].

## 1.2 Interferometric gravitational-wave detectors

In contrast to the very narrowband sensitivity of resonant bar detectors, interferometric gravitational-wave detectors provide a comparatively broad detection bandwidth. The spectrum of gravitational-waves is expected to cover a wide frequency range. A low frequency detector covering the detection band in the mHz regime, which is not accessible by earth-bound detectors due to seismic noise, will be realized in space with the LISA detector. Within a collaboration of the European Space Agency (ESA) and the American National Aeronautics and Space Administration (NASA) LISA will be launched after 2018 [6].

Currently, an international network of first generation earth-bound interferometric gravitational-wave detectors is in operation covering the detection band from 50 Hz to a few kHz. These detectors are all based on improved Michelson interferometers with arm lengths on the kilometer scale. The Laser Interferometer Gravitational wave Observatory (LIGO) built in the USA consists of three single detectors. One long-base line interferometer (L1) with an arm length of 4 km is located at Livingston. Another two (H1 and H2) with arm lengths of 4 km and 2 km are operated at Hanford. In Europe there are two interferometers, the British-German GEO 600 detector with an arm length of 600 m located close to Hannover, and the French-Italian VIRGO detector in Cascina near Pisa with 3 km long arms. In Japan the TAMA300 detector with an arm length of 300 m is based close to Tokyo. At present these detectors are able to detect relative length changes in the order of  $10^{-19}$  representing a sensitivity of astrophysical interest.

The principle of these interferometric detectors operated at the dark fringe is based on the readout of a differential arm length change caused by a gravitational-wave. The differential modulation of the interferometer arm length produces a signal in the detection port at the gravitational-wave frequency. Since the amplitude of these signals is proportional to the light power

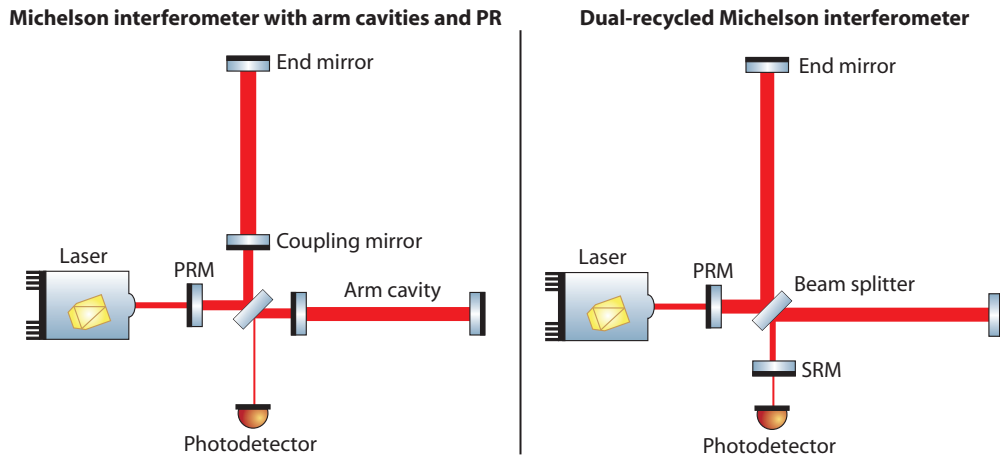


**Figure 1.1** — Topologies of current gravitational-wave detectors. **Left:** Michelson interferometer with arm cavities and power recycling (PR). **Right:** Dual-recycled interferometer as realized in the GEO 600 detector.

circulating in the interferometers, high laser powers are one essential requirement to achieve the targeted sensitivity. In the current detectors circulating powers in the order of 10 kW are realized. Optical resonators in each interferometer arm are used to resonantly enhance the power emitted by the laser source (refer to Fig. 1.1). To maintain a considerable detection bandwidth, the linewidth of these cavities is in the order of 100 Hz. The light reflected at these arm resonators is recycled using the so-called *power-recycling* (PR) technique [7]. Here, an additional mirror – the so-called *power-recycling mirror* (PRM) – is placed in the interferometers input. The light leaving the interferometer at its input port is back reflected and thus resonantly enhanced in the PR cavity. Accordingly, the power build-up in the arm cavities is further increased.

The GEO 600 detector is realized as a *dual-recycled* Michelson interferometer combining PR and the advanced *signal-recycling* (SR) technique [8]. Similar to the PR technique, an additional mirror – the *signal-recycling mirror* (SRM) – is placed in the detection port (refer to Fig. 1.1). Thus, the signal fields leaving the interferometer towards the detection port are resonantly enhanced leading to an improved sensitivity at the resonance frequency of the SR cavity. Here, two operating modes are possible. A broadband mode can be realized with a SR cavity tuned to the carrier frequency. In this case, both, upper and lower signal sideband fields produced by a phase modulation are recycled within the linewidth of the SR cavity. The detuned (narrowband) mode turns the

interferometer into a resonant detector. Here, only the upper or the lower side-band field is recycled whereas the counterpart is suppressed. Nevertheless, in this mode high peak sensitivities at arbitrary frequencies beyond the SR cavities linewidth are achievable.

## 1.2.1 Noise sources in interferometric gravitational-wave detectors

### 1.2.1.1 Seismic noise

At frequencies below approximately 40 Hz, the sensitivity of the earth-bound interferometers is limited by the coupling of seismic noise to the interferometers optics (test-masses) positions. Using multi-stage pendulum suspensions for the mirrors in combination with active control systems, at higher frequencies this coupling can be reduced. Each pendulum stage suppresses the noise transfer with  $1/f^2$  at frequencies above the pendulum resonance frequency. Additionally, the location of the detectors are chosen under consideration of the local seismic activity. The future gravitational-wave detector LCGT [9] will be operated underground leading to an overall seismic noise reduction as the coupling of seismic surface waves to the test-mass motion is suppressed.

### 1.2.1.2 Thermal noise

The limiting noise source in the mid-frequency detection band is the thermally driven motion of the test-masses [10]. There are three dominant thermal noise sources coupling to the interferometers signal: the coating thermal noise [11], the substrate thermal noise [12] and the thermorefractive noise [13]. The first two result in a displacement of the mirrors reflecting surfaces. The latter one causes fluctuations of the refraction index of the optics substrates and thus phase fluctuations of the transmitted fields. All three mechanisms cause a phase modulation of the light competing with potential signals induced by gravitational-waves. There are several possibilities to minimize the impact of thermal noise. First, in test-masses made of substrate materials with high mechanical Q-factors the thermal energy is stored in narrowband, high amplitude vibration eigenmodes. By a proper design the corresponding resonance frequencies can be shifted aside of the interferometers detection band. By cooling the test-masses down to cryogenic temperatures a further reduction of the thermal noise can be achieved. At present, the implementation issues are investigated within the Japanese LCGT project [9]. Furthermore, as the coating thermal noise is the limiting factor in the mid-frequency band, coating

free mirrors based on optical gratings are investigated for the application in gravitational-wave detectors [14].

### 1.2.1.3 Quantum noise

Besides the classical noise sources described above, the detector sensitivity is ultimately limited by photon quantum noise, at high frequencies by *shot noise* and at low frequencies by *radiation pressure noise*.

Considering a classical Michelson interferometer, the shot noise contributes to the interferometers output according to

$$h_{\text{SN}}(\Omega) = \frac{1}{L} \sqrt{\frac{\hbar c \lambda}{\pi P_{\text{circ}}}}. \quad (1.2)$$

Here  $L$  is the interferometer arm length,  $\lambda$  the laser wavelength and  $P_{\text{circ}}$  the circulating light power. This equation demonstrates, that the shot noise limited sensitivity can be improved by increasing both the circulating power and the arm length. Note, that in the case of arm cavities or SR, the shot noise limited sensitivity (given as noise to signal ratio) is not white due to the frequency dependent transfer function of these detectors.

Whereas an increased circulating power improves the shot noise limited sensitivity the radiation pressure noise originated from photon number (amplitude) fluctuations of the light field gets enhanced according to [15]

$$h_{\text{RP}}(\Omega) = \frac{1}{2m\Omega^2 L} \sqrt{\frac{8\pi\hbar P_{\text{circ}}}{c\lambda}}. \quad (1.3)$$

As this noise source falls with  $1/\Omega^2$  it is most significant at low frequencies. A reduction of the radiation pressure for given circulating powers can be achieved by using heavy interferometer test masses. Although in future gravitational-wave detectors like Advanced LIGO [16] the test masses will have an weight of about 50 kg, radiation pressure noise is expected to limit the sensitivity at low frequencies.

## 1.3 The next generation of interferometric gravitational-wave detectors

### 1.3.1 Realization of high circulating powers

In the next generation of interferometric gravitational-wave detectors the shot noise limited sensitivity will be enhanced by a factor of about 10 by increasing

the circulating laser power. Using high-power lasers together with high-finesse arm cavities and PR, the circulating powers will reach the Megawatt regime. The power in the PR cavity including the interferometer beam splitter and the substrate of the arm-cavity coupling mirrors will be in the order of a few kW. Here the maximum allowable power is limited by the non-zero absorption of the used optics. The inevitable heating of the optics will produce thermal lensing [17, 18] and thermal expansions of the optics surfaces. These effects lead to phase front distortions which result in a poor interference quality at the interferometer beam splitter. Therefore higher optical powers in higher order modes are leaving the interferometer towards the detection port resulting in an increased shot noise. Accordingly, methods for active thermal compensation [19, 20, 21, 22] and alternative substrate materials such as sapphire were investigated [23]. As well, alternative interferometer topologies such as all-reflective interferometer topologies [24] came into consideration.

### 1.3.2 High power laser noise reduction

For the next generation of gravitational-wave detectors the use of high power lasers with an output power of up to 200 W is aimed. The increased laser power inside the interferometers results in an increased radiation pressure on the suspended test-masses. Accordingly, fluctuations in the laser power lead to a fluctuation of the mirrors positions therefore causing additional noise in the interferometers signal. Passive noise filtering by the transmission through optical resonators efficiently reduces the power noise, but only at frequencies above the resonator linewidth. Hence, for the stabilization at low frequencies active control schemes are required. Novel high-power photodetectors [25] and detection schemes [26] were developed for error signal generation by sensing the power fluctuations. Although the achieved stability is close to the requirements, at low frequencies they are limited by the photodetectors internal noise. Within this context, the *optical Kerr effect* came into consideration for passive filtering. From several theoretical investigations [27, 28, 29, 30] it can be deduced that a Kerr non-linear resonator can be used to efficiently reduce the noise in the laser fields amplitude quadrature. The noise reduction can be achieved *within* the linewidth of these resonators and does not require high-power photodetectors. Thus, Kerr non-linear resonators represent a promising alternative to the methods used so far.

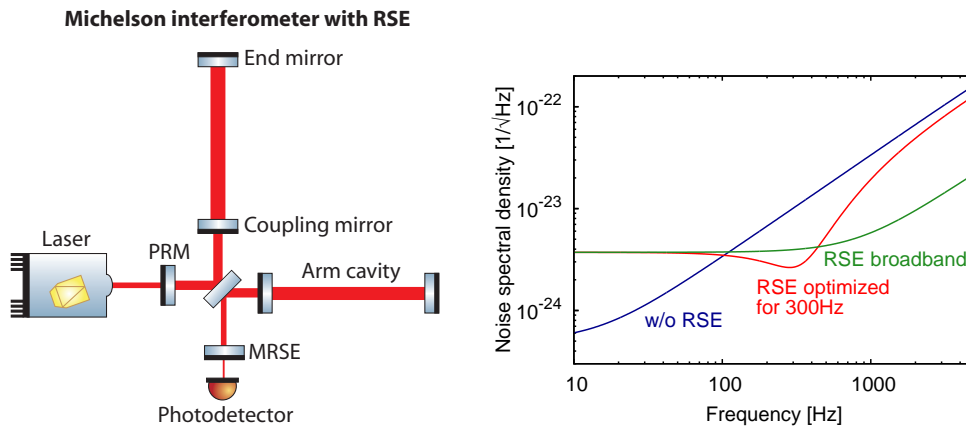


**Figure 1.2** — **Left:** Illustration of the RSE topology. The extraction cavity is built by the mirror MRSE and the arm cavities coupling mirrors. This cavity has a frequency dependent reflection which is lower than that of the coupling mirrors. Accordingly, for signal sidebands resonating in the RSE cavity the effective arm cavities linewidth is increased. **Right:** Shot noise limited sensitivities of the Advanced LIGO optical configuration [16] achieved with RSE optimized for 300 Hz and tuned (broadband) RSE. In comparison the sensitivity without RSE are shown. For visualization purposes the effect of radiation pressure noise was not considered in these cases.

### 1.3.3 The RSE topology

As high-finesse arm cavities will be used to achieve the required power build-up, the detection bandwidth would be limited by the cavities linewidth. To broaden the effective linewidth for signal sidebands, the *Resonant-Sideband-Extraction* technique (RSE) [31] will be realized in future detectors. Similar to the SR technique, an additional mirror is placed in the detection port. Compared with the arm-cavity coupling mirrors, the RSE cavity has a reduced effective reflectivity around its resonance. Accordingly, sidebands at frequencies above the arm-cavities linewidth can be extracted if the resonance frequency of the RSE cavity is chosen properly. Figure 1.2 illustrates the RSE topology and compares the shot noise limited sensitivities achieved with and without RSE.

### 1.3.4 Injection of squeezed states of light

The improvement of the quantum noise limit sensitivities of gravitational-wave detectors by using *squeezed states* of light was first proposed by Caves [32].

He showed, that the injection of a broadband squeezed field into the interferometers detection port can be used either to relax the high-power requirements or to further improve the sensitivity for a given circulating power. Recently, squeezed fields covering the entire detection band of earth bound gravitational-wave detectors were demonstrated [33]. Here a squeezing level of about 6.5 dB was achieved. Moreover, in the MHz regime impressive squeezing values of 10 dB could be realized [34]. Based on these results, a squeezed light source is currently developed for the application at GEO 600 in the very near future. The shot noise reduction of a suspended interferometer by squeezed field injection was already demonstrated at the Caltech 40 m-prototype [35].

Compared to the vacuum state, a squeezed state yields a reduced uncertainty in one of the field quadrature – the *squeezed quadrature*. In the orthogonal quadrature – the *anti-squeezed quadrature* – the uncertainty is increased by the same amount. Accordingly, the reduction of quantum noise can be achieved by replacing the vacuum state that enters the interferometer through the detection port by a squeezed state. Considering a simple Michelson interferometer, the shot noise level can be reduced by injection of a state squeezed in the phase quadrature. Unfortunately, the increased noise in the anti-squeezed amplitude quadrature enhances the radiation pressure noise by the same amount. It was revealed by Unruh [36] and others [37, 27, 38] that the quantum noise can be reduced in the entire detection band by a squeezed state with a *frequency dependent* squeezed quadrature. Based on these results, the use of so-called *filter cavities* was proposed by Kimble *et al.* [39]. By reflecting the squeezed field at these cavities, the squeezed quadrature can be rotated optimally in a frequency dependent manner.

## 1.4 Structure of the thesis

Within the framework of this thesis new interferometer topologies based on coupled optical resonators were investigated theoretically and experimentally. Motivated by the problem of thermal lensing in future gravitational-wave detectors, the four-mirror cavity enhanced Michelson interferometer presented in Chapter 3 was analyzed as a possible alternative to the RSE topology. This topology consists of three linearly coupled optical resonators in each interferometer arm. Since the analytical expressions of the shot-noise limited sensitivities depend on 11 free parameters, applicable configurations are not obvious. To allow a systematic analysis a detailed investigation of coupled

resonators was necessary. This required analysis is presented in Chapter 2.

In Chapter 4 a novel interferometer technique is proposed for the use as squeezed light enhanced gravitational-wave detector. This topology termed *Detuned Twin-Signal-Recycling* (TSR) efficiently exploit the resonance doublet of a linearly coupled three-mirror cavity at a particular operating point. As a specific characteristic the sensitivity in the entire shot noise limited detection band can be improved by the injection of *frequency independent squeezing*. A detailed comparison with the GEO 600 topology for technical design parameters is presented. It will be shown, that TSR is favorable compared to single side-band recycling techniques like signal recycling as it provides an broadband improved sensitivity. Furthermore, the possible shaping of the sensitivity curve with respect to an exemplary target frequency will be demonstrated. In the final part of this Chapter possible parameters for an application in the future GEO-HF detector [40] are reviewed. As well, the improvement from a conversion of RSE to Twin-RSE by an elongation of the extraction cavity is exemplary demonstrated for the optical configuration of the Advanced LIGO detector.

The first experimental realization of a table-top squeezing enhanced TSR interferometer is presented in Chapter 5. Accompanied by extensive numerical simulations an upgrade of an existing table-top dual-recycled Michelson interferometer [41] was possible. A broadband reduction of the TSR interferometers shot noise of up to 4 dB was achieved whereby the experimental results were in good agreement with numerical simulations.

In Chapter 6 the experimental investigation of a Kerr non-linear resonator is reported. In this experiment the *cascaded Kerr-effect* [42] was exploited for passive laser power noise reduction. Several measurement results are presented demonstrating together with numerical simulations the presence of a strong effective third-order non-linearity. It is shown that the power noise of a 750 mW continuous-wave laser beam can be reduced by means of a Kerr non-linear resonator. A maximum reduction of 32 dB was achieved at a frequency of about 1 MHz corresponding to about one fifth of the resonators linewidth. Finally, a tomographic analysis including the reconstruction of the Wigner function of the manipulated noise distribution is presented.

In Chapter 7 a summary and an outlook are given.

In the Appendix source codes used for numerical simulations are provided.



---

# Optical resonators

In this thesis Fabry-Pérot resonators play an essential roll. Especially coupled Fabry-Pérot resonators yield a variety of possible applications in interferometric gravitational wave detectors. Hence, in Section 2.1 the simplest resonator consisting of only two mirrors is described in detail. The analytical expressions for the light fields and the frequency response (transfer function) are derived. In Section 2.2 the results are transferred to the case of linearly coupled resonators .

## 2.1 Analytical description of a two-mirror cavity

Generally, a Fabry-Pérot resonator is built by at least two, spatially separated mirrors (or reflecting surfaces in the case of an etalon) which are oriented such that the light propagates on one path between these mirrors. This can be realized as a linear resonator in which the reflecting surfaces are orientated orthogonal to the light path. In this Chapter the description is constricted to the case of linear Fabry-Pérot resonators consisting of two mirrors (denoted as two-mirror cavity in the following) . The obtained expressions for the carrier fields and transfer functions can be easily adapted to the case of so-called ring resonators.

To derive the analytic description of a two-mirror cavity, several assumptions are made for simplicity. First, it is assumed that the incident light matches perfectly the eigenmode defined by the resonator [43]. Second, it is assumed that the resonator is in equilibrium whereby effects of the resonator's dynamic can be neglected. Third, the resonator is assumed to be optical loss-free. Afterwards the gained analytical expressions are transferred to lossy resonators.

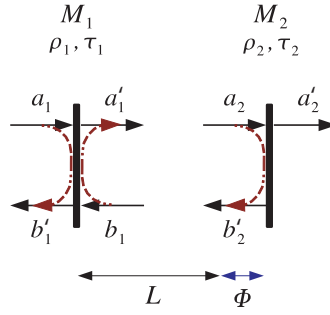


**Figure 2.1** — Illustration of the labeling used throughout this Section for the quantities at a two-mirror cavity.  $L$ : macroscopic resonator length,  $\Phi$ : microscopic resonator length (referred to as *tuning* of the resonator),  $M_i$ : Mirror,  $\rho_i$ : amplitude reflectance,  $\tau_i$ : amplitude transmittance,  $a_j$  fields in forward propagation and  $b_j$  field in backward propagation.

Additionally, the dynamics of a resonator will be discussed. Here, the *ringing effect* [44] is considered occurring at a resonator crossing its resonance within a short time .

### 2.1.1 Carrier fields

In this Section the expressions describing the resonance feature of a light field with the angular frequency  $\omega_0 = 2\pi/\lambda \cdot c$  inside a two-mirror cavity are derived. In the following this light field will be called *carrier* based on the sideband picture used for describing the modulation of light fields. An illustration of the classical sideband picture can be found in [45].

Figure 2.1 shows the labeling of the used quantities. Here  $a_j$  and  $a'_j$  denotes the fields in forward propagation and  $b_j$  and  $b'_j$  those in backward propagation. The macroscopic length  $L$  separating the cavity mirrors  $M_i$  is assumed to be an integer multiple of the carrier light's wavelength  $\lambda$ . Accordingly, the resonance of the two-mirror cavity needs to be determined by a tuning  $\Phi = \Omega L/c$ . Here the frequency  $\Omega$  is added to the carrier frequency  $\omega_0$ . Note, that  $\omega_0 L/c$  corresponds to the tuning  $\Phi_0 = N \cdot 2\pi$ .

To describe the coupling of the four light fields at a mirror  $M$  the matrix

$$M = \begin{pmatrix} \rho & i\tau \\ i\tau & \rho \end{pmatrix} \quad (2.1)$$

is used. Considering a single light field (in) impinging on a mirror  $M$ , the

resulting fields in reflection (refl) and transmission (trans) of this mirror can be obtained by solving the equation

$$\begin{pmatrix} \text{refl} \\ \text{trans} \end{pmatrix} = \begin{pmatrix} \rho & i\tau \\ i\tau & \rho \end{pmatrix} \begin{pmatrix} \text{in} \\ 0 \end{pmatrix}. \quad (2.2)$$

One obtains

$$\text{refl} = \rho \cdot \text{in} \quad \text{and} \quad (2.3)$$

$$\text{trans} = i\tau \cdot \text{in}. \quad (2.4)$$

In this formalism the transmitted field gains a phase shift of  $i = \exp(i\pi/2)$  whereas the reflected field has no additional phase shift. Since it was assumed that the two-mirror cavity is in equilibrium, the light fields at the two-mirror cavity are given by the self-consistent equations (refer to Fig. 2.1)

$$a'_1 = i\tau_1 a_1 + \rho_1 b_1 \quad (2.5)$$

$$b_1 = a'_1 \rho_2 e^{2i\Phi} \quad (2.6)$$

$$b'_1 = i\tau_1 b_1 + \rho_1 a_1. \quad (2.7)$$

The phase factor  $e^{2i\Phi}$  in Eq. (2.6) accounts for the light's phase delay occurring while traveling twice the geometric cavity length  $L + \lambda\Phi/(2\pi)$ . Inserting Eq. (2.6) into Eq. (2.5) leads to the expression for the enhancement of the carrier field inside of the resonator

$$CF = a'_1 = \frac{i\tau_1}{1 - \rho_1 \rho_2 e^{2i\Phi}} \cdot a_1. \quad (2.8)$$

From this equation the carrier field  $\tau_{2\text{MC}}$  transmitted through the two-mirror cavity can be derived to

$$\tau_{2\text{MC}} = i\tau_2 \cdot a'_1 e^{i\Phi} = -\frac{\tau_1 \tau_2 e^{i\Phi}}{1 - \rho_1 \rho_2 e^{2i\Phi}} \cdot a_1. \quad (2.9)$$

Inserting Eq. (2.8) into Eq. (2.6) leads together with Eq. (2.7) to the carrier field  $\rho_{2\text{MC}}$  in reflection of the two-mirror cavity

$$\begin{aligned} \rho_{2\text{MC}} = b'_1 &= \frac{-\tau_1^2 \rho_2 e^{2i\Phi}}{1 - \rho_1 \rho_2 e^{2i\Phi}} \cdot a_1 + \rho_1 \cdot a_1 \\ &= \frac{-\tau_1^2 \rho_2 e^{2i\Phi}}{1 - \rho_1 \rho_2 e^{2i\Phi}} \cdot a_1 + \frac{\rho_1 (1 - \rho_1 \rho_2 e^{2i\Phi})}{1 - \rho_1 \rho_2 e^{2i\Phi}} \cdot a_1 \\ &= \frac{\rho_1 - (\tau_1^2 + \rho_1^2) \rho_2 e^{2i\Phi}}{1 - \rho_1 \rho_2 e^{2i\Phi}} \cdot a_1. \end{aligned} \quad (2.10)$$

Since the two-mirror cavity is assumed to be loss-free,  $\tau_1^2 + \rho_1^2 = 1$  is valid and Eq. (2.10) can be simplified to

$$\rho_{2\text{MC}} = \frac{\rho_1 - \rho_2 e^{2i\Phi}}{1 - \rho_1 \rho_2 e^{2i\Phi}} \cdot a_1. \quad (2.11)$$

### 2.1.2 Characteristic quantities

The expressions for the reflectance Eq. (2.11), the internal field Eq. (2.8) and the transmittance Eq. (2.9) of a two-mirror cavity have the common factor

$$d(\Phi) = \frac{1}{1 - \rho_1 \rho_2 e^{2i\Phi}} \quad (2.12)$$

which describes the periodic resonance condition of the resonator. Its squared absolute value

$$D(\Phi) = |d(\Phi)|^2 = \frac{1}{1 + \rho_1^2 \rho_2^2 - 2\rho_1 \rho_2 \cos 2\Phi} \quad (2.13)$$

becomes maximum if  $\Phi = 0 \pmod{\pi}$ . Thus, the resonance frequencies are determined by the relation

$$2 \frac{(\omega_0 + \Delta\Omega^{\text{res}} j) L}{c} = 2\pi j. \quad (2.14)$$

The so-called *free spectral range* (FSR) of a two-mirror cavity is defined as the distance between two sequent resonances leading to

$$\text{FSR} = \Delta\Omega^{\text{res}} = \Omega_{j+1}^{\text{res}} - \Omega_j^{\text{res}} = \frac{c}{2L}, \quad (2.15)$$

where  $\Phi_0 = \omega_0 L / c = N \cdot 2\pi$  was used.

Furthermore, from Eq. (2.13) the *full width at half maximum* (FWHM) can be derived. With

$$D_{\text{max}} = \frac{1}{(1 - \rho_1 \rho_2)^2} \quad \text{for } \Phi = 0 \quad (2.16)$$

one has to solve the equation

$$\frac{1}{2} D_{\text{max}} = D(\Phi_{\text{HM}}) \quad (2.17)$$

leading to

$$\Phi_{\text{HM}} = \pm \frac{1}{2} \arccos \left( 1 - \frac{(1 - \rho_1 \rho_2)^2}{2\rho_1 \rho_2} \right). \quad (2.18)$$

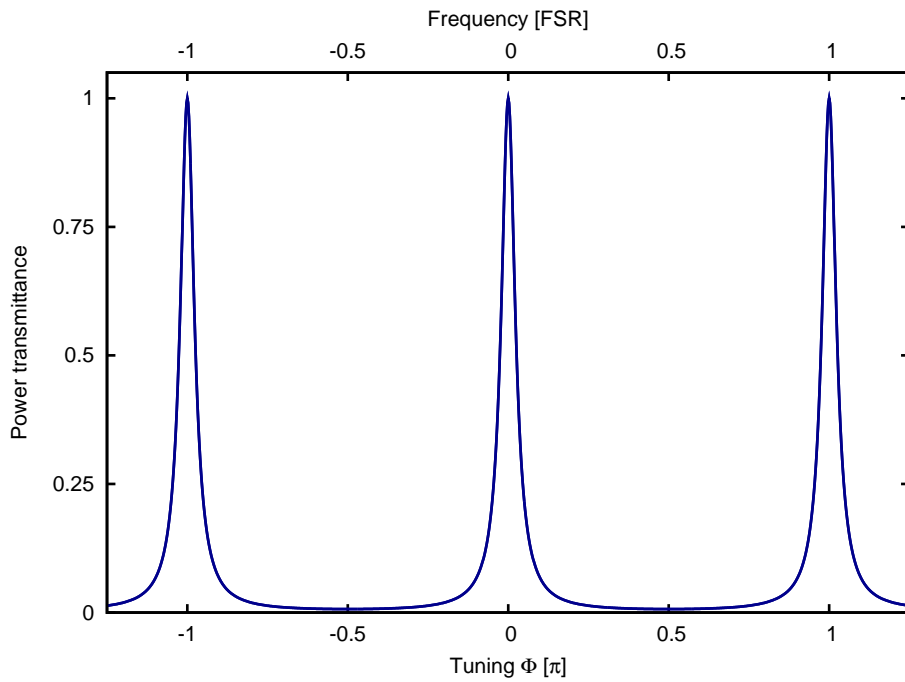


**Figure 2.2** — The figure shows the power transmittance of a two-mirror cavity while it is tuned over two free spectral ranges (FSRs).

With  $\Phi_{\text{HM}}$  the full width at half maximum can be expressed in Fourier frequencies  $f = \Omega/2\pi$  according to

$$\text{FWHM} = \frac{2 \cdot \Phi_{\text{HM}} \cdot c}{2\pi L}. \quad (2.19)$$

The third characteristic quantity of a Fabry-Pérot resonator is the so-called finesse which is defined as

$$\mathcal{F} = \frac{\text{FSR}}{\text{FWHM}}. \quad (2.20)$$

This definition resembles the so-called Q-factor of mechanical and electrical LC-oscillators, respectively.

### 2.1.3 Description of a lossy two-mirror cavity

If optical losses are considered as well, all equations derived in the previous sections can simply be adapted. If one accounts for losses of the mirrors

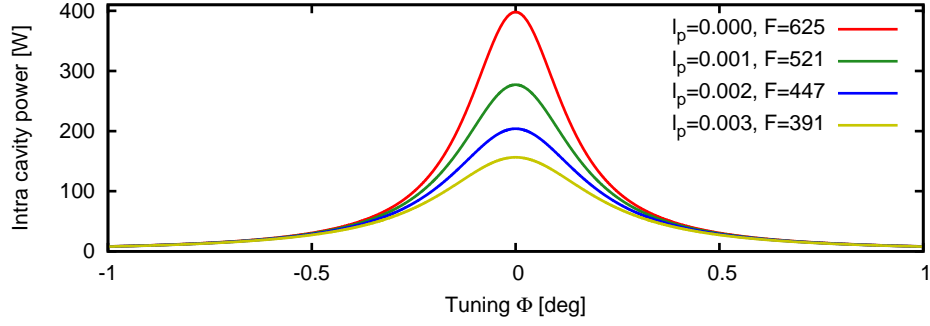


**Figure 2.3** — Airy peak of a two-mirror cavity with various values of the internal loss. The reflectance of  $M_1$  and  $M_2$  was set to  $\rho_1 = \sqrt{0.8}$  and  $\rho_2 = \sqrt{0.9}$ , respectively. The intra-cavity power was calculated for an input power of 1 W.

themselves, the relations

$$\rho_1^2 + \tau_1^2 + A_1^2 = 1 \quad \text{and} \quad (2.21)$$

$$\rho_2^2 + \tau_2^2 + A_2^2 = 1 \quad (2.22)$$

are valid. The attenuation of the light field occurring while propagating between the cavity mirrors is described as

$$A_p = \sqrt{1 - l_p^2}. \quad (2.23)$$

Here  $l_p$  is the amplitude attenuation per half round trip. Thus, by replacing the term  $\rho_2 e^{2i\Phi}$  describing the round trip in the loss-free case by  $\rho_2 A_p^2 e^{2i\Phi}$  the light fields  $\rho_{2MC}$  in reflection,  $\tau_{2MC}$  in transmission and the carrier field enhancement  $CF$  inside of the two-mirror cavity can be written as

$$\rho_{2MC} = \frac{\rho_1 - (\rho_1^2 + \tau_1^2) \rho_2 A_p^2 e^{2i\Phi}}{1 - \rho_1 \rho_2 A_p^2 e^{2i\Phi}} \cdot a_1, \quad (2.24)$$

$$CF = \frac{i\tau_1}{1 - \rho_1 \rho_2 A_p^2 e^{2i\Phi}} \cdot a_1 \quad \text{and} \quad (2.25)$$

$$\tau_{2MC} = \frac{-\tau_1 \tau_2 A_p e^{i\Phi}}{1 - \rho_1 \rho_2 A_p^2 e^{2i\Phi}} \cdot a_1. \quad (2.26)$$

The FWHM and the finesse  $\mathcal{F}$  can be calculated by replacing  $\rho_2$  by  $\rho_2 A_p^2$  according to the derivation of Eq. (2.19) and Eq. (2.20), respectively.

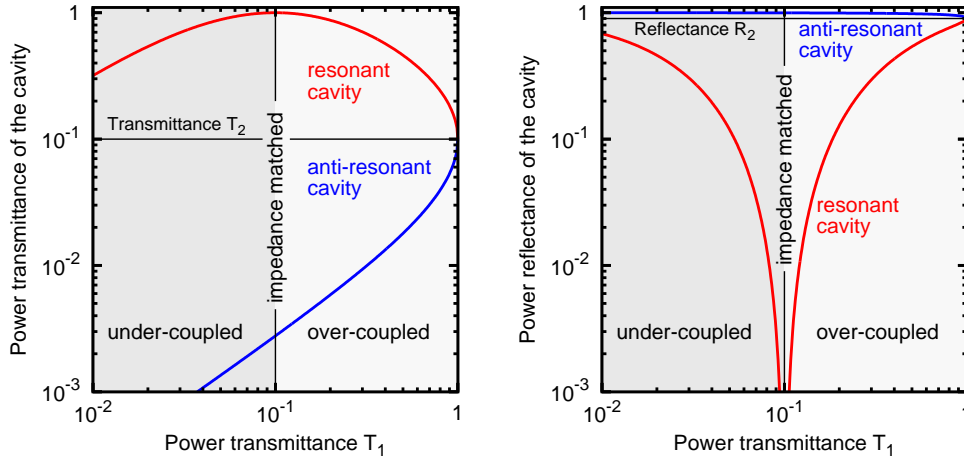


**Figure 2.4** — Dependence of the power transmittance (left) and reflectance (right) of a two-mirror cavity with a fixed round-trip loss (here given by the transmittance  $T_2 = \tau_2^2$  of the end-mirror) but different couplings determined by  $T_1 = \tau_1^2$ .

### 2.1.4 Coupling to a two-mirror cavity

For a given reflectivity  $\rho_2$  of the commonly called end-mirror  $M_2$  (refer to Fig. 2.1) the power build-up in the two-mirror cavity becomes maximum if the transmittance  $\tau_1$  of mirror  $M_1$  (commonly called coupling mirror) matches the light fields attenuation (loss) per round trip according to

$$\tau_1 = A_p^2 \tau_2. \quad (2.27)$$

In this so called impedance-matched case the power reflectance of a two-mirror cavity becomes zero on resonance. Either increasing or decreasing the transmittance  $\tau_1$  leads to a power reflectance of the cavity greater than zero and a lower build-up of the intra cavity field. This behavior is shown in Fig. 2.4 assuming  $A_p = 0$ . One distinguishes between the so-called over-coupled case where  $\tau_1$  is greater than the round-trip loss according to

$$\tau_1 > A_p^2 \tau_2 \quad (2.28)$$

and the so-called under-coupled case with

$$\tau_1 < A_p^2 \tau_2. \quad (2.29)$$

To demonstrate the difference between these three cases, it is useful to utilize the phasor diagram of the light field reflected from the two-mirror

cavity. For simplicity  $A_p$  was set to zero so that the round-trip loss of the cavity is given by the transmittance of the end-mirror. Furthermore, rewriting the expression for the reflected field given in Eq. (2.25) as

$$\rho_{2MC} = \rho_1 - \rho_2 \frac{\tau_1^2 A_p^2 e^{2i\Phi}}{1 - \rho_1 \rho_2 A_p^2 e^{2i\Phi}} = \rho_1 + c_{out}. \quad (2.30)$$

allows to distinguish between the part of the field directly reflected from the coupling mirror  $M_1$  (first term in Eq. (2.30)) and the out-coupling  $c_{out}$  of the internal light field (second term). Here the input field  $a_1$  was set to unity. Whereas as the first term is constant, the second one depends on the tuning  $\Phi$  of the resonator. It should be mentioned that this term can also be derived from the geometric series

$$s = -\tau_1^2 \rho_2 A_p^2 e^{2i\Phi} \cdot \sum_{n=0}^{\infty} \rho_1^n \rho_2^n A_p^{2n} e^{2in\Phi} \quad (2.31)$$

which illustrates the build-up of the internal carrier field until it reaches an equilibrium.

In Figures 2.5- 2.7 the reflectance of a two-mirror cavity is illustrated for two different tunings (red and blue phasors). The left circle of each figure corresponds to the second term ( $c_{out}$ ) of Eq. (2.30) represented by a rotating phasor depending on the cavity tuning  $\Phi$ . The right circle of each figure describes the cavity reflectance given by the sum of  $c_{out}$  and the black phasor that represents the direct reflected part which is proportional to  $\rho_1$ . The red colored phasors show the fields for a two-mirror cavity tuned close to resonance. The gained phase shift per round-trip is close to zero, which is illustrated with the arrow sequence (light-red) corresponding to Eq. (2.31). These phasors add up to the red phasor pointing on the circle representing the field coupled out of the resonator if the internal field has reached equilibrium. The sum of this phasor and the black phasor add up to the reflectance of the two-mirror cavity illustrated with the dark-red phasor. In the same manner, the blue phasors represents the fields for an arbitrary cavity tuning. One can deduce from these phasor diagrams that on resonance the field coupled out of the resonator is phase-shifted by  $\pi$  ( $180^\circ$ ) against the direct reflected field. Thus, on resonance, these two parts interfere destructively clarifying the minimum reflectance of a tuned two-mirror cavity. On the other hand, on anti-resonance both phasors point in the same direction leading to maximum reflectance.

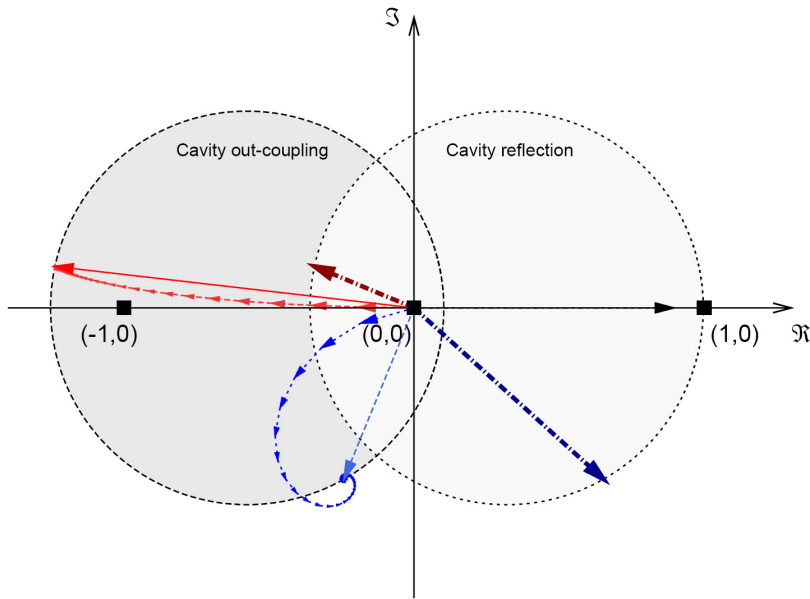


Figure 2.5 — Phasor diagram of the light field reflected by an over-coupled cavity.

In Fig. 2.5 the phasor diagram of an over-coupled cavity is shown. At resonance the phasor representing the field  $c_{\text{out}}$  is longer than the fixed one corresponding to the direct reflection at  $M_1$ . Thus, the sum of these phasors representing the cavity reflection points in opposite direction of the fixed one. That means that on resonance the reflected field has a phase shift of  $\pi$  or  $180^\circ$ , respectively. In contrast to this, in the case of an under-coupled cavity (see Fig. 2.6) the rotating phasor is smaller than the fixed one for all cavity tunings. Thus, the phasor representing the reflection of the resonant cavity points in the same direction as the fixed phasor. Here, the phase-shift of the field reflected by the cavity is zero. Note, that the length of the phasors describing the cavity reflection is equal in both cases, because the exemplary chosen values for the reflectance of the coupling- and end-mirror were simply inverted for the two cases.

Fig. 2.7 shows the phasor diagram of an impedance-matched cavity. Here the phasor describing the field coupled out of the cavity matches exactly the length of the fixed one. Consequently, the reflectance of an impedance-matched cavity tuned to resonance is zero. Since there is no field reflected, the phase is not defined. Considering the dark-red phasor shown in Fig. 2.7 it

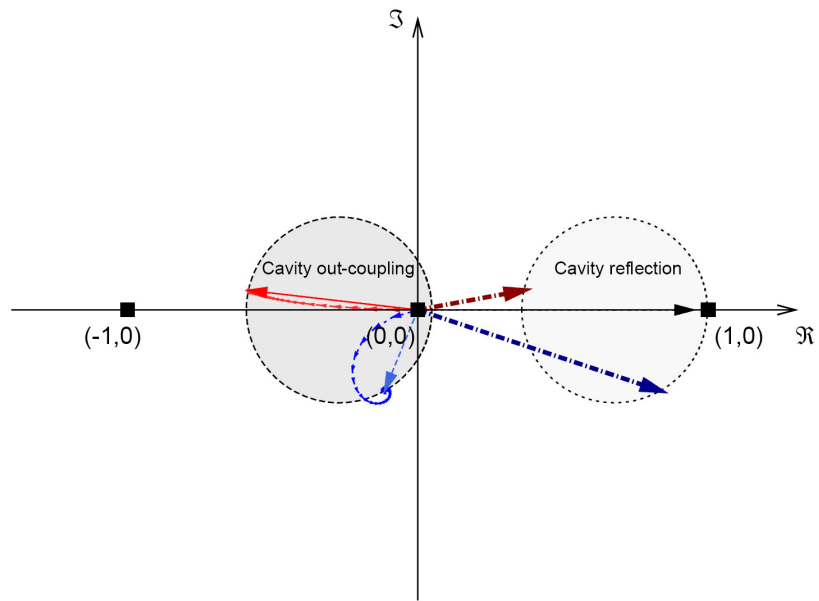


Figure 2.6 — Phasor diagram of the light field reflected by an under-coupled cavity.

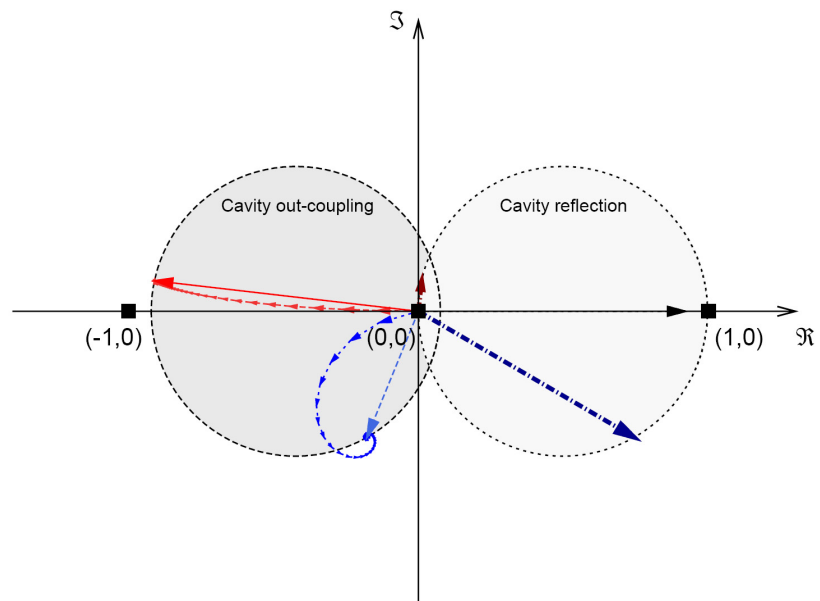
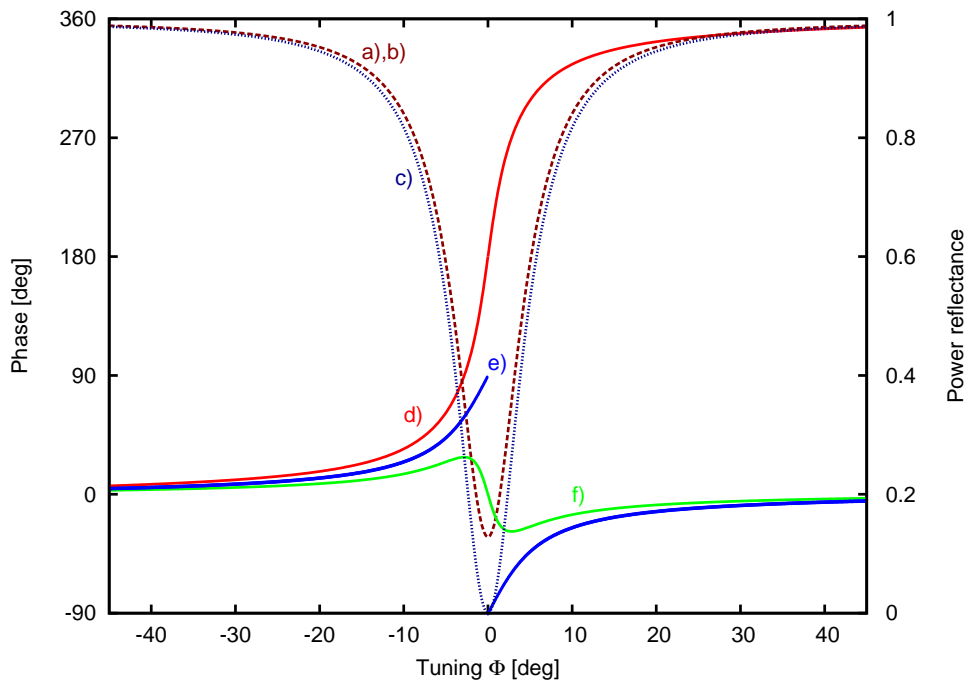


Figure 2.7 — Phasor diagram of the light field reflected by an impedance-matched cavity.



**Figure 2.8** — Power reflectance of an a) over-coupled, b) under-coupled and c) impedance-matched cavity. The power reflectance is  $R_1 = 0.8$  for the coupling-mirror and  $R_2 = 0.9$  for the end-mirror in the over-coupled case. For the under-coupled cavity these reflectivities were simply inverted. In the case of the impedance-matched cavity the power reflectance of both mirrors is  $R = \sqrt{0.8 \cdot 0.9}$  leading to the same bandwidth for all three cases. Also the phase-shifts are shown for the d) over-coupled, e) impedance-matched and f) under-coupled case.

becomes clear, that the phase of the field reflected at an impedance-matched cavity shows a real phase jump (from  $\pi/2$  ( $90^\circ$ ) to  $-\pi/2$  ( $-90^\circ$ ) or vice versa) when crossing the resonance.

To demonstrate the difference of the three cases again – especially with respect to the phase – Fig. 2.8 shows the cavity reflectance in dependence on the tuning  $\Phi$ .

### 2.1.5 Resonator dynamics

For the previous description of a static two-mirror cavity the intra cavity field was assumed to be in equilibrium. That means, that the discussed dependencies of the resonator tuning  $\Phi$  are only valid in the static case. In this

Section the light fields of a two-mirror cavity with a time dependent tuning  $\Phi(t)$  will be discussed. If the tuning is changed such that the resonance is crossed within a short time in the order of the cavities' storage time

$$t_s = \frac{L}{c(1 - \rho_1\rho_2)}, \quad (2.32)$$

the ringing effect occurs [44]. It was shown by Matone *et al.* [46] that the characteristics of the ringing effect allows an evaluation of a resonator's finesse and expansion rate on the basis of a fit of numerical simulations to the measured data. Within the experimental investigations of a Kerr non-linear resonator the presence of an effective third order non-linearity was demonstrated by hysteresis measurements as described in Chapter 6. Here, the resonance of the Kerr non-linear resonator needed to be crossed in a very short time to reduce the influence of thermal effects. Accordingly, the resonator dynamics needs to be considered for an interpretation of these measurements.

In section 2.1.4 the resonator light fields were explained inter alia by the aid of phasor diagrams. The build-up of the internal resonator field was illustrated using the geometric series (Eq. 2.31). Now the light fields are considered for a certain constant expansion rate  $\nu$  of the cavity. The length of the cavity at the time  $t$  is then given by

$$L(t) = L(0) + \nu t, \quad (2.33)$$

which corresponds to the time dependent tuning

$$\Phi(t) = \Phi(0) + \frac{2\pi}{\lambda} \nu t. \quad (2.34)$$

Thus, using the geometric series again the internal field at a time  $n \cdot t_{rt}$  can be written as

$$CF(n \cdot t_{rt}) = i\tau_1 a_1(0) \sum_{k=0}^n (\rho_2 \rho_1)^k \exp \left[ 2i \sum_{l=0}^{k-1} \Phi_{n-1-k} \right] \quad (2.35)$$

with the resonators round-trip time  $t_{rt} = 2L/c$  and

$$\Phi_n = \Phi(0) + \frac{2\pi}{\lambda} \cdot \nu \cdot n \cdot t_{rt}. \quad (2.36)$$

Unfortunately, the internal circulating power  $|CF(t)|^2$  can not be calculated analytically with Eq. (2.35). But when starting the expansion of a static resonator

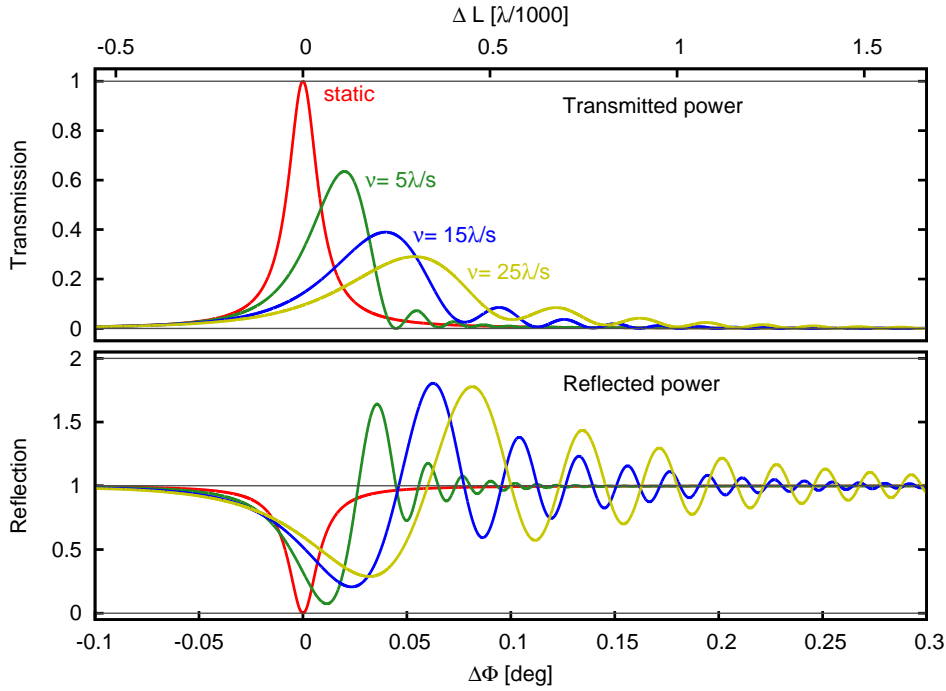


**Figure 2.9** — The figure shows the ringing effect of a two-mirror cavity. Top: Transmitted power. Bottom: Reflected power. With increasing expansion rates  $\nu$  the maximum transmission decreases (the minimum reflection increases, respectively) and is shifted towards stronger detunings  $\Phi(t)$ . Also the oscillatory behavior becomes more considerable at high expansion rates. It is interesting to note, that for some tunings  $\Phi(t)$  the reflected power is higher than the incident power.

(whose internal field is in equilibrium) at the time  $t = -t_{rt}$  and assuming that the effect of the length change of the resonator can be neglected within the round-trip time  $t_{rt} = 2L/c$ , the internal field after each time step  $dt = t_{rt}$  can be written as

$$CF(n \cdot dt) = i\tau_1 a_1 + \rho_2 \rho_1 e^{2i\phi((n-1) \cdot dt)} \times CF((n-1)dt) \quad \text{with } n > 0. \quad (2.37)$$

Based on this equation a numerical evaluation of the evolving field is possible. Fig. 2.9 shows the power transmittance and reflectance of a resonator with a finesse of approximately 10500 for three different expansion rates  $\nu = 5\lambda/s$ ,  $\nu = 15\lambda/s$  and  $\nu = 25\lambda/s$ . These three cases are shown in comparison to the static Airy peak. One can observe, that with a rising expansion rate  $\nu$  the maximum of the transmission decreases. This phenomenon can be explained

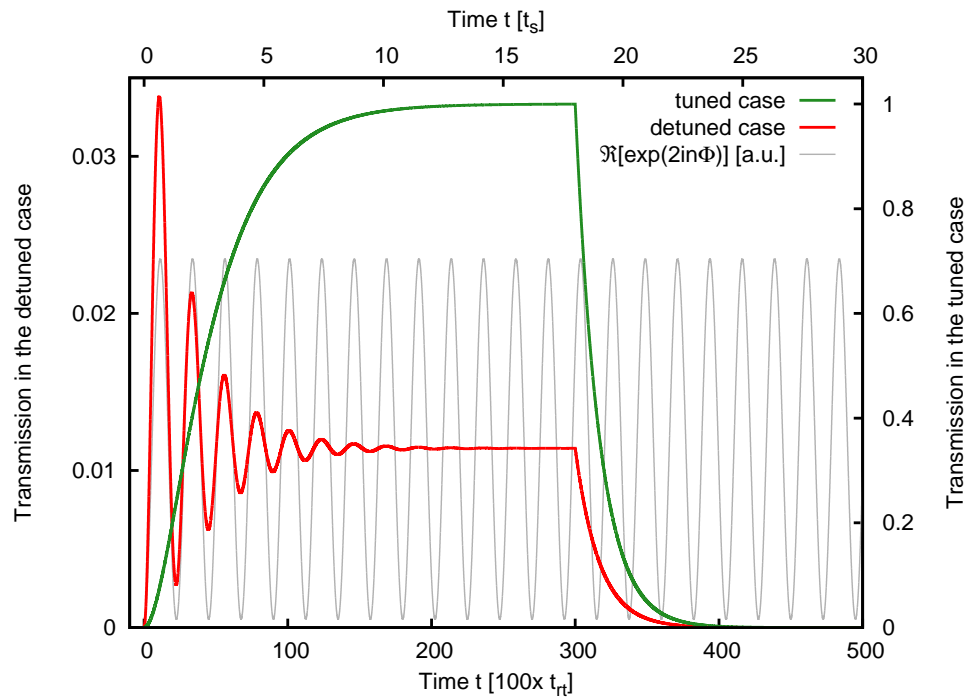


**Figure 2.10** — Transmission of a static two-mirror cavity during the build-up time for the tuned ( $\Phi = 0^\circ$ ) and detuned ( $\Phi = 0.08^\circ$ ) case, respectively. The internal field evolves until it tends to converge after approximately 25000 round-trips. At the time  $t = 30000 \cdot t_{rt}$  the input field is switched off. In the tuned case no ringing occurs within the build-up time whereas the detuned case shows a clear oscillation. After the input field is switched off, both cases show the pure decay of the internal field. The grey curve shows the real part of the phasing  $e^{2in\Phi}$  for the detuned case to illustrate the origin of the ringing-effect (see text).

by considering the storage time (build-up time) of a two-mirror cavity. At high expansion rates  $\nu$  the resonance of the resonator is crossed in a very short time in the order of the storage time. Accordingly, the internal build-up does not reach the value expected from the static resonator. Also the origin of the oscillatory behavior in the transmitted and reflected fields can be related to the fact, that at high expansion rates the fields do not reach an equilibrium at a certain tuning  $\Phi(t)$ . To comprehend this behavior it is convenient to consult the time evolution of the internal resonator field of the considered two-mirror cavity in the *static* case and the corresponding phasor diagram (as already shown in Figs. 2.5- 2.7 for a low-finesse cavity).

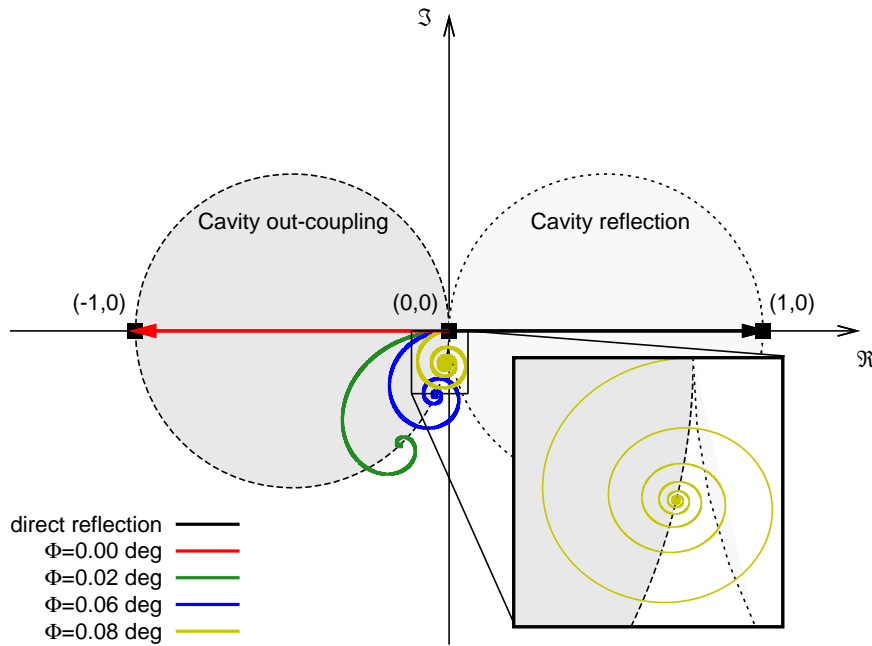


**Figure 2.11** — Phasor diagram of the field build-up for various *static* tunings  $\Phi$  of the resonator. The inset shows a close-up view for  $\Phi = 0.08^\circ$  to emphasize the spiral form described by the phasors.

When looking at the evolving power transmission shown in Fig. 2.10 one can observe that in the tuned case no ringing occurs. From the corresponding phasor diagram shown in Fig. 2.11 one can deduce that for the tuned resonator the phasors add up constructively. The accumulated phase shift is zero within the build-up time. In contrast to this in the detuned case a phase factor of  $e^{2i\Phi}$  per round-trip is accumulated. Hence, the time evolution of the phasors shows an inspiral behavior until the equilibrium is reached. With greater detunings  $\Phi$  the number of cycles increases (refer to the inset of Fig. 2.11). Thus, at some times these phasors point in the direction of the phasor describing the direct reflection (black phasor in Fig. 2.11) and at other times they point in the opposite direction. For illustration in Fig. 2.10 the real part of the accumulated phase factor  $e^{2in\Phi}$  at a certain time  $t$  is shown. In fact, the oscillation of the time evolving transmitted power and the term  $\Re(e^{2in\Phi})$  shows the same period. The period of this oscillation can be deduced to  $T = \pi/\Phi \cdot t_{rt}$ . In this time the phase of the internal field gains a factor of

$\pi$  leading to constructive or destructive interference, respectively, clarifying the oscillation in the transmitted as well as in the reflected power. Also the fact, that at some times the reflected power is greater than the input power can be understood by consulting the phasor diagram. At some times the phasor describing the field coupled out of the cavity lies outside of the circle describing the intra-cavity fields when the equilibrium is reached (refer to Sec. 2.1.4). Accordingly, at these times the sum of the direct reflection and the leakage of the internal field is greater than one.

Now, the case of a dynamic resonator is considered again taking the above findings into account. If the time needed for crossing the resonance is in the order of the build-up time, the situation is similar to that shown for a certain fixed tuning in Fig. 2.10. Additionally, since the tuning changes with the time, the period of the ringing – which were found to be reciprocal proportional to the tuning in the static case - shows a time dependence. As the tuning  $\Phi(t)$  increases with time it becomes clear that the period of the ringing decreases correspondingly (refer to Fig. 2.9).

### 2.1.6 Transfer function

In this Section the analytical expressions describing the transfer function of a two-mirror cavity are derived. For an exemplary set of parameters the properties of the transfer function is analyzed for the tuned and detuned case, respectively. In Section 2.1.1 the carrier fields in a two-mirror cavity were described using the tuning  $\Phi = \Omega L/c$ . If one wants to consider the frequency dependent transfer function of a two-mirror cavity set to a certain tuning  $\Phi$  (related to the carrier frequency) one has to replace

$$\Phi \text{ by } \Phi + \frac{\Omega L}{c} \quad (2.38)$$

in Eqs. (2.8), (2.9) and (2.11). Figure 2.12 a) and b) show the transmittance of a carrier-tuned two-mirror cavity for light frequencies counted as offset from the carrier frequency  $\omega_0 = 2\pi f_0$ . Here the transfer function is symmetric around  $f_0$  in its amplitude and phase. In contrast to this, Fig. 2.12 c) and d) show the transmittance of a carrier-detuned cavity. In this example the cavity is tuned to 10 kHz. Accordingly the transfer function is not symmetric around  $f_0$  but  $f = 10$  kHz.

Now the transfer function for phase modulation signal sidebands generated inside the cavity due to a periodic change of the optical cavity length (caused i.e. by a moving end-mirror or a gravitational wave) is considered. A

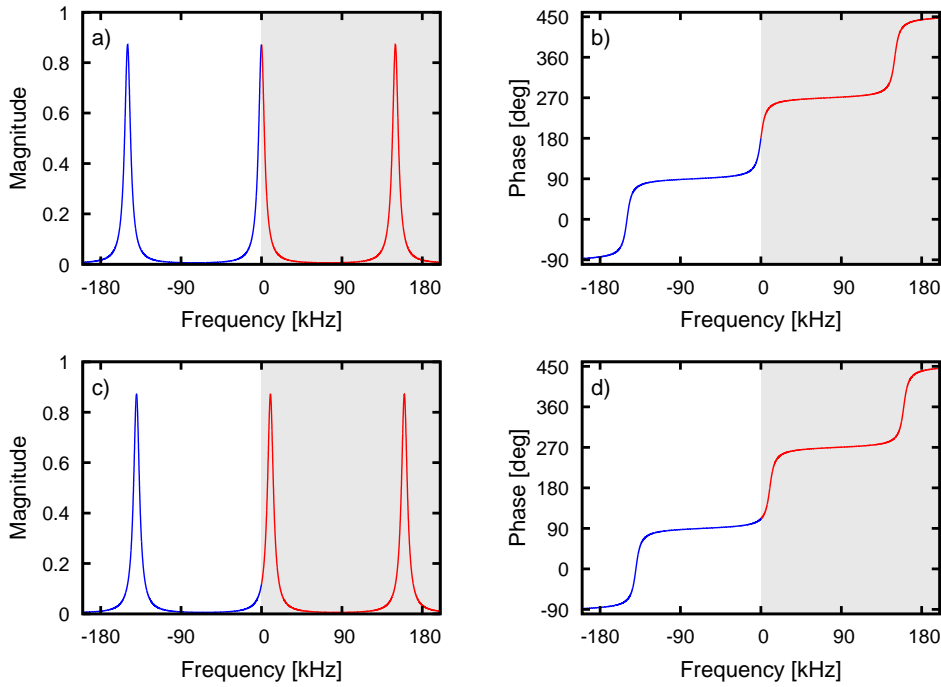


**Figure 2.12** — Frequency dependent power transmittance of a two-mirror cavity. The length of the cavity was chosen to 1 km leading to a FSR of approximately 150 kHz. a) Power transmittance  $|\tau_{2MC}|^2$  and b) phase  $\arg(\tau_{2MC})$  of the transmitted field of the tuned cavity according to Eq. (2.9). c) Transmission and d) phase for the detuned case.

modulation at the frequency  $\Omega$  produces upper and lower sideband fields at  $\omega_0 \pm \Omega$ . Thus, the transfer function is composed of two parts, each describing the transfer of the lower and upper sidebands, respectively. For simplicity the strength of this modulation and the resulting sideband amplitudes are normalized to unity. It is assumed, that the signal fields are detected in the reflection port (in front of the coupling mirror) of the cavity. Then, the frequency dependent enhancement of upper and lower signal sidebands inside the cavity and the transfer out of the cavity to the detection port are given by

$$SF_{\pm}(\Omega) = \frac{i\tau_1 e^{i(\Phi \pm \Omega L/c)}}{1 - \rho_1 \rho_2 e^{2i(\Phi \pm \Omega L/c)}}. \quad (2.39)$$

This expression equals Eq. (2.9) describing the transmittance  $\tau_{2MC}$  except for the fact that the transmittance  $\tau_2$  of the end-mirror does not appear in

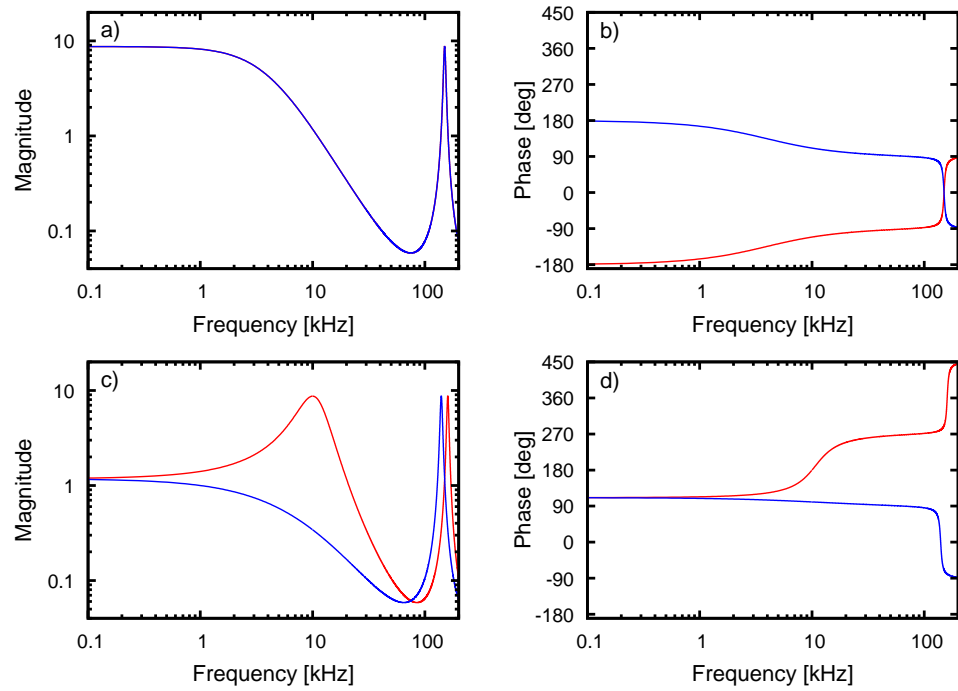


**Figure 2.13** — Transfer function of phase modulation induced sidebands. a) Magnitude and b) phase for the tuned case. c) Magnitude and d) phase for the detuned case. The red curves correspond to the transfer function of upper sidebands, whereas the blue curves correspond to the lower sidebands.

the numerator. Since the sidebands are generated inside the cavity and are transmitted through the coupling mirror towards the detection port, only the transmittance  $\tau_1$  needs to be considered.

Fig. 2.13 shows the transfer functions  $SF^+$  for upper sidebands (red curves) and  $SF^-$  for the lower sidebands (blue lines) in the tuned and detuned case. Note, that the exemplary sets of parameters are the same as used for Fig. 2.12. Again, in the tuned case the transfer function is symmetric around  $\omega_0$ . Considering the phase of upper and lower sidebands reveals that the transfer function  $SF(\Omega)$  of phase modulation signal sidebands is maximum in the carrier light's phase quadrature according to

$$SF(\Omega) = SF_+(\Omega) + SF_-^*(-\Omega). \quad (2.40)$$

In contrast to this, in the detuned case  $SF(\Omega)$  is maximum in the carrier light's phase quadrature only at frequencies above the resonance frequency

$f_{\text{res}} = 10 \text{ kHz}$ . Below  $f_{\text{res}}$  the transfer function is maximum in the amplitude quadrature according to

$$SF(\Omega) = i(SF_+(\Omega) - SF_-^*(-\Omega)) . \quad (2.41)$$

## 2.2 Coupled optical resonators

Linear coupled resonators yield a variety of possible applications in interferometric gravitational-wave detectors. One example is the combination of the power recycling technique with a Michelson interferometer containing a two-mirror cavity in each arm. Another application of linear coupled resonators in gravitational-wave detectors is the *Resonant-Sideband-Extraction* topology first proposed in [47]. Here a comprehensive description of a linear coupled three-mirror cavity and its frequency response was already presented. However, the strategy of explaining the resonance feature and deriving analytical expressions differs in some essential points from the explanation provided within this thesis. Furthermore, in this Section some continuative relations will be derived that were used for the analysis of a *four-mirror cavity enhanced Michelson interferometer* and the *Twin-Signal-Recycling* topology.

### 2.2.1 Carrier field in a three-mirror cavity

In this Section the analytical expression for the carrier field with the angular frequency  $\omega_0$  in a three-mirror cavity will be derived similar to the discussion of the two-mirror cavity in Sec. 2.1. Again, for simplicity the three-mirror cavity is assumed to be loss-free and to be in equilibrium. The used labeling is illustrated in Fig. 2.14.

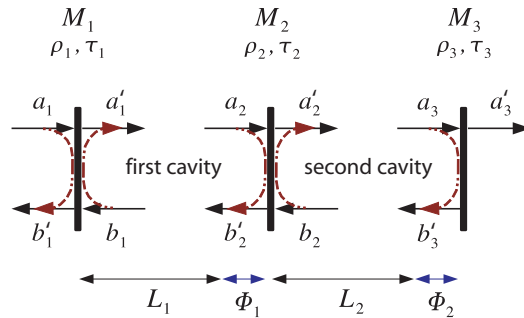


Figure 2.14 — Notation of a three-mirror cavity.

It is convenient to start with the derivation of the expression describing the carrier fields in the second cavity. Just as in the case of a single two-mirror cavity these expressions can be obtained from solving the equations

$$a'_2 = i\tau_2 a_2 + \rho_2 b_2 \quad (2.42)$$

$$b_2 = a'_2 \rho_3 e^{2i\Phi_2} \quad (2.43)$$

$$b'_2 = i\tau_2 b_2 + \rho_2 a_2. \quad (2.44)$$

Inserting Eq. (2.43) into Eq. (2.42) leads to the result for the carrier field  $CF_2$  in the second cavity given by

$$CF_2(\Phi_1, \Phi_2) = \frac{i\tau_2}{1 - \rho_2 \rho_3 e^{2i\Phi_2}} \cdot a_2. \quad (2.45)$$

This expression is identical to the case of a two-mirror cavity (refer to Eq. (2.8)). The only difference is that the input field  $a_2 = CF_1(\Phi_1, \Phi_2) e^{i\Phi_1}$  is not a constant anymore, because the internal carrier field of the first cavity also depends on  $\Phi_2$  and thus on the resonance state of the second cavity. Inserting Eq (2.45) into Eq. (2.42) leads under consideration of Eq. (2.44) to the expression for the field reflected at the second cavity given by

$$b'_2 = \underbrace{\frac{\rho_2 - \rho_3 e^{2i\Phi_2}}{1 - \rho_2 \rho_3 e^{2i\Phi_2}}}_{\rho_{23}} \cdot CF_1(\Phi_1, \Phi_2) e^{i\Phi_1}. \quad (2.46)$$

Here the abbreviation  $\rho_{23}$  was introduced describing the reflection coefficient of the second cavity for a given tuning  $\Phi_2$ .

In an analogous manner one can derive the expression for the internal carrier field  $CF_1(\Phi_1, \Phi_2)$  in the first cavity by solving the equations

$$a'_1 = i\tau_1 a_1 + \rho_1 b_1 \quad (2.47)$$

$$b_1 = a'_1 \rho_{23} e^{2i\Phi} \quad (2.48)$$

$$b'_1 = i\tau_1 b_1 + \rho_1 a_1. \quad (2.49)$$

One obtains

$$CF_1(\Phi_1, \Phi_2) = \frac{i\tau_1}{1 - \rho_1 \rho_{23} e^{2i\Phi_1}} \cdot a_1. \quad (2.50)$$

With the above results one can derive the field reflected by a three-mirror cavity to

$$\rho_{3MC} = \frac{\rho_1 - \rho_{23} e^{2i\Phi_1}}{1 - \rho_1 \rho_{23} e^{2i\Phi_1}} \cdot a_1. \quad (2.51)$$

The field transmitted by a three-mirror cavity is given by  $i\tau_3 \cdot CF_2(\Phi_1, \Phi_2) e^{i\Phi_2}$  leading to

$$\tau_{3MC} = -\frac{\tau_2\tau_3 e^{i\Phi_2}}{1 - \rho_2\rho_3 e^{2i\Phi_2}} \cdot CF_1(\Phi_1, \Phi_2) e^{i\Phi_1}. \quad (2.52)$$

In Eq. (2.46) the abbreviation  $\rho_{23}$  for the reflexion coefficient of the second cavity was introduced to maintain the appearance of a simple two-mirror cavity in the above equations. Note, that  $\rho_{23}$  is a complex number depending on the tuning  $\Phi_2$ . Furthermore, the input field of the second cavity is given by the internal carrier field in the first cavity depending in turn on the state of the second cavity. Nevertheless, writing the analytical expressions for the carrier fields at a three-mirror cavity similar to the two-mirror cavity case offers an easier understanding of these complex expressions.

In [47] a similar expression for the transmission of a three-mirror cavity was derived. Certainly, the abbreviation for  $\rho_{21}$  describing the field in reflexion of the first cavity (with  $M_2$  as coupling mirror and  $M_1$  as end mirror) was used. Furthermore, the analysis was restricted to the transfer function of a RSE topology. However, for the investigation of a four-mirror cavity presented in Section 3 the power build-up and the transfer function of signal sidebands generated in the first resonator needs to be considered as well. Accordingly, for this case it is necessary to use the expression containing the field  $CF_1$ .

### 2.2.2 Explaining the resonance feature

In this Section the resonance feature of a three-mirror cavity is explained and visualized using the exemplary values of  $\rho_1 = \sqrt{0.7}$ ,  $\rho_2 = \sqrt{0.8}$  and  $\rho_3 = \sqrt{0.9}$  for the mirrors' amplitude reflectance factors. These parameters were chosen almost arbitrarily and not with respect to a possible application in a gravitational-wave detector but with respect to visualization purposes. First, the following discussion is restricted to the determination of resonance states of the carrier field. Its resonance is determined by the tunings  $\Phi_1$  and  $\Phi_2$  whereby the investigation can be performed independently of the resonator lengths. The actual lengths are solely relevant for the characteristic of the transfer function of a three-mirror cavity set to a certain operating point (OP) as discussed in Section 2.2.4).

From Eqs. (2.45) and (2.50) it can be deduced, that the resonance pattern of a three-mirror cavity is periodic in  $\Phi_1 \bmod(\pi)$  as well as in  $\Phi_2 \bmod(\pi)$ . Figure 2.15 shows the enhancement of the carrier light power in the first (left) and second cavity (right), respectively. Looking for example at the enhancement in the first cavity, one can recognize that it behaves exactly like an ordinary two

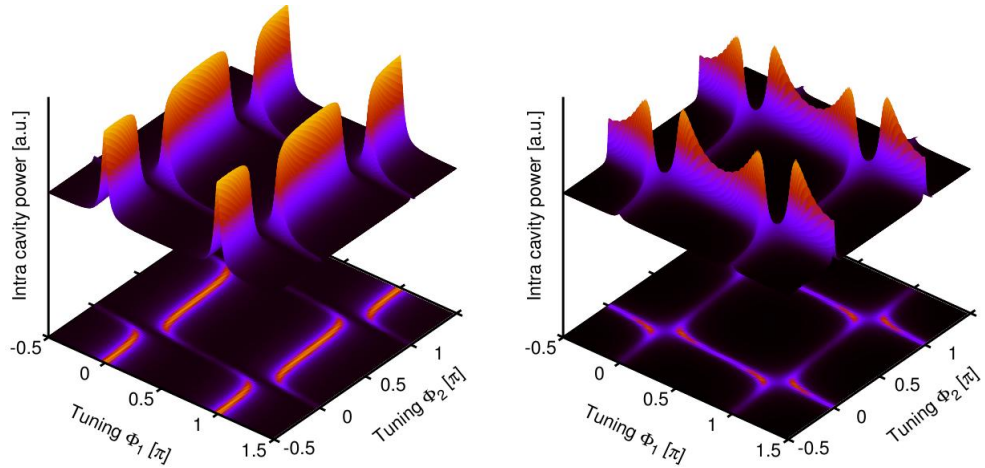


**Figure 2.15** — The figure shows the carrier light enhancement  $|CF_1(\Phi_1, \Phi_2)|^2$  in the first cavity (left) and the enhancement  $|CF_2(\Phi_1, \Phi_2)|^2$  in the second cavity (right) in dependence of the tunings  $\Phi_1$  and  $\Phi_2$ . The resonance patterns are shown as a surface plot and the corresponding color coded projection on the  $\Phi_1$ - $\Phi_2$ -plane. In the following only the latter one will be used for the visualization of resonance features of a three-mirror cavity.

mirror cavity if the second cavity is on anti-resonance (e.g.  $\Phi_2 = -0.5\pi$ ). The cross-section through the surface plot along the  $\Phi_1$ -axes (keeping  $\Phi_2$  fixed) gives the scan over one FSR of the first cavity similar to Fig. 2.3. Likewise, for a fixed tuning  $\Phi_1 = 1.5\pi$  corresponding to the anti-resonance of the first cavity, the cross section along the  $\Phi_2$ -axis shows the FSR of the second cavity. In contrast to this, if the tunings are changed simultaneously ( $d\Phi_1 = d\Phi_2$ ) one obtains the transmission shown in Fig. 2.16 which demonstrates one key feature of coupled optical resonators: The presence of a resonance doublet. Already this special cases show the manifoldness of possible resonance states of a three-mirror cavity. The resonance feature of a three-mirror cavity is exploited e.g. in the *Resonant-Sideband-Extraction* topology which will be realized in the Advanced LIGO, Advanced VIRGO and the LCGT gravitational wave detectors. Also the *four-mirror cavity enhanced Michelson interferometer topology* (refer to Chapter 3) and the *Twin-Signal-Recycling interferometer topology* (refer to Chapter 4) are based on the resonance doublet of linearly coupled optical resonators.

Considering a two-mirror cavity the resonance condition is determined by the corresponding tuning  $\Phi$ . Here the enhancement of the carrier field

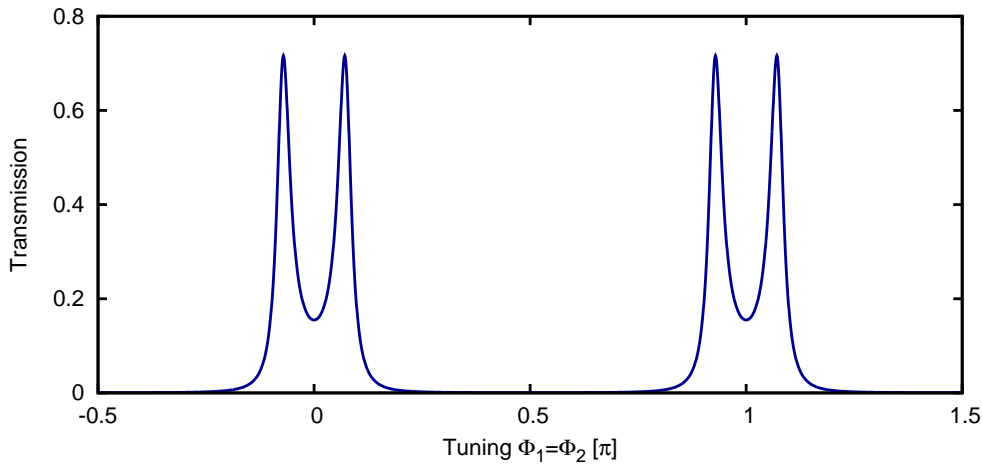


**Figure 2.16** — Power transmittance of a three-mirror cavity if the tunings  $\Phi_1$  and  $\Phi_2$  are changed simultaneously.

inside the resonator and thus the transmission (as long as the end mirror has a finite transmittance) are maximum. In analogy to this, the resonance condition of the three-mirror cavity corresponds to local maxima in the transmitted field. Remember, that the tuning  $\Phi$  is a measure for the phase delay occurring while traveling the length of the resonator given by  $L + \lambda\Phi/(2\pi)$ , where  $L$  is assumed to be an integer multiple of the wavelength  $\lambda$ . Concerning a two-mirror cavity the incident carrier light resonates if the accumulated phase delay per round-trip equals  $0 \bmod(2\pi)$ . In the case of the three-mirror cavity, the phase delay per round-trip in the first resonator is composed of the part accumulated while traveling twice the resonator length  $L_1 + \lambda\Phi_1/(2\pi)$  and the phase shift  $\arg[\rho_{23}(\Phi_2)]$  occurring at the reflexion on the second cavity. Thus, for an arbitrarily chosen OP of the second cavity the resonance condition of the carrier field in the first cavity can be determined according to

$$\Phi_1^{\text{res}} = -\frac{1}{2} \arg[\rho_{23}(\Phi_2^{\text{op}})] . \quad (2.53)$$

This equation demonstrates that on resonance the tuning  $\Phi_1^{\text{res}}$  (adjustable e.g. by the microscopic mirror position of mirror  $M_1$ ) compensates the phase shift occurring when reflecting off the second cavity. Since the tuning  $\Phi_1$  is accumulated twice per round-trip, the factor  $1/2$  needs to appear on the right hand side of Eq. (2.53).

The fact that the internal carrier field resonates in the first cavity and becomes maximum at  $\Phi_1^{\text{res}}$  can be clarified by rewriting Eq. (2.50) according to

$$CF_1(\Phi_1, \Phi_2^{\text{op}}) = \frac{i\tau_1}{1 - \rho_1 |\rho_{23}(\Phi_2^{\text{op}})| e^{i \arg[\rho_{23}(\Phi_2^{\text{op}})]} e^{2i\Phi_1}} \cdot a_1. \quad (2.54)$$

Inserting  $\Phi_1 = \Phi_1^{\text{res}}$  leads to

$$CF_1^{\text{res}} = \frac{i\tau_1}{1 - \rho_1 |\rho_{23}(\Phi_2^{\text{op}})|} \cdot a_1. \quad (2.55)$$

This equation is identical to the case of a resonant two-mirror cavity (refer to Eq. (2.8) for  $\Phi = 0$ ). Furthermore, looking at Eq. (2.52) makes clear that for a fixed tuning  $\Phi_2^{\text{op}}$  a local maximum of the field in the first cavity ( $CF_1(\Phi_1^{\text{res}}, \Phi_2^{\text{op}})$ ) gives a local maximum in transmission of the three-mirror cavity. Since  $\Phi_2^{\text{op}}$  is fixed, these local maxima are related to cross-sections of the resonance pattern parallel to the  $\Phi_1$ -axis.

Consistently, for the case of a fixed tuning  $\Phi_1^{\text{op}}$  the resonance condition for the carrier in the second cavity can be determined considering the phase shift when reflecting off the first cavity. One obtains

$$\Phi_2^{\text{res}} = -\frac{1}{2} \arg[\rho_{21}(\Phi_1^{\text{op}})]. \quad (2.56)$$

Here it is important to account for the phase shift of the field that gets reflected on the backside of the first cavity ( $b_2$  in Fig. 2.14). Accordingly, in Eq. (2.56) the term  $\rho_{21}(\Phi_1^{\text{op}})$  needs to appear. Since the transmission of the three-mirror cavity is given by  $i\tau_3 \cdot CF_2$  it is evident that a maximal field in the second cavity corresponds to a maximum in transmission. These maxima determined by Eq. (2.56) are related to cross sections of the resonance pattern parallel to the  $\Phi_2$ -axis.

The above results are visualized in Fig. 2.17. The main graph shows a color coded map of the transmission (resonance pattern). The horizontal axis shows the tuning  $\Phi_2$  of the second cavity and on the vertical axis the tuning  $\Phi_1$ , respectively. It can be seen that the resonance pattern is dominated by two resonance branches which are identified by the phase shifts in reflexion of the first and second cavity. In the following, the lower left resonance branch is referred to as *lower resonance branch* whereas the upper right is referred to as *upper resonance branch*. These resonance branches are point symmetric around the origin because the arg-function is point symmetric. The left graph shows the transmission in dependence of  $\Phi_1$  for two exemplary values of  $\Phi_2^{\text{op}}$  (refer

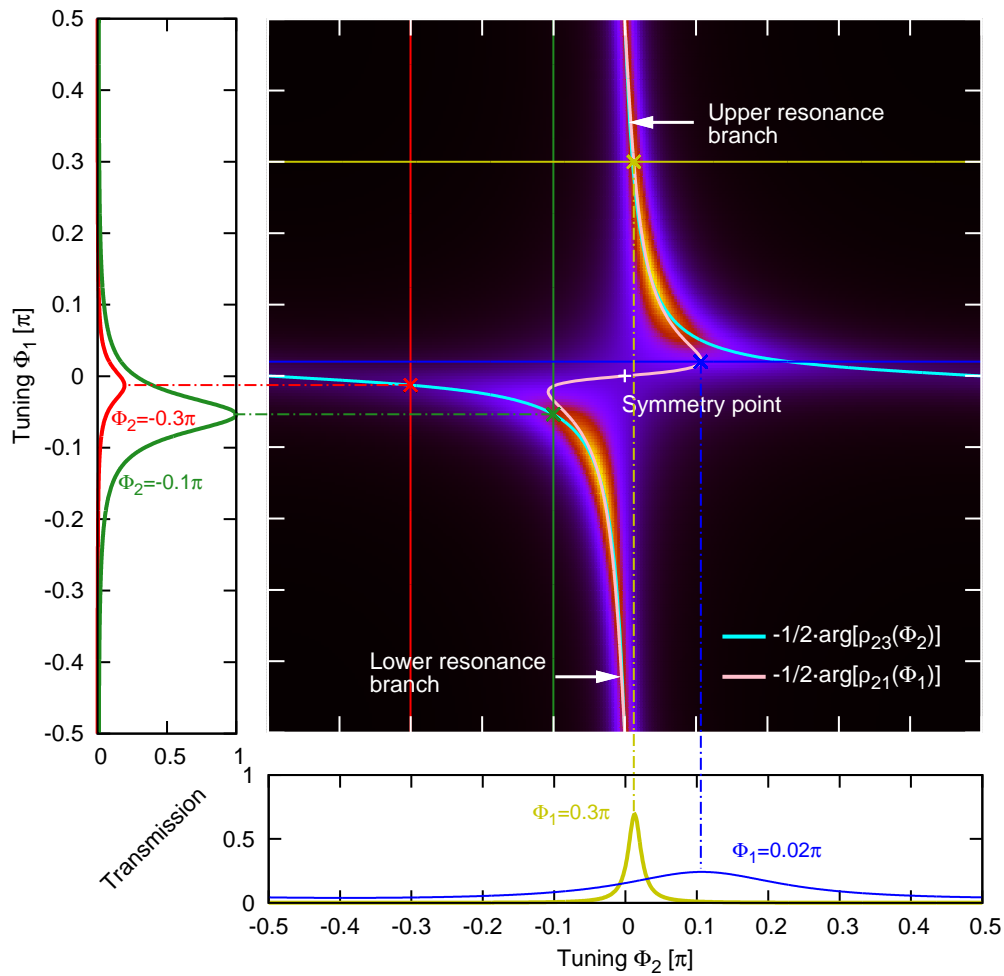


**Figure 2.17** — The main graph shows a color coded map of the transmission (resonance pattern) of the exemplary three-mirror cavity. Here, bright colors indicate high values, dark colors low values. The point symmetry around the origin is emphasized by the white cross. The resonance branches are identified with the phase shifts in reflexion of the first (pink curve) and the second cavity (cyan curve), respectively. The left and lower graphs show the transmission for two exemplary values for  $\Phi_1^{\text{OP}}$  and  $\Phi_2^{\text{OP}}$ , respectively (see text).

to the labeling in the graph). The red and green curves correspond to the cross sections of the resonance pattern parallel to the  $\Phi_1$ -axis marked by the red and green vertical solid lines. The intersections of these lines with the lower resonance branch are highlighted by the red and green cross, respectively. Furthermore, to illustrate the meaning of Eq. (2.53) the horizontal dashed-dotted red and green curves connect these intersection points with the maxima in the transmission shown in the left graph. In the same manner, the meaning of Eq. (2.56) is demonstrated by the lower graph and the corresponding dark-yellow and blue curves or lines, respectively.

The above discussion revealed, that the resonance condition of the carrier field in a three-mirror cavity is clearly determined by Eq. (2.53) and Eq. (2.56). Besides the tunings  $\Phi_1$  and  $\Phi_2$  these equations depend only on the reflectance factors. Accordingly, the qualitative shape of the resonance pattern changes if another combination for the reflectance factors is chosen. In Section 2.2.3.2 this dependence on the reflectance factors and the resulting coupling of the three-mirror cavity will be discussed in more detail.

### 2.2.3 Coupling of a three-mirror cavity

#### 2.2.3.1 Coupling of the impinging carrier light to the three-mirror cavity

In contrast to a two-mirror cavity whose coupling is solely determined by the reflectance factors of the coupling and end-mirror (refer to Section 2.1.4), a three-mirror cavity with given power reflectance factors  $R_1$ ,  $R_2$  and  $R_3$  can be over-coupled, under-coupled or impedance matched. Here, the actual coupling depends on the resonance state of the carrier light. In this Section, this behavior is illustrated for three exemplary configurations. For simplicity, it is assumed, that the tuning of the first cavity is constant and the resonance feature is analyzed in dependence of the tuning of the second resonator. It should be noted, that in general this condition can not be fulfilled. Especially concerning the investigation of the frequency response at a certain operation point, where *both* tunings change with the frequency according to  $\Delta\Phi_i = \Delta\Omega/L_i$  this assumption is only meaningful for configurations with one cavity length much smaller compared to the other (for details refer to Section 2.2.4). However, from the demonstration of these special configurations an intuitive understanding can be gained.

If the tuning  $\Phi_1$  is kept constant and thus the first cavity is interpreted as a *compound mirror*, one can understand the three-mirror cavity as a two-mirror cavity built by an end-mirror  $M_3$  and a coupling mirror  $M_{12}$  that has

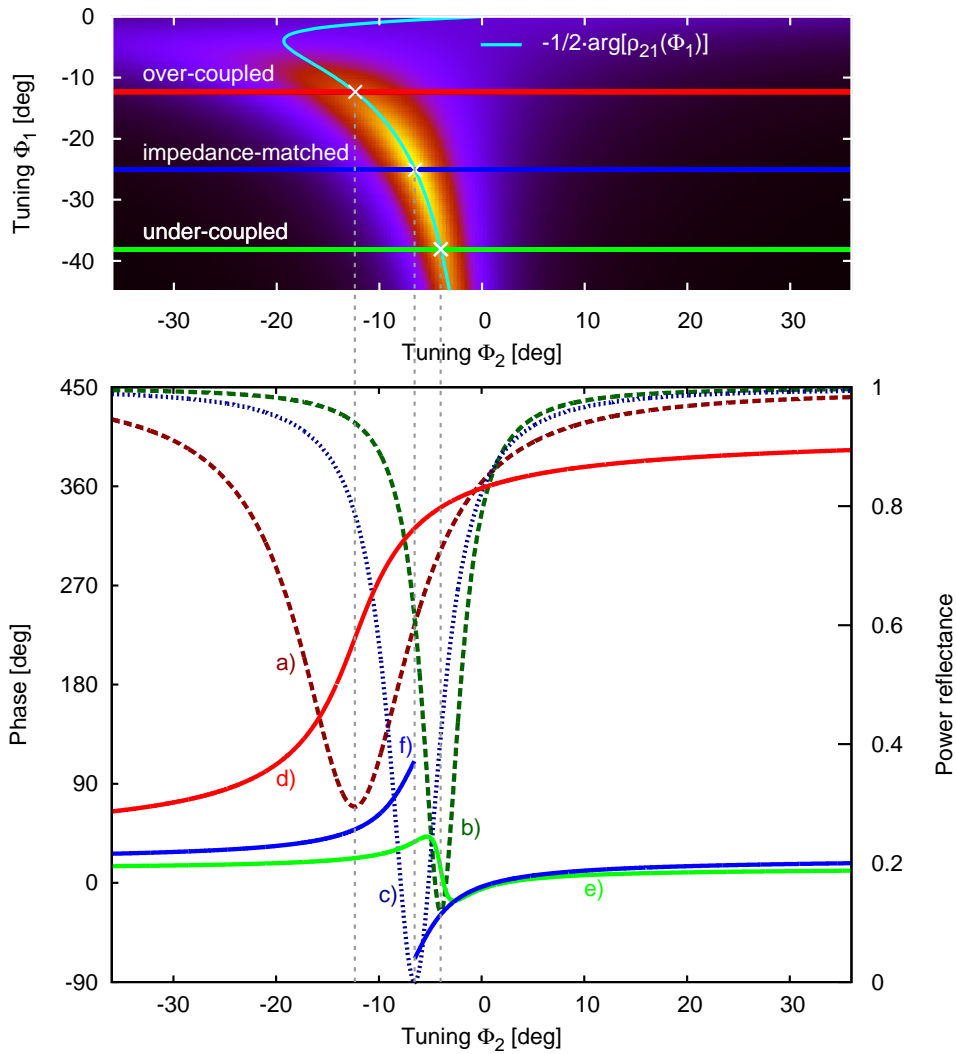


**Figure 2.18** — The lower graph shows the reflectance of a three-mirror cavity in dependence of  $\Phi_2$  while  $\Phi_1$  is constant. The three exemplary values of  $\Phi_1$  were chosen according to Eq. (2.58) leading to  $|\rho_{12}|^2 = 0.7$  for the over-coupled case (curve a) and d)),  $|\rho_{12}|^2 = 0.95$  for the under-coupled case (curve b) and e)) and  $|\rho_{12}|^2 = 0.9$  for the impedance matched case (curve c) and f)). The upper graph shows the corresponding resonance branch of the three-mirror cavity. Also the cross-sections through the  $\Phi_2 - \Phi_1$ -plane according to the curves shown in the lower graph and the resonance branch determined by  $\Phi_2^{\text{res}} = -1/2 \arg[\rho_{21}(\Phi_1)]$  are displayed.

the reflectance  $|\rho_{12}|$ . In analogy to a loss-free two-mirror cavity this three-mirror cavity is over-coupled if  $|\rho_{12}| < \rho_3$ , under-coupled if  $|\rho_{12}| > \rho_3$  and impedance matched if  $|\rho_{12}| = \rho_3$ . The tuning of the first cavity leading to a certain power reflectance  $R_c = |\rho_{12}|^2$  can be obtained from solving

$$R_c = \left| \frac{\rho_1 - \rho_2 e^{2i\Phi_1^c}}{1 - \rho_1 \rho_2 e^{2i\Phi_1^c}} \right|^2 \quad (2.57)$$

for  $\Phi_1^c$  leading to

$$\Phi_1^c = \pm \frac{1}{2} \arccos \left( \frac{R_c - \rho_1^2 - \rho_2^2 + R_c \rho_1^2 \rho_2^2}{2\rho_1 \rho_2 (1 - R_c)} \right). \quad (2.58)$$

Fig. 2.18 shows the power reflectance of the considered three-mirror cavity for the three cases of coupling.  $\Phi_1$  was chosen according to Eq. (2.58) giving  $|\rho_{12}|^2 = 0.7$  for the over-coupled case,  $|\rho_{12}|^2 = 0.95$  for the under-coupled case and  $|\rho_{12}|^2 = 0.9$  for the impedance-matched case.

One can see, that the qualitative behavior is essentially the same as in the two-mirror cavity case. Certainly, the resonances are not located at  $\Phi_2 = 0$  but at

$$\Phi_2^{\text{res}} = -\frac{1}{2} \arg [\rho_{21}(\Phi_1^c)]. \quad (2.59)$$

Furthermore, compared with a two-mirror cavity where the phase-shift on resonance is exactly  $180^\circ$  (refer to Section 2.1.4) the phase in reflexion of the three-mirror cavity has an offset. Here a constant additional part is gained which is caused by the constant phase-shift  $\phi_{\text{off}}$  in reflexion of the compound-mirror  $M_{12}$  given by

$$\phi_{\text{off}} = \arg [\rho_{12}(\Phi_1^c)]. \quad (2.60)$$

These facts are visualized in Fig. 2.19.

Please remember, that for the above discussion it was assumed, that only  $\Phi_2$  is changed while  $\Phi_1$  is fixed. It is worth mentioning that in the case of the Advanced LIGO optical configuration the transfer function can be estimated by that of a two-mirror cavity. Since the arm-cavities will have a length of 4 km each while the length of the extraction cavity will be about 8 m, the deviation of the extraction cavities tuning is negligible compared with that of the arm cavities. Thus, the situation is very similar to the situation shown in Fig. 2.18.

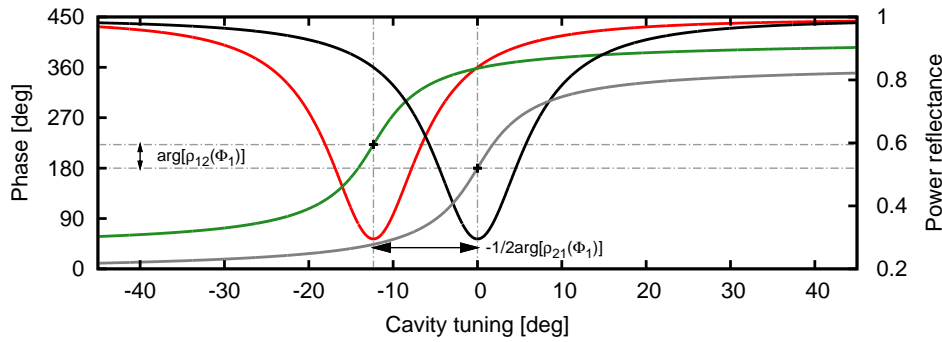


**Figure 2.19** — The figure shows the reflexion of an over-coupled three-mirror cavity in comparison with a two-mirror cavity of the same bandwidth and coupling to the impinging carrier light. The red curve shows the power reflectance of the three-mirror cavity in dependence of the tuning  $\Phi_2$  while  $\Phi_1$  is fixed according to Eq. (2.58). The green curve shows the corresponding phase. The black curve shows the power reflexion and the grey curve the phase of the equivalent two-mirror cavity. It can be seen that the characteristic is the same for the three-mirror cavity and the two-mirror cavity. In the case of the three-mirror cavity solely the locus of resonance differs by  $\Phi_2^{\text{res}}$  and the corresponding phase is shifted by  $\arg[\rho_{12}(\Phi_1^c)]$ .

### 2.2.3.2 Coupling of both resonators in a three-mirror cavity

In Section 2.2.2 the resonance feature was explained considering the phase shifts occurring due to the reflexion at the first and second resonator, respectively. It was shown, that the three-mirror cavity is resonant for the impinging carrier light if the phase delay corresponding to the tuning of one resonator compensates the phase shift in reflexion of the other resonator. Accordingly, since the characteristic of the phase shift in reflexion of a two-mirror cavity depends on the coupling (see Fig. 2.8) the qualitative behavior of the resonance feature of a three-mirror cavity differs according to the chosen reflectance factors and the resulting coupling of the resonators. Thus, in this Section the resonance of the carrier light in the three-mirror cavity will be analyzed in dependence of the mirror reflectance factors. For exemplification purposes, the discussion will be related to the case of gravitational-wave detectors with arm cavities and power-recycling. In the following, the second resonator built by  $M_2$  and  $M_3$  will be associated with the arm-cavity and the first cavity with the power-recycling cavity with  $M_1$  as the power-recycling mirror.

From the visualization of the resonance feature shown in Fig. 2.17 one can deduce a general property of a three-mirror cavity: For all chosen tunings

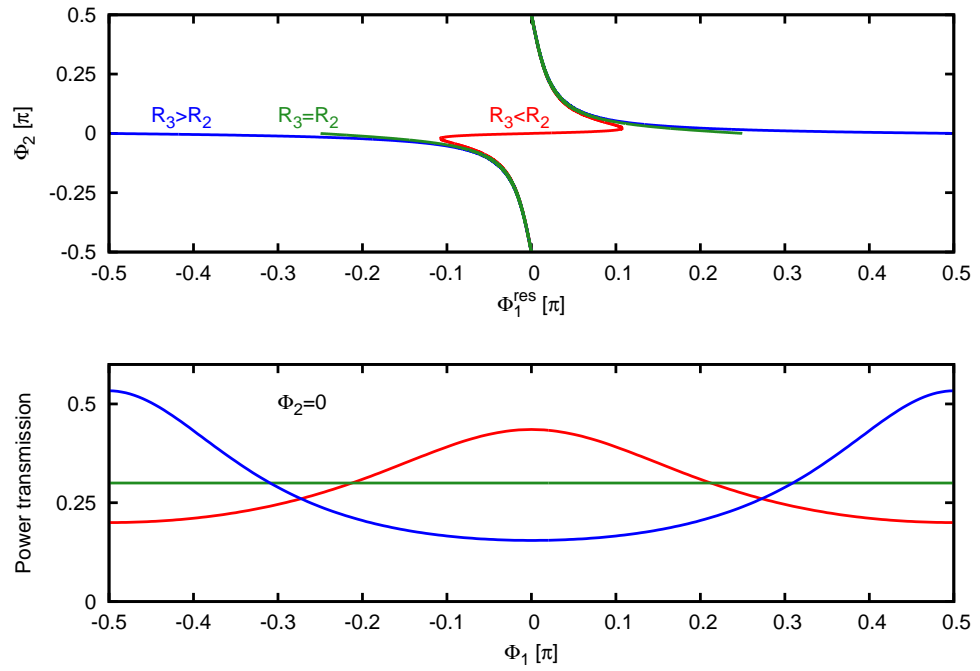


**Figure 2.20** — The figure shows the effect of the coupling of the carrier field in the first cavity to the second cavity. **Top:** On the y-axis the tuning  $\Phi_2$  is shown determining the tuning  $\Phi_1^{\text{res}} = -1/2 \arg[\rho_{23}(\Phi_2)]$  (here shown on the x-axis for visualization purposes). The red curve shows  $\Phi_1^{\text{res}}$  in dependence of  $\Phi_2$  for the under-coupled case, the green curve for the impedance-matched case and the blue curve for the over-coupled case. **Bottom:** The power transmission of the three-mirror cavity in dependence of  $\Phi_1$  for the three cases of coupling. The tuning  $\Phi_2$  was set to zero.

$\Phi_2$  there exists a tuning  $\Phi_1$  leading to resonance. Since this tuning is given by Eq. (2.53) based on the phase shift in reflection of the second cavity, it is obvious that the shape of the resonance pattern changes with the coupling to the second resonator. Figure 2.20 demonstrates the influence of the coupling to the location of the resonance branches. It can be seen that the difference between the three cases of coupling is most significant for tunings  $\Phi_2 \approx 0$ . Hence, in the bottom graph the power transmittance of the three-mirror cavity is shown in dependence of  $\Phi_1$  while the tuning of the second cavity is set to zero. For an over-coupled second cavity ( $R_3 > R_2$ ) the tuning  $\Phi_1$  of the first cavity must be  $\pm\pi/2$  to fulfill the resonance condition (blue curves in Fig. 2.20). In contrast to this, for an under-coupled second cavity with  $R_3 < R_2$

the tuning  $\Phi_1$  needs to be 0 (red curves). In the case of an impedance-matched second cavity ( $R_3 = R_2$ ) its reflectance is zero. Thus, the field in the first cavity is given by the input field attenuated by the reflectance of  $M_1$ . The enhancement of the input field in the impedance-matched second cavity is attenuated by the same amount. Accordingly, the power transmittance of the three-mirror cavity is that of the mirror  $M_1$  ( $R_1 = 0.3$ ).

Since the PR technique targets on a maximum power build-up in the second cavity, for a given set of mirror reflectance factors the OP of the three-mirror cavity needs to be chosen accordingly. The maximum power build-up in the second cavity corresponds to the global maximum of the resonance pattern shown in Fig. 2.17. In analogy to a two-mirror cavity the transmission and thus the build-up is maximum if the three-mirror cavity is impedance matched for the carrier light. Together with Eq. (2.58) for almost any configuration of a three-mirror cavity the OP corresponding to the impedance matched case can be deduced from the equations

$$\left| \rho_{12}(\Phi_1^{\text{IMP}}) \right| = \rho_3 \quad (2.61)$$

$$\wedge \left| \rho_{23}(\Phi_2^{\text{IMP}}) \right| = \rho_1. \quad (2.62)$$

This fact is visualized in Fig. 2.21 for the exemplary configuration of a three-mirror cavity used throughout this Section.

In the case of a loss-free single ended arm-cavity (i.e. the reflectance of the end-mirror is unity) the three-mirror cavity will be always over-coupled and no impedance matching is possible. Here the power build-up in the second cavity increases with the reflectance  $R_1$ . The optimum OP is given by  $\Phi_1 = \pm\pi/2$  and  $\Phi_2 = 0$  according to the blue curves in Fig. 2.20. This situation is similar to that in gravitational-wave detectors where the end-mirrors reflectance is close to unity. Here, the reflectance of the arm-cavity coupling mirror is chosen to give a desired bandwidth. Additionally, the arm-cavities are tuned to the carrier light whereby the OP fulfilling the resonance condition is already given. Since the field present in the PRC is optimally enhanced in tuned arm-cavities, the required power build-up inside the PRC leading to the impedance-matching of the three-mirror cavity is minimized at this OP. Accordingly, tuned arm-cavities are favorable in view of thermal lensing in the beam splitters and arm cavities coupling mirror substrates. Thus, the impedance matching is only realizable by a proper choice of  $R_{\text{PRM}}$  under consideration of the internal interferometer loss. The required reflectance can

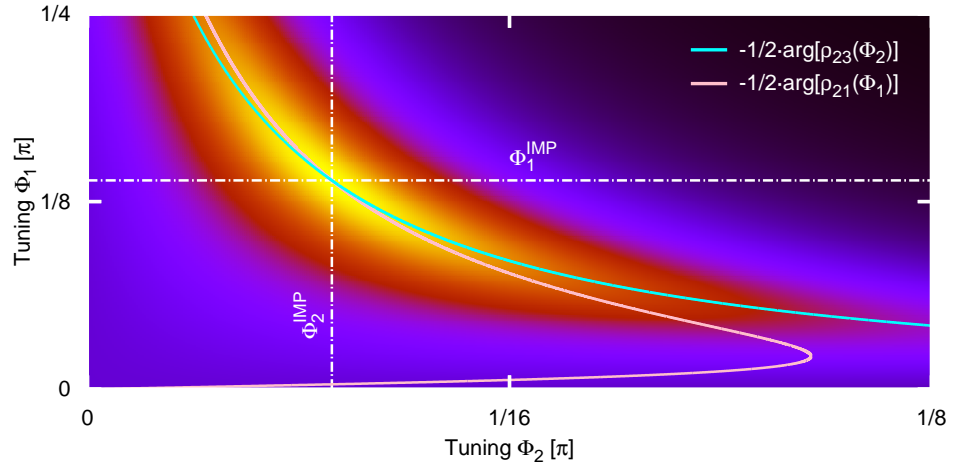


**Figure 2.21** — The figure shows a section of the resonance pattern around the maximum achievable power build-up on the upper resonance branch. The horizontal and vertical white dashed-dotted lines highlight the tunings  $\Phi_1^{\text{IMP}}$  and  $\Phi_2^{\text{IMP}}$ , respectively. Also the location of the local maxima along cross-sections through the resonance pattern parallel to the  $\Phi_1$ -axis (cyan line) determined by Eq. (2.53) and parallel to the  $\Phi_2$ -axis (pink line) determined by Eq. (2.56) are shown. These curves intersect in the global maximum of the resonance pattern located at  $(\Phi_1^{\text{IMP}}/\Phi_2^{\text{IMP}})$ .

be obtained from the condition

$$R_1 = \left| \rho_{23} \left( \Phi_2^{\text{OP}} \right) \right|^2. \quad (2.63)$$

In some cases it might be suitable to operate the arm-cavities detuned with a certain  $\Phi_2^{\text{OP}}$  (see for example [48]). For this situation the optimum parameter configuration can be deduced from Eqs. (2.53) and (2.56) giving the required OP and Eqs. (2.61) and (2.62) giving the power reflectance of the PRM leading to the impedance matching.

The equations obtained from the above discussion allow a deterministic parameter study and the modeling of any required three-mirror cavity configuration with respect to the carrier build-up inside the cavities. Basing on these relations it was e.g. possible to analyze the carrier enhancement in a four-mirror cavity as described in Chapter 3.

### 2.2.4 Transfer function of a three-mirror cavity

To comprehend the characteristic of the frequency dependence in a three-mirror cavity set to a certain OP it is very useful to consult the visualization of the transmission as shown in Fig. 2.17 again. Please remember that the tuning  $\Phi$  of a resonator with the macroscopic length  $L$  changes with the frequency according to

$$\Delta\Phi = \frac{\Delta\Omega L}{c}. \quad (2.64)$$

Hence, the frequency dependent transmission (or transfer function) of a three-mirror cavity is given by a cross-section through the resonance pattern (as shown in Fig. 2.17) along a line  $u(\Omega)$  determined by the OP (related to the carrier frequency  $\omega_0$ ) and the ratio of the resonator lengths. This line determining the tunings in the  $\Phi_2 - \Phi_1$ -plane corresponding to the frequency  $\Omega$  is thus given by

$$u(\Omega) = \frac{L_1}{L_2} \left( \underbrace{\frac{\Omega L_2}{c}}_{\Phi_2} - \Phi_2^{\text{OP}} \right) + \Phi_1^{\text{OP}}. \quad (2.65)$$

Accordingly, resonances in the transfer function of a three-mirror cavity are indicated by the intersections of  $u(\Omega)$  with the resonance branches determined by Eq. (2.53) or Eq. (2.56), respectively.

Fig. 2.22 illustrates the facts discussed above for some special cases. The left column of Fig. 2.22 demonstrates the influence of the resonator length ratio  $L_1/L_2$ .  $L_2$  was arbitrarily set to 1 m whereas  $L_1$  was set to various values  $L_1 \leq L_2$  (refer to the labels in graph b) of Fig. 2.22). In graph a) the resonance pattern of the transmission is shown. The OP (marked with the white square) was chosen such that  $\Phi_2^{\text{OP}} = \Phi_1^{\text{OP}} = 0$  corresponding to the symmetry point. Furthermore, the resonance branches determined by Eq. (2.53) and Eq. (2.56) as well as  $u(\Omega)$  are shown for the various ratios of  $L_1/L_2$ . Graph b) shows the frequency response corresponding to these cross-sections along  $u(\Omega)$ . It can be seen that for given reflectance factors the resonance frequencies and the corresponding bandwidth depends on the ratio of  $L_1/L_2$ . Since these transfer functions are symmetric around the carrier frequency, they are interesting for applications with respect to the injection of squeezed light. In particular the main feature of the *Twin-Signal-Recycling* interferometer topology discussed in Chapter 4 is based on this symmetry in the transfer function.

In the same manner, the right column shows the dependence on the chosen OP for *equal resonator lengths* ( $L_1$  and  $L_2$  were both set to 1 m). Here, three

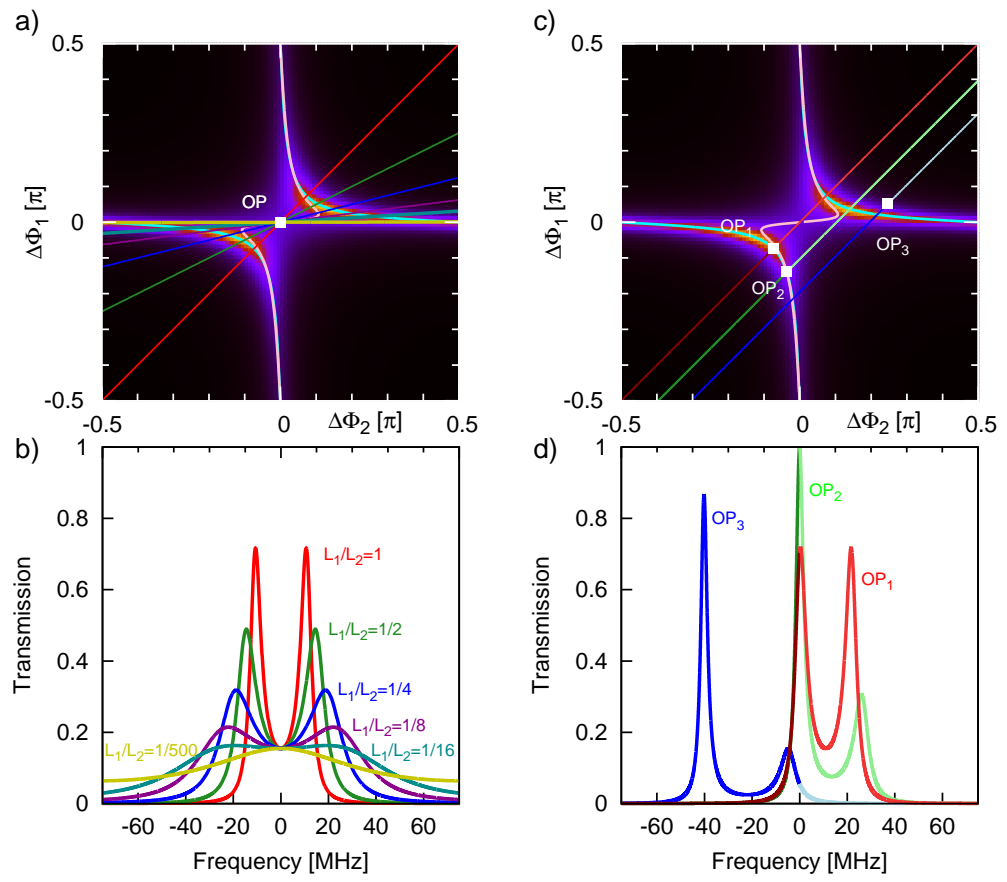


**Figure 2.22** — The figure illustrates the transfer functions of the three-mirror cavity for exemplary OPs. The upper graphs show the resonance pattern of the three-mirror cavity and the cross-sections related to the transfer functions shown in the lower graphs. The left graphs illustrate the transfer function for various length ratios  $L_1/L_2$ . The OP is set to  $\Phi_1^{\text{OP}} = \Phi_2^{\text{OP}} = 0$ . The right graphs show the transfer function for equal resonator length, but various OPs.

exemplary configurations are demonstrated showing essential features of a three-mirror cavity's transfer function. OP<sub>1</sub> was chosen such that the carrier fulfills the resonance condition of the lower resonance branch. Accordingly, a certain frequency  $\Omega > \omega_0$  determined by the *frequency splitting* which will be further discussed in Section 2.2.5 fulfills the resonance condition of the upper resonance branch. Additionally, OP<sub>1</sub> was chosen such that the corresponding cross-section  $u(\Omega)$  intersects the origin and thus the symmetry

point of the resonance pattern. Accordingly, the red curve in graph d) of Fig. 2.22 shows the same characteristic as the red curve in graph b). The resonance doublet is just shifted by the corresponding frequency splitting. These types of OPs are interesting for the analysis of a four-mirror cavity enhanced Michelson interferometer (refer to Chapter 3), because they allow a simultaneous enhancement of the carrier field (e.g. on the lower resonance branch) and of signal sidebands resonating at the upper resonance branch.

The transfer functions obtained at  $OP_2$  and  $OP_3$  demonstrate the manifoldness of possibilities to 'shape' the transfer function of a three-mirror cavity. It can be seen in graph d) that the bandwidth and the optical gain of the resonances depends on the OP. Hence, the sensitivity curve (e.g. in the Twin-Signal-Recycling topology as discussed in Section 4.4) can be designed by a proper choice of the OP with respect to a known gravitational-wave source. Additionally, to demonstrate the influence of the OP on the coupling for the sideband fields,  $OP_2$  was chosen such that the resonance characteristic on the lower resonance branch is that of an impedance-matched cavity, whereas the resonance on the upper resonance branch corresponds to the over-coupled case. In contrast to this, for  $OP_3$  the resonance on the upper resonance branch is under-coupled but on the lower resonance branch over-coupled. For further illustration of these facts Fig. 2.23 emphasizes the phase of the transfer functions obtained at  $OP_1$ ,  $OP_2$  and  $OP_3$ . Especially to comprehend the characteristic of squeezing spectra in reflexion of a three-mirror cavity, the different possible types of coupling for the sideband fields need to be considered.

### 2.2.5 Determination of characteristic quantities

In Section 2.1.2 the characteristic quantities yielding a well-defined description of the basic properties of a two-mirror cavity were derived. However, the properties of coupled Fabry-Pérot resonators (e.g. the resonance frequency and the bandwidth) depend on all parameters – especially on the choice of the OP. Thus, a general simple analytical description for all of the characteristic quantities is not possible. Accordingly, if one wants to find a parameter setup giving desired properties of the optical system one is always reliant on parameter studies. The intention of this Section is to derive analytical relations which predict some of the basic properties (e.g. the resonances in the transfer function) allowing a deterministic analysis of linearly coupled resonators. The discussion is restricted to possible configurations as gravitational-wave detector giving some boundary conditions for the parameter choice.

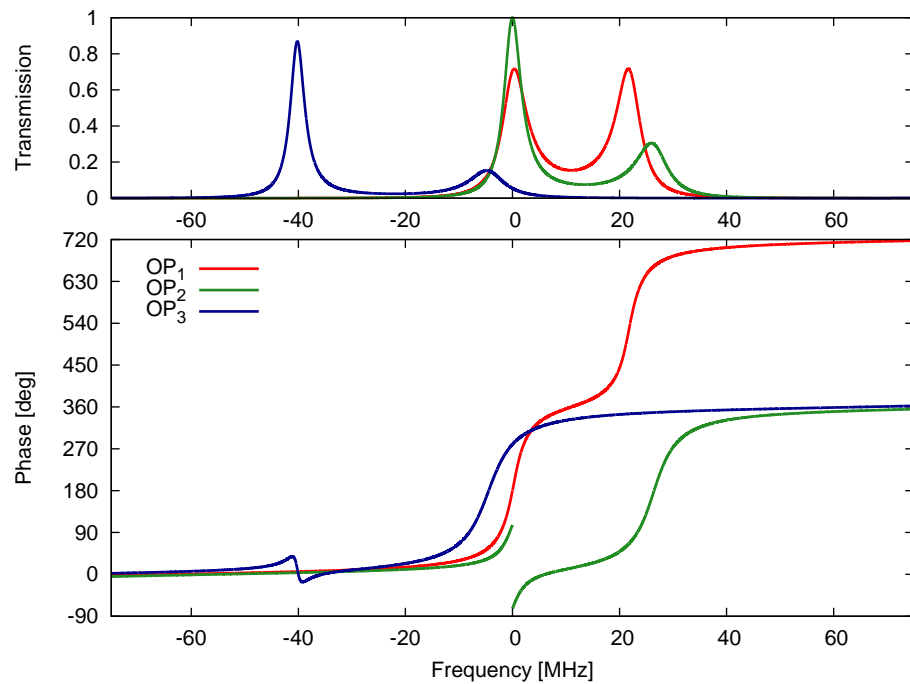


**Figure 2.23** — The figure shows the transfer function of the three-mirror cavity obtained at exemplary OPs. These OPs were chosen to demonstrate the phasing around the resonances of a three-mirror cavity which can show the characteristics of an over-coupled, under-coupled and impedance matched cavity.

### 2.2.5.1 Periodicity of frequency response

The periodicity of a two-mirror cavities' resonance feature –the FSR– depends solely on the macroscopic resonator length  $L$ . But in the case of linearly coupled Fabry-Pérot resonators the ratio of both resonator lengths needs to be considered. Figure 2.16 shows the frequency response for various ratios of  $L_2/L_1$ . It can be seen, that the periodicity of the response is given as  $L_2/L_1 \cdot \pi \bmod(L_2/L_1 \cdot \pi)$ .

In the context of earth bound gravitational-wave detectors where the macroscopic resonator lengths are on the kilometer scale, the periodic frequency response is in the order of 100 kHz. Since one aims for an optimized signal transfer function in the frequency band between 10 Hz and 10 kHz one can not profit by the resonances occurring at a frequency of one FSR. Accordingly, the following discussion does not need to account for the periodicity

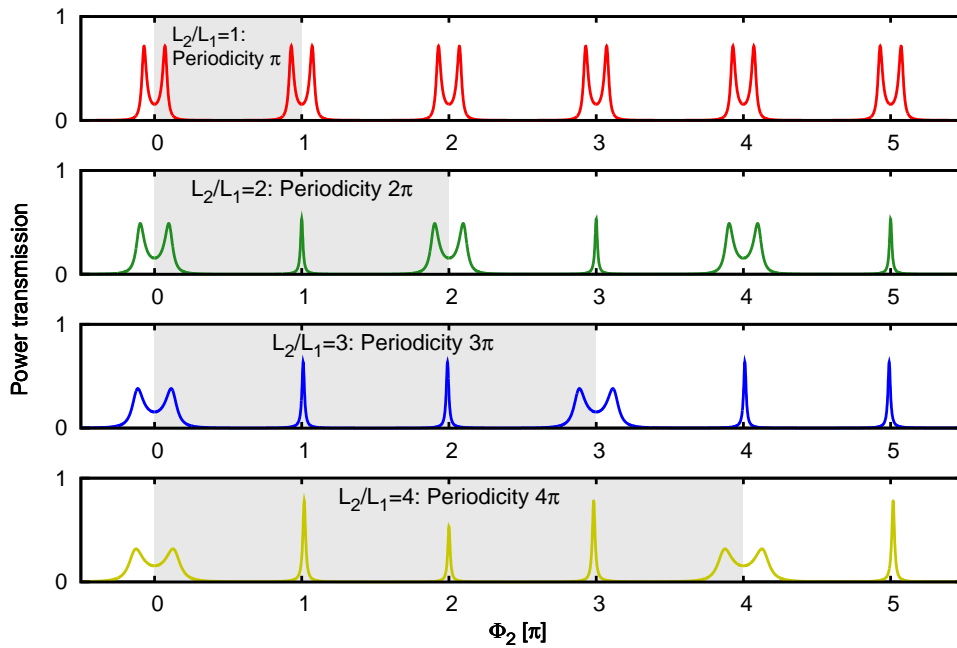


**Figure 2.24** — The figure shows the periodicity of the frequency response for the length ratios  $L_2/L_1 = 1, 2, 3$  and  $4$ .

and it is sufficient to limit the investigations of the three-mirror cavity to the range of one FSR.

### 2.2.5.2 Resonance frequencies and frequency splitting

The discussion in Section 2.2.4 revealed, that the resonance frequencies in the transfer function of a three-mirror cavity depend on the ratio of the resonator lengths. In consideration of the infra-structure of existing earth bound gravitational-wave detectors and possible upgrades of these topologies two obvious configurations arise: The first is the Resonant-Sideband-Extraction topology first proposed by Mizuno [31]. This topology will be realized e.g. in the Advanced LIGO detectors [16]. Here, the length of the extraction-cavity will be in the order of 10 m whereas the length of the arm-cavities will be 4 km. Accordingly, the ratio of the resonators can be approximated to  $L_{RSE}/L_{ARM} \approx 0$ . In Section 2.2.3 it was already stated that in this case the transfer function can be reduced to that of an ordinary two-mirror cavity. The second obvious case is a three-mirror cavity configuration with equal

lengths of both cavities, respectively. In the framework of this Thesis such a configuration was investigated for the four-mirror cavity (refer to Chapter 3) and TSR topology (refer to Chapter 4). In the following formulas are presented for these two special three-mirror cavity configurations allowing a calculation of the resonance frequencies in the respective transfer functions.

### RSE with a short extraction cavity

For the Advanced LIGO optical configuration the first boundary condition for the investigation of the frequency response arises from the necessity to achieve a high power build-up in the arm-cavities. Accordingly, these cavities need to be resonant for the carrier light whereby the tuning can be set to zero. In the following the arm-cavity will be associated with the second resonator of the three-mirror cavity giving  $\Phi_2 = 0$  (refer to the labeling shown in Fig. 2.14). Furthermore, the reflectance factors of the arm-cavities mirrors (associated with  $\rho_2$  and  $\rho_3$ ) are fixed as well. These values demonstrate a compromise between a considerable high bandwidth of the arm-cavities and a moderate PR factor. Here, the effect of thermal lensing [17, 18] limits the amount of the allowable power in the PRC. Hence, the shape of the transfer function can only be affected and optimized by the tuning of the extraction cavity and the reflectance of the extraction mirror. The extraction cavity is associated with the first resonator and the extraction mirror with  $M_1$ . Within these boundaries, the resonance frequency in the transfer function for a certain tuning  $\Phi_1^{\text{res}}$  and a certain reflectance  $\rho_1$  are given by Eq. (2.59). Expressed in Fourier frequencies one obtains

$$f_{\text{res}} = \frac{1}{2\pi} \frac{c}{L_2} \Phi_2^{\text{res}} = -\frac{\text{FSR}_2}{\pi} \arg[\rho_{21}(\Phi_1)]. \quad (2.66)$$

The bandwidth  $\gamma$  of the resonance at  $f_{\text{res}}$  can be calculated according to Eq. (2.18). Since the dispersion  $\Delta\Phi_1 = \Delta\Omega L_1/c$  is insignificant compared with that of the arm-cavities, the first resonator can be considered as a compound mirror having a fixed reflectance  $|\rho_{21}|$  leading to

$$\gamma = \arccos\left(1 - \frac{(1 - |\rho_{21}|\rho_3)^2}{2|\rho_{21}|\rho_2}\right) \frac{\text{FSR}_2}{\pi} \quad (2.67)$$

with

$$\rho_{21} = \frac{\rho_2 - \rho_1 e^{2i\Phi_1^{\text{res}}}}{1 - \rho_2 \rho_1 e^{2i\Phi_1^{\text{res}}}}. \quad (2.68)$$

Two operating modes are likely for the RSE topology, the tuned mode with  $\Phi_1 = 0$  giving a broadband response, and the detuned case with  $\Phi_1 \neq 0$

leading to narrowband resonances at a certain target frequency  $f_{\text{tar}}$ . In the latter case, the tuning  $\Phi_1^{\text{tar}}$  leading to a dedicated resonance frequency needs to be deduced from Eq. (2.66). Unfortunately, this equation can not be solved analytically for  $\Phi_1$ . However, in Sec. 2.2.3.2 it was shown that the difference in the location of the resonance branches determined by Eqs. (2.53) or (2.56), respectively, is most significant for tunings  $\Phi_2 \approx 0$ . Accordingly, using not Eq. (2.66) but

$$\Phi_1^{\text{tar}} = -\frac{1}{2} \arg \left[ \rho_{23} \left( \frac{2\pi f_{\text{tar}} L_2}{c} \right) \right] \quad (2.69)$$

allows a precise estimation of the required tuning  $\Phi_1^{\text{tar}}$ .

The broadband operating mode is aimed at a flat transfer function from DC to a considerable high corner frequency. From Fig. 2.20 which shows the dependency of the resonance branches on the mirror reflectance factors, one boundary for the choice of  $\rho_1$  can be deduced. Only if  $\rho_1 < \rho_2$  a three-mirror cavity operated at  $\Phi_1^{\text{OP}} = \Phi_2^{\text{OP}} = 0$  is resonant for the carrier frequency whereby the desired characteristic of the transfer function can be achieved.

Figure 2.25 compares transfer functions calculated based on the reduction to a two-mirror cavity (i.e. taking  $L = 4000$  m and a coupling mirror reflectance of  $\rho = |\rho_{21}(\Phi_1^{\text{tar}})|$ ) with the three-mirror cavity transfer function calculated for  $L_1 = 8.3$  m and  $L_2 = 4000$  m. In both cases the mirror reflectance factors were chosen in accordance with [16] as  $\rho_1 = \sqrt{0.93}$ ,  $\rho_2 = \sqrt{0.995}$  and  $\rho_3 = \sqrt{0.999925}$ . The vertical lines according to the target frequencies  $f_{\text{tar}} = 50$  Hz,  $f_{\text{tar}} = 100$  Hz of the narrowband mode are in very good agreement with the actual resonance frequencies in the transfer function. For  $f_{\text{tar}} = 300$  Hz the tuning  $\Phi_1^{\text{tar}} \approx 2.85^\circ$  is already close to zero explaining the slight deviation of the actual resonance of the three-mirror cavity. However, in all cases the according two-mirror cavity model as well as the calculation of the tunings with Eq. (2.69) allow a good prediction.

### Equal resonator length

If a three-mirror cavity configuration with equal or comparable resonator lengths is considered, the deduction of its characteristic properties is more complicated. In this case, the tunings of the cavities changes simultaneously according to

$$\Delta\Phi_1 = \frac{\Delta\Omega L_1}{c} \quad \text{and} \quad \Delta\Phi_2 = \frac{\Delta\Omega L_2}{c}, \quad (2.70)$$

whereby the treatment as compound mirror of these cavities is not possible. However, as shown in Sec. 2.2.4 resonances in the transfer function can be

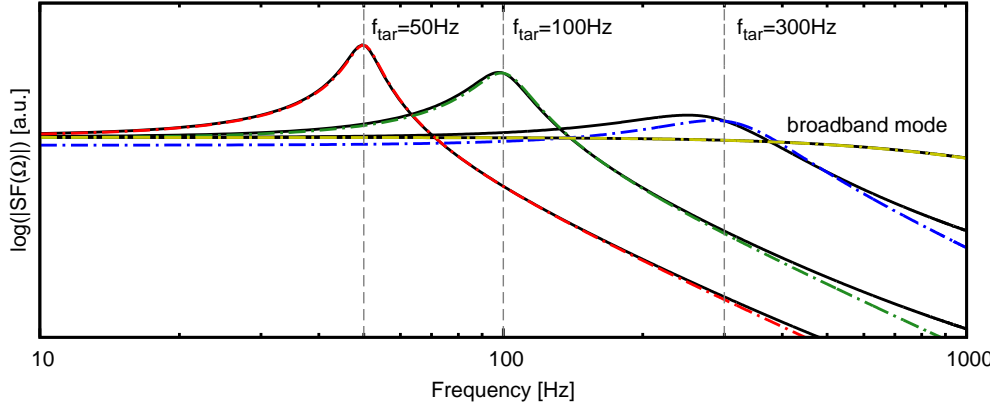


**Figure 2.25** — Exemplary phase modulation signal transfer functions of the Advanced LIGO optical configuration. The transfer functions displayed by the colored dashed-dotted lines were calculated for a two-mirror cavity with a coupling mirror reflectance of  $\rho = |\rho_{21}(\Phi_1^{\text{tar}})|$  and a tuning  $\Phi = 2\pi f_{\text{tar}}/L_2$ . In comparison the transfer function of the three-mirror cavity calculated with the parameters presented in [16] are displayed by the solid black curves. The vertical lines highlight the respective narrowband target frequencies  $f_{\text{tar}}$ . The corresponding tunings  $\Phi_1^{\text{tar}}$  for the three-mirror cavity were calculated with Eq. (2.69). For the broadband mode the tunings  $\Phi$  and  $\Phi_1$  were set to zero.

estimated by the intersection of the line  $u(\Omega)$  with the resonance branches. This fact allows the determination of one characteristic quantity, the *frequency splitting*  $f_{\text{sp}}$ . Within this thesis,  $f_{\text{sp}}$  is related to the symmetry point of the resonance pattern. In the case of equal resonator length  $L$  the equation

$$-\frac{1}{2} \arg \left[ \rho_{23} \left( \frac{\Omega_{\text{sp}} L_2}{c} \right) \right] = \frac{\Omega_{\text{sp}} L_1}{c} \quad (2.71)$$

can be solved easily for  $\Omega_{\text{sp}} = 2\pi f_{\text{sp}}$  leading to

$$f_{\text{sp}} = \arccos \left( \frac{1 + \rho_3^2}{2\rho_3^2} \rho_2^2 \right) \frac{1}{2\pi} \frac{c}{2L}. \quad (2.72)$$

Also the transmittance  $T_c$  (determining the coupling of both resonators) can be calculated to give a dedicated frequency splitting. One obtains

$$T_c = 1 - \rho_2^2 = 1 - \underbrace{\frac{4 \cos^2 \left( 2 \frac{\Omega_{\text{sp}} L_2}{c} \right) \rho_3^2}{(1 + \rho_3^2)^2}}_{R_c}. \quad (2.73)$$

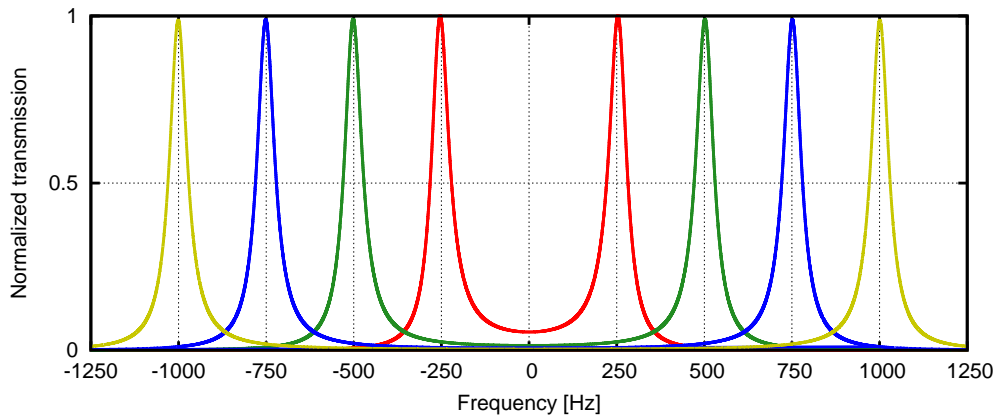


**Figure 2.26** — Exemplary resonance doublets of a three-mirror cavity. The vertical grid lines correspond to the targeted frequency splittings achieved by a proper choice of  $T_c$  according to Eq. (2.73).

Accordingly, the location of the resonance branches and thus the resonance frequencies of a three-mirror cavity can be predetermined by the above equations.

Figure. 2.26 shows exemplary resonance doublets of a three-mirror cavity with equal resonator lengths  $L = L_1 = L_2 = 2000$  m. The OP was set to  $\Phi_1^{\text{OP}} = \Phi_2^{\text{OP}} = 0$  showing a symmetric response for upper and lower sideband frequencies. The mirror reflectance factors of the coupling- and end-mirror were set to  $\rho_1 = \sqrt{0.99}$  and  $\rho_3 = \sqrt{0.999925}$ . The reflectance  $\rho_2$  of the center mirror  $M_2$  was calculated with Eq. (2.73) to give various frequency splittings. Firstly, it can be seen that the actual resonances in the transfer function can be precisely predicted from Eq. (2.72). Secondly, in the considered special case the gain and bandwidth of the respective resonances are nearly unaffected by the chosen value for  $T_c$ . Obviously, the bandwidth of the resonances is only determined by the reflectance factors of the coupling- and end-mirror. It was shown by van de Stadt *et al.* [49] and Mizuno [47] that it is possible to approximate the transfer function of a three-mirror cavity by that of a two-pole low-pass filter allowing an estimation of the bandwidth. However, in the special case considered here, the bandwidth is well approximated by that of a two-mirror cavity with a macroscopic length of  $L' = 2 \cdot L$  and identical coupling- and end-mirror reflectance factors (i.e.  $\rho'_1 = \rho_1$  and  $\rho'_2 = \rho_3$ ). This is demonstrated in Fig. 2.27.

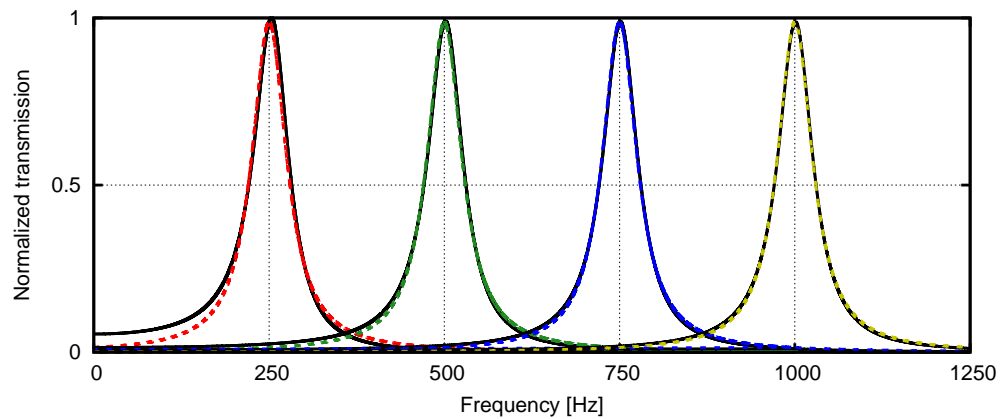


**Figure 2.27** — Upper resonances of a three-mirror cavities doublet in comparison with the resonance of a accordingly detuned two-mirror cavity. The overall macroscopic length (4000 m in this example) and the reflectance factors of the respective coupling- and end-mirrors are the same in both cases. The agreement is very good especially for high frequency splittings.

### 2.3 Summary

The presented investigations of optical resonators led to important analytical expressions required for a systematical analysis of the complex four-mirror cavity enhanced Michelson topology as presented in Chapter 3. Furthermore, the parameters of the TSR topology proposed in Chapter 4 and the corresponding table-top experiment (Chapter 5) could be determined and optimized by using the results shown in this Chapter.

---

# Analysis of a four-mirror cavity enhanced Michelson interferometer

In this Chapter the shot-noise-limited sensitivity of a four-mirror-cavity enhanced Michelson interferometer is presented. The intention of this interferometer topology is the reduction of thermal lensing and its impact on the interferometers contrast although transmissive optics are used with high circulating powers. The analytical expressions describing the light fields and the frequency response are derived. It will be shown that the transfer function of a four-mirror cavity that is applicable as a gravitational-wave detector can be reduced to that of a three-mirror cavity. Thus, although the parameter space has 11 dimensions, the detailed analysis of the three-mirror cavities' resonance feature presented in Sec. 2.2 gives boundary conditions allowing systematic parameter studies.

The investigations discussed in this Chapter were published in

- “*Analysis of a four-mirror-cavity enhanced Michelson interferometer*”  
André Thüring, Harald Lück, and Karsten Danzmann  
*Physical Review E*, 72, 066615 (2005).

### 3.1 Introduction

To improve the strain sensitivity of interferometric gravitational wave detectors advanced interferometer topologies such as Resonant Sideband Extraction [31] will be realized in the next generation. The sensitivity in the shot noise limited region will be increased by a factor of about 10 over the current detectors by increasing the circulating laser power. Using the Power Recycling technique together with high finesse arm cavities in each interferometer arm and high power lasers, the circulating light power will almost reach the Megawatt regime. But the performance and sensitivity of these topologies strongly depend on the interferometers contrast. In this context, in the framework of this thesis the four-mirror cavity enhanced Michelson topology was investigated. This topology has the potential to minimize the influence of imperfections in the interferometers contrast on the signal transfer functions. As the interferometers beam splitter is not embedded in a cavity the optical loss corresponding to the mode mismatch at the beam splitter is less significant when compared to the RSE topology. Additionally, the effect of thermal lensing can be reduced although transmissive optics are used with high circulating powers.

In this Chapter the investigation of the four-mirror cavity with respect to the shot noise limited sensitivity is presented. In Section 3.2 the analytic expressions for the carrier field and the frequency response of the four-mirror cavity will be derived. Again, the calculation will be accomplished in analogy to a two-mirror cavity offering an intuitive understanding of the whole coupled system. Because of the huge parameter range, configurations yielding satisfactory sensitivities are not obvious. Thus, to analyze the four-mirror cavity systematically some basic assumptions and boundary conditions are necessary. In Section 3.3 such boundary conditions will be derived from a detailed analysis and visualization of the resonance feature. This analysis reduces the number of free parameters from 11 to 6. Furthermore, it will be shown that the parameters for the second cavity can be chosen to give peak sensitivities at selectable frequencies. These parameters serve as a starting point for all other parameters which drastically reduces the number of steps in numerical parameter studies. In Section 3.4 the dependence on the free parameters is demonstrated for special cases and exemplary shot noise limited sensitivities and properties of the four-mirror cavity are shown in comparison to Advanced LIGO [16].

The intention of the future interferometric gravitational wave detectors is the enhancement of the shot noise limited sensitivity by increasing the

circulating light powers inside the interferometer. Here, the available laser input field would be ideally exploited if no power is reflected to the interferometers input. This can be realized using impedance matched cavities in each interferometer arm. Using high finesse resonators would also provide desirable high circulating powers. But the bandwidths of these resonators are very small leading to an unsatisfactory sensitivity in the detection band beyond the arm resonators' bandwidth. To broaden the bandwidth for signal sidebands the RSE topology was proposed. Here, an additional mirror is placed in the interferometer output forming together with the arm cavities' coupling mirrors the extraction cavity. Since this cavity includes the beam splitter, the performance of the sideband extraction strongly depends on the interferometers contrast. If the intra cavity loss (mainly caused by an imperfect interferometer contrast) becomes comparable to the transmission of the arm cavities' coupling mirrors, the sideband extraction collapses. To overcome this problem, the power-recycling technique [7] is used. This technique allows the increasing of the coupling mirrors transmission so that the intra cavity loss in the extraction cavity become less significant. To maintain the effective power build-up in the arm cavities, the wasted power (now reflected from the over-coupled arm cavities) is recycled in the power recycling cavity (also including the beam splitter) in such a way, that the complete optical configuration is still impedance matched. However, the power recycling leads to relative high optical powers in the recycling cavity. Here the amount of allowable power is limited by the non-zero absorption of the used transmissive optics and their coatings. Due to the effects of thermal lensing [17, 18] and thermal expansion of the optics surfaces the heating by optical absorption causes phase front distortions leading to poor interference quality (critical for the RSE-scheme) at the dark port operating point. This causes higher optical power on the photo detector and therefore higher shot noise. Furthermore, the thermal lensing in the substrates of the arm cavities' coupling mirrors leads to an unstable cavity for the RF-modulation sidebands needed for controlling the interferometers [50].

The strong dependence on the contrast and the effect of thermal lensing in these advanced interferometers were the motivation for investigating techniques and alternative interferometer topologies to solve these problems. The use of alternative substrate materials, for example sapphire, is one solution [23]. Active thermal compensation provides a further opportunity to reduce thermally induced phase front distortions [19, 20, 21, 22]. Basically different and promising is the use of all-reflective interferometer topologies [24]. Recently the application of gratings in future detector topologies and im-

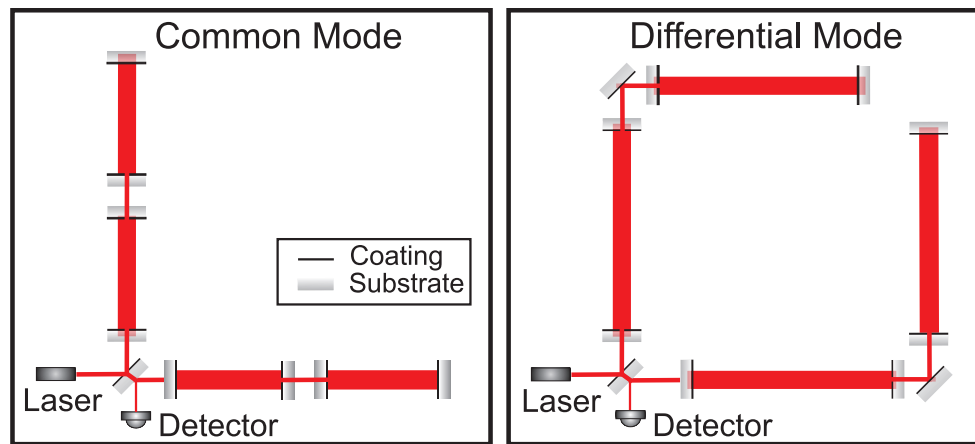


**Figure 3.1** — Two configurations of a four-mirror cavity enhanced Michelson interferometer: The left shows the unfolded realization. The right setup includes an angle of ninety degrees between the first and third resonators exploiting the quadrupole nature of gravitational waves. Here the sidebands are generated differentially in the first and third resonators.

plementation issues were investigated [51, 52]. However, the fabrication of appropriate reflection gratings with the dimensions and quality needed for the application in interferometric gravitational wave detectors still poses a problem. Additionally, it was shown by Freise *et al.* [53] that interferometers based on gratings suffers from a strong coupling of alignment into phase noise. This coupling leads to challenging requirements for the isolation and suspension of the optics.

In the topology investigated here additional mirrors in each interferometer arm and not in the input and output are used. If an additional mirror is placed in each interferometer arm the power-build up and the extraction of signal sidebands could be performed without including the beam splitter in a cavity. Thus, the loss at the beam splitter would not limit the performance of the interferometer. But with a three-mirror cavity the effect of thermal lensing could not be avoided because at least one optical substrate is embedded in a resonator with high circulating power. Also, the resonance condition of carrier and sidebands would not be decoupled. Thus, with a three-mirror arm cavity there would be no way to tune the resonators for carrier and sidebands independently. But if a fourth mirror is placed in the arms, a second long resonator is formed (Figure 3.1). This configuration yields resonance states where the circulating light power in the second cavity embedding the

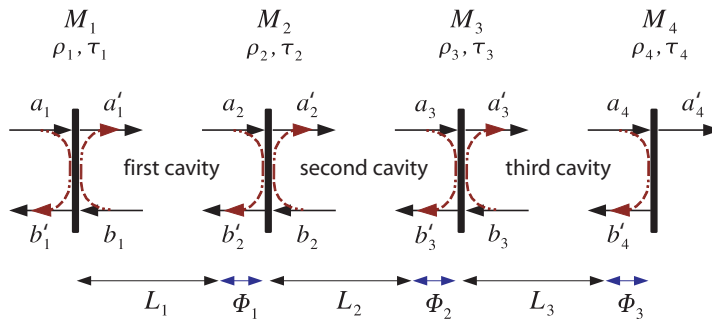


Figure 3.2 — Illustration of the used notation.

optical substrates is small compared to those of the first and third resonators. In this configuration, the resonance conditions of carrier and sidebands are also coupled. However, the coupling between the first and third resonator can be varied with the effective transmission of the second resonator. Thus, the frequencies of the corresponding resonance doublet of these coupled resonators are tunable. In fact the four-mirror cavity has a resonance triplet. But the length of the second resonator is chosen to be small (see Section 3.3) leading to a high resonance frequency with no effect in the frequency range of interest.

## 3.2 Analytical description

### 3.2.1 Carrier fields

Since the reason for increasing the circulating light power in advanced topologies is the improvement of the sensitivity in the shot noise limited frequency region, initially the impact of radiation pressure noise is not considered. Moreover, taking radiation pressure noise into account would expand the parameter range as the masses of the mirrors and the input power also influence the frequency response. Thus, it is suitable to select parameter configurations at first with respect to satisfying shot noise limited sensitivities. After that the selected configurations can be tested for the effect of radiation pressure.

If the mirrors are assumed to be ideal (loss-free) the carrier fields  $CF_k$  in the four-mirror cavity can be calculated in analogy to a two-mirror cavity. The enhancement of the input fields  $a_k$  inside the corresponding cavities is given

by (the notation refers to Figure 3.2)

$$CF_3 = a'_3 = \frac{i\tau_3}{1 - \rho_3\rho_4 e^{2i\Phi_3}} a_3, \quad (3.1a)$$

$$CF_2 = a'_2 = \frac{i\tau_2}{1 - \rho_2\rho_{34} e^{2i\Phi_2}} a_2, \quad (3.1b)$$

$$CF_1 = a'_1 = \frac{i\tau_1}{1 - \rho_1\rho_{234} e^{2i\Phi_1}} a_1. \quad (3.1c)$$

The derivation of these equations were accomplished as presented in Section 2.2.1 for a three-mirror cavity. Likewise, in Eq. (3.1b) and Eq. (3.1c) the abbreviations  $\rho_{34}$  and  $\rho_{234}$  are used to maintain the appearance of a simple two-mirror cavity. They stand for the reflection of the third cavity ( $M_{34}$ ) given by

$$\rho_{34}(\Phi_3) = \frac{\rho_3 - \rho_4 e^{2i\Phi_3}}{1 - \rho_3\rho_4 e^{2i\Phi_3}} \quad (3.2)$$

and the reflection of the three-mirror cavity containing  $M_2$ ,  $M_3$  and  $M_4$  (labeled  $M_{234}$  in the following) given by

$$\rho_{234}(\Phi_2, \Phi_3) = \frac{\rho_2 - \rho_{34} e^{2i\Phi_2}}{1 - \rho_2\rho_{34} e^{2i\Phi_2}}. \quad (3.3)$$

Note, that these complex expressions are frequency dependent values. Furthermore, the input field of the third resonator is  $a_3 = CF_2 e^{i\Phi_2}$  and that of the second one is  $a_2 = CF_1 e^{i\Phi_1}$ . However, as already presented for the three-mirror cavity, writing  $CF_k$  similar to the two-mirror cavity case and thinking of  $M_{34}$  and  $M_{234}$  as compound mirrors offers an easier understanding of these expressions.

### 3.2.2 Signal sidebands

The basics of the response to gravitational waves are described for example in [54] for a Michelson interferometer with ordinary two-mirror arm cavities. In this section we transfer these results to the four-mirror cavity case.

The normalized transfer function  $\mathbf{G}(\Omega)$  to the detection port for signal sidebands generated in the four-mirror cavity by gravitational waves (called *GW-transfer function* in the following) is composed of three parts corresponding to the three resonators formed by the four-mirror cavity. Each of the three parts is the sum of the transfer function for the upper sidebands ( $\omega_0 + \Omega$ ) and

the lower sidebands ( $\omega_0 - \Omega$ ). One obtains

$$\mathbf{G}(\Omega) = \sum_{k=1,2,3} G_k(\Omega) + G_k^*(-\Omega) \quad (3.4)$$

for the readout of the carrier lights phase quadrature and

$$\mathbf{G}(\Omega) = \sum_{k=1,2,3} -i(G_k(\Omega) - G_k^*(-\Omega)) \quad (3.5)$$

for the readout of the amplitude quadrature. For an arbitrary operating point  $\Phi_k^{\text{OP}}$  the terms  $G_k(\Omega)$  have the form

$$\begin{aligned} G_k(\Omega) = & \underbrace{CF_k(\Phi_k^{\text{OP}})}_{\text{carrier amplitude}} \times \underbrace{G_k^{\delta\phi}(\Omega)}_{\text{modulation per round-trip}} \dots \\ & \underbrace{\hspace{10em}}_{\text{sideband generation in the cavity}} \\ & \times \underbrace{SF_k(\Phi_k^{\text{OP}} + \Omega L_k/c)}_{\text{sideband enhancement and transfer to detection port}}. \end{aligned} \quad (3.6)$$

Since sidebands generated by a traversing gravitational wave are impressed due to a modulation process, their amplitudes are proportional to the carrier field. Accordingly the expression for the corresponding carrier field  $CF_k$  (first term of Equation (3.6)) is contained in  $G_k(\Omega)$ . Note that here the input field  $a_1$  is assumed to be unity because  $G_k$  represents a normalized transfer function.

The expression describing the transfer from a gravitational wave to phase shift (modulation depth) is given by [54]

$$X_{h \rightarrow \phi} = \frac{\omega_0}{2} \frac{1 - e^{i\Omega l/c}}{-i\Omega}, \quad (3.7)$$

where  $l$  is the optical path length. Each sideband impressed on the carrier  $CF_k$  by this weak phase modulation has the amplitude  $CF_k J_1(X) = C_k X/2$ , where  $J_1$  is the first order Bessel function. To obtain the magnitude of the sidebands generated per round-trip in the respective cavity (second term in Eq. (3.6)), the amplitude attenuation (per round-trip) of this cavity needs to be taken into account. In the case of the first and second cavity the reflecting mirror  $M_r$  and thus the attenuation is frequency dependent. Accordingly, the first half

and the second half round-trip needs to be considered independently. One obtains

$$G_k^{\delta\phi}(\Omega) = \left( \rho_k^r(\Omega)e^{i\Phi_k} + \rho_k^r(\omega_0)e^{i\Phi_k^{\text{OP}}} \right) \frac{\omega_0}{4} \frac{1 - e^{i\frac{\Omega L_k}{c}}}{-i\Omega} \quad (3.8)$$

where  $\rho_k^r$  is the reflection of the respective reflecting mirror  $M_r$  (i.e. in the case of the first cavity  $\rho_k^r$  is  $\rho_{234}$ ). The first term in the parentheses describes the attenuation of the sidebands generated on the first half round-trip. These sidebands are reflected at  $M_{234}$  with  $\rho_{234}(\Omega)$ . The phase  $\Phi_k = \Phi_k^{\text{OP}} + \Omega L_k/c$  accounts for the delay incurring on the second half round-trip. The second term in the parentheses describes the sidebands generated on the second half round-trip. The amplitude of these sidebands is proportional to the reflected carrier field. Thus, in this case the attenuation  $\rho_k^r(\omega_0)$  is that of the carrier amplitude. Here the phase factor  $e^{i\Phi_k^{\text{OP}}}$  describes the carriers phase delay incurred on the first half round-trip.

In addition the phase relation between the signal sidebands induced in different cavities needs to be included. Thus, the geometric layout of the resonators (refer to Figure 3.1) needs to be taken into account as well. If the four-mirror cavity is not folded, signal sidebands of gravitational waves are impressed in common mode. But if for example the first and third resonator are orientated orthogonally to each other, the corresponding sidebands are impressed differentially (due to the quadrupole nature of gravitational waves). Thus, in the differential mode  $G_1^{\delta\phi}$  and  $G_3^{\delta\phi}$  have different signs.

Whereas the first two terms of Eq. (3.6) principally describe the sideband generation in the respective cavities, the frequency response is mainly determined by the third term. The frequency dependent enhancement of the sidebands inside the cavities and the transfer out of the cavities to the detection port can be obtained from  $CF_k$  by substituting

$$CF_k(\Phi_k) \rightarrow CF_k\left(\Phi_k^{\text{OP}} + \frac{\Omega L_k}{c}\right) = SF_k(\Omega) \quad (3.9)$$

where  $\Omega L_k/c$  describes the phase delay incurring while propagating over the length  $L_k$ . This becomes clear considering for example the first cavity. The expression  $CF_1$  describes the enhancement of the amplitude  $a_1$  injected at  $M_1$  into the first cavity (refer to Figure 3.2). The signal sidebands are generated inside the cavities, get resonantly enhanced, and are then transmitted through  $M_1$  to the detection port. Hence one does not need to multiply the sideband amplitudes by  $\tau_1$  upon injection but during the extraction (transmission through  $M_1$ ) of the cavity and Eqs. (3.1a)-(3.1c) are valid not only for the externally injected carrier but also for the internally generated sidebands.

The shot noise limited sensitivity is given by the noise to signal ratio of the signal  $\mathbf{G}(\Omega)$  and the phase fluctuation equivalent to shot noise [55]

$$\delta\tilde{\phi} = \sqrt{\frac{2\hbar\omega_0}{P_0}} \quad (3.10)$$

leading to

$$\tilde{h}(\Omega) = \frac{1}{2|\mathbf{G}(\Omega)|} \sqrt{\frac{2\hbar\omega_0}{P_0}}, \quad (3.11)$$

where  $P_0$  is the power of the incident carrier light. Note, that  $\mathbf{G}(\Omega)$  is calculated for a single interferometer arm. This results in an additional factor of 1/2 for the sensitivity of the whole interferometer [47]. Since this sensitivity depends on eleven parameters (3 macroscopic lengths, 3 tunings, 4 reflectivities and the geometric layout), a qualitative and intuitive understanding of the resonance feature is necessary to find some basic assumptions and boundary conditions which allow a systematic analysis of the configuration.

### 3.3 Reduction of parameter space

#### 3.3.1 Basic assumptions

Since the four-mirror cavity is meant as an alternative to RSE-topologies, some basic boundary conditions for the comparison with the Advanced LIGO optical configuration needs to be derived [16]. Consequently, the maximum interferometer arm length is set to 4 km. The calculated strain sensitivities are related to an input power of 125 W. The transmission of the end mirror  $M_4$  is set to 50 ppm. In addition, to avoid thermal effects in the optical substrates embedded in the second cavity, the power in this cavity needs to be relatively small. Thus, signal sidebands induced in this cavity are small compared to those induced in the first and third one. Accordingly, the length  $L_2$  does not need to be long to enhance the sensitivity for gravitational waves. It can be shown that even the shape of the GW-transfer functions is not significantly affected by  $L_2$ . Thus,  $L_2$  is arbitrarily set to 10 m for all calculations. Hence, the second cavity can be understood as an etalon whose transmission  $T_c$  determines the coupling of the first and third cavity and thus the frequency splitting  $\Omega_{sp}$  of the corresponding resonance doublet. This is one key feature of the topology. The four-mirror cavity behaves like a three-mirror cavity with variable coupling. The properties of the second cavity solely determine the frequency splitting.

### 3.3.2 Resonance feature

The resonance feature of the four-mirror cavity can be analyzed just as in the case of the three-mirror cavity (Sec. 2.2.2). Likewise, the resonance branches are determined by the equations

$$\Phi_1^{\text{res}} = -\frac{1}{2} \arg(\rho_{234}(\Phi_2, \Phi_3)) \quad \text{and} \quad (3.12)$$

$$\Phi_3^{\text{res}} = -\frac{1}{2} \arg(\rho_{321}(\Phi_1, \Phi_2)) . \quad (3.13)$$

This relations drastically reduces the parameter range for the resonances of the four-mirror cavity.

### 3.3.3 Power in substrates

Another boundary condition can be derived from the point symmetry of the resonance branches. Concerning the pattern of the internal fields in the  $\Phi_3$ - $\Phi_1$ -plane, those of the first and third resonator are point symmetric whereas that of the second one is not (refer to Figure 3.3). Considering the absolute values of the carrier fields  $CF_k$  (Eqs. (3.1a)-(3.1c)) reveals that these are point symmetric in the tunings  $\Phi_k$ . Due to the fact that all tunings in  $C_k$  appear with the factor  $i$  the relation

$$|CF_k(\Phi_k)| = |CF_k^*(\Phi_k)| = |CF_k(-\Phi_k)| \quad (3.14)$$

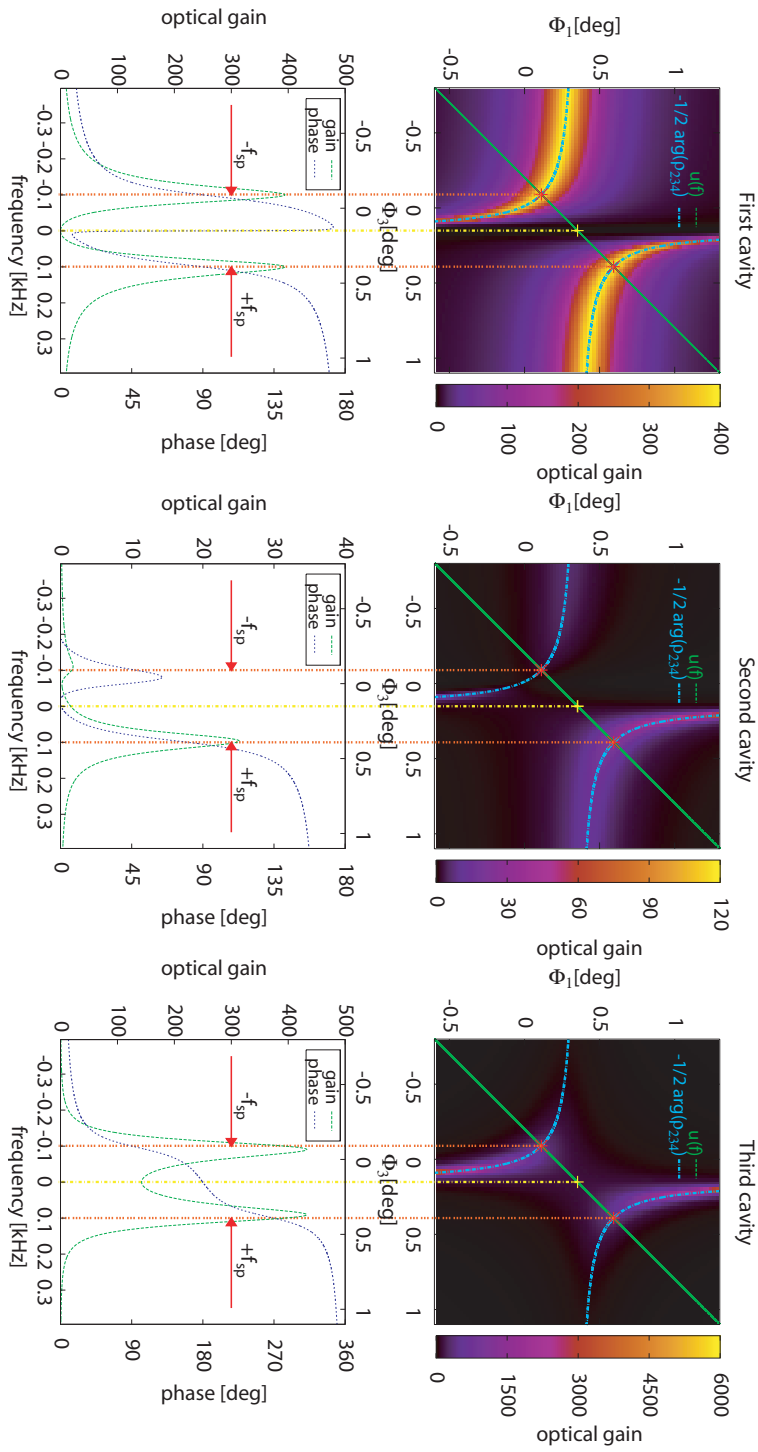
is valid explaining the point symmetry around the origin ( $\Phi_k = 0$ ). Since in general  $\Phi_2$  is not zero but tuned ( $\Phi_2^c$ ) to give a certain frequency splitting, the relation of Eq. (3.14) is not fulfilled. In this case

$$|CF_k(\Phi_1, \Phi_2^c, \Phi_3)| \neq |CF_k(-\Phi_1, \Phi_2^c, -\Phi_3)| . \quad (3.15)$$

---

**Figure 3.3 (following page)** — Resonance pattern of a four-mirror cavity. The upper three graphs show the intra-cavity powers  $|CF_k|^2$  in dependence of  $\Phi_3$  and  $\Phi_1$ . The tuning of the second cavity is fixed. The cyan curve highlights the resonance branches determined by Eq. (3.12). The function  $u(f)$  is displayed by the green lines. Here  $L_1$  and  $L_3$  are 2 km each. The point symmetry of the resonance condition is illustrated with the yellow crosses. The red crosses mark the intersections of  $u(f)$  with the resonance branches.

The lower graphs show the frequency response in magnitude (green curves) and phase (blue curves) along the green line  $u(f)$  in the upper graphs. The frequency scale is calculated as  $f = (\Phi_3^{\text{sym}} - \Phi_3)c/L_3$ . Thus,  $f = 0$  Hz is related to the symmetry point. The frequency splitting  $\omega_{\text{sp}} = 2\pi f_{\text{sp}}$  is defined with respect to this symmetry point.



showing that  $|CF_2|^2$  is not point symmetric in the  $\Phi_3$ - $\Phi_1$ -plane. The symmetry still existent in the pattern of  $|CF_1|^2$  and  $|CF_3|^2$  comes from the point symmetric phase shift  $\arg(\rho_{234})$  in reflection around the resonance in  $M_{234}$ . Here,  $M_{234}$  is considered as a two-mirror cavity with  $M_{23}$  as the coupling mirror. Accordingly the phase shift in reflection of  $M_{234}$  must correspond to the point symmetric two-mirror cavity case. From this phase shift the coordinates of the symmetry point can be determined in analogy to the derivation of Eq. (2.60) as

$$\Phi_3^{\text{sym}} = -\frac{1}{2} \arg(\rho_{32}(\Phi_2^c)) \quad \text{and} \quad (3.16)$$

$$\Phi_1^{\text{sym}} = -\frac{1}{2} \arg(\rho_{234}(\Phi_2^c, \Phi_3^{\text{sym}})). \quad (3.17)$$

To fulfill the condition of low power in the second resonator, only those operating points lying on the lower left resonance branch are suitable (refer to the optical gain of the second cavity shown in the middle of Figure 3.3).

### 3.3.4 Frequency response

Similar to the three-mirror cavity the frequency response of the four-mirror cavity is represented by a cut through the  $\Phi_3$ - $\Phi_1$ -plane (upper graphs in Figure 3.3) along an oblique line given by

$$u(\Omega) = \frac{L_1}{L_3} (\Phi_3 - \Phi_3^{\text{OP}}) + \Phi_1^{\text{OP}}, \quad (3.18)$$

where  $\Phi_3^{\text{OP}}$  and  $\Phi_1^{\text{OP}}$  corresponds to the operating point of the carrier light. As the transmission

$$T_c = 1 - \frac{4 \cos^2(2 \frac{\omega_{\text{sp}} L_3}{c}) \rho_4^2}{(1 + \rho_4^2)^2} \quad (3.19)$$

of the second cavity determines the coupling between the first and third resonator and thus the frequency splitting  $\Omega_{\text{sp}}$ , an expression can be derived giving the tuning  $\Phi_2^c$  as a function of  $T_c$ . For fixed reflectivities  $\rho_2$  and  $\rho_3$  one obtains

$$\Phi_2^c = \frac{1}{2} \arccos \left( \frac{R_c - \rho_2^2 - \rho_3^2 + R_c \rho_2^2 \rho_3^2}{2 \rho_2 \rho_3 T_c} \right). \quad (3.20)$$

Since the effective transmission  $T_c$  of the second cavity is the decisive parameter for the frequency splitting,  $\rho_2$  and  $\rho_3$  initially can be chosen almost arbitrarily. Only the coordinates of the symmetry point depend on  $\rho_2$  and

$\rho_3$ . The pattern of  $|CF_1|^2$  and  $|CF_3|^2$  related to this symmetry point stay the same. Later the optimal values are determinable by the boundary condition of low power in the second cavity. Accordingly, for a certain  $T_c$  the enhancement of the carrier light only depends on  $\Phi_1$ ,  $\Phi_3$  and  $\tau_1$  ( $\tau_4$  is 50 ppm). The GW-transfer function additionally depends on  $L_1$  and  $L_3$ . Thus, the parameter space for the sensitivity of the investigated topology is reduced to a six dimensional one. Additionally,  $\Phi_2$  can be chosen from Eq. (3.20) to give a certain frequency splitting. Then, the symmetry point from Eqs. (3.16) and (3.17) serves as starting point for  $\Phi_3$  and  $\Phi_1$  leading to a reduction of the parameter range for the tunings.

## 3.4 Parameter studies

### 3.4.1 Special cases

The analysis of the resonance feature in Section 3.3 revealed that the resonance of the carrier light does not depend on the macroscopic lengths  $L_k$ , because the resonance is determined by the microscopic lengths (tunings). Furthermore, it was stated that the sensitivity for gravitational waves is proportional to the carrier amplitudes in the cavities. Thus, operating points yielding satisfying sensitivities are restricted to states where the carrier is on resonance (or close to resonance). For given reflectivities these states are determined by Eq. (3.12). First, the power build-up (optical gain) in the first and third cavity was investigated in dependence of the frequency splitting induced by the tuning  $\Phi_2^c$  of the second cavity. Here, the reflectivities  $\rho_2^2$  and  $\rho_3^2$  were set to 0.999 each and  $\rho_1^2$  was set to 0.993. This value of  $\rho_1$  was chosen to obtain moderate circulating powers in the first and third resonator, respectively. The frequency splitting  $f_{sp} = \Omega_{sp}/2\pi$  was investigated in a range from 50 Hz to 1 kHz corresponding to the detection band of terrestrial gravitational-wave detectors. Furthermore, the respective operating points were chosen as the intersection point of  $u(\Omega)$  with the lower left resonance branch. Note, that the carrier is resonant on these states (refer to Figure 3.3). Then the upper sidebands are expected to be resonant at frequencies  $\Omega = 2\Omega_{sp}$ . The corresponding tuning  $\Phi_2^c$  was determined by Eqs. (3.19) and (3.20). The cavity lengths  $L_1$  and  $L_3$  were set to 2 km each. Figure 3.4 shows the shot noise limited sensitivities for various tunings  $\Phi_2^c$ .

Since for these states the tunings and the cavity lengths were determined with respect to certain frequency splittings and resonances in the frequency response,  $\rho_1$  is the only remaining free parameter affecting the optical gains.

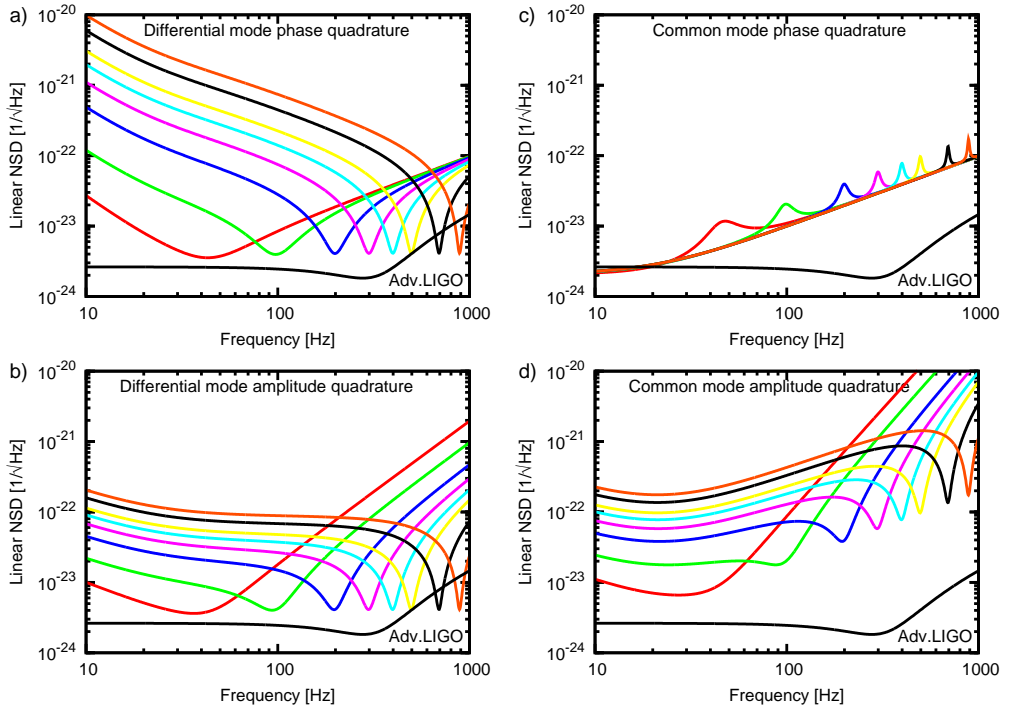


**Figure 3.4** — Linear noise spectral density (NSD) of the four-mirror cavity for various frequency splittings induced by the tuning  $\Phi_2^c$ . The graphs a) and b) show the sensitivities in the carrier lights phase and amplitude quadrature for a folded geometry (differential mode). Graphs c) and d) correspond to the unfolded setup (common mode). It can be seen that the best sensitivities can be achieved in the differential mode.

Accordingly, these states are investigated for the dependence on  $\rho_1$ . The results are shown in Figure 3.5. For low  $\rho_1$  the frequency response becomes maximum on the symmetry point (refer to Fig. 2.20) explaining the peak sensitivity around 50 Hz for  $\rho_1 = 0.95$  (solid curve in Figure 3.5). Furthermore it can be seen, that the impedance matched case optimally exploiting the laser input field yields a better sensitivity compared to Advanced LIGO only in a very narrow region.

Figure 3.6 shows the sensitivity for different ratios  $L_1/L_3$ . This ratio determines the slope of the oblique line  $u(f)$  in Figure 3.3 representing the frequency response. Accordingly, the intersection points of this line with the resonance branches vary with this ratio (refer to Fig. 2.22). Also the magnitude of the signal sidebands induced in a cavity scale with its length according to

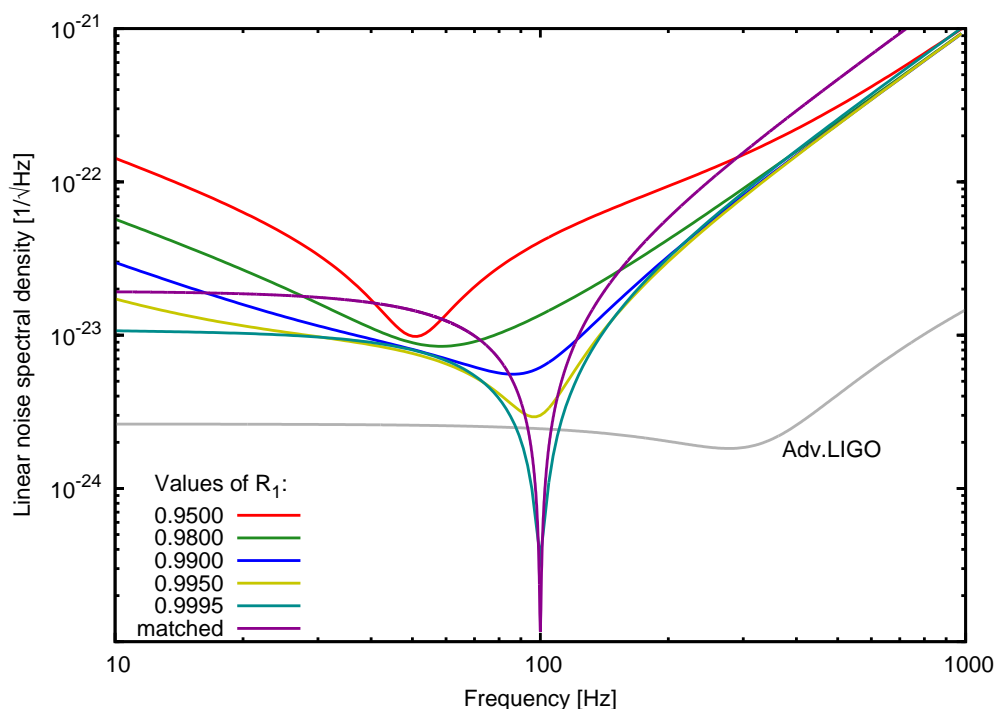


**Figure 3.5** — Sensitivity in the amplitude quadrature for the differential mode with different values for  $R_1 = \rho_1^2$ . Here the tuning  $\Phi_2^c$  corresponds to a splitting of 50 Hz.

Eq. (3.7). Hence, if  $L_1$  is greater than  $L_3$  the GW-transfer function is dominated by the sidebands induced in the first cavity (if the powers in the first and third cavity are similar).

The optical gain  $|CF_1|^2$  is very low around the symmetry point as it can be seen in Figure 3.3. This low optical gain corresponds to the bad sensitivity around 50 Hz for  $L_1/L_3 = 2.5 \text{ km}/1.5 \text{ km}$  (red curve in Figure 3.6). This fact indicates, that satisfying sensitivities in a broad frequency range are only achievable for configurations with  $L_1/L_3 \leq 1$ . Also configurations with very short  $L_1$  (or  $L_3$ ) yield no satisfying sensitivities. In these cases, the four-mirror cavity behaves like an ordinary two-mirror cavity with the resonance frequencies determined by the corresponding FSRs  $c/2L_3$  (or  $c/2L_1$ ).

All other non-special cases were investigated with a numerical code developed for this purpose. With this code, the parameters were systematically varied considering all relations and dependencies obtained in Sec. 2.2 and Sec. 3.3. The frequency splitting  $f_{sp}$  was varied between 50 Hz and 1000 Hz.

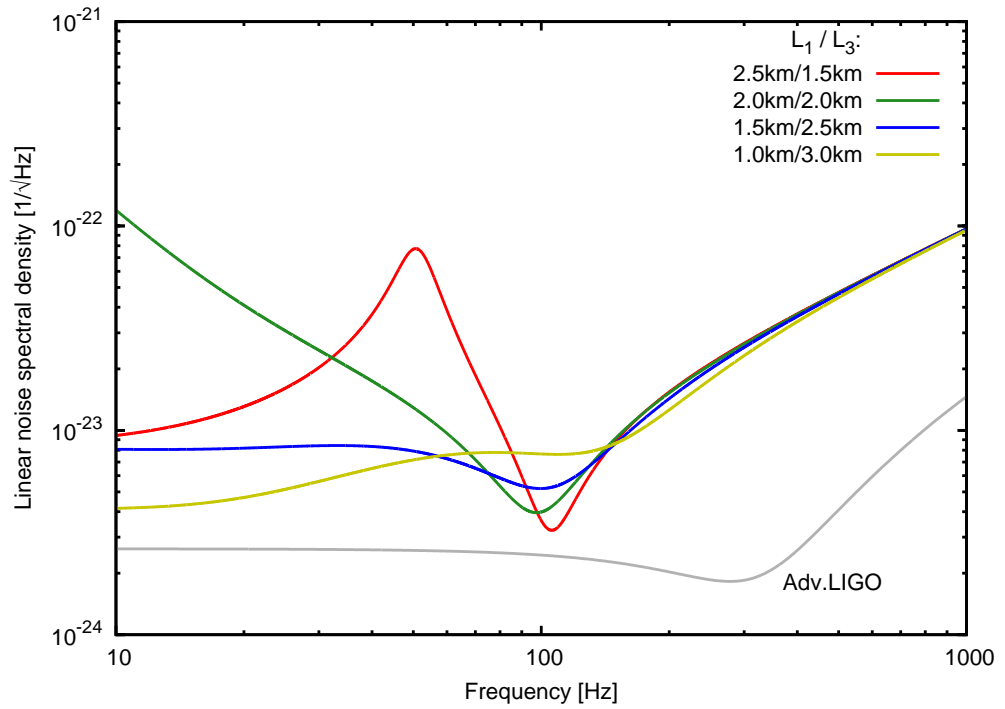
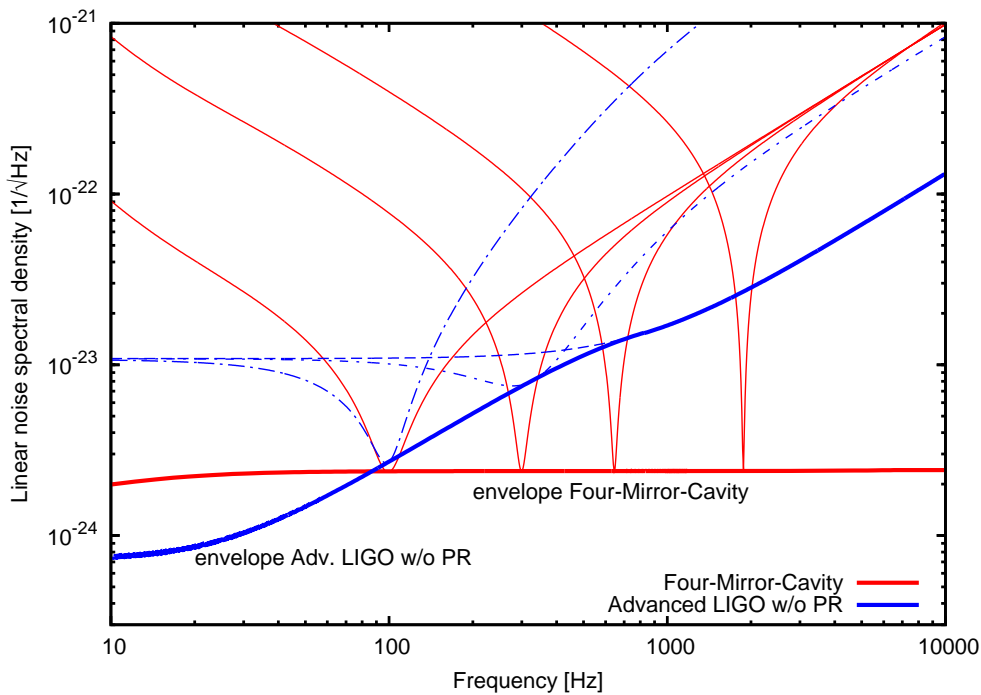


Figure 3.6 — Sensitivity in the phase quadrature of the differential mode with different ratios of  $L_1/L_3$ .

The tunings  $\Phi_3$  and  $\Phi_1$  were scanned around the lower left resonance branch. Various ratios of  $L_1/L_3$  were investigated. As already expected from the investigation of the special cases described above, there were no impedance matched configurations found having sensitivities comparable in a wide frequency range to the Advanced LIGO optical configuration. Thus, also for the four-mirror cavity the Power Recycling technique comes in consideration to broaden the bandwidth for signal sidebands.

### 3.4.2 Exemplary configuration

In this Section the properties of one exemplary configuration which yields sensitivities typical for a four-mirror cavity enhanced Michelson interferometer are presented. Figure 3.7 shows the envelope of the tunable peak sensitivity and exemplary sensitivity curves for different frequency splittings, whereas the reflectivities are fixed. The reflectivities  $\rho_2 = \rho_3 = 0.999$  were chosen to



**Figure 3.7** — Comparison of the envelopes of the tunable peak sensitivity in the phase quadrature. Exemplary sensitivity curves with different tunings but fixed reflectivities are shown.

ensure low powers in the second cavity embedding optical substrates. The reflectivity  $\rho_1 = 0.996$  was chosen as compromise between a high peak sensitivity and a broad bandwidth. With this setup, the power in the first and third cavity are identical (approximately 61 kW with 125 W input power) and independent of the frequency splitting. The power in the second cavity is  $P_2 \approx 16$  W. Thus, the boundary condition of low powers in optical substrates can be fulfilled with remarkable low powers in the second cavity. The sensitivity of this configuration is as good as the Advanced LIGO ones, if identical powers at the beam splitter are assumed. It should be mentioned, that the four-mirror cavity can be tuned to high frequencies with a constant peak sensitivity in contrast to the Advanced LIGO optical configuration. Also the detection bandwidth is not limited by the arm cavities' finesse (refer to the envelopes shown in figure 3.7), because the effective finesse is adjustable by the transmission of the second cavity. This fact also implies that the intra cavity loss in the second cavity caused by the AR-coatings and absorption

in the optics' substrates are not limiting the performance of the four-mirror cavity.

### 3.5 Conclusion

The expressions describing the shot noise limited sensitivity of a four-mirror cavity enhanced Michelson interferometer were derived. The detailed analysis of the resonance feature using expressions similar to the ordinary two-mirror cavity case offers a qualitative and intuitive understanding of this complex configuration. With this understanding it was possible to systematically investigate the configuration for shot noise limited sensitivities throughout the whole 11-dimensional parameter space. Despite the huge parameter space giving a variety of possibilities to adapt the shape of the sensitivity curve to the requirements, contrary to expectations there are no parameter configurations optimally exploiting both the frequency splitting and the laser input field yielding better sensitivities compared to Advanced LIGO in a wide frequency range. Only if identical powers at the beam splitter are assumed, the four-mirror cavity provides sensitivities comparable to the Advanced LIGO ones. However, these powers at the beam splitter would still be restricted by the problem of thermal lensing. Moreover, only in the differential mode of the four-mirror cavity enhanced Michelson interferometer reasonable sensitivities can be achieved. This setup is hardly to implement in the infra-structure of existing gravitational-wave detectors. Thus, the results of the above investigations confirm the choice of RSE-topologies for the second generation of interferometric gravitational detectors.

---

# Detuned Twin-Signal-Recycling

## 4.1 Introduction

In this Chapter the Twin-Signal-Recycling (TSR) interferometer technique for gravitational-wave detection is proposed. This technique bases on the coupling of two optical resonators leading to a frequency splitting as described in Chapter (2.2). There exists an operating point (referred to as *optimum operating point* in the following) providing symmetrical resonance conditions for upper and lower phase modulation signal sidebands. On the one hand this symmetry allows a broadband sensitivity enhancement of a factor of up to 2 compared to single sideband recycling techniques (such as Signal-Recycling and Resonant-Sideband-Extraction) [56]. On the other hand the injection of squeezed states of light is less demanding and enables a broadband quantum noise reduction in the shot noise limited frequency regime without the need for additional filter cavities. Furthermore there is a variety of possibilities to shape the sensitivity curve with respect to known gravitational-wave sources by properly adjusting the tunings of the TSR-resonators.

The advantages of TSR will be discussed in comparison to the sensitivity of GEO 600 assuming technical design parameters. The noise spectral densities (sensitivities) were calculated utilizing the Caves-Schumaker two photon formalism (TP) [57]. For further details of the TP and the *input-output relation* of an interferometer please refer to [58, 59]. An introduction to the theory of non-classical light can be found e.g. in [60]. The MATLAB-scripts used here are attached in the Appendices A.1 and A.2.

Since the potential of a broadband quantum noise reduction by means of squeezed states is a main feature of the TSR technique, first a brief review on the history of squeezed field injection at interferometric gravitational-wave detectors is given in the next section.

The main results of the investigation discussed in this chapter were published in

- “*Detuned Twin-Signal-Recycling for ultrahigh-precision interferometer*”  
André Thüring, Roman Schnabel, Harald Lück, and Karsten Danzmann  
*Optics Letters*, 32, 985 (2007).

#### 4.1.1 History of squeezed field injection for gravitational-wave detectors

The use of squeezed states of light for improving the sensitivity of gravitational-wave detectors was first proposed in 1981 by Caves [32]. He showed that the quantum noise limited sensitivity in a shot noise dominated interferometer can be enhanced by the injection of a broadband (frequency independent) squeezed field into the interferometers signal port. Furthermore he stated that “[...]the greatest potential usefulness of squeezed states lies in its ability to increase the sensitivity without increasing the circulating laser light power[...]”. Accordingly at a point, where the interferometer performance will be limited by the thermal load in its optics and the resulting wavefront distortion (refer to Sec. 3.1) squeezed field injection can be used to either relax the high power requirement or increase the sensitivity further. The reduction of shot noise by the aid of squeezing was later experimentally shown in [61, 62, 63].

However, at first view the enhancement of a interferometers sensitivity with frequency independent squeezing (squeezed light with a fixed quadrature angle) can only be achieved in a certain frequency range. This is a direct consequence of the Heisenberg uncertainty principle. Considering a simple Michelson interferometer the quantum noise in its phase quadrature (shot noise) can be reduced by the amount of squeezing. Unfortunately, the quantum noise in the amplitude quadrature (radiation pressure noise) will be increased by the same amount enhancing the noise at low frequencies. Later it was revealed by Unruh [36] and others [37, 27, 38] that squeezed field injection with frequency dependent squeezing angle allows an overall quantum noise reduction including the radiation pressure noise thereby beating the standard quantum limit (SQL).

Motivated by the work of Unruh and Jackel & Reynaud the use of additional input and output optics — namely filter cavities — was proposed by Kimble *et al.* [39]. Applying these filters (commonly referred to as KLMTV filters) converts a conventional interferometer into a broadband quantum non-demolition (QND) interferometer. The filters allows the preparation of squeezed states providing a frequency dependent squeezed quadrature which is adapted to the interferometers quadrature rotation. The injection of such a prepared squeezed state leads to a quantum noise reduction over the complete detection band. Furthermore, a so-called squeezed variational homodyne readout of the interferometers output can be performed with a frequency dependent optimal detection quadrature.

The investigation of Kimble *et al.* was restricted to broadband tuned detectors (e.g. Ini.LIGO) without SR or RSE, respectively. It was shown by Harms *et al.* [58] that such filters applied in a detuned SR topology (e.g. GEO 600) also allows a broadband quantum noise reduction by squeezed light and a optimization of the detection angle. Unfortunately, quite generally two or more low-loss, narrow-linewidth, and therefore long-baseline optical filter cavities are necessary to prepare the squeezed states in an optimum way to achieve this goal. Thus an implementation in the infrastructure of existing and future gravitational-wave detectors poses a problem. But taking into account that the quantum noise at low frequencies, especially in the radiation pressure noise dominated regime is covered by other noise sources such as seismic and thermal noise, an improvement within this frequency regime from the squeezed field injection can not be achieved anyway. Consistently, Schnabel *et al.* [64] found that in the case of GEO 600 just one additional filter cavity preparing the squeezed light is sufficient to improve the whole shot noise limited frequency range. Correspondingly, the generation of frequency dependent squeezing utilizing one filter cavity was experimentally characterized by Chelkowski *et al.* [65] followed by the shot noise reduction of a table-top Dual-Recycled Michelson interferometer demonstrated by Vahlbruch *et al.* [41].

Another way to avoid the use of multiple long base line filter cavities but achieving still an enhancement in the high frequency range without drastically worsen the low frequency sensitivity was proposed by Corbitt *et al.* [66]. Here, the use of Fabry-Perot cavities was suggested acting as high-pass filters (termed amplitude filters within this context) for the squeezed field. In reflection of these filter cavities the squeezing at sideband frequencies beyond the filter cavities bandwidth is preserved whereas at low frequencies the squeezing is lost and replaced by ordinary vacuum noise. Since any optical loss of the filters mainly affect the transmitted part the baseline of the filters

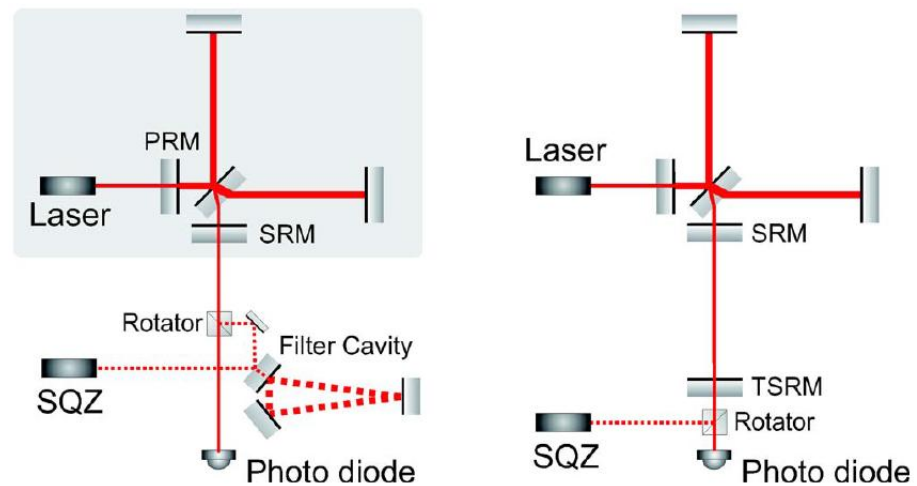


**Figure 4.1** — Top left (shaded): Topology of the current gravitational-wave detector GEO 600. The mirror PRM in the laser input port realizes so-called power-recycling. The signal-recycling mirror (SRM) in the output port establishes a carrier light detuned single-sideband signal recycling cavity. Bottom left: Extension for a broadband shot-noise reduction utilizing squeezed states. Right: Topology, proposed here. Two optically coupled cavities are formed with the help of an additional mirror TSRM. Their resonance doublet enables detuned twin-signal-recycling resulting in lower shot noise. Squeezed states can be used without additional filter cavity.

can be chosen comparatively small. However, this technique seems only to be useful for broadband tuned detectors. In the case of single sideband recycling detectors the rotation of the squeezing ellipse around the optical resonance could not be compensated by these filters leading to a decreased sensitivity even below that of the un-squeezed interferometer.

Within this context, the TSR interferometer technique was analyzed and proposed. Here, a quantum noise reduction in the shot noise limited sensitivity can be achieved by the injection of frequency independent squeezing without the need for an additional long base line filter cavity.

## 4.2 The Twin-Signal-Recycling topology

A schematic illustration of the TSR topology is shown in Fig. 4.1 in comparison to the GEO 600 topology extended by a single long baseline filter cavity for broadband shot noise reduction.

The shaded upper left-hand part of Fig. 4.1 shows a Michelson interferometer topology with the techniques of PR and SR as used in the GEO 600 detector. Such an interferometer is operated close to a dark fringe, which is a requirement for recycling techniques. To form a detuned SR cavity, mirror SRM is positioned such that not carrier laser light but signal light is resonating. A modulation signal at the frequency  $\Omega$  produces an upper sideband field at  $\omega_0 + \Omega$  and a lower sideband field at  $\omega_0 - \Omega$  where  $\omega_0$  is the carrier light's angular frequency. Thus, if the recycling frequency (target frequency) is higher than the bandwidth of the SR cavity, only the upper or the lower sideband field can be enhanced whereas the counterpart is suppressed, thereby losing half of the maximum signal. Nevertheless, the recycling of one of these signal sideband fields still leads to an enhanced sensitivity compared to an ordinary Michelson interferometer. The lower left-hand part of Fig. 4.1 shows the extension to employ squeezed states of light. A source of a broadband squeezed field (SQZ), a long-baseline filter cavity, and a Faraday rotator for coupling to the signal modes [63] is required for a broadband sensitivity improvement as proposed in [64] and experimentally demonstrated in [41].

The right-hand part of Fig. 4.1 shows the topology proposed here. Starting from the standard SR topology, an additional mirror (TSRM) is placed in the signal output port of the interferometer. This mirror forms a new long-baseline cavity that is optically coupled with the initial SR cavity. Similar to two coupled mechanical oscillators, two coupled optical cavities feature a resonance doublet (refer to Section 2.2 in Chapter 2). The frequency splitting  $f_{sp}$  of this resonance doublet is determined by the coupling of the two resonators, i.e., the transmission of the center mirror (SRM). The transmission  $T_c$  of the mirror SRM corresponding to this coupling can be obtained from Eq. (2.72) giving

$$T_c = 1 - \frac{4 \cos^2 \left( 2 \frac{\omega_{sp} L_{TSR1}}{c} \right) \rho_{end}^2}{(1 + \rho_{end}^2)^2}. \quad (4.1)$$

For ideal interferometer end mirrors with a reflectance of  $\rho_{end} = 1$ , Eq. (4.1) further reduces to

$$T_c = 1 - \cos^2 \left( 2 \frac{\omega_{sp} L_{TSR1}}{c} \right). \quad (4.2)$$

Thus, the transmission  $T_c$  of the mirror SRM has to be chosen with respect to the required frequency splitting  $\omega_{sp} = 2\pi f_{sp}$ . Then the resonances' bandwidth of the doublet can be determined by the reflectivity of the mirror TSRM. Fig. 4.2 shows the resonance doublet for  $L_{TSR1} = L_{TSR2} = 1200$  m,

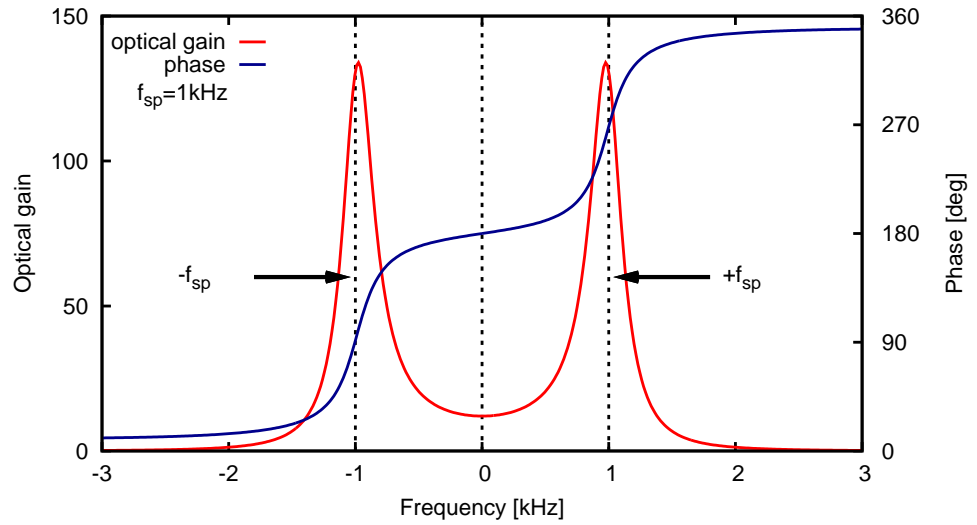


**Figure 4.2** — The resonance doublet of the TSR interferometer for technical design parameters allowing a direct comparison with GEO 600.

$\rho_{\text{end}}^2 = 0.99995$  and  $\rho_{\text{TSRM}}^2 = 0.963$  (note, that the choice of these parameters originates from the comparison with the extended GEO 600 topology as discussed in the next section). The resonance doublet is symmetric around the carrier frequency  $f_0$  in magnitude and phase, respectively. Thus, if the three-mirror coupled cavity is tuned to  $f_0$ , upper and lower signal sidebands have identical resonance conditions.

## 4.3 Comparison of TSR with GEO 600

### 4.3.1 The quantum noise limited sensitivities

The following discussion assumes technical design parameters for both interferometer topologies (refer to Table 4.1). These parameters were chosen according to the comprehensive investigation of the possible squeezing enhanced sensitivity of GEO 600 presented in [58]. The length of the TSR cavities were set to 1200 m each accounting for an realizable implementation in the infrastructure of the GEO 600 facility. Then, the reflectivity of TSRM was chosen to reach the peak sensitivity of GEO 600. In the case of GEO 600 the recycling frequency  $f_{\text{rec}}$  (where the best sensitivity is obtained) is adjustable by the SR cavity detuning according to  $\Phi_{\text{SR}} = 2\pi f_{\text{rec}} L_{\text{SR}}/c$ . On the contrary

**Table 4.1** — The parameters for the comparison of GEO 600 and TSR.

Symbol	Physical meaning	GEO600	TSR
$m$	Mirror masses (each)	5.6 kg	5.6 kg
$L_{\text{arm}}$	Effective arm length	1200 m	1200 m
the $L_{\text{SR}}$	Length of SR-cavity	1200 m	-
$L_{\text{TSR1,TSR2}}$	Length of TSR cavities	-	1200 m
$P$	Circulating light power	10 kW	10 kW
$\rho_{\text{SRM}}$	Reflectivity of $M_{\text{SRM}}$	$\sqrt{0.99}$	Eq. (4.1)
$\rho_{\text{TSRM}}$	Reflectivity of $M_{\text{TSRM}}$	-	$\sqrt{0.963}$
$\rho_{\text{end}}$	Reflectivity end mirrors	$\sqrt{0.99995}$	$\sqrt{0.99995}$
$\Phi$	detuning	$\Phi_{\text{SR}} \approx 0.0252 \text{ rad}$	$\Phi_{\text{TSR1,TSR2}} = 0$

the peak sensitivity of TSR topology is reached at  $f = f_{\text{sp}}$  determined by  $T_c$  thereby inhibiting the tunability. However, if one wants to realize a tunable TSR one have to replace the SRM by an etalon. This aspect is treated briefly in Section 4.4.3.

Fig.4.3 compares the quantum noise limited sensitivities (without squeezed input) of SR and TSR for various SR cavity detunings and the according couplings of the TSR resonators. In the shot-noise dominated regime below the recycling frequency the TSR technique proposed here provides an improved noise spectral density. Above the resonance, the sensitivity of TSR decreases with higher frequency compared with SR. For lower frequencies, quantum radiation pressure noise dominates shot noise and the detuned SR topology with resonating lower signal sideband shows a further resonance dip. This is the so-called *optical spring* resonance [67]. Such a resonance does not appear in the TSR topology proposed here, because the resonances of upper and lower sidebands are symmetrically arranged around the carrier frequency  $\omega_0$ . Note, that also for that reason a phase modulation as introduced by gravitational-waves only appears in the carrier lights phase quadrature as it is expected from a simple Michelson interferometer. This contrasts with detuned SR where signal sidebands appear in phase and amplitude quadratures and in any linear combination of both whereby the optimum detection quadrature gets frequency dependent. In Fig. 4.3 for instance the optimum case of a variational readout is shown for GEO 600.

For further investigations the recycling frequency (splitting frequency) was set to 1 kHz for two reasons. First, in the lower frequency regime the sensitivity of GEO 600 and TSR will be limited by thermal noise so that the

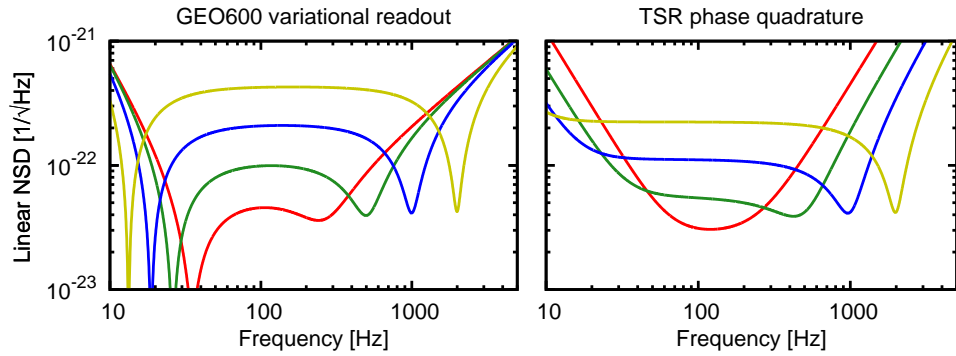


**Figure 4.3** — Quantum noise limited sensitivities of GEO 600 and TSR. Left: The curves shows the sensitivity of GEO 600 tuned to 250 Hz, 500 Hz, 1000 Hz and 2000 Hz assuming an optimal frequency dependent detection. Right: Sensitivity of detuned TSR for  $f_{sp} = 250$  Hz, 500 Hz, 1000 Hz and 2000 Hz achieved with a readout of the phase quadrature.

use of squeezed states can not lead to an improvement. Second, in the TSR case the transmission of SRM determining the frequency splitting decreases with the required splitting frequency (e.g.  $f_{sp} = 250$  Hz requires  $T_c \approx 80$  ppm). Thus, for small a  $f_{sp}$  the performance of TSR might be limited by the internal interferometers losses. For the frequency splitting of 1 kHz a transmission of greater than 1000 ppm is necessary which is not that critical.

Fig. 4.4 shows the quantum noise limited sensitivities of GEO 600 and TSR for the recycling frequency  $f_{rec} = 1$  kHz. For GEO 600 the sensitivity curves corresponding to a variational readout, a readout of the phase and amplitude quadrature respectively are shown. The detection of the phase quadrature yields a better sensitivity in the frequency regime beyond the recycling frequency whereas at low frequency the sensitivity in the amplitude quadrature is much better (upto one order of magnitude). These sensitivity are optimally combined in the variational readout case. For TSR the readout of the phase quadrature is displayed. It can be seen, that — except of the optical spring resonance — TSR yields a better sensitivity over the entire frequency band below approximately 1500 Hz. Note, that the detection of the phase quadrature already yields the optimum sensitivity without the need for further input-output optics.

Fig. 4.5 compares the optimum detection angles of a homodyne readout as well as the optimum (frequency dependent) squeezing angles which are required to allow a broadband quantum noise reduction. It can be seen, that

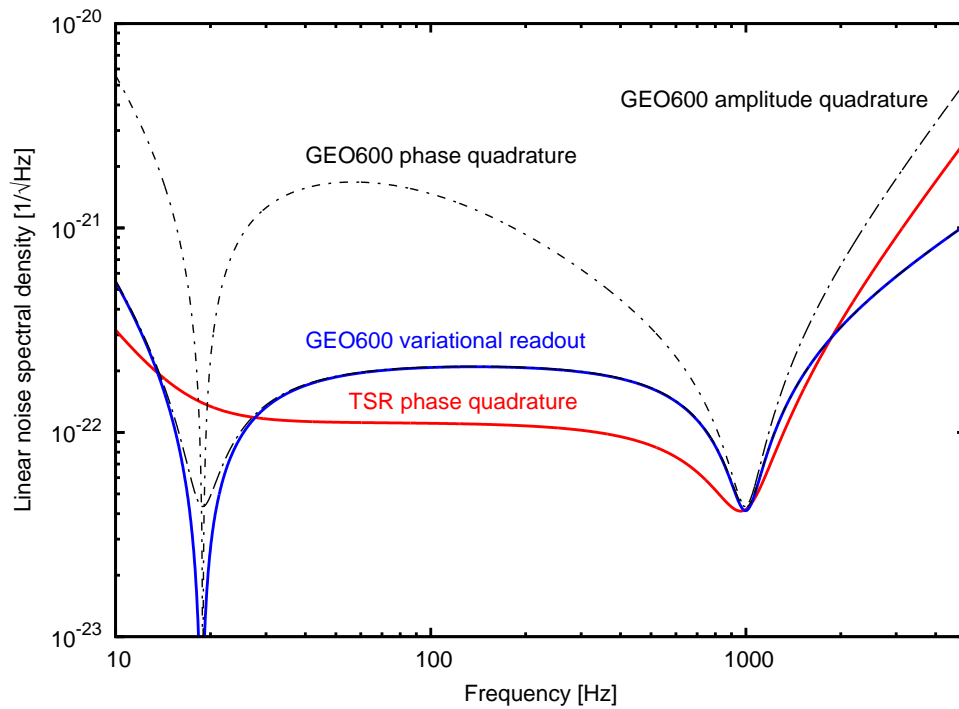


**Figure 4.4** — The figure shows the quantum noise limited sensitivities for a recycling frequency of 1 kHz. For GEO 600 the cases of a variational readout, a detection of the amplitude and phase quadrature respectively are shown. In the TSR case the optimum sensitivity is achieved with a readout of the carrier lights phase quadrature.

for TSR the intrinsic optimum detection angle  $\zeta_{\text{opt}}$  corresponds to the readout of the carrier lights phase quadrature. As well, the optimal squeezing angle  $\lambda_{\text{opt}}$  in the shot noise limited region corresponds to the squeezing of the phase quadrature.

In contrast to TSR, for GEO 600 the optimum detection angle as well as the optimum squeezing angle are frequency dependent even in the pure shot noise limited region around the optical resonance. That means, that — if a homodyne readout is considered — for GEO 600 additional output optics are required to achieve the optimum frequency dependent readout. In addition, at least a single filter cavity will be necessary to prepare the squeezed states optimal leading to a quantum noise reduction in shot noise limited detection band.

Please note the following: In the case of a heterodyne readout scheme an

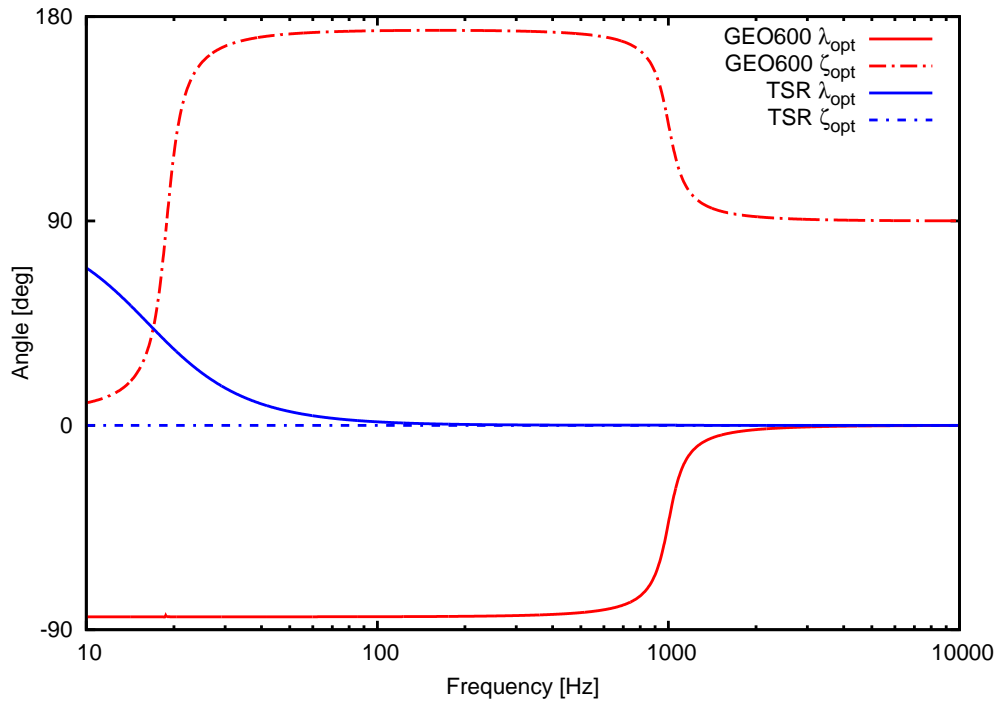


**Figure 4.5** — The figure compares the optimal detection angle  $\zeta_{opt}$  and the optimal squeezing angle  $\lambda_{opt}$  for GEO 600 (red curves) and TSR (blue curves).

optimal, frequency dependent linear combination of amplitude and phase quadrature can be achieved as currently performed at GEO 600 [68] without additional output optics. Here, the electronic signal of the photo detector is demodulated at the heterodyne frequency. Similar to the homodyne readout, for single sideband SR the gravitational-wave signal is contained in both demodulation quadratures (*inphase* and *quadrature* demodulation) and any linear combination of them. Accordingly, by splitting the photo detectors signal and demodulating the two parts *inphase* and in *quadrature* allows an optimal frequency dependent combination. However, in general a homodyne readout provides a better signal to noise ratio compared with the corresponding heterodyne readout in which an additional quantum noise contribution is induced due to the demodulation process (for further details refer to [69, 70, 71, 72]). In addition, the presence of the RF sidebands applied for the heterodyne readout in the detection port can lead to an increased technical noise distribution. As well, phase noise of the RF-modulation and a potentially imperfect

spatial overlap of the gravitational-wave signal fields with the RF-sideband fields would probably limit the sensitivity. An investigation of these facts related to GEO 600 can be found in [73]. Moreover, especially in view of the injection of squeezed states the homodyne readout has advantages over a heterodyne readout. It was shown by Gea-Banacloche and Leuchs [69] and later by Chickarmane *et al.* [74] that for a heterodyne readout a broad squeezing spectrum within the detection bandwidth and around twice the heterodyne frequency is required to achieve an optimal sensitivity enhancement. This requirement leads to further restrictions regarding the implementation of squeezed field injection (see for example [75]).

Owing to the circumstances discussed above, for the next advanced generation of interferometric gravitational-wave detectors as well as for the upgrades of current detectors the decision was made to perform a homodyne readout. More precisely, a so-called DC-readout (also referred to as *self-homodyning*) will be realized by operating the interferometers slightly offset from the ideal dark fringe condition. As a result a small fraction of the carrier light is transferred to the detection port and serves as local oscillator. Note, that in this special case of homodyning the detection quadrature is fixed since there exists no possibility to change the relative phase between LO (carrier) and signal sidebands barring an optimization. Recently, a DC-readout was performed and analyzed at GEO 600 [76] and at the Caltech 40m-prototype [77].

Within this context, the advantages of TSR over detuned single sideband SR as currently established in GEO 600 and proposed for Advanced LIGO [16, 78], Advanced VIRGO [79] and LCGT [9] are inherent in the fact that the simultaneous recycling of both signal sidebands leads not only to a sensitivity enhancement of up to a factor of two but also to an intrinsic optimal sensitivity achievable by a *frequency independent* detection of the carrier lights phase quadrature.

### 4.3.2 Broadband shot noise reduction by squeezed field injection

This section compares detuned SR (GEO 600) with the detuned TSR technique in combination with the injection of squeezed fields, as shown in Fig 4.1. Here a broadband squeezed field is assumed with a squeezing parameter  $r = 1$ , which corresponds to about 8 dB squeezing of noise variance. For GEO 600 just an additional filter cavity for generation of frequency dependent squeezing is considered as proposed in [64]. Furthermore, a variational readout is not taken into account. From Fig. 4.5 can be deduced that an optimization of the detection angle in the pure shot noise limited would require one further long

baseline output filter cavity hardly to implement in the existing infrastructure besides the required squeezing filter cavity.

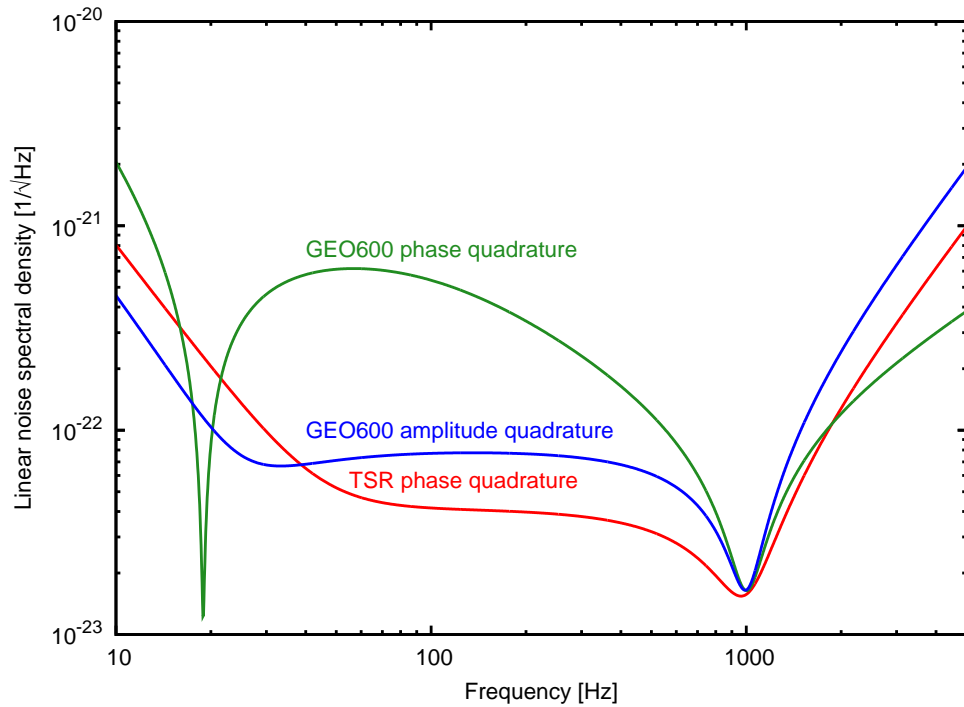


**Figure 4.6** — Squeezed light enhanced sensitivities of GEO 600 and TSR.

Figure 4.6 shows the squeezing enhanced sensitivities of detuned SR (GEO 600) and TSR. Again, for frequencies between 40 Hz and approximately 1500 Hz, TSR achieves a lower noise spectral density than detuned SR. Comparing TSR with and without squeezed-state input shows that the TSR technique provides quantum noise reduction from squeezed states over a wide band without an additional filter cavity. Please note, that the detection of the phase quadrature of GEO 600 which provides slightly better sensitivities in the detection band beyond the recycling frequency, is not accessible with an appropriate DC-readout (refer to [76]). Also, the slightly increased noise spectral density at frequencies below 40 Hz in TSR will not be significant as long as this frequency regime is not limited by quantum but by classical noise (thermal and seismic noise).

In conclusion, detuned TSR operated at its optimum operating point is favorable compared with detuned SR as it solves three problems at the same

time. First, a simultaneous recycling of upper and lower signal sidebands is achieved leading to an increased signal-to-shot-noise ratio. Second, similar to an simple Michelson interferometer (or carrier tuned broadband topologies) detuned TSR facilitates an optimal readout without the need for further output filter optics even accessible with a DC-readout. Third, the injection of *frequency-independent squeezing* leads to an improvement in the complete shot noise limited detection band.

#### 4.4 Further possibilities of shaping the sensitivity curve

The investigation in Sec. 4.3.1 and Sec. 4.3.2 was limited to the optimum OP with a resonance doublet arranged symmetrical around the carrier. However, besides this OP that is distinguished by its potential for an easy implementation of squeezed field injection, there exists further suitable OPs allowing a shaping of the sensitivity curve. In this section two further operating modes of the TSR technique will be presented assuming the same parameters (except of the tunings) as before. Compared with the sensitivity achieved at the optimum OP the one modus allows an improved peak sensitivity at a dedicated frequency by altering the bandwidth of the resonance. Simultaneously, an improvement in the upper frequency regime can be achieved. In the second modus, a combination of the broadband (tuned) SR modus and the narrowband (detuned) SR is possible leading to an improved sensitivity in the low frequency regime when compared with GEO 600. Note, that in these cases the sensitivity enhancement due to injection of squeezed fields are secondary.

Fig. 4.7 shows the resonance pattern of the coupled TSR resonators. Since the tunings of these resonators can be adjusted by the microscopic mirror positions of SRM and TSRM (refer to Fig. 4.1) without affecting the resonance condition of the PR cavity and thereby the amount of laser light power circulating in the interferometer, any desired OP of the TSR resonators can be chosen to alter the signal sidebands transfer function. Two obvious types of OPs will be analyzed. First the OPs i)-iii) along the red line in Fig. 4.7 allows a tuning of the recycling frequency  $f_{\text{res}}$  similar to detuned SR. Additionally, a second resonance in the transfer function appears whereby the combination of tuned (broadband) SR and detuned SR (narrowband) becomes possible. The sensitivity achieved at these OPs is discussed in Sec. 4.4.1. Second, the potential to vary the peak sensitivity (and so the bandwidth) at a certain frequency (here 3 kHz) will be discussed in Sec. 4.4.2. The considered OPs are

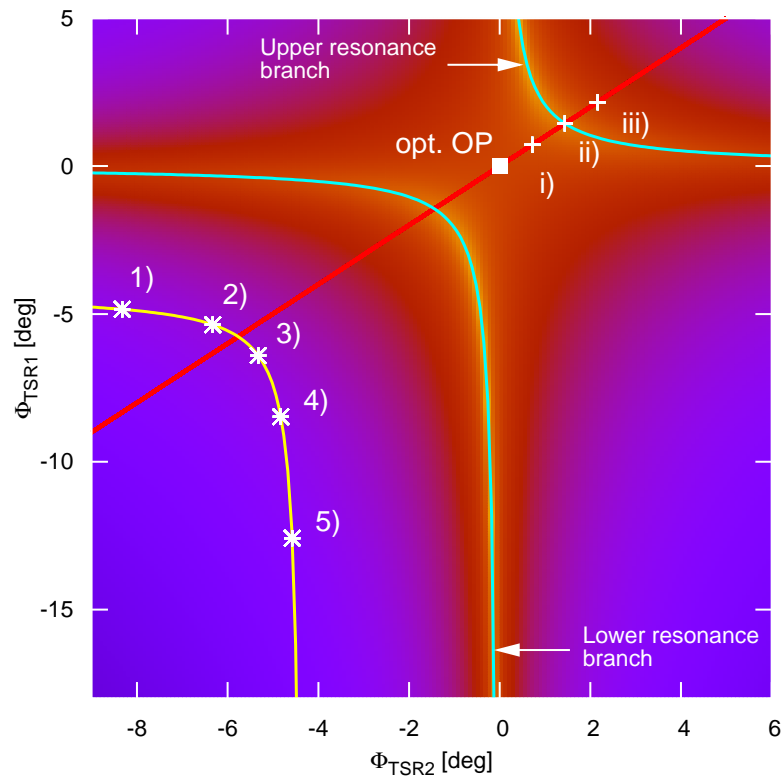


**Figure 4.7** — The figure shows the resonance pattern of the TSR resonators for the technical design parameters used throughout this Chapter. Note, that the optical gain is logarithmic color coded for visualization purposes. The origin corresponding to the optimum OP is highlighted by the white square. Additionally, the line  $u(\omega)$  (refer to Eq. (2.65) in Sec. 2.2.4) related to the optimum OP as well as to the OPs i)-iii) is shown. The yellow curve is separated by -3 kHz from the lower resonance branch. Accordingly, for the OPs 1)-5) a resonance at 3 kHz with different bandwidths each appears in the transfer function.

labeled from 1)–5) in Fig. 4.7.

#### 4.4.1 Combination of tuned and detuned SR

By leaving the optimum OP of the TSR topology the resonance condition for upper and lower sidebands became asymmetric whereby two resonances appear in the transfer function at different frequencies. Note, that in general the optical gain of each single resonance is lowered by a factor of two compared

to the symmetric case. The OPs i)-iii) considered here yield two resonances of identical gain and bandwidth since the transfer function corresponds to a cross-section along a line  $u(\omega)$  (red line in Fig. 4.7) running through the symmetry point (for details refer to Sec. 2.2.4). In general, the smallest realizable distance of two resonances in the transfer function of a three-mirror cavity is exactly the splitting frequency  $f_{sp}$ . This case is demonstrated with OP i). Here, the tunings were chosen to obtain a resonance for the upper sidebands at 500 Hz and for the lower sidebands at -1500 Hz (both related to the carrier frequency). Accordingly, the sensitivity curve features peak sensitivities at 500 Hz and 1500 Hz. The other OPs lead to resonances separated by exactly  $2f_{sp}$ . One special case is considered with OP ii). Here the tunings were chosen such that the carrier is resonant on the upper resonance branch. Thus, lower and upper sidebands are recycled within the respective bandwidth. Additionally, the lower sideband field is resonant at  $-2f_{sp}$ . This special case represents the combination of tuned SR, where both sidebands are recycled, and detuned single sideband SR here performed simultaneously leading to a further sensitivity enhancement at  $f_{rec} = 2f_c$ .

Fig. 4.8 compares TSR operated at the OPs i)-iii) with GEO 600 tuned to 2500 Hz. At low frequencies OP ii) achieves a sensitivity improved by one order of magnitude and provides additionally an enhancement at 2000 Hz. However, since at low frequencies the quantum noise limited sensitivity is expected to be covered by thermal noise, configurations yielding an increased sensitivity in the mid-frequency region are exemplary considered with OP i) and OP iii). Here a peak at 500 Hz is realized for both OPs. A further enhancement resulting from the second resonance is achieved at 1500 Hz for OP i) and at 2500 Hz for OP iii). Considering the direct comparison of OP iii) with GEO 600 reveals, that this modus of TSR represents a compromise of the tuned and detuned SR since at low frequency the improvement is considerably (shaded area in Fig. 4.8) whereas at the second recycling frequency (here 2500 Hz) GEO 600 yields a better peak sensitivity. Nevertheless, the decreasing sensitivity of TSR above approximately 2000 Hz is not that significant if compared to the gained improvement in the mid-frequency range. Accordingly, this mode of TSR might find application where both, a satisfactory sensitivity at mid frequencies and a high narrowband sensitivity at high frequencies are required.

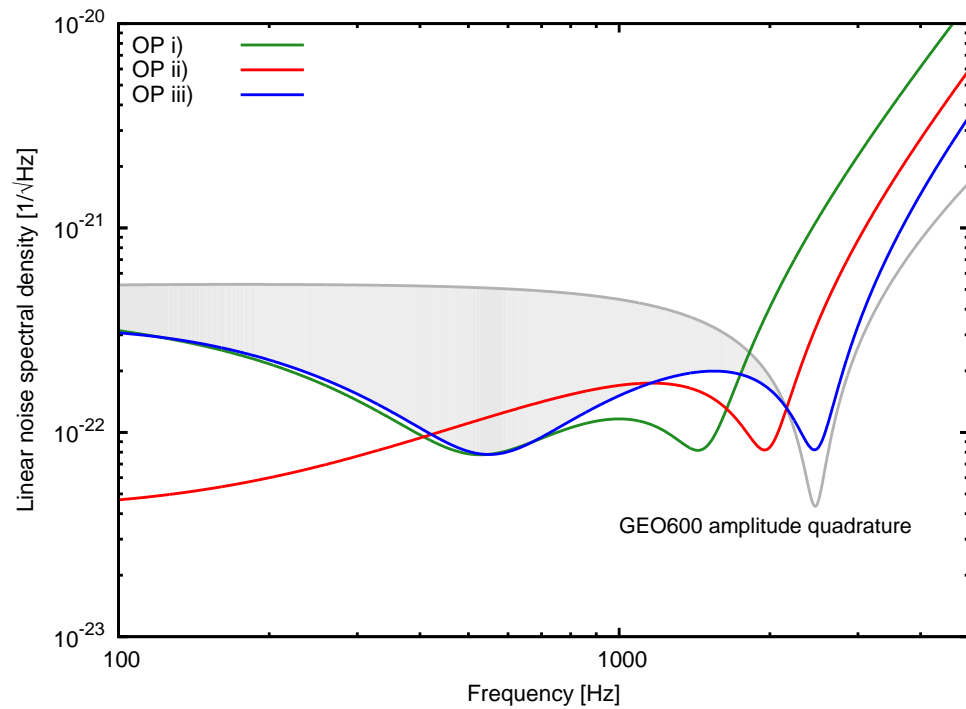


**Figure 4.8** — The figure shows the sensitivities (assuming a readout of the amplitude quadrature) achieved at the OPs i)-iii) illustrated in Fig. 4.7. The red curve demonstrates the combination of tuned and detuned SR. In comparison the sensitivity of GEO 600 (tuned to 2500 Hz) is displayed by the grey curve. The shaded area emphasize the improvement at OP iii) in the lower frequency band.

#### 4.4.2 Tunable bandwidth

The use of mirrors with a controllable reflectivity to simply adapt the finesse of an optical resonator were proposed for interferometric gravitational-wave detectors years ago by Strain and Hough [80]. Here, two potential applications were suggested. First, to use such a controllable mirror as arm cavity end mirror providing a balancing of the laser power stored in the arms. This application realizable with an etalon used as end mirror was recently investigated for the use in Advanced VIRGO [81].

Second with respect to SR and RSE Strain and Hough stated that “[...] if a variable reflectivity mirror can be used as the signal recycling or signal extraction mirror then a range of frequency responses can be obtained by simple electronic control of the mirror. The response could even be altered

dynamically to follow the development of a signal with a predictable evolution, e.g., that expected from coalescing binary neutron stars [82][. . .]”. In subsequent experiments the flexibility gained from a mirror with variable reflectivity (in form of a two-mirror cavity or a Michelson interferometer) was demonstrated by G. de Vine [83, 84]. A thermal tunable etalon used as SRM in a dual-recycled Michelson interferometer was demonstrated in [85, 86].

The investigation of a three-mirror cavity presented in Sec. 2.2 showed inter alia that the coupling depends on the chosen OP. Consistently, the bandwidth of resonances appearing in the transfer function of a three-mirror cavity can be adapted by a proper choice of the OP. Here, serving as a pattern a resonance at 3 kHz is considered. The yellow curve shown in Fig. 4.7 is separated by -3 kHz from the lower resonance branch. Thus, by shifting the OPs along this curve the bandwidth of the resonance can be varied. This can be understood by considering the TSR-resonator build by SRM and TSRM (refer to Fig. 4.1) as compound mirror whose effective reflectivity depends on its tuning which accords to the suggestion of Strain and Hough for a mirror with variable reflectance .

Fig. 4.9 a) shows the shot noise limited sensitivities of TSR operated in the narrowband modus optimized for 3 kHz. It can be seen that the peak sensitivity is continuously increased by going from OP 1) to OP 5). The maximum peak sensitivity is achieved at a detuning  $\Phi_{\text{TSR2}} = \pm\pi/2$ . Compared with the optimum OP (grey curve), the sensitivity at 3 kHz can be improved by two order of magnitudes. Also, a broadband enhancement in the upper frequency band can be achieved. The shaded grey area highlights the enhancement gained at OP 2) where also at 5000 Hz a considerably high sensitivity is realized.

Fig. 4.9 b) compares the noise spectral densities for the optimum OP and OPs 1)-5) in combination with squeezed field injection. Although for OP 1)-5) no optimization of the squeezing angle is performed, the injection of *frequency independent* squeezing still leads to a relatively broadband enhancement as exemplary highlighted for OP 2).

Generally, with this modus of TSR high peak sensitivities can be achieved at any recycling frequency. The characteristics of the sensitivity curves (peak sensitivity, bandwidth and distances between both appearing resonances) shown in Fig. 4.9 can be moved to higher (lower) frequencies by shifting the OPs (yellow curve in Fig. 4.7) off (towards) the lower resonance branch. Therefore, in view of the static frequency splitting which forbids a tuning of the peak sensitivity when TSR is operated at the optimum OP, the modus

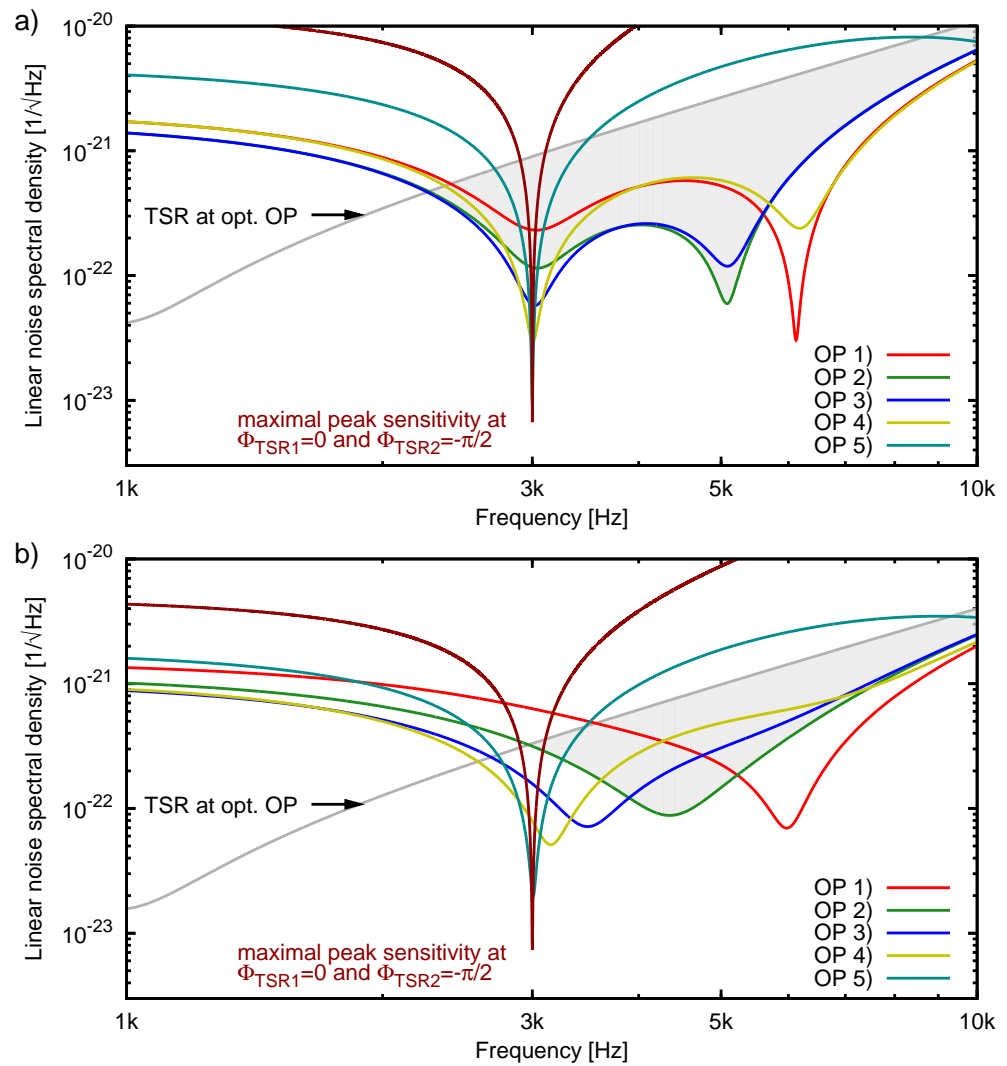


**Figure 4.9** — Comparison of the sensitivities of TSR optimized for 3 kHz and TSR at the optimal OP without (a) squeezed input and (b) with squeezed input. Here, the readout of the phase quadrature as well as a frequency independent squeezing ( $r = 1$ ) of the phase quadrature are assumed.

of TSR discussed above provides a suitable method to adapt the sensitivity curve to signals of possible gravitational-wave sources.

#### 4.4.3 Tunable frequency splitting

The frequency splitting of the TSR resonators is determined by the fixed transmission  $T_c$  of the center mirror (SRM). Accordingly, an in situ tuning of the frequency becomes possible if SRM is replaced by a mirror with variable reflectivity. Here, it is preferable to use a monolithic etalon instead of a short three-mirror cavity. Since a cavity requires additional length control and auto alignment servo loops, a realization is challenging. In contrast to this, if an etalon is used, no additional angular degrees of freedom need to be realized. Furthermore, the length control and thus the effective transmission can be adjusted by the etalon's substrate temperature [86]. Thus, in an independent measurement the transmission in dependence of the temperature could be determined.

The resonance feature of the etalon enhanced TSR resonators is that of an four-mirror cavity. Accordingly, the optimum operating point needs to be determined according to the Eqs. 3.16 and 3.17 obtained in Sec. 3. Except of this, the resonance feature is still that of a three-mirror cavity. Thus, for example the sensitivity curves shown in the right graph of Fig. 4.3 for different values of  $T_c$  can be realized by a proper adjustment of the etalon's temperature.

### 4.5 Parameters for a possible application in GEO-HF

Exemplary parameters and requirements for the implementation of TSR in the existing infrastructure of GEO 600 were already presented in [87]. The main emphasis was to shape the squeezing enhanced sensitivity curves of SR and TSR with respect to the expected thermal noise limiting the sensitivity of the enhanced GEO-HF detector [40]. It was shown, that a broadband tuned SR yields satisfactory sensitivities and allows the implementation of squeezed field injection without the need for filter cavities. For the sake of completeness, in this Section exemplary sensitivity curves of GEO-HF and TSR are shown. Here, the parameters for the TSR configuration were reviewed leading to a slightly improved sensitivity compared to those shown in [87].

Figure 4.10 shows the squeezing enhanced sensitivity curves in the detection band from 1 kHz to 10 kHz for various parameters of the interferometers. The circulating laser power is set to 70 kW and the squeezing value of about

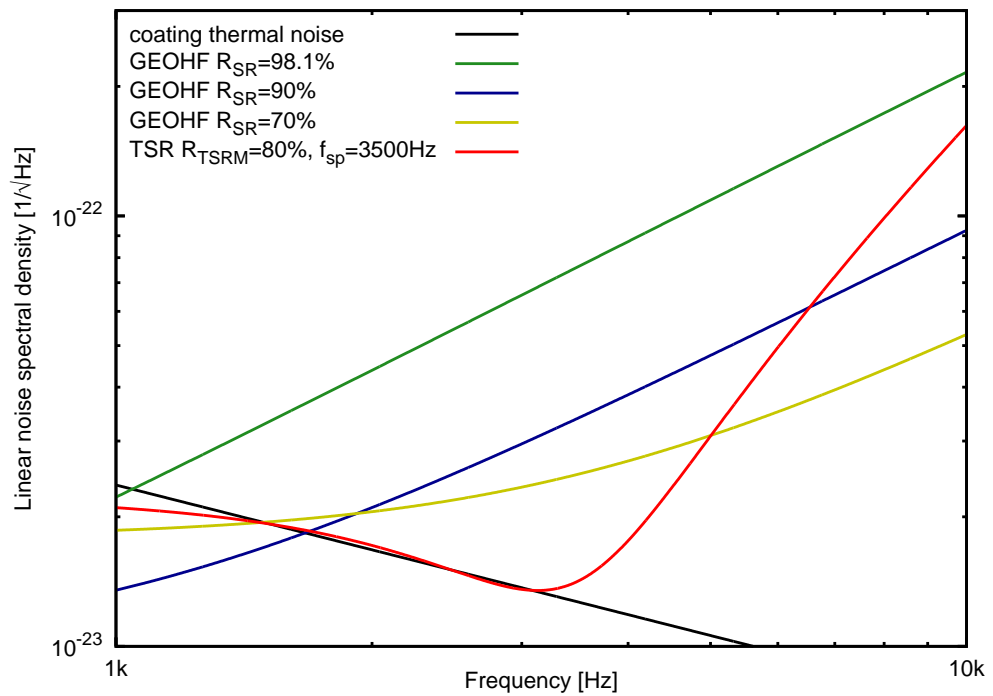


**Figure 4.10** — The figure compares the squeezing enhanced sensitivities of tuned SR for three values of  $R_{SR}$  and detuned TSR optimized to the expected coating thermal noise.

8 dB ( $r = 1$ ) was assumed. For tuned (broadband) GEO-HF three values of  $R_{SRM}$  are considered. The green curve was calculated with  $R_{SRM} = 98.1\%$  which corresponds to the reflectance of the SRM currently used in GEO 600. In the near future GEO 600 will be operated in the tuned mode with squeezed field injection. Once the thermal noise level is reached, a change of the SRM reflectivity (with respect to the thermal noise) will be considered. Accordingly, the blue and yellow curves show the sensitivity for increased bandwidths realized with  $R_{SRM} = 90\%$  and  $R_{SRM} = 70\%$ , respectively.

In comparison a TSR configuration with  $R_{TSRM} = 80\%$  is shown assuming a frequency splitting of 3500 Hz (red curve). It can be seen that the response of the TSR configuration is almost perfectly adapted to the thermal noise. Compared to the SR configuration with  $R_{SRM} = 70\%$  an improved sensitivity in the detection band up to 5 kHz can be realized. Additionally, TSR might find application when high peak sensitivities are required in the detection band at even higher frequencies which could not be covered with the tuned

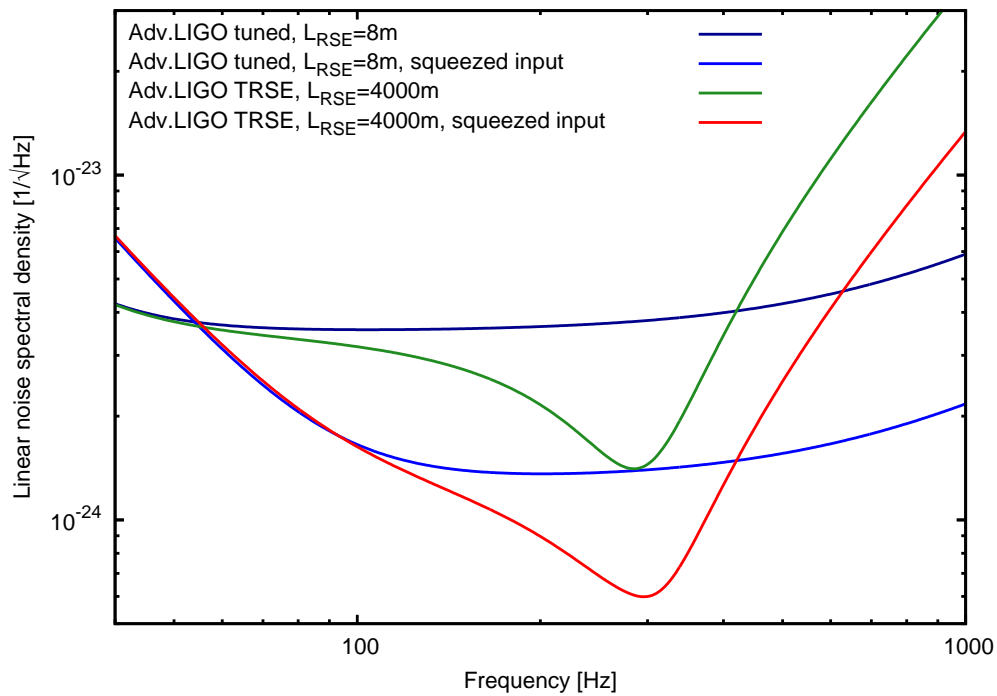


**Figure 4.11** — Sensitivity curves of RSE and TRSE. The parameters of the RSE topology accords to the Advanced LIGO optical configuration. In the TRSE configuration the extraction cavity length was set to 4 km.

SR configuration.

## 4.6 Application in Advanced LIGO: Conversion of RSE to TRSE

As the RSE topology is based on a coupled linear three-mirror cavity as well, it is evident that the elongation of the extraction cavity can lead to a simultaneous enhancement of upper and lower signal sidebands at a certain frequency and a broadband shot noise reduction by injection of frequency independent squeezing. Here, an exemplary configuration is presented under consideration of the parameters targeted for the Advanced LIGO optical configuration [16]. Figure 4.11 compares the squeezing enhanced sensitivities of the tuned (broadband) RSE and detuned TRSE configurations. In both cases, the arm cavities

where considered with  $L = 4$  km,  $R_c = 0.995$  and  $R_{\text{end}} = 1.0$ . The reflectance of the extraction mirror was set to  $R_{\text{RSE}} = 0.96$ . In the case of TRSE the extraction cavity length was set to 4 km. The shown sensitivity curves are related to an input power of 125 W and a squeezing factor of  $r = 1$  corresponding to about 8 dB squeezing of the noise variance. It can be seen, that the sole elongation of the extraction cavity leads to an improvement in peak sensitivity by more than a factor of two at 300 Hz. Accordingly, a TRSE configuration should be considered for future detector topologies aimed at an optimal sensitivity in the mid-frequency detection band.

---

# Experimental realization of Twin-Signal-Recycling

In this Chapter the first experimental realization of a Twin-Signal-Recycling (TSR) Michelson interferometer and also its enhancement by squeezed light injection is reported. All longitudinal degrees of freedom were stably controlled, and a broadband quantum noise reduction of the interferometers shot noise by a factor of up to 4 dB was demonstrated. The system was characterized by measuring its quantum noise spectra for several tunings of the TSR cavities. A good agreement between the experimental results and numerical simulations was found.

The main results of the experimental realization of TSR were published in

- “Broadband squeezing of quantum noise in a Michelson interferometer with Twin-Signal-Recycling ”  
André Thüring, Christian Gräf, Henning Vahlbruch, Moritz Mehmet, Karsten Danzmann, and Roman Schnabel  
*Optics Letters*, 34, 824 (2009)

## 5.1 Parameter choice

There was the opportunity to reuse and upgrade the experimental setup developed for the foregone demonstration of a squeezed-light-enhanced Power- and Signal-Recycled Michelson interferometer [41]. Accordingly, by means of comprehensive parameter studies and FINESSE [88] simulations it was re-

viewed to what extent the demonstration of a Michelson interferometer with Twin-Signal-Recycling could be realized within the given infrastructure.

### 5.1.1 TSR resonator length

At first, possible geometries of the TSR resonator (built by the SRM and the TSRM) were investigated. Here, the choice of the resonator length was subject to several boundary conditions:

- 1 | The realizable frequency splittings of the coupled TSR resonators had to be within a frequency range from 5 MHz to 15 MHz. The lower boundary accounted for the fact that the squeezing is expected to be masked by classical laser noise below 3 MHz. The upper boundary results from the presence of a modulation field at 15 MHz (used inter alia for the length control of the OPA) possibly disturbing the measured spectrum. The frequency splitting of a three-mirror cavity is determined by the coupling of both resonators and by the ratio of their lengths (refer to Sec. 2.2.5). Since the coupling was already determined by the existing SRM,  $L_{\text{TSR2}}$  had to be chosen properly.
- 2 | The beam profile (interferometer mode) was defined by the existing setup of the dual-recycled Michelson interferometer (DRMI). In the context of already available mirrors with radii of curvature (ROC) of 1 m, 1.5 m and 2 m the length of the TSR resonator had to be chosen such that a matching to the predefined interferometer mode was ensured.
- 3 | The RF-modulation frequencies used in the DRMI experiment should be reused also for the extended setup. Since the coupling of error signals for the various longitudinal degrees of freedom (DOFs) depends on the resonator lengths as well, the existing RF-scheme gave a further boundary condition for the choice of  $L_{\text{TSR2}}$ .

Fig. 5.1 shows the frequency splitting (lower graph) achievable with the resonator length determined by the mirrors radius of curvature (upper graph). Here, the reflectivity of the TSRM affecting the gain (bandwidth) of the resonances was tentatively set to  $R_{\text{TSRM}} = 0.95$ . The resonator geometry with  $L_{\text{TSR2}} = 1.94$  m gives a frequency splitting of approximately 5 MHz which coincides with the lower bound of the possible spectrum. Accordingly, this solution was excluded a priori. The configuration with  $L_{\text{TSR2}} = 0.29$  m gives a resonance already close to the upper bound of the spectrum. Additionally,

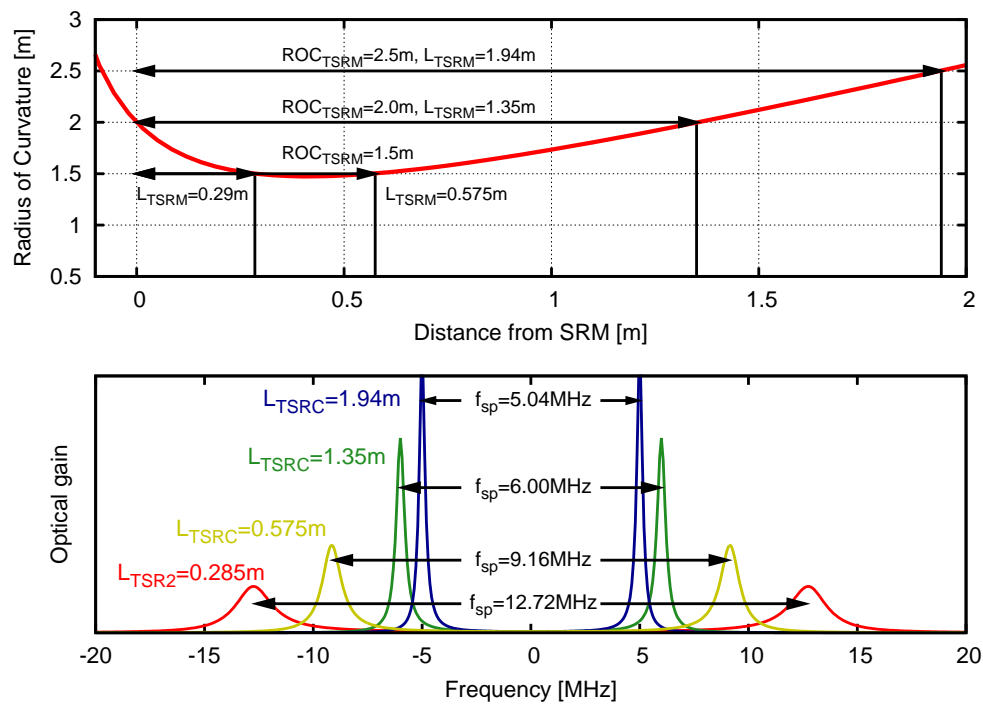


**Figure 5.1** — The upper graph shows the radius of curvature of the beam propagating from the SRM towards the TSRM. From this investigation possible positions of the TSRM with the respective ROC can be deduced. The lower graph shows the resonance doublet for these resonator geometries.

the bandwidth of the TSR resonators is comparatively large. Hence, this resonance doublet might not lead to distinct structures (i.e. sharp resonances) in the squeezing spectrum. The intention was to deduce the actual OP of the TSR interferometer from the measured squeezing spectrum. Accordingly, clear resonances in the spectrum would allow an easier interpretation/identification of the interferometers state. By increasing the reflectivity of the TSRM a narrower resonance can be achieved. However, in presence of internal interferometer losses a higher reflectivity of the TSRM would increase the losses of the incoupled squeezed light limiting the shot noise reduction around the resonance. Satisfying solutions (with respect to the frequency splitting) are obtained for  $L_{TSR2} = 0.575\text{ m}$  and  $L_{TSR2} = 1.35\text{ m}$ . Besides the bounded possibilities given by the available curved mirrors also a combination of a lens and a flat mirror was considered. Such a combination allows the realization of

almost any resonator length providing a great flexibility in the experimental setup. These possible configurations were reviewed with respect to a realizable locking scheme (Sec. 5.1.2).

### 5.1.2 Simulation of error signals

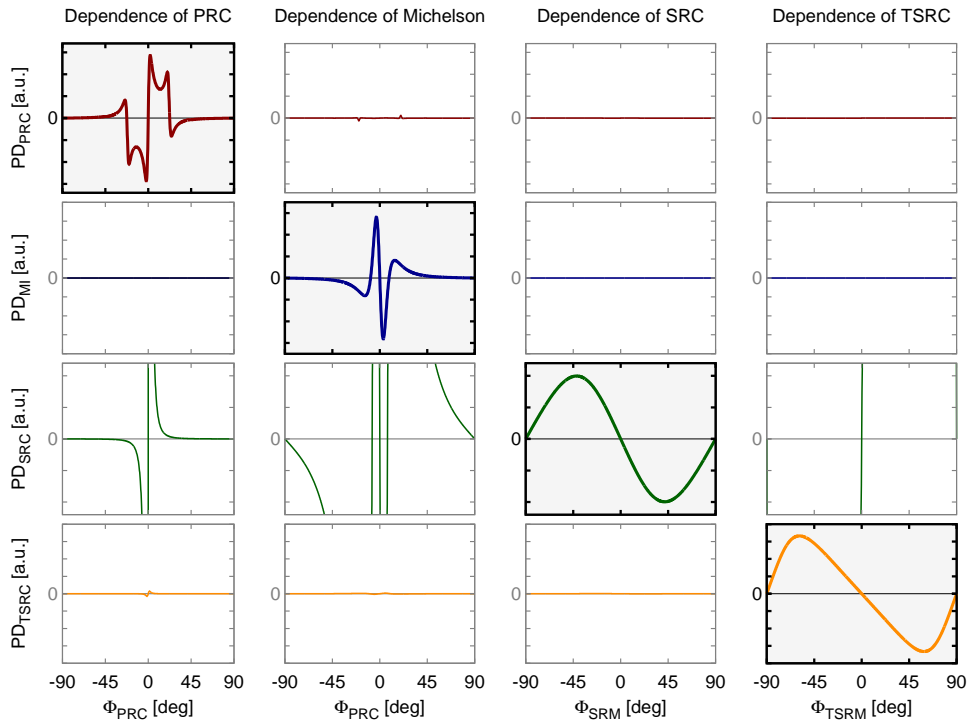
The control scheme of the DRMI was based on RF phase modulations at 15 MHz and a variable modulation frequency in the order of the FSR (123.6 MHz) of the SRC. Furthermore, two polarization modes were used to decouple the error signal for the dark port condition from all other DOFs (for further details refer to [41, 87]). Within these conditions, the control scheme for the TSR interferometer was investigated by means of FINESSE [88] simulations. The corresponding kat-files are documented in Appendix B. Appropriate error signals were found by the consideration of any possible detection port accessible in the experimental setup. Initially, the simulations were accomplished without taking the effect of higher order modes into account.

One main result of the control scheme investigations was that configurations with unequal lengths of the TSR resonators show a strong coupling in the error signals for the positions of the SRM and the TSRM to all other DOFs. The investigation revealed that in the case of equal resonator length ( $L_{\text{TSR1}} = L_{\text{TSR2}} = 1.21 \text{ m}$ ) at least the coupling of the SRM position and the dark port condition of the Michelson Interferometer (MI) to the TSRM error signal can be reduced. The normalized control matrix obtained for this configuration is given in Tab. 5.1. The corresponding error signals are shown in Fig. 5.2. It can be seen that the error signals for the position of the PRM (first row in Tab. 5.1/ Fig. 5.2) and the dark fringe condition of the MI (second row) are perfectly decoupled from the other DOFs. But in the error signal for the position of the TSRM there exists a strong dependence on the PRC state. However, since the signals for the PRC and the MI are perfectly decoupled a hierarchic stabilization was realizable. Aside from the strong coupling, the error signal for the TSRM provides a capture range of one FSR of the TSRC. Thus, at a point of the locking procedure where the PRC and the MI are already stabilized and the SRM is close to the target OP, one immediately obtains an appropriate error signal for the position of the TSRM.

The error signal for the position of the SRM shows the least decoupling. In fact, this signal is dominated by the other DOFs. However, the control matrix is at least linearly independent allowing again a hierarchic stabilization. It should be mentioned that the calculation of the control matrix implies that while error signals are investigated in dependence on a certain DOF all other

**Table 5.1** — Normalized control matrix. Unsatisfactory values meaning a strong coupling are highlighted in red.

Assigned DOF	PRC	MI	SRC	TSRC
PRC	<b>1</b>	$1.18 \times 10^{-6}$	$1.84 \times 10^{-11}$	$5.88 \times 10^{-9}$
MI	$-9.32 \times 10^{-4}$	<b>1</b>	0	0
SRC	<b>-579.19</b>	<b>-32.18</b>	<b>1</b>	<b>-55.70</b>
TSRC	<b>-3.07</b>	-0.12	$8.18 \times 10^{-3}$	<b>1</b>

**Figure 5.2** — The control matrix for the stabilization of the longitudinal DOFs of the TSR interferometer. Each row shows the error signals depending on the four DOFs (columns) obtained from one single photo diode. Note, that the y-axis scale is fixed for plots within on row. The diagonal of the control matrix represents the error signals of that photo diode assigned for the stabilization of the respective degree of freedom.

**Table 5.2** — Final set of the TSR interferometer parameters.

Interferometer arm lengths	1 m, Schnupp asymmetry of 7 mm
Distance of PRM/SRM to BS	0.21 m
Length of TSR resonator	1.21 m
FSRs (PRC/SRC/TSRC)	123.6 MHz
Finesse	$\mathcal{F}_{\text{PRC}} = \mathcal{F}_{\text{SRC}} \approx 60, \mathcal{F}_{\text{TSRC}} \approx 40$
Radius of curvature $M_{\text{end}}$	1.5 m
Radius of curvature PRM/SRM	1.5 m
Radius of curvature TSRM	0
Internal TSRC lens	$f = 0.5$ m
waist size in PRC/SRC	$499 \mu\text{m}$
waist size on TSRM	$181 \mu\text{m}$

**Table 5.3** — Parameters of the developed control scheme.

Assigned DOF	$f_{\text{demod}} / \phi_{\text{demod}}$	Detection port
PRC	15 MHz / $0^\circ$	Interferometer reflection
MI	123.6 MHz / $90^\circ$	PBS in front of SRM
SRC	123.6 MHz / $0^\circ$	Interferometer reflection
TSRC	123.6 MHz / $0^\circ$	Interferometer transmission

DOFs are at their target OP. Hence, in the experiment the interferometer state has to be prepared accordingly to obtain the required error signals. Furthermore, the control scheme does not provide the opportunity to define the OP of the coupled TSR resonators (e.g. by a variable modulation frequency as it was accomplished in [89]). Moreover, it could be shown that error signals (similar to those shown in Fig. 5.2) are obtained also for OPs close to the optimum OP. Therefore, the intention was to determine the actual OP on the basis of the measured squeezing spectrum serving as a appropriate monitor.

### 5.1.3 The final choice of parameters

According to the above considerations the decision was made to use an interferometer configuration with equal length of the TSR resonators. Furthermore, the reflectivity was chosen to  $R_{\text{TSRM}} = 0.95$  to obtain distinct structures in the squeezing spectrum allowing the identification of the actual OP. The final set of design parameters is given in Tab. 5.2 and Tab 5.3.

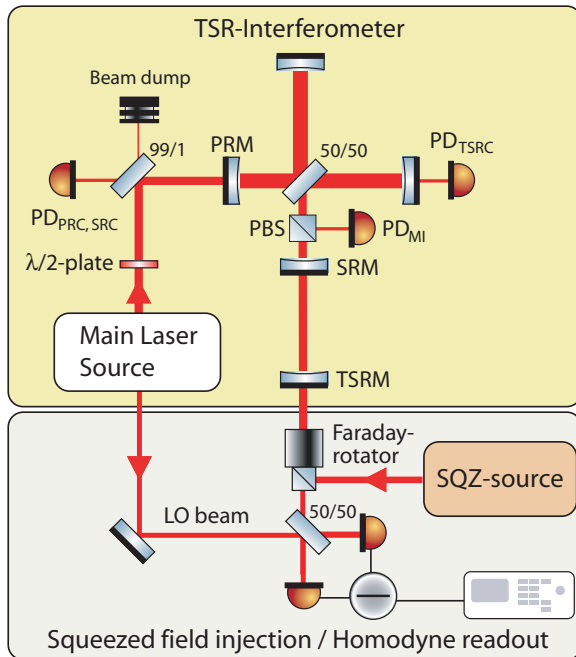


**Figure 5.3** — Simplified schematic of the TSR experimental setup. PD: photo diode; PBS: polarizing beam splitter; PRM, SRM, TSRM: Power-, Signal-, and Twin-Signal-Recycling mirror. LO: local oscillator. SQZ: Squeezed light.

## 5.2 The experimental setup

To simplify matters a reduced schematic is shown in Fig. 5.3. The main laser source was a Nd:YAG non planar ring oscillator with a cw single-mode output power of up to 2 W at 1064 nm. The laser beam was transmitted through a ring resonator providing spatial and high-frequency amplitude and phase-noise filtering. A major part of the laser power was frequency doubled in a non-linear resonator; details can be found in [65, 87]. About 1.5 mW of the filtered beam at the fundamental frequency served as local oscillator beam for homodyne detection.

Approximately 35 mW s-polarized light was injected into the TSR Michelson interferometer through the PRM. The PRM had a power reflectance of 90% and, together with the interferometers end mirrors having a reflectance of 99.92%, formed the carrier resonating PRC. The length of the PRC was approximately 1.21 m, corresponding to a free spectral range of 123.6 MHz. Its finesse was measured to 60, leading to a bandwidth of about 2 MHz when the interferometer was locked to a dark fringe at the signal output port. The PRC length, the MI dark port, and the TSR cavity lengths were stabilized by RF-modulation/demodulation schemes (refer to Sec. 5.1.2) and by piezo actua-

tion of mirror positions. For this purpose the s-polarized interferometer input beam was phase modulated at 15 MHz as well as 125.6 MHz and accompanied by a 10 mW p-polarized beam of the same frequency carrying the same two phase modulations. Note, that the modulation frequency of 125.6 MHz differed from that used for the FINESSE simulation presented in Sec. 5.1.2. Since the actual SRC length was realized with approximately 1.19 m giving a FSR of 125.6 MHz, the modulation frequency was adapted accordingly. The error signal for the PRC length control was gained from the 15 MHz modulation on the s-polarized light reflected from the PR cavity ( $PD_{\text{PRC}}$  in Fig. 5.3). The MI dark fringe error signal was derived from the 125.6 MHz modulation on the p-polarization ( $PD_{\text{MI}}$ ) detected behind a PBS placed between the interferometer beam splitter and the SRM to decouple the polarization modes. The length control of the two coupled TSR cavities built by the end mirrors, the SRM and the TSRM utilized the sidebands at 125.6 MHz in the s polarization detected in reflection of the PRM ( $PD_{\text{SRC}}$ ) and in transmission of one end mirror ( $PD_{\text{TSRC}}$ ), respectively. Since the sidebands at 125.6 MHz were within the bandwidth of the PRC and were thus enhanced, the interferometer arm length difference of 7 mm was still sufficient to obtain proper error signals for the positions of the SRM and the TSRM. The optical length of the cavity built by the SRM and the end mirrors was approximately 1.19 m, the length of the resonator formed by the SRM, and the TSRM was realized with about 1.26 m. With the SRM power reflectance of 90% this leads to an expected frequency splitting of approximately 6.1 MHz.

Another 15 mW of the filtered main laser beam was used for length control of the squeezed light source cavity (not shown in Fig. 4.1). The squeezed light source used type I optical parametric amplification (OPA) and was realized as a single-ended standing-wave nonlinear resonator formed by two mirrors and a PPKTP crystal (see Sec. 5.5.1). The squeezed light source was pumped by 450 mW of 532 nm radiation and provided a dim amplitude squeezed field of approximately 45  $\mu\text{W}$  at 1064 nm. The squeezed field passed a combination of a polarizing beam splitter, a  $\lambda/2$ -plate, and a Faraday rotator and was matched to the interferometer mode with a visibility greater than 99%. Since the TSR interferometer was locked at its dark port, the squeezed field was reflected by the interferometer and, owing to the polarizing optics mentioned before, was found in the interferometer signal output spatial mode [5]. This combined mode was matched to the local oscillator beam of the homodyne detector with a measured visibility of about 95%.

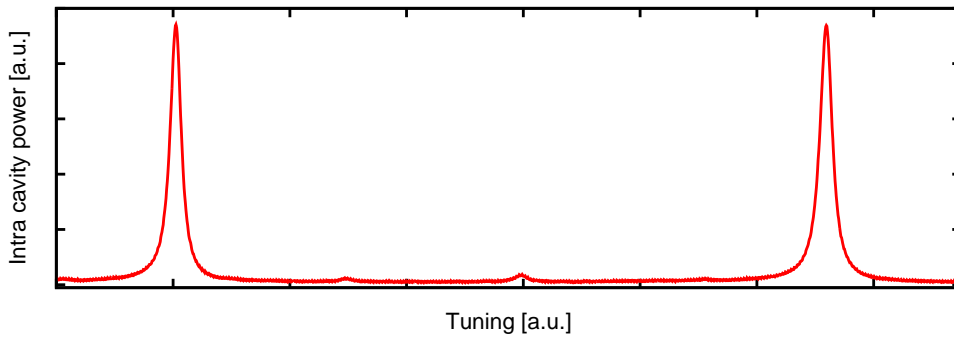


Figure 5.4 — Measured mode spectrum of the PRC.

### 5.3 Alignment procedure

The locking scheme of the experiment included only the stabilization of longitudinal degrees of freedom. Therefore, the alignment of the angular degrees of freedom were accomplished manually. In this Section the single steps of the alignment procedure and the achieved mode matchings are demonstrated. Note, that the procedure demonstrated here differs from that applied for the DRMI (see [87] for details) with respect to the alignment of the TSR resonators and the squeezed field injection.

#### 5.3.1 Interferometer alignment

At first the fringe visibility of the MI (without PR) was aligned. The light fields were detected in reflexion of the interferometer ( $PD_{\text{PRC}}$ ) and in the dark port ( $PD_{\text{MI}}$ ) giving the visibility of the s-polarized beam and the p-polarized beam, respectively. In both cases, a measured visibility of better than 99.9 % was achieved. In a next step, the PRC was aligned whereat solely the position and the angular DOFs of the PRM were modified to keep the pre-aligned visibility of the MI. Fig. 5.4 shows a measured mode spectrum of the scanned PRC. From this measurement a mode matching efficiency of about 96 % can be deduced assuming that the input beam was a pure  $TEM_{00}$  mode. Actually, the input beam showed an elliptical beam profile caused by the EOM used for the phase modulation at 125.6 MHz. Accordingly, the beam consisted of higher order modes for which reason the mode matching efficiency of the  $TEM_{00}$  mode to the PRC mode was probably better than 96 %.

For the initial alignment of the SRC the PRM was tilted to suppress the

buildup in the PRC. Additionally, to couple a small fraction of the light circulating in the interferometer into the SRC the MI was locked slightly offset from the dark fringe. In this stage, the SRC could be pre-aligned without the need for a stabilization of the PRC. Afterwards the PRM was aligned again and the SRC was matched to the mode defined by the locked PRC. The mode spectra measured at these two stages of the SRC alignment are shown in Fig. 5.5. The mode matching efficiency is almost 96 % in both cases. However, in the case with locked PRC just one dominating HOM (that was identified with the  $TEM_{01}$  mode) appears in the spectrum. There are three reasons explaining the difference of the spectra. First, the tilt of the PRM applied in the first step of the SRC alignment causes a displacement of the beam. Second, the mode matching of the input beam to the PRC mode was not 100 %. Thus, if the PRC is locked, the circulating  $TEM_{00}$  mode differs from that of the input beam. Third, when locked to the  $TEM_{00}$  mode the PRC filters out the HOMs present on the input beam. Note, that this measurement confirm the assumption, that the actual mode matching efficiency to the PRC was better than 96 %. The fact that the HOMs (except of the  $TEM_{01}$  mode) spectrum of the SRC vanishes when the PRC is locked to the  $TEM_{00}$  mode could be traced back to the mode cleaning effect of the PRC. Consistently, assuming that the two dominating HOMs present in the spectrum of the scanned PRC (Fig.5.4) came already with the input beam leads to an actual mode matching efficiency of about 99.5 %.

In the final step of the SRC alignment procedure the MI was locked on its dark fringe. From the mode spectrum obtained in this case (Fig. 5.6) it can be deduced that the presence of the  $TEM_{01}$  mode in the spectrum shown in the right part of Fig. 5.5 does not originate from a misalignment of the SRC but from the imperfect fringe visibility of the MI. The left graph of Fig. 5.6 compares the measurements with (black curve) and without (red curve) offset from the dark fringe. It can be seen, that the amount of the  $TEM_{01}$  mode is almost the same in both cases. The right part of Fig. 5.6 demonstrates, that an online adjustment of the MI visibility led to a reduction of the  $TEM_{01}$  mode by a factor of about 25. Accordingly, from the measurement shown in Fig. 5.5 the actual mode matching efficiency of the SRC to the PRC mode can be calculated to 99.5 %.

For the subsequent alignment of the TSRC the PRM was tilted again and one arm of the interferometer was blocked. In this case, the SRM together with one end mirror formed a low finesse cavity ( $\mathcal{F}_{\text{SRC}}^{\text{BS}} \approx 4$ ) since the lossy beam splitter is included. Together with the TSRM this cavity built a linear three-mirror cavity. Accordingly, the coupling to the TSRC resonator built

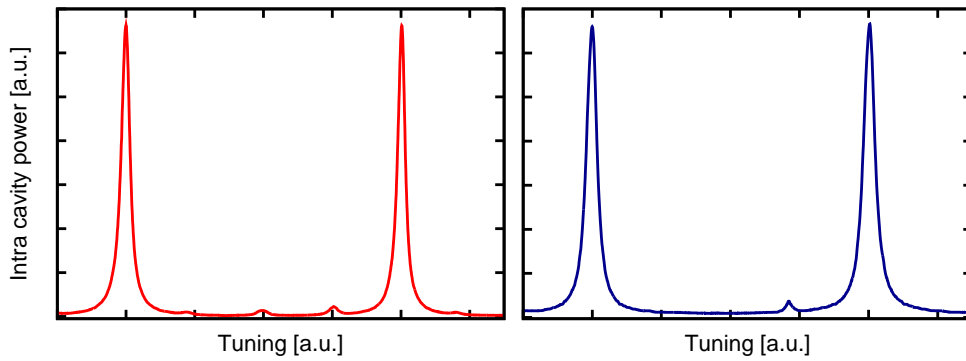


**Figure 5.5** — Pre-alignment of the SRC. Left: Mode spectra of the scanned SRC without aligned PRM. Right: Modes spectra with aligned and stabilized PRC. In both cases the MI was locked slightly offset from the dark fringe. The residual HOM in the spectrum shown on the right was identified with the  $TEM_{01}$  mode originating from the imperfect fringe visibility of the MI. In a further stage of the alignment procedure the amount of the  $TEM_{01}$  could be reduced by a factor of about 25 (refer to Fig. 5.6).

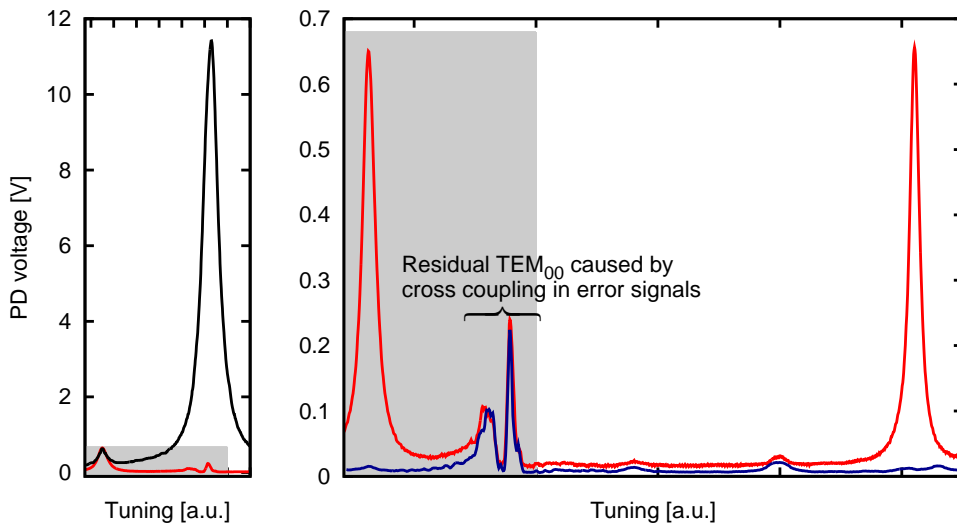


**Figure 5.6** — Mode spectrum of the SRC at the final stage of alignment. Left: Comparison of the measurements with (black curve) and without (red curve) offset from the dark fringe. Note that the amount of the  $TEM_{01}$  mode is the same in both cases. The shaded area corresponds to that shown on the right. Right: Spectrum before (red curve) and after (blue curve) the adjustment of the MI fringe visibility. The  $TEM_{01}$  mode was reduced by a factor of approximately 25.

by the SRM and the TSRM was strongly dependent on the tuning of the SRC which complicated the alignment of the TSRC. This procedure was however obligatory to ensure that the adjustment of the lens position inside the TSRC resonator occurred with respect to the mapping of the interferometer mode on the flat TSRM. The mode spectra of the TSRC for three arbitrary tunings of the SRC are shown in the left graph of Fig. 5.7. It can be seen that the absolute peak height of the  $TEM_{00}$  mode as well as the relative amount of the dominating HOM depend on the actual tuning of the SRC. For that reason a calculation of the mode matching efficiency could not be accomplished. However, the alignment and the mode matching of the TSRC was checked using the transmitted control beam of the locked OPA as described in the following Section.

### 5.3.2 Coupling of the squeezed light source to the interferometer

To match the squeezed light mode to the TSR interferometer mode, the OPA was stabilized on the  $TEM_{00}$  mode utilizing the control beam. Here, the pump field at the second harmonic was blocked so that the fundamental field (control beam) was not parametrically amplified or deamplified. So the transmitted control beam served as reference for the  $TEM_{00}$  mode of the later generated squeezed light and was matched to the single TSRC. Unfortunately, it could be observed that in some cases an apparently satisfying mode matching efficiency of the control beam to the TSRC did not necessarily imply appropriate mode matchings to the SRM and the MI. For that reason, the alignment of the OPA was checked using the beam transmitted through the TSRC. For this purpose, the TSRC was stabilized by means of a DC offset lock. The transmitted  $TEM_{00}$  mode was coupled to the (scanned) OPA and the mode spectra was analyzed. Indeed, mode spectra similar to those obtained for the control beam when coupled to the OPA could be observed confirming the proper alignment. This procedure led to an achieved mode matching efficiency of better than 99.5 % calculated from the spectrum measured for the control beam coupled to the TSRC (right graph in Fig. 5.7).

### 5.3.3 Alignment of the homodyne detector

In the final step the mode reflected at the signal port of the TSR interferometer was matched to the local oscillator beam. For simplicity, the TSR interferometer was dumped such that only the part directly reflected at the TSRM served

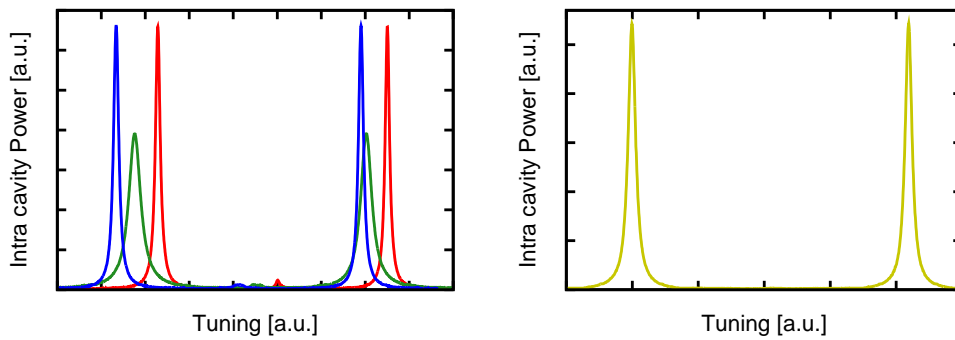


**Figure 5.7** — Mode spectra of the TSRC. Left: Spectra for three arbitrarily tunings of the SRC. Right: Spectra obtained for the control beam coupled to the TSRC from the signal port side.

as reference for the interferometer mode. A fringe visibility of about 95 % could be achieved whereat the imperfect beam profile of the local oscillator beam could be identified as the limiting factor. Since some of the lenses in the LO beam path possibly causing the observed distortion were also used for the coupling of the main interferometer beam to the PRC the realized visibility of 95 % represents (in view of the complexity of the experimental setup) a satisfying result. In addition, it could be estimated that despite the imperfect fringe visibility a sufficient shot noise reduction can be achieved allowing a demonstration of the squeezing enhanced TSR interferometer.

#### 5.4 Hierarchic stabilization of the TSR interferometer

In this Section the hierarchic stabilization of the TSR interferometer (performed in accordance to the control scheme developed in Sec. 5.1.2) is presented by means of an exemplary measurement. Here, the states of the four DOFs were monitored during the stabilization process by detecting the light powers in that four ports used for error signal generation. As well, the control signals fed back onto the actuators for the PRC (PZT-PRM), the MI (MI-PZT), the SRC (SRM-PZT) and the TSRC (TSRM-PZT) were monitored. From these eight traces (which were recorded with two LeCroy WJ314 oscilloscopes) the actual state of the interferometer can be deduced. Figures 5.8 and 5.9 show the traces corresponding to the measured light powers and the feedback signals, respectively. In the first stage of the stabilization procedure the PRC was locked (red traces). Afterwards, the MI was stabilized on its dark fringe

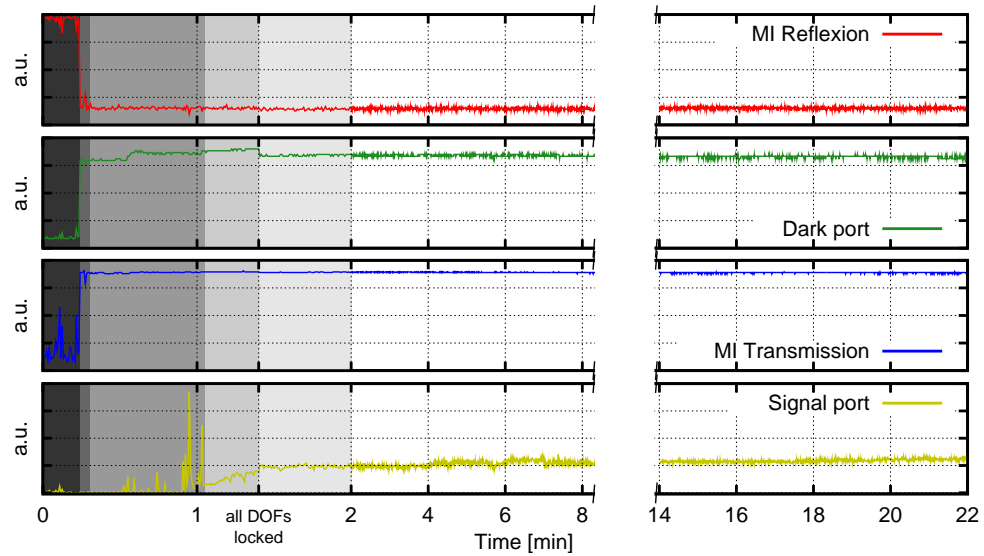


**Figure 5.8** — Hierarchic stabilization of the TSR interferometer. The demonstration of the long time stability shown here bases on two subsequent measurements performed with a time-lag of 14 minutes. The shown traces (DC powers) were detected in reflection of the MI (red trace), in the dark port (green trace), in transmission of one end mirror (blue trace) and in the signal detection port (yellow trace). The shaded areas on the left highlight the four stages of the hierarchic stabilization. From dark to bright: un-stabilized, PRC locked, PRC+MI locked, PRC+MI+TSRC locked. The stabilization of all DOFs (PRC+MI+TSRC+SRC) was realized at  $t = 1.4$  min.

(green traces). Please note, that the MI state was monitored by detecting the p-polarized light transmitted from the PBS placed in front of the SRM. Since the dark fringe condition for the p- and s-polarized beams were *not degenerated* due to different penetration depth in the steering mirror placed in one MI arm, the p-polarized beam has a non-zero transmission into the dark port although the dark fringe condition is fulfilled for the s polarized beam. In the third stage it was possible to scan the TSRC length identifiable with the triangular driving voltage applied on PZT-TSRM (yellow trace in Fig. 5.9). Simultaneously, the SRM was manually (i.e. by adjusting the offset of the corresponding feed back voltage) moved towards its target position to achieve a proper error signal for the TSRC. In the last stage – after the TSRC was locked – the SRC was stabilized on its target OP. Note the correlated jump in the feed back signals of PZT-SRC (blue trace in Fig. 5.9) and PZT-TSRC (yellow trace). Since a length change of the SRC caused by a movement of the SRM also changed the length

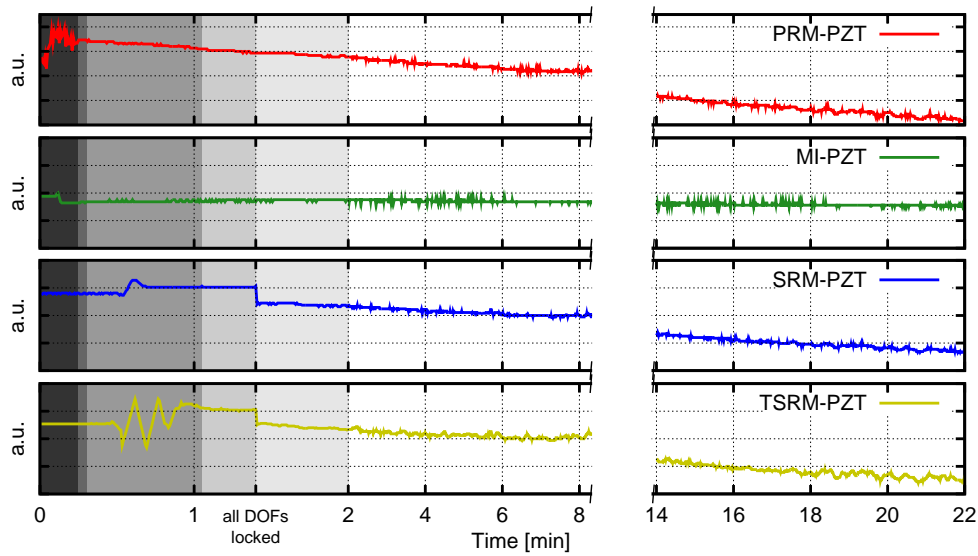


Figure 5.9 — Feed back signals corresponding to Fig. 5.8.

of the TSRC, the TSRM must follow the SRM to maintain the targeted tuning of the TSRC.

The measurement presented here demonstrates that the developed control scheme — despite strong couplings of the DOFs — allowed a longtime stable operation of the TSR interferometer. The duty cycles achieved were sufficient to perform the subsequent injection of squeezed light into the TSR interferometer and the measurement of its quantum noise spectra. So it was possible to modify the actual OP of the TSR under consideration of the measured spectrum whereby the targeted optimum OP could be reached (refer to 5.5).

## 5.5 Broadband squeezing of quantum noise

### 5.5.1 Characterization of the injected squeezed field

The squeezed light source was developed as described in [90]. A PPKTP crystal was used as non-linear medium and placed in a two-mirror cavity with a finesse of about 150. The control scheme for the length stabilization of the squeezed light source and the relative phase lag between the fundamental and the harmonic pump field (obtained from SHG in a further non-linear cavity) was similar to that used in [65]. For a detailed description of the

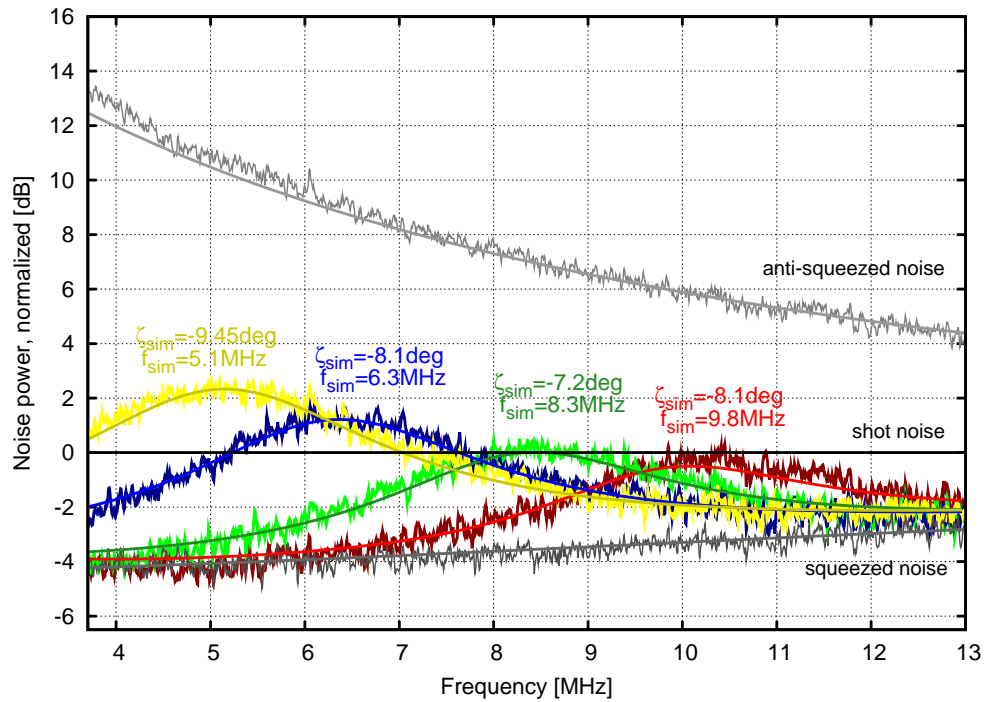


**Figure 5.10** — Comparison of measured and simulated (straight lines) squeezing spectra for several detunings of the TSRC. The upper and lower boundaries correspond to the anti-squeezing and the squeezing, respectively. Here the TSRC was on anti-resonance for the carrier. The homodyne detection angle in the experiment were chosen to give maximum shot noise suppression below the TSRC resonance leading to a distinct structure of the spectrum. Note, that these detection angles does not correspond to the detection of the amplitude quadrature. In the simulation values in a range from  $-7.2^\circ$  to  $-9.45^\circ$  for the detection quadrature were used. The detuning was determined by means of the resonance structure in the spectrum.

squeezed light source please refer to [90]. The discussion in this Section is restricted to the characterization of the squeezed field and its coupling to the TSR interferometer on the basis of an exemplary measurement.

At first, the squeezed field reflected at the TSRC (the SRC and the MI were blocked) was characterized by means of a measurement of the squeezed and anti-squeezed quadrature. Here, the TSRC was held on anti resonance allowing an investigation of the initially injected squeezed field. As well, the homodyne detection and the corresponding control loops could be proved

without the influence of the complete TSR interferometer. In a next step, the coupling of the squeezed light to the TSRC was analyzed. Here the TSRC was locked on several tunings within a range from 5 MHz to 15 MHz. The error signal for the applied DC offset lock was gained from the detection of the dim (deamplified) control beam in transmission of the TSRC. Figure 5.10 shows measured and simulated spectra. An overall detection efficiency of almost 70 % can be deduced. The best agreement of measurement and simulation was obtained by setting  $R_{\text{TSRM}} = 0.94$  and  $R_{\text{SRM}} = 0.905$ . The internal loss of the TSRC was assumed with 0.2 %. Note, that the TSRC builds an under coupled cavity for the squeezed field injected in the signal port (through TSRM). Accordingly, the quadrature rotation of the detuned TSRC is less than  $90^\circ$ . For that reason the noise level at the resonance of the TSRC does not reach the level of the anti-squeezed quadrature. Furthermore, if the internal loss in the simulation is assumed to be greater than 0.2 %, the quadrature rotation decreases further and no adequate fit to the measurement could be achieved.

### 5.5.2 Quantum noise spectra of the TSR interferometer

Figure 5.11 shows quantum noise spectra of the TSR interferometer for different suboptimal tunings of the TSR cavities. Curves (a)–(d) provide upper and lower bound references and represent the noise spectra with strong under-coupling to the TSR cavities. For these measurements these coupled cavities were on antiresonance (similar to the measurement described in Sec. 5.5.1). For all the other curves in Fig. 5.11 the TSR cavities' lengths were close to but not at the optimum OP and therefore produced dispersion and a frequency-dependent rotation of the squeezing ellipse. The noise spectra for the optimum OP of the TSR cavities are shown in Fig. 5.12, providing the lowest quantum noise floor for a strong coupling to the TSR cavities. The optimum OP is realized if the detunings of the two TSR cavities are such that the resonances of upper and lower sidebands are arranged symmetrically around the carrier frequency (i.e.  $\Phi_{\text{TSRC1}} = \Phi_{\text{TSRC2}} = 0$ ). Only in this case no dispersion is produced by the TSR cavities, the squeezing ellipse is not rotated, and a broadband shot noise reduction from frequency-independent squeezed light injection is achieved, as proposed in [91]. Starting with the interferometer stabilized at suboptimal tunings, the optimum OP was reached by smoothly adjusting the offsets of the error signals for the SRM and the TSRM. As illustrated in Fig. 5.12 the resonance peaks were brought together until the rotation into the anti-squeezed quadrature vanished. The remaining bump at approximately 6.1 MHz arises not from quadrature rotation but from losses

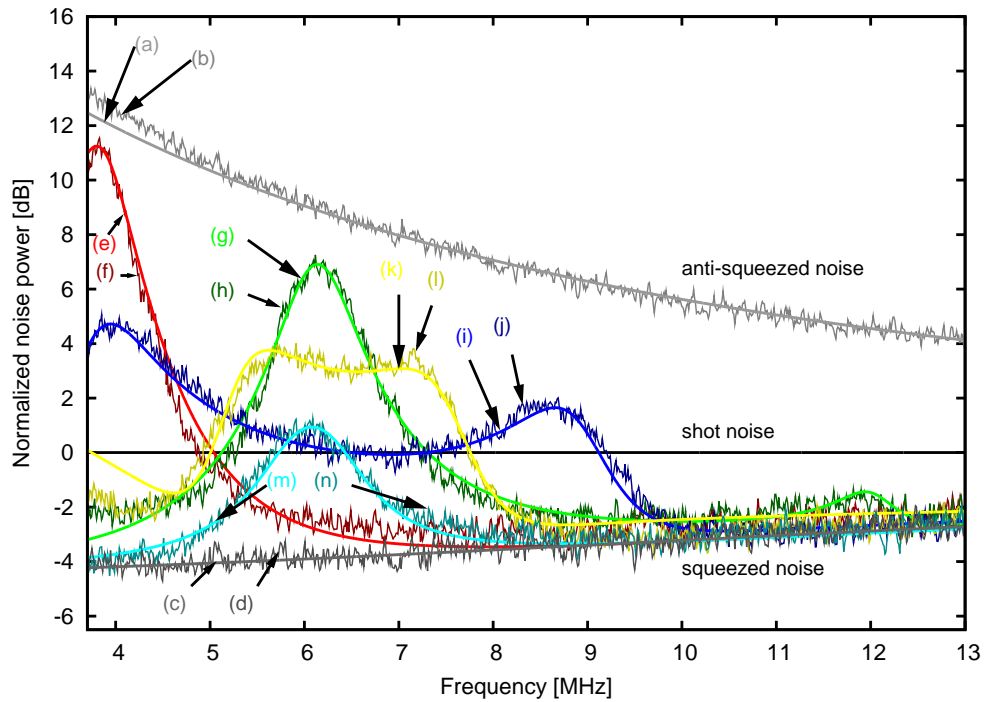


**Figure 5.11** — Comparison of measured and simulated quantum noise spectra of the squeezing-enhanced TSR interferometer at suboptimal OPs: (a), (b) Simulated and measured anti-squeezing spectra as well as (c), (d) simulated and measured squeezing spectra when the TSR interferometer was tuned to antiresonance. (e)(n) Simulated and measured spectra when the TSR cavities were locked close to but not at the optimum OP.

inside the interferometer. Notice that the squeezing is just affected by interferometer losses at sideband frequencies fulfilling the resonance condition of the coupled TSR resonators and thus entering the interferometer. Hence from this measurement the frequency splitting can be deduced to approximately 6.1 MHz, which agrees with the TSR parameters.

The straight lines in Figs. 5.11 and 5.12 represent the numerical simulations, which are based on the mirror reflectivities, macroscopic cavity lengths, cavity detunings, optical loss, and the homodyne angle. The cavity detunings for each measurement were derived from the resonance frequencies in the noise spectra. The values for the homodyne angle and for the optical loss due to an interferometer dark port offset were then fitted and were found to match the results of independent measurements within their uncertainties. For the

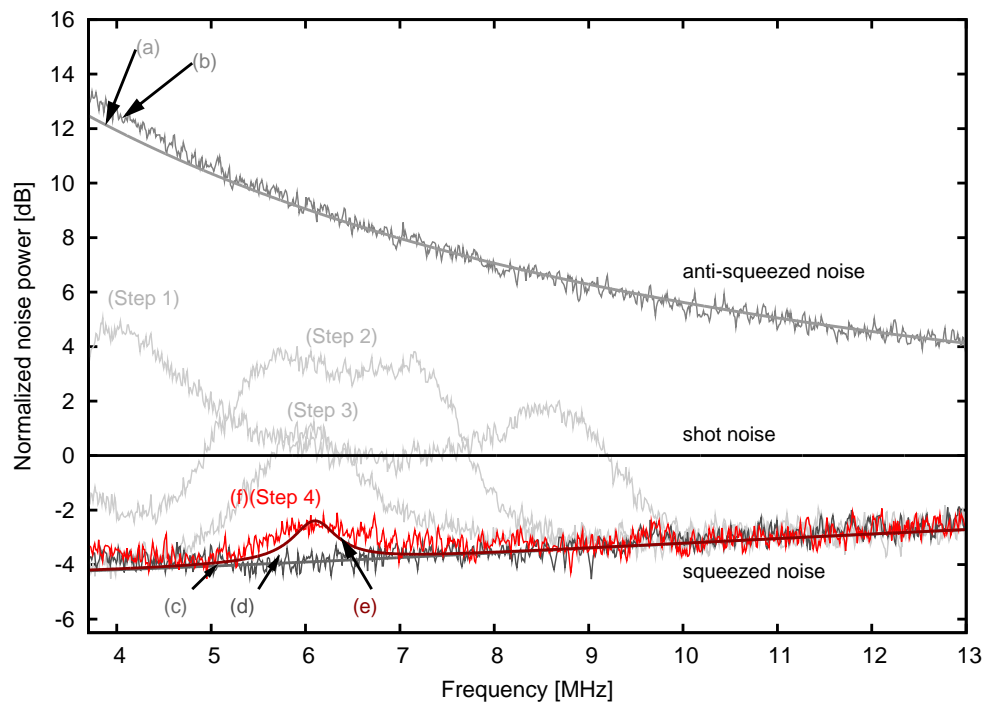


**Figure 5.12** — Measured (f) and simulated (e) broadband squeezing of quantum noise in the TSR interferometer achieved at the optimum OP. For traces (a)(d) see caption of Fig. 5.11

experimental data shown in Fig. 5.11 the uncertainty for the actual homodyne angles was untypically high, for two reasons. First, the quadrature angle could not be determined by simply minimizing the squeezed noise variance in Fig. 5.11 because of the quadrature rotation and frequency-dependent quantum noise. Second, when varying the TSR cavity detunings the mode degeneracy and therefore the power in residual transversal higher-order modes caused an offset change of the homodyne quadrature error signal. For this reason the homodyne angle also varied from trace to trace in Fig. 5.11. For the simulations of curves (i) and (k) detection angles of  $9^\circ$  and  $12.6^\circ$ , respectively, were used and detection angles between  $0^\circ$  and  $1.4^\circ$  for all other curves. The optical loss of the interferometer was also dependent on the cavity detunings. First, the error signals for the length control of the two TSR cavities and the PR cavity coupled with the error signal of the dark port control. Notice, that an offset from the perfect dark port condition increases

the loss on the squeezed states. Second, the changes in the degeneracy with higher-order transversal modes changed the strength of the according loss channels. The simulation in Fig. 5.11 is based on values for the loss inside the TSR interferometer in a range from 0.4% to 3.9%.

In contrast to Fig. 5.11, the simulation for the optimum OP shown in Fig. 5.12 was not based on any fitting. Here, the homodyne quadrature angle could easily be optimized and precisely locked to  $0^\circ$  by minimizing the noise floor. Spatial mode degeneracy was not observed, and the dark port condition could be realized by minimizing the loss peak. The remaining loss corresponded to the minimum loss of 0.4% in the setup, which was given by the transmittivities of the end mirrors and non-perfect anti-reflection coatings of the cavity mirrors and beam splitters.

## 5.6 Summary

By means of detailed parameter studies and numerical simulations the necessary extensions for an upgrade of a table-top Dual-Recycled Michelson interferometer to a TSR interferometer were determined and implemented. It was experimentally demonstrated that an interferometer with TSR and properly chosen detunings (optimum operating point) of its two coupled cavities show a broadband quantum noise reduction from the injection of a non-classical field with a white squeezing spectrum (Fig. 5.12). Although the experimental realization targeted on the verification of the broadband shot noise reduction as proposed in [91], the spectra obtained at the other OPs (Fig. 5.11) demonstrate the possible shaping of the TSR transfer function as presented in Sec. 4.4.1 and Sec. 4.4.2.

# Analysis of a Kerr non-linear resonator

## 6.1 Introduction

Since a Kerr non-linear resonator (KNLR) yields an improved response to phase modulation signals, it came into consideration for gravitational-wave detectors. Here, its so-called *critical state* is favorable as it is characterized by an infinite slope for a particular detuning (see Fig. 6.1). However, compared

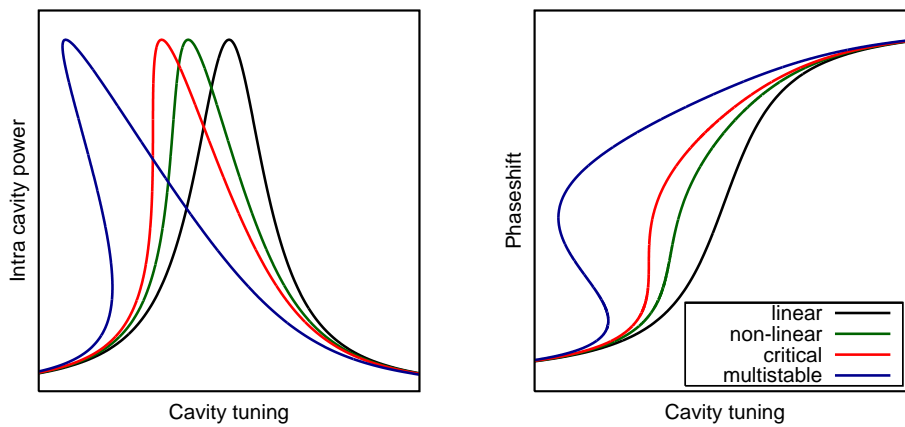


**Figure 6.1** — Intra cavity power (left) and phase shift (right) of a KNLR for different strength of the Kerr effect. The critical state (red curves) is characterized by an infinite slope for a particular detuning.

to Michelson interferometers with linear arm cavities, the increased signal to noise ratio is not based on an enhanced transfer function for signal sidebands but on the *self-squeezing* of the vacuum noise. It was shown by Pace *et al.* [27] that the radiation pressure noise in a Michelson interferometer with tuned KNLRs can be canceled at certain sideband frequencies. A detuned topology similar to the RSE configuration was proposed by Rehbein *et al.* [28]. Here an additional cavity is placed in the interferometers detection port forming together with the non-linear arm resonator a four-mirror cavity. The featured resonance doublet allows to shift the Kerr noise reduction to arbitrary frequencies. This topology was also considered as a new scheme for a continuous wave (cw) squeezed light source because it reduces the problem of driving noise in these sources. The high finesse resonators can be operated on resonance providing the required power build-up with moderate input powers, and the squeezing can be extracted at frequencies where the classical laser noise is reduced.

The investigations presented by Rehbein *et al.* [28] and earlier works [92, 30, 29] are focused on the squeezing of quantum noise. However, it can be deduced that Kerr non-linear resonators allows an passive pure optical reduction of laser power noise within their linewidth. Thus, together with active power noise reduction schemes [25, 26] the Kerr effect can be employed to achieve the required stabilization of high-power laser required for future gravitational-wave detectors.

Within this context, a KNLR was investigated experimentally in the framework of this thesis. In order to exploit the optical Kerr effect for laser noise reduction or squeezed light generation, a high-quality third-order non-linear optical material is required. Typical third-order non-linearities of optical media are, unfortunately, rather small. In the pulsed laser regime high laser intensities can be used to compensate for this. In the continuous-wave laser regime, interacting  $\chi^{(2)}$  non-linearities can be employed to obtain an effective Kerr effect. It was indeed shown that by the means of second harmonic generation and a subsequent frequency down-conversion, an intensity dependence of the refractive index can be realized. Such a scheme represents an effective third-order non-linear Kerr medium but utilizes the second-order non-linearity of, for example, lithium niobate or KTP [42]. The lower order of non-linearity results in a comparatively strong effective third-order non-linearity.

## 6.2 Cascaded Kerr effect in second order non-linear materials

Interacting non-linearities have been discussed analytically and numerically since the first days of non-linear optics [93, 94, 95, 96]. Here the results are summarized focusing on the physical understanding of the mechanism that leads to a cascaded Kerr non-linearity and hence to a noise suppression. For this purpose, a loss-less second-order non-linear material and the second harmonic generation in such a material of length  $L$ , driven by a field of fundamental frequency  $\omega_0$  is considered. In case of optimum phase matching between the fundamental and the second harmonic mode of the EM field, the second-harmonic light generated along the length  $L$  interferes constructively over the whole interaction length. Now let's assume the phase matching is artificially worsened until the first conversion minimum is reached. The new situation can be conceptually understood by splitting the crystal in two parts of lengths  $L/2$ . In both parts, when considered independently, SHG still occurs, although this process is no longer optimized any more. However, the contributions of both parts now exhibit a differential phase shift. This phase shift leads to a complete destructive interference after the full crystal length  $L$ . Consequently, no light at frequency  $2\omega_0$  exits the crystal. The fundamental field exiting the crystal can be thought of as a composition of two parts. One part represents the field that previously has experienced up-conversion to the second-harmonic frequency. The second part represents the field that never experienced up-conversion. The phases of the two parts are different because the phase matching is not optimized as said before, and the refractive indices at the two wavelengths are therefore different. Since up-conversion is a non-linear ( $\chi^{(2)}$ ) process, the two parts change their weights if the input intensity changes. Effectively, the transmitted fundamental light experiences an intensity-dependent phase shift formally identical to the optical Kerr effect observed in a  $\chi^{(3)}$  medium.

A simple mathematical description is obtained by solving the non-linear wave equation for the involved modes of the optical field assuming a weak conversion of the fundamental field (*fixed intensity approximation*) [97]. In this case one obtains the expression

$$\phi(z) = \phi_{\text{prop}}(z) + \frac{\Delta kz}{8 + \frac{(\Delta k)^2}{\chi' I_{\text{fund}}}} \left[ 1 - \text{sinc} \left( z \cdot \sqrt{\left( \frac{\Delta k}{2} \right)^2 + 2\chi' I_{\text{fund}}} \right) \right] \quad (6.1)$$

describing the phase dependence of the fundamental field on the coordinate of propagation,  $z$ . Here  $\Delta k$  is the wave vector mismatch between the fundamental and the second harmonic wave,  $\phi_{\text{prop}}$  is the intensity-independent phase shift due to propagation while  $\chi'$  contains material-specific information (as the effective non-linearity and the propagation speed inside the crystal) and further depends on both frequencies involved. In the case of minimal conversion efficiency (at the first phase matching minimum with  $\Delta k \approx 2\pi/z$ ) this expression simplifies to

$$\phi(z) \approx \phi_{\text{prop}}(z) \pm \frac{\chi'}{2\pi} z^2 I_{\text{fund}} \quad (6.2)$$

whereas in the case  $\Delta k = 0$  the intensity dependence vanishes. Thus, the resonator can be operated as pure frequency doubler or pure Kerr non-linear resonator by simply adjusting the corresponding phase matching condition (i.e. by using the temperature dependence of the refractive index in birefringent crystals). Following this approach, the investigated KNLR was realized as two-mirror cavity embedding a second-order MgO:LiNbO<sub>3</sub> crystal.

## 6.3 The experimental methods

### 6.3.1 Preparation of the laser source

This Section is aimed at the description of the length (frequency) stabilization of the three-mirror ring resonator (referred to as mode cleaner (MC) in the following). The MC was used for spatial higher order modes and high frequency amplitude and phase noise filtering of the laser source. Additionally, this MC allowed the decoupling of the filtered laser carrier (serving as pump beam for the Kerr non-linear resonator) and the Kerr affected noise sidebands (see Sec. 6.3.3 for details).

As laser source a commercially available (Mephisto 2000 NE from Inno-Light [98]) continuous wave Nd:YAG Laser system at 1064 nm with a maximal output power of 2 Watts was used. This source provides a low-noise continuous-wave single-mode single-frequency laser beam with a very clean spatial beam profile with typically less than 2.5% of the power in higher-order modes. The relative power noise is below  $1 \times 10^{-6} \text{Hz}^{-1/2}$  for Fourier frequencies  $f = \Omega/2\pi$  above 30 Hz and shows an approximately 40 dB high peak at the frequency corresponding to the laser relaxation oscillation at frequencies around 1 MHz. Above these frequencies the power noise falls with  $1/f^2$  and

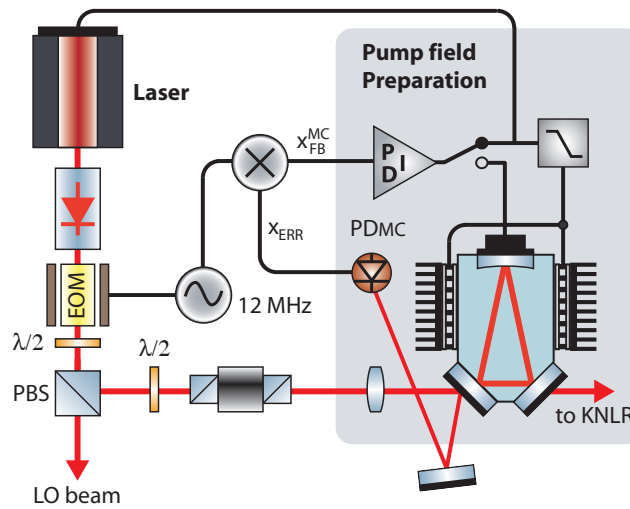
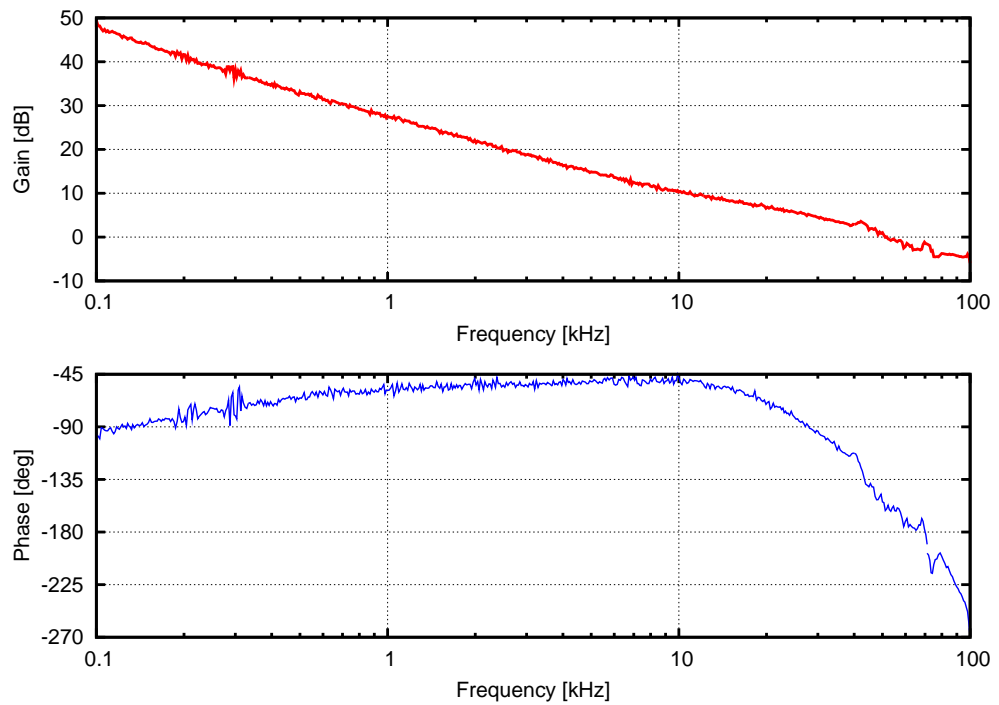


Figure 6.2 — Illustration of the mode cleaner and laser stabilization.

is less than 3 dB above the shot noise of 100 mW for frequencies above 10 MHz. A detailed characterization of eight similar lasers can be found in [99].

The MC was realized as ring resonator built by three mirrors glued on a quasi-monolithic aluminum spacer giving a round-trip length of approximately 52 cm corresponding to a free spectral range of about 577 MHz. Whereas the curved end mirror (ROC=2 m) was highly reflective, the plano-plano in-coupling and out-coupling mirrors had a polarization dependent transmittance whereby two modes of operation – the low-finesse (LF) mode and the high-finesse (HF) mode – could be performed depending on the lasers' polarization. In the LF-mode the MC had a Finesse of  $\mathcal{F}_{LF} \approx 555$  and a half bandwidth (pole frequency) of about 1 MHz. In the HF-mode the Finesse was  $\mathcal{F}_{HF} \approx 10500$  with a half bandwidth of about 55 kHz.

Fig. 6.2 shows a schematic of the MC and the length (resonance) control loop. For the length control of the MC (frequency control of the laser source) accomplished with a Pound-Drever-Hall (PDH) locking scheme a phase modulation of the laser beam at 12 MHz was applied utilizing a resonant EOM. The error signal was generated by demodulating the AC signal of  $PD_{MC}$ . The control loop was based on a so-called *split feedback*. A low pass filtered part of the feedback signal ( $x_{FB}^{MC}$ ) was applied to peltier elements thermally contacted with the aluminum spacer. Due to this, the MC's resonator length followed longtime frequency drifts. Additionally, a feedback without the need for a



**Figure 6.3** — Open-loop gain of the lasers frequency stabilization. A maximal unity gain frequency of approximately 50 kHz could be achieved.

HV-amplifier was possible. This method was performed when the MC was operated in its HF-mode to avoid the coupling of high frequency noise present on the HV-amplifier output into the servo loop [100].

The high frequency part was applied either on the PZT mounted end-mirror or the PZT of the laser crystal. Feeding back on the end mirror resulted in an open-loop gain of up to 7 kHz which was adequate for alignment purposes of the further experimental stages. For the measurements of the noise transformation caused by the non-linear resonator, the feedback signal was applied on the laser crystal PZT. Here, a stabilization of the laser frequency on the MC resonance with an open loop gain of up to 50 kHz was achieved. Fig. 6.3 shows the corresponding measured open loop transfer function.

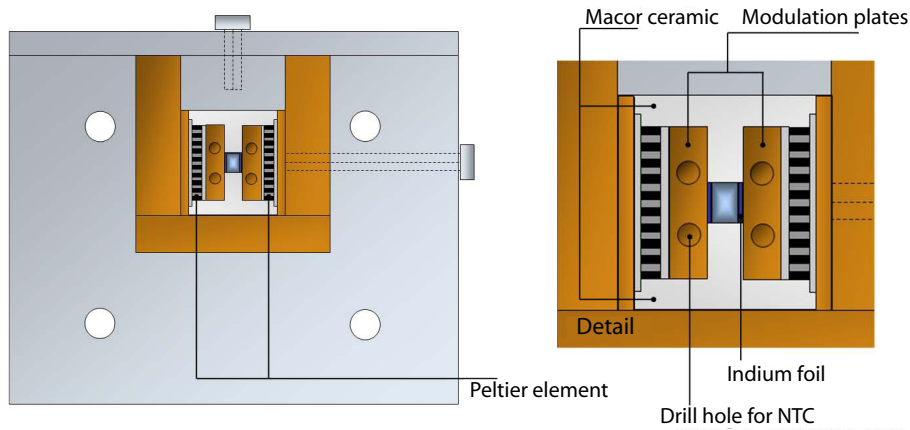


Figure 6.4 — Oven housing embedding the non-linear crystal. Illustration by A. Khalaidovski.

### 6.3.2 The Kerr non-linear resonator

#### 6.3.2.1 Optical and mechanical layout

The Kerr non-linear resonator (KNLR) consisted of a  $1.5 \times 2.0 \times 6.3 \text{ mm}^3$  7% MgO:LiNbO<sub>3</sub> crystal placed in between two curved mirrors of 25 mm radius of curvature. The coupling mirror had the reflectivities  $\rho_c(1064 \text{ nm}) = \sqrt{0.983}$  at the fundamental and  $\rho_c(532 \text{ nm}) = \sqrt{0.01}$  at the generated second harmonic, whereas the end mirror was highly reflective at 1064 nm and weakly reflective at 532 nm ( $\rho_{\text{end}}(532 \text{ nm}) = \sqrt{0.02}$ ). The intra cavity crystal surfaces were anti-reflective coated ( $\rho_{\text{AR}} \leq \sqrt{0.001}$ ) at both 1064 nm and 532 nm. The crystal was separated from the mirrors by 23.6 mm air gaps, creating a cavity mode for the resonant fundamental light with a  $27 \mu\text{m}$  waist at the center of the crystal. Together with the round-trip loss that was estimated to 0.5% (each AR-coating gives 0.1% per transmission, the absorption in the crystal was considered with  $0.077\% \text{ cm}^{-1}$  corresponding to the results obtained in Sec. 3.3.3 of [101]) the KNLR had a Finesse of about  $\mathcal{F} = 274$  and a half-bandwidth (pole) of approximately 4.5 MHz.

Fig. 6.4 illustrates the oven housing enclosing the non-linear crystal. An active temperature control loop utilizing two peltier elements for actuation allows the acclimatization of the phase matching condition of the fundamental and harmonic light field. These peltier elements were thermally contacted with two copper plates (used for the intra cavity phase modulation via the pockels

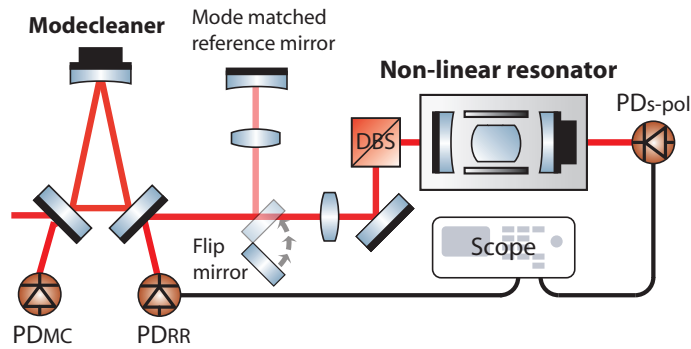


Figure 6.5 — Detection ports used during the alignment of the KNLR and the reference mirror.

effect) placed at both sides of the crystal. Furthermore, a thin indium foil in-between crystal and modulation plates was used for thermally contacting the plates and the crystal. A negative temperature coefficient (NTC) thermistor was placed in one of the copper modulation plates for error signal generation. For further details of the temperature control loop developed by H. Vahlbruch refer to Sec. 3.3.1 and App.B in [101]). Two aluminum plates containing a stack of a PZT, the coupling- or end-mirror, respectively, and a viton ring were mounted to the oven housing.

### 6.3.2.2 Alignment of the non-linear cavity

The alignment of the KNLR was accomplished in three subsequent steps. At first, the KNLR housing without the coupling and end-mirror was placed in the pre-aligned pump beam. The housing was positioned with respect to the beam transmitted through the crystal. By minimizing the beam displacement an optimal orientation of the crystal to the laser beam path could be ensured. At second, the aluminum plate containing the KNLR coupling mirror was attached to the oven housing. Since the reflected beam propagated back to the MC and was filtered again, higher order modes were reflected towards the detector PD<sub>RR</sub> (see Fig. 6.5). Accordingly, the coupling mirror was aligned with respect to the DC-signal of PD<sub>RR</sub> whereby a very high mode matching efficiency could be achieved. The corresponding measurement is shown in Fig.6.6.

Finally, the end-mirror was aligned to the beam transmitted through the coupling mirror and the non-linear crystal. In this stage of the alignment procedure, the MC was stabilized and the KNLR length was scanned. The mode

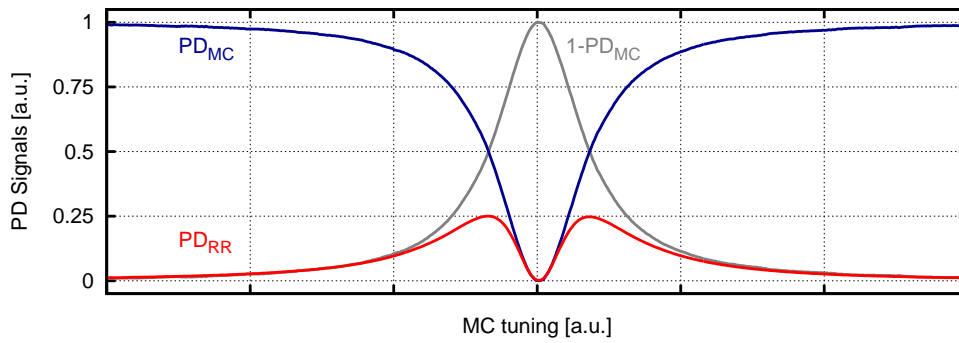


**Figure 6.6** — Dark noise corrected and normalized signals of  $PD_{MC}$  (blue curve) and  $PD_{RR}$  (red curve). For visualization purposes  $1-PD_{MC}$  (grey curve) was plotted to display the MC's transmission. The line shape of the signal obtained from  $PD_{RR}$  accords to the expected product of the MC's transmission and reflection. If the MC is tuned to the carrier light this signal is almost zero. Thus, a mode matching efficiency close to 100 % of the filtered beam to the KNLR's coupling mirror can be deduced.

spectrum was monitored with the detector  $PD_{s-pol}$  placed in transmission of the KNLR. At a point where the mode matching efficiency to the entire KNLR was in the order of about 95 % the aluminum plate containing the end-mirror was fixed. Then, only small corrections of the beam lag were necessary to enhance the mode matching further. Figure 6.7 shows the measured mode spectrum of the KNLR. From this measurement a mode matching efficiency of about 99 % can be deduced.

As shown in Fig. 6.5 an auxiliary mode matched mirror was implemented in the experiment. The beam reflected at this mirror served as reference for the initial laser beam whereby a comparison with the beam affected by the KNLR was possible. The mode matching to this reference mirror was accomplished also with respect to the monitor signal of  $PD_{RR}$ .

### 6.3.2.3 Control schemes for length stabilization

For the length control of the KNLR either a PDH scheme or a DC offset lock was used depending on what resonance state (tuned or detuned) needed to be stabilized. For measuring the conversion efficiency the KNLR was held on resonance using the PDH locking scheme. To avoid additional optical loss and mode distortions possibly caused by a further EOM placed between MC and KNLR the 12 MHz phase modulation sidebands already applied

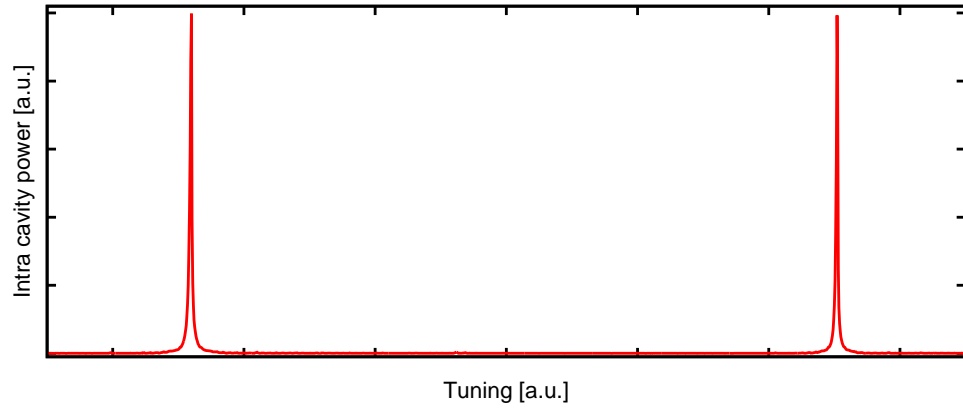


Figure 6.7 — Mode spectrum of the scanned KNLR. Second harmonic generation was minimal.

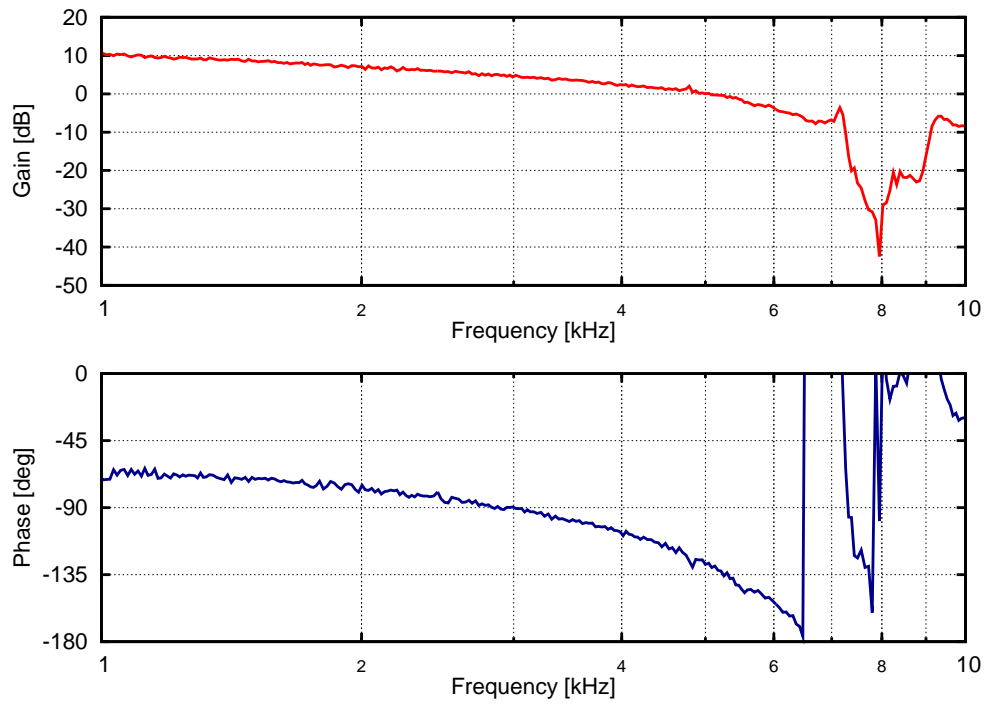


Figure 6.8 — Open-loop transfer function of the KNLR length stabilization by means of a DC offset lock.

for the MC control scheme were used for error signal generation. Although the modulation sidebands got attenuated due to the low-pass filtering of the MC (operated in its LF mode) and the KNLR, a proper error signal was obtained from the demodulation of the AC signal of  $PD_{s-pol}$ . But within the measurements of the KNLR induced noise transformation occasional strong detunings were required. Here an offset applied to the PDH error signal was not sufficient to reach all targeted OPs. Hence, in these cases a DC-lock was performed. The corresponding error-signal was obtained from  $PD_{s-pol}$  by adding an appropriate offset to its DC-signal. The respective feedback signals were HV amplified and applied on the PZT mounted end-mirror. Fig. 6.8 shows the open-loop transfer function measured for the DC lock control loop. The unity gain frequency of about 5 kHz was limited by resonances around 8 kHz (here over-compensated with a notch-filter included in the servo electronics).

### 6.3.3 Detection schemes

#### 6.3.3.1 Self-homodyning of the carrier light's amplitude quadrature

From the investigations in [28] it can be deduced, that the laser's power noise can be reduced by means of a KNLR. Thus, for demonstrating this noise reduction a self-homodyning detection scheme corresponding to the readout of the laser's amplitude quadrature was performed. The laser beam reflected off the KNLR was detected with  $PD_{X1}$  as shown in Fig. 6.9. The noise of the initial laser beam was investigated utilizing the mode matched reference mirror. A combination of a  $\lambda/2$  - plate and a PBS was used to attenuate the detected light powers to exactly the same reference value for all measurements. Note, that the readout with  $PD_{X1}$  gives the noise power of the initial laser beam transmitted and thus low-pass filtered *twice* by the MC. However, as these measurements aimed at the demonstration of a noise reduction only the relative noise levels at the same sideband frequency were of interest.

With this self-homodyning scheme only the amplitude quadrature noise of the laser beam can be measured. Moreover, this method is restricted to the detection of classical noise. Here an attenuation of the laser beam in the order of 90 % was required to obtain manageable powers on the photodetector  $PD_{X1}$ . Thus, any squeezing of quantum noise generated in the KNLR will be destroyed by this high optical loss.

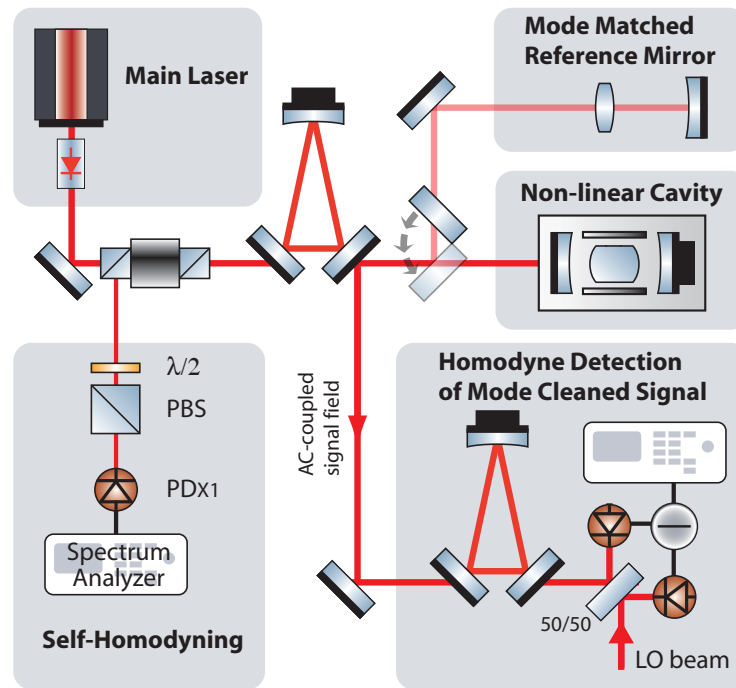


**Figure 6.9**— Readout of the laser's spectral noise. The lower left box shows the self-homodyning of the laser's amplitude quadrature. The beam reflected at the KNLR or the reference mirror respectively passed the MC a second time and were guided by means of a Faraday rotator towards a single photodetector ( $\text{PDX}_1$ ). The detected light power was attenuated by a combination of a  $\lambda/2$  - plate and a PBS. The lower left box illustrates the balanced homodyne readout with external local oscillator beam. An output mode cleaner (OMC) was implemented to suppress spatial higher order modes reflected at the back reflection port of the MC.

### 6.3.3.2 Balanced homodyne readout with external local oscillator beam

In order to investigate the manipulated laser noise in phase space, a homodyne readout with external local oscillator (LO) beam was performed. Since the power of the LO beam must dominate that of the detected signal, it was necessary to decouple the sidebands from the strong carrier having a power of up-to 1 W. Such an optical AC-coupling is provided by the MC's ring resonator topology. Whereas the DC and low frequency parts are transmitted, the sidebands at frequencies far above the MC's half-linewidth are reflected and thus spatially separated from the carrier field. Thus, the sole sidebands

present in the back reflection port of the MC can be guided to downstream homodyne readout. Optical AC-coupling enables the detection of the noise sidebands present on a high power carrier field without the need for high power photodetector. In addition, this method introduces marginal optical loss on the sideband fields whereby squeezing generated in the KNLR is preserved. A similar approach for an active power stabilization scheme of high power lasers was reported by Kwee *et al.* [26].

Besides the AC-coupled sidebands also spatial higher order modes propagated towards the homodyne detector. These modes are originated by the imperfect mode matching of the filtered pump beam to the KNLR. Although a mode matching efficiency of about 99 % was achieved the residual higher order modes (HOMs) led to a considerable power on the homodyne detectors photodiodes. As high pump powers in the order of 1 W were required to obtain a strong Kerr effect, these powers in the HOMs were in the order of 10 mW. Hence, an output mode cleaner (OMC) was implemented in the signal path to suppress the HOMs. The bandwidth of the OMC was approximately 65 MHz and represents a compromise of the achievable mode suppression and the optical loss of squeezed sidebands within the OMC's half-bandwidth. E.g. at a sideband frequency of 5 MHz the low-pass filtering of the OMC led to an attenuation of approximately 2.5 %. At 10 MHz the attenuation was already 9 %. However, since the half-linewidth of the KNLR was approximately 4.5 MHz a considerable amount of squeezing at higher sideband frequencies could not be obtained anyway.

The calculated mode spectrum of the OMC is shown in Fig. 6.10. HOMs were considered up to the order of five. Although the smallest suppression is about 4.5 for the fourth order, the implementation of the OMC led to a relaxed power requirement for the LO beam of the homodyne detector. A ratio of the LO beam power to the overall DC-power of the signal beam (including HOMs) of 30 was targeted. Hence, the homodyne photodetectors were designed such that a light power of up to 80 mW could be detected (per PD). Figure 6.11 shows a measurement demonstrating the linearity of the detector.

## 6.4 Prove of the Kerr effect

### 6.4.1 Dependence on phase matching temperature

At first, the SHG conversion efficiency of the KNLR was investigated in dependence on the phase matching condition adjusted by the crystal's temperature. From this measurement the phase matching temperature yielding a cascaded

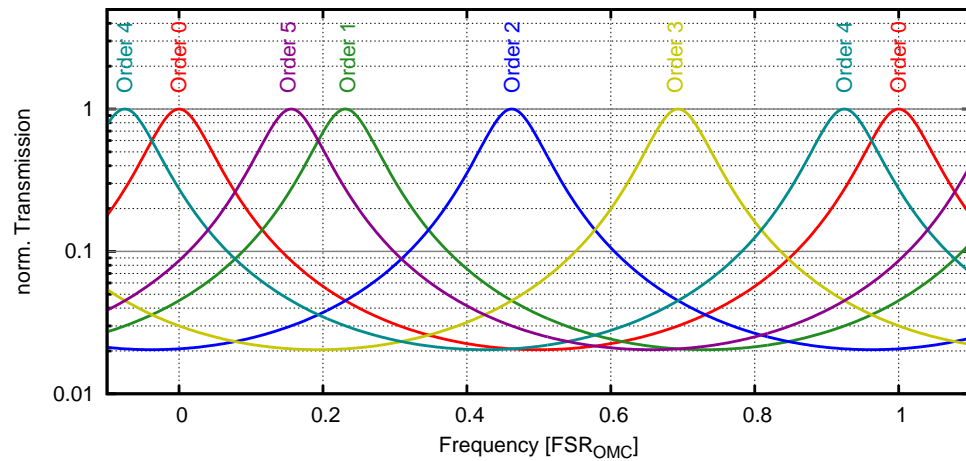


**Figure 6.10** — Mode separation of the OMC calculated with FINESSE. The normalized transmission of HOMs up to the order five is displayed. The weakest suppression of about 4.5 is obtained for the fourth order.

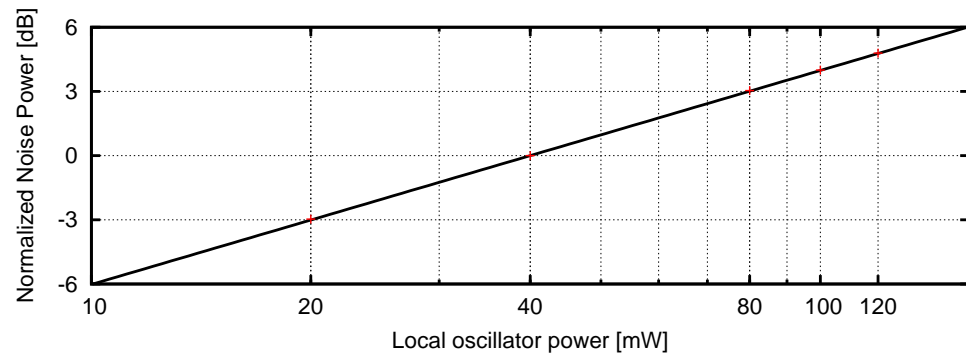


**Figure 6.11** — Linear fit to the normalized power noise variance for five different detected LO beam powers. Each measured data point corresponds to the average of 20 zero span measurements (RBW=100 kHz, VBW=100 Hz) at 3 MHz. These data were dark noise corrected. For a LO power of 80 mW the dark noise was about 6 dB below the shot noise level.

Kerr effect could be deduced. Figure. 6.12 shows the normalized phase matching curve for a  $TEM_{00}$  input mode for crystal temperatures between  $61^\circ\text{C}$  and  $67^\circ\text{C}$ . As expected, the curve in Fig. 6.12 is well described by a sinc-function. The additional peak at a temperature of about  $64.9^\circ\text{C}$  is most likely due to the non-zero reflectivity of the cavity mirrors at 532 nm and its effect on the

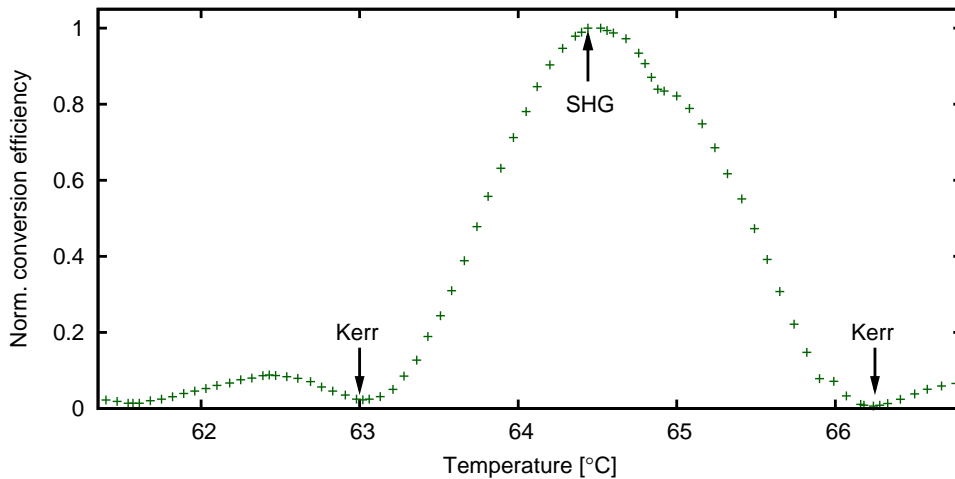


**Figure 6.12** — Measured second-harmonic generation (SHG) conversion efficiency versus crystal temperature (input laser power  $P_{\text{TEM}_{00}} = 95$  mW). The temperature was measured via a thermo resistor, the absolute values could be calculated with an accuracy of  $\pm 1$  °C. The Kerr effect can be observed in conversion minima slightly offset from the optimum SHG temperature:  $(T_{\text{Kerr, lower}} - T_{\text{SHG}}) = -1.41$  °C and  $(T_{\text{Kerr, upper}} - T_{\text{SHG}}) = +1.77$  °C.

differential phase between the reflected fields at 1064 nm and 532 nm [102]. At the SHG operation point of the KNLR a maximum conversion efficiency of  $\eta_{\text{SHG}} \approx 72\%$  was observed.

The theory predicts a sign change of the cascaded non-linearity induced phase shift when going from lower to upper conversion minimum (refer to Eq. 6.1). Accordingly, by measuring the Airy peak profile of the KNLR operated at the conversion minima the existence of an effective third-order non-linearity could be verified. To minimize the influence of any thermal effects caused by the heating of the crystal due to the non-zero absorption at the fundamental wavelength, the resonance of the KNLR was scanned in a short time of a few  $\mu\text{s}$ . The Airy peaks were recorded in both conversion minima, in each case for a reducing resonator length. The results approving the presence of an optical Kerr effect are shown in Fig. 6.13. The Airy peaks clearly show the predicted phase matching dependent declination.

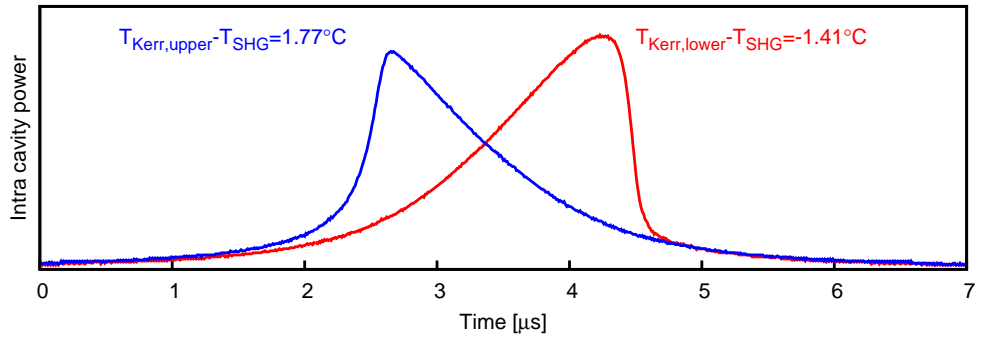


**Figure 6.13** — Airy peaks for a reducing KNLR length measured in the first conversion minima at  $T_{\text{Kerr,lower}} - T_{\text{SHG}} = -1.41^\circ$  (red curve) and  $T_{\text{Kerr,upper}} - T_{\text{SHG}} = 1.77^\circ$  (blue curve). The Kerr effect induced phase shift and the corresponding deformation of the Airy peak's line shape changes with the phase matching condition as expected from the theory.

### 6.4.2 Hysteresis measurements of the dynamic resonator

Since the squeezing of the pump field noise (classical as well as quantum noise) is expected to be most significant at the so-called *critical state* of the KNLR, it was essential to investigate whether the cascaded Kerr non-linearity was strong enough to reach this state. Here, one possible analysis is a measurement of a hysteresis effect of the intra cavity power for an expanding and reducing resonator length. When the KNLR is already in its multi-stable regime a strong hysteresis is expected as illustrated in Fig. 6.14. In the case of the expanding resonator the line shape of the dynamic Airy peak follows that of the static case until the maximum power build-up is reached. Immediately beyond, the intra cavity power drops to the level of the static Airy peak in the wings of the multi-stable region (grey shaded area). Likewise, in the case of the reducing resonator length the cavity field jumps to the level of the static Airy peak when the multi-stable region is left. The slopes at the jumps are limited by the cavity storage time. Furthermore, an overshoot can be observed resulting from the fact that the field does not reach equilibrium at these tunings.

Unfortunately, such short scanning times as assumed in the numerical simulation did not lead to satisfactory results in the experiment due to thermal effects caused by the absorption of the non-linear crystal. Accordingly, in order to minimize the impact of thermal (as well as acoustic distortions), the resonance of the KNLR was crossed within a time of a few  $\mu\text{s}$ . Due to this, the cavity dynamics accounting for the cavity build-up and storage time need to

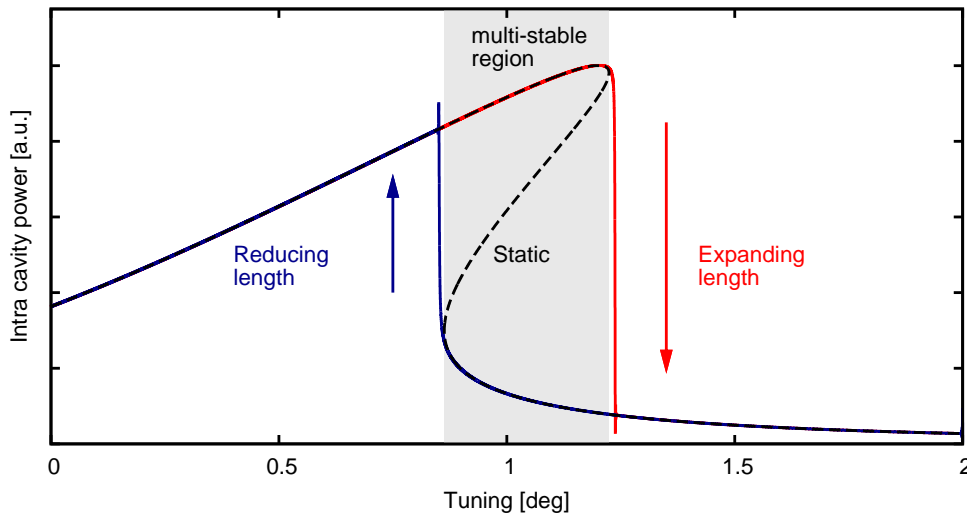


**Figure 6.14** — Illustration of the hysteresis effect of a multi-stable resonator. The black curve shows the Airy peak of the static resonator (i.e. the intra cavity field reaches equilibrium at each tuning). The data for the expanding (red curve) and the reducing (blue curve) resonator length were calculated in the time-domain assuming an end mirror velocity of  $50\lambda/s$ . The used c-script is attached in App. C

be considered. Here, to allow an interpretation of measured hysteresis curves a numerical model (basing on Eq. 2.37) was consulted. The used source code is attached in C. One major result was, that just a presence of a hysteresis effect is not a sufficient condition to infer the multi-stability of the KNLR. The comparison of the Airy peaks of a scanned KNLR that is close to the critical state (top graph in Fig. 6.15) with those of KNLR that has just entered the multi-stable regime (center graph) shows, that in both cases already a significant hysteresis effect can be observed. The strength of the hysteresis effect grows with strength of the Kerr effect as shown in the bottom graph.

Consequently, the intention was to estimate the strength of the Kerr non-linearity by the comparison of the numerical model with the measurements. Unfortunately, the PZT used for scanning the resonator length showed a strong non-linear behavior so that the actual end-mirror velocity fluctuated even within the time needed for crossing the resonance. Furthermore, the measured line shapes at that points of the Airy peak where a ringing effect was expected (see Fig. 6.15) strongly depended on the response function of the used photodetectors. Accordingly, the comparison with numerical sim-

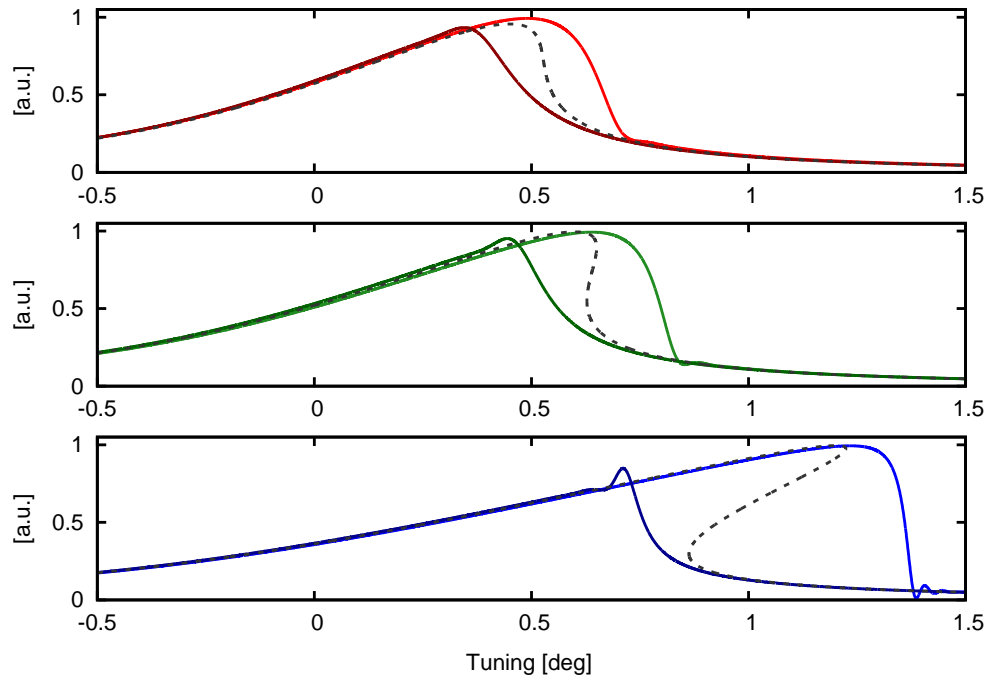


**Figure 6.15** — Comparison of a scanned KNLR close to the critical state (top) with a KNLR just entered the multi-stable regime (center) and a strong multi-stable KNLR (bottom). The dashed curves show the respective static Airy peak. The light colored curves shows the Airy peaks for the expanding resonator length and the dark colored curves those for a reducing resonator length, respectively. The end mirror velocity was the same for all cases.

ulations yields a great uncertainty. Figure 6.16 shows the best measurement result in comparison with the numerical simulation. The KNLR was operated at the upper conversion minimum ( $T_{\text{Kerr,upper}} - T_{\text{SHG}} = 1.77^\circ$ ) with a pump power of 780 mW. A sinusoidal signal at a frequency of 1 kHz with an amplitude of  $7 V_{\text{pp}}$  was applied to the HV-amplifier driving the PZT mounted end-mirror. The Airy peaks were recorded in the linear region of the sine wave. The mean end-mirror velocity during the measurement time was expected to be about  $2024 \lambda/s$ . This value is based on the PZT hub of approximately  $0.054 \lambda/V$  determined by independent measurements. In the numerical model scanning velocities of  $v_{\text{exp}} = 1850 \lambda/s$  for the expanding resonator length and  $v_{\text{red}} = -0.93 \cdot v_{\text{exp}}$  for the reducing length led to the best agreement. These values corresponds to a deviation of approximately 8.6% and 15%, respec-

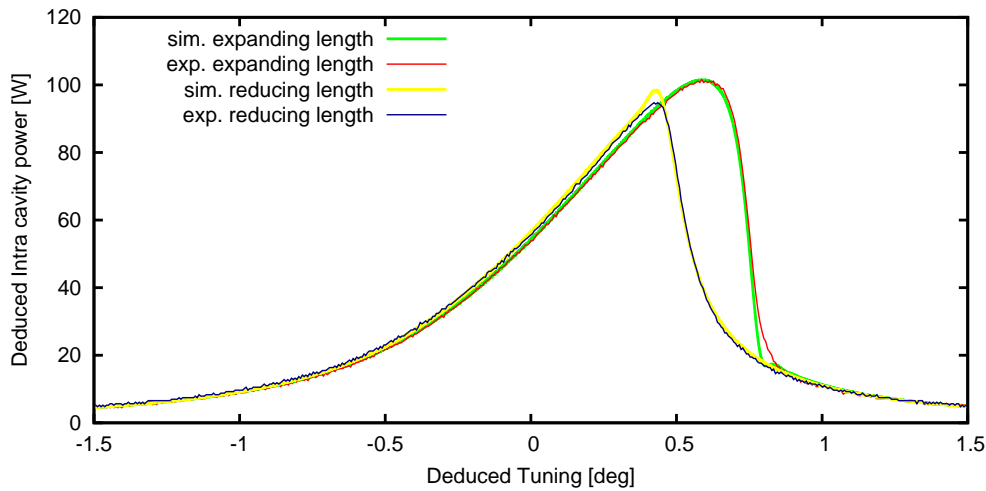


**Figure 6.16** — Comparison of simulated and measured hysteresis curves. The experimental data were normalized to the tuning and the intra cavity power deduced from the simulation.

tively. In view of the PZT's non-linear behavior these deviations present an acceptable error. The properties of the KNLR accords to the description in Sec. 6.3.2.1. The intensity dependent phase shift inside the KNLR  $\phi_{\text{Kerr}} = \theta \cdot P$  (with the intra cavity power  $P$ ) was considered with  $\theta = 5.54 \times 10^{-3}$  rad/W. Except of that points where the simulation predicts a ringing effect, the line shapes of the simulated and measured Airy peaks are in good agreement. Then, the simulation based on  $\theta = 5.54 \times 10^{-3}$  rad/W implies, that the KNLR has just entered the multi-stable regime. Although the estimation on the basis of the above measurement yields a great uncertainty, it could be deduced at least that the Kerr non-linearity was strong enough to reach the multi stable regime and thus the targeted critical state if input powers  $P_{\text{in}} \geq 800$  mW are chosen.

## 6.5 Enhancement of phase modulation signals

Since a KNLR – compared to a linear cavity – has an enhanced sensitivity for phase modulation signals, the investigation of its transfer functions provides a further opportunity to demonstrate the presence of an effective third-order non-linearity in the experiment. Additionally, together with numerical models a further estimation of the actual strength of the Kerr effect was possible. Two

types of measurements were performed. First, the response of the KNLR on strong phase modulation signals applied at discrete frequencies was measured. Second, for OPs on the steep and shallow resonance slope the transfer function was measured in a frequency band from 100 kHz to 15 MHz (see Sec. 6.5.2).

### 6.5.1 Strong modulation of the geometrical length

The response for a strong phase modulation was investigated at frequencies of 30 kHz and 1.76 MHz. Since the modulation depth of the KNLR internal EOM was frequency dependent, the modulation frequencies were chosen to give a strong modulation by simply applying the output of a frequency generator on the modulation plates. Additionally, the intention was to choose a frequency close to DC where the enhancement is expected to be maximum. Here, a frequency of 30 kHz led to a satisfactory modulation depth. Likewise, for the investigation of the response at higher frequencies (within the bandwidth of the KNLR) a modulation frequency of 1.76 MHz was selected. Furthermore, the input power was set to 750 mW and 510 mW, respectively. The OP (tuning) was chosen to give a distinct characteristic of the detected AC-signals. Here, the KNLR was operated slightly off-resonance on the steep flank of the Airy peak leading to an intra cavity power corresponding to 40 % of the maximum build-up reached at resonance.

Fig. 6.17 shows the results of the measurements in comparison with fitted numerical data. For the fit of the data the reflectivities  $R_{M_c} = 0.983$  and  $R_{M_{end}} = 0.9992$ , the round-trip loss  $a_{rt} = 0.005$  and the optical length of the KNLR  $L_{opt} = 122.19 \times 10^{-3} \text{m}$  were kept constant. At first, on the basis of the measurement performed with  $P_{in} = 750 \text{ mW}$  and  $f_{mod} = 1.76 \text{ MHz}$  (blue curve in the upper graph of Fig. 6.17), the actual modulation depth and Kerr non-linearity were fitted. The obtained values leading to the best agreement between simulation and measurement were then also assumed for the measurement at  $f_{mod} = 1.76 \text{ MHz}$  with  $P_{in} = 510 \text{ mW}$ . For the measurement at  $f_{mod} = 30 \text{ kHz}$  the modulation depth was fitted again, whereas all other parameters were kept constant. Furthermore, all experimental data were scaled with the same factor and shifted on the x-axis to obtain an overlap with the numerical data allowing a direct comparison.

To estimate the accuracy of this fitting method, the procedure described above was repeated considering values for the Kerr non-linearity increased and decreased by 10 %. Then the modulation depth was fitted again whereas all other parameter were the same. The results of these fits are displayed in Fig. 6.18 and Fig. 6.19. It can be seen, that in both cases the agreement between

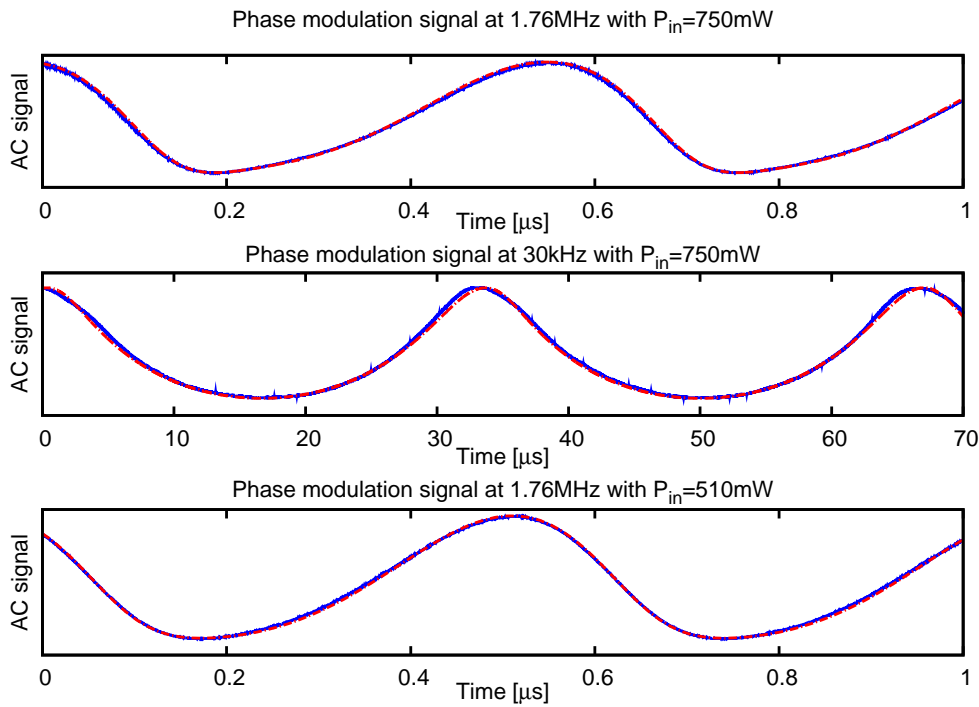


**Figure 6.17** — Comparison of measured (solid blue curves) and simulated (dashed red curves) phase modulation signals detected in transmission of the KNLR. For an input power of 750 mW strong modulations were applied at frequencies of 1.76 MHz (top) and 30 kHz (center), respectively. Additionally, for a modulation at 1.76 MHz the response was investigated for an input power of 510 mW (bottom).

measurement and simulation is not as good as in Fig. 6.17.

From the method described above, the product  $\theta \cdot P$  giving the Kerr effect induced phase shift can be deduced. For the fits the input powers  $P_{\text{in}}$  were considered with 510 mW and 750 mW as measured in the experiment. However, these values were measured with a power meter (Coherent FM-GS) having a specified accuracy of 7%. Thus, the overall error of the fitted value for  $\theta$  was roughly estimated as 20% leading to

$$\theta = (4.5 \pm 0.9) \times 10^{-3} \frac{\text{rad}}{\text{W}}. \quad (6.3)$$

The effective non-linear refraction index  $n_2^{\text{eff}}$  of the cascaded Kerr effect

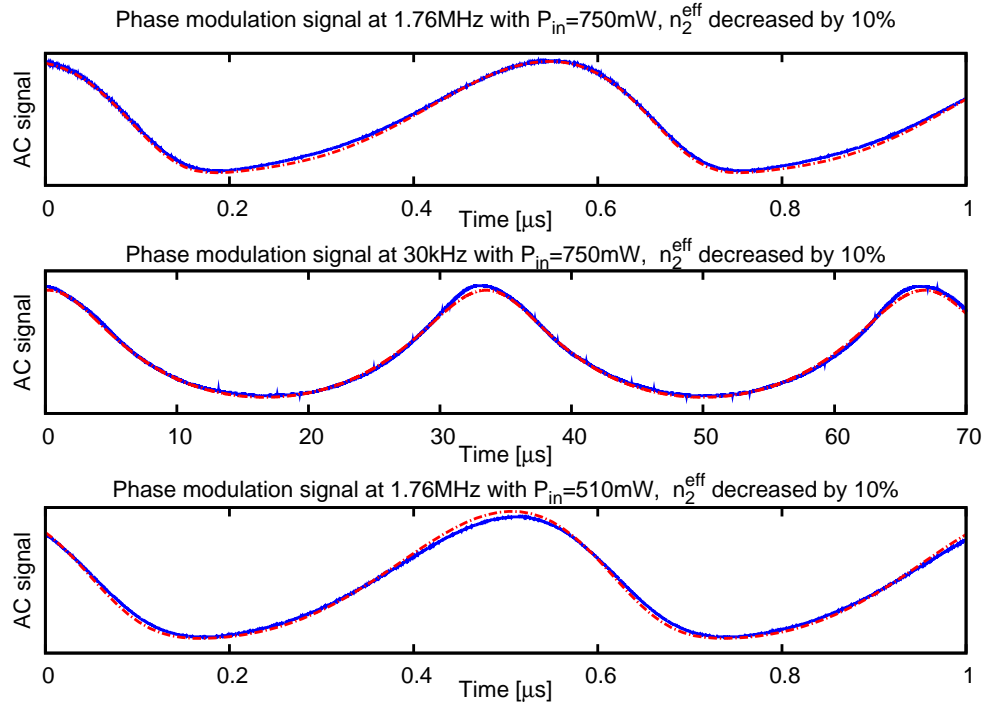


Figure 6.18 — Non-optimal fitting. Here the  $n_2^{\text{eff}}$  was kept on a fixed value 10% below the actual fit result.

can be obtained from the relation [103]

$$\theta P = \frac{n_2^{\text{eff}} \omega_0 L_{\text{KM}}}{\mathcal{A} c} P. \quad (6.4)$$

Here  $L_{\text{KM}}$  is the length of the Kerr medium,  $P$  the intra cavity power and  $\mathcal{A}$  the cross-sectional area of the laser beam. By a rigorous assumption of a beam waist  $w_0 = 27.6 \mu\text{m}$  located in the center of the crystal, the mean beam size over the entire crystal can be calculated to  $w_{\text{mean}} = 59.3 \mu\text{m}$ . Thus, with  $\mathcal{A} = \pi w_{\text{mean}}^2$  the effective non-linear refractive index can be calculated from Eq. (6.4) leading to

$$n_2^{\text{eff}} = (1.7 \pm 0.3) \times 10^{-18} \frac{\text{m}^2}{\text{W}}. \quad (6.5)$$

This value is about 2 orders of magnitude greater than the non-linear refraction indices corresponding to the  $\chi^{(3)}$  non-linearity of e.g. sapphire, BK7 and fused silica.

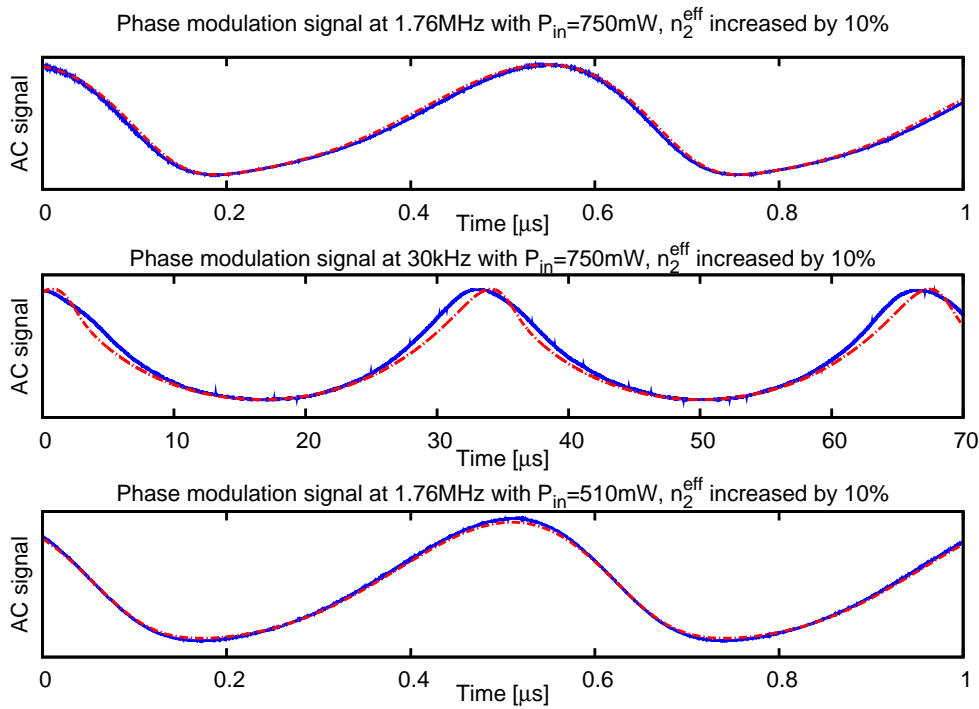


**Figure 6.19** — Non-optimal fitting. Here the  $n_2^{\text{eff}}$  was kept on a fixed value 10% above the actual fit result.

### 6.5.2 Transfer function of phase modulation signals

As already stated, the modulation depth of the KNLR internal EOM was strongly dependent on the frequency. Nevertheless, the observation of different transfer functions obtained for OPs on the steep or shallow resonance slope would have been sufficient to prove the presence of an effective Kerr effect. But the line shape and the frequency dependent characteristics could not be determined. For that reason, the attempt was made to calibrate the frequency dependent modulation depth of the EOM. When locked to resonance, the transfer function of a two-mirror cavity is flat within the cavity bandwidth. Since the internal loss of the KNLR was dependent on the amount of SHG, at the crystal temperature  $T_{\text{SHG}}$  (refer to Fig. 6.12) the bandwidth of the KNLR was maximum. Figure 6.20 shows the resonance peaks measured for  $T_{\text{SHG}}$  and  $T_{\text{Kerr,upper}}$ . Again, to minimize thermal effects the resonances were crossed within a few  $\mu\text{s}$ . Hence, the maximum build-up and the bandwidth of the

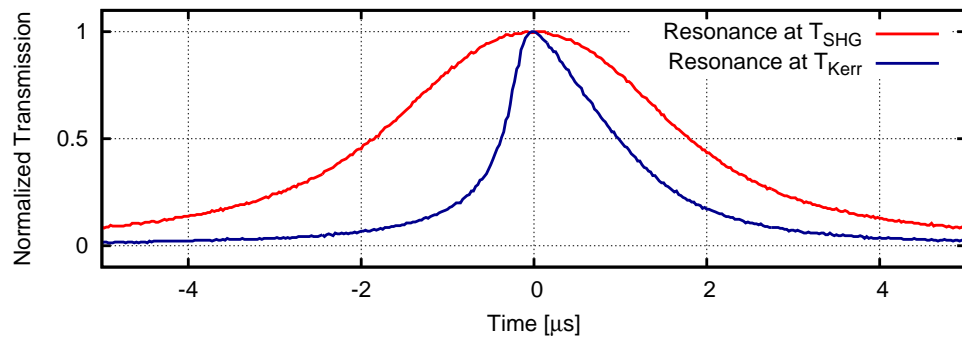


**Figure 6.20** — The figure shows the transmission of the KNLR depending on the SHG. The measurement were normalized to the respective maxima. the x-positions are arbitrary.

KNLR operated at the conversion minimum are affected by the resonator dynamics. Additionally, the observed non-linearity of the PZT used for scanning the resonator length leads to a further uncertainty. However, from these measurements it can be deduced, that the bandwidth at the SHG maximum is increased by a factor of more than 2.5. Thus, when estimating this bandwidth with 11 MHz, the transfer function at the SHG can be assumed to be flat up to frequencies of about 10 MHz. Accordingly, the measured transfer function of the KNLR locked close to resonance was used as reference for the EOM frequency response.

Figure 6.21 shows the normalized phase modulation transfer function of the KNLR at phase matching temperatures around  $T_{\text{Kerr,upper}}$ . The source of a network analyzer was applied to the EOM. The signals were detected with  $PD_{\text{s-pol}}$ . The laser input power was approximately 650 mW and the KNLR was locked on its steep and shallow resonance slope corresponding to  $P/P_{\text{res}} \approx 0.6$ . At first, the response was measured when locked to the shallow slope (yellow trace). Subsequently, the transfer functions were analyzed for the OP on the steep slope. Starting from the red trace, the crystal temperature was slightly adjusted whereby an improved response was achieved as shown with the green and blue traces.

Please note, that these measurements are just of a qualitative character. First, at high frequencies the calibration of the EOM yields a great uncertainty. Second, the dependence on the strength of the Kerr effect was demonstrated by varying the phase matching condition. Accordingly, the internal loss (corresponding to the SHG) and thus the bandwidth were not the same for all cases.

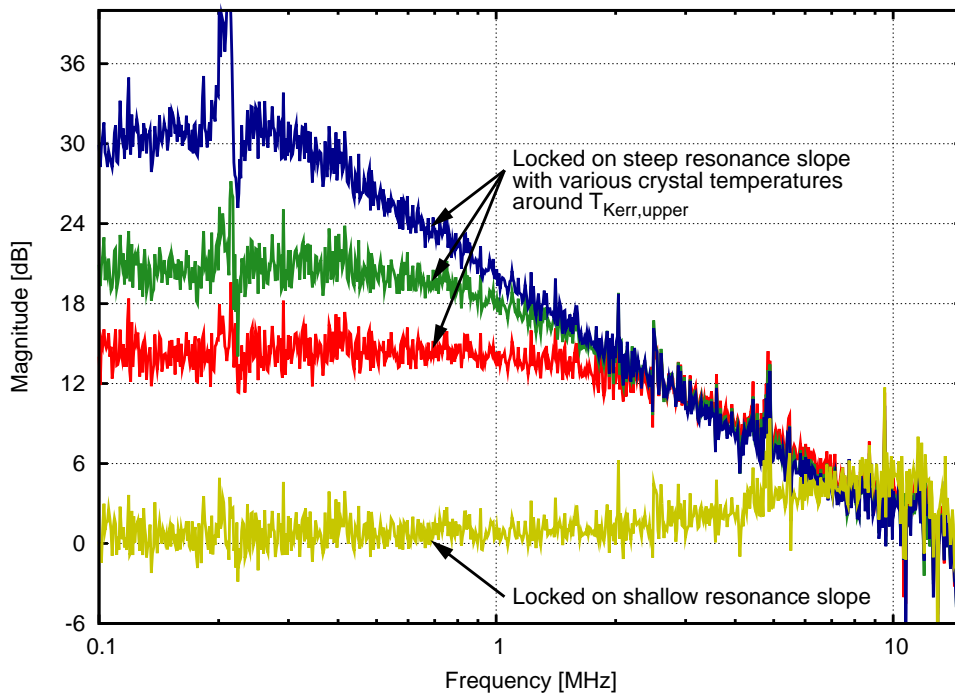


**Figure 6.21** — Normalized transfer function of the KNLR. The yellow trace was measured for an OP on the shallow resonance slope. All other curves corresponds to OPs on the steep resonance slope. Here, the crystal temperature was slightly varied to demonstrate the dependence on the effective Kerr non-linearity. All curves were divided by the reference transfer function measured in the SHG maximum. The y-positions of the curves were arbitrarily normalized to the low frequency response of the yellow trace.

However, as expected the frequency response of the KNLR depends on the chosen OP (steep or shallow resonance slope) in contrast to a linear two-mirror cavity. Additionally, these measurements demonstrate the enhancement of phase modulation signals depending on the strength of the Kerr effect.

## 6.6 Laser power noise reduction

In this Section the power noise reduction of a continuous-wave laser field by means of an effective third-order KNLR is demonstrated. In contrast to conventional noise reduction schemes relying on linear cavities, a strong noise suppression at Fourier frequencies *below* the linewidth of the non-linear cavity

was possible. The laser light was reflected off the KNLR that was operated slightly off-resonance at approximately 3/4 of the maximum power build-up, close to its so-called critical state. A power noise reduction of up to 32 dB at Fourier frequencies below 1 MHz was observed after reflection. The laser had a power of 0.75 W.

### 6.6.1 Introduction

An active laser power stabilization is essential for many high-precision optics experiments. Passive noise filtering provided by the transmission through optical cavities can efficiently be used in order to reduce power fluctuations at Fourier frequencies above the cavity linewidth. More adequate in most cases are active feedback control circuits. Here, a certain fraction of the laser power is detected by photodiodes in order to sense the power fluctuations, and different kinds of actuators like acousto-optical modulators are then used to reduce the laser noise on the residual beam. Especially in applications that require high power stability at low frequencies a constraint arises for active stabilization schemes, which is caused by (presumably photodiode internal) unknown noise sources associated with the large photocurrent. At 10 Hz this photo-diode noise already exceeds the shot-noise of a 100 mW laser beam which corresponds to a relative power noise of approximately  $2 \times 10^{-9} \text{ Hz}^{-1/2}$  [25]. At just slightly lower relative power noise levels (corresponding to slightly higher powers) an additional problem arises and the sensing sensitivity would be limited by the available dynamic range of photo-diodes and their amplifiers. Hence novel schemes are required that either reduce the required dynamic range and the detected power of the sensing device [26]. But again these schemes are typically limited to frequencies comparable or above the linewidth of the optical cavity involved.

Another way out, proposed quite a while ago, is based on the optical Kerr effect. It does not require any photo detection [104, 30] and can be combined with optical cavities in order to yield a power noise reduction by self-modulation [28]. One problem of this approach is the typically rather low third-order non-linearity of high-quality optical materials. In the pulsed laser regime high laser intensities can be used to compensate for this and strong noise reductions of certain field quadratures even below the shot-noise, i.e. into the non-classical regime of squeezed states, were demonstrated [105, 106].

In the continuous-wave laser regime an intensity increase through tight focusing and power build-ups in optical resonators are typically not sufficient,

and materials with higher third-order non-linearities are desired. A promising solution is the use of interacting  $\chi^{(2)}$  non-linearities as proposed for the first time already four decades ago (refer to Sec. 6.2), however, up to now no strong noise suppression of continuous-wave (cw) light had been demonstrated. In [94] the classical noise of a cw laser beam of less than 30 mW power was reduced by 1.5 dB. In [107] the more demanding regime of non-classical states was targeted, and squeezed states of a 0.45 mW cw beam were observed. The measured noise reduction was 30 % (approx. 1.5 dB) below the vacuum noise level.

### 6.6.2 Measurements

Figure 6.22 shows the measurement results that demonstrate the laser power noise reduction by means of the KNLR. The top peaked curve shows the initial laser power noise detected with the single photodetector  $PD_{X1}$  after two transmissions through the MC (refer to Sec. 6.3.3.1). For this reference measurement the flip mirror was used as shown in Fig. 6.9. The other curves show the power noise spectra of the same laser when being reflected off the detuned Kerr cavity and when the OP on the steep slope of the Airy peak (Fig. 6.16) was varied and stabilized by an appropriate DC offset lock. The reflected laser power was attenuated to exactly the same reference value and was detected also with  $PD_{X1}$ . A maximum noise suppression of 32 dB was observed slightly below 1 MHz. This suppression value was observed for a KNLR operating point at about 3/4 of the Airy peaks maximum where the steepest slope is predicted from theory. All curves in Fig. 6.22 were shot noise limited at frequencies above 9 MHz. At intermediate frequencies they showed additional noise that increased with an increasing Kerr effect and most likely arose from internal Brillouin scattering.

Several experiments were performed which confirm that the observed noise reduction is due to the Kerr effect. The essential measurements discussed in Sec. 6.4 demonstrate the presence of a cascaded Kerr effect in the used second order non-linear crystal. Furthermore, when the KNLR was locked to points on the steep slope, the observed maximum noise suppression was merely independent of the choice of the two conversion minima, but always dependent on the input power, as predicted from theory and the achievable noise suppression decreased with decreasing input powers.

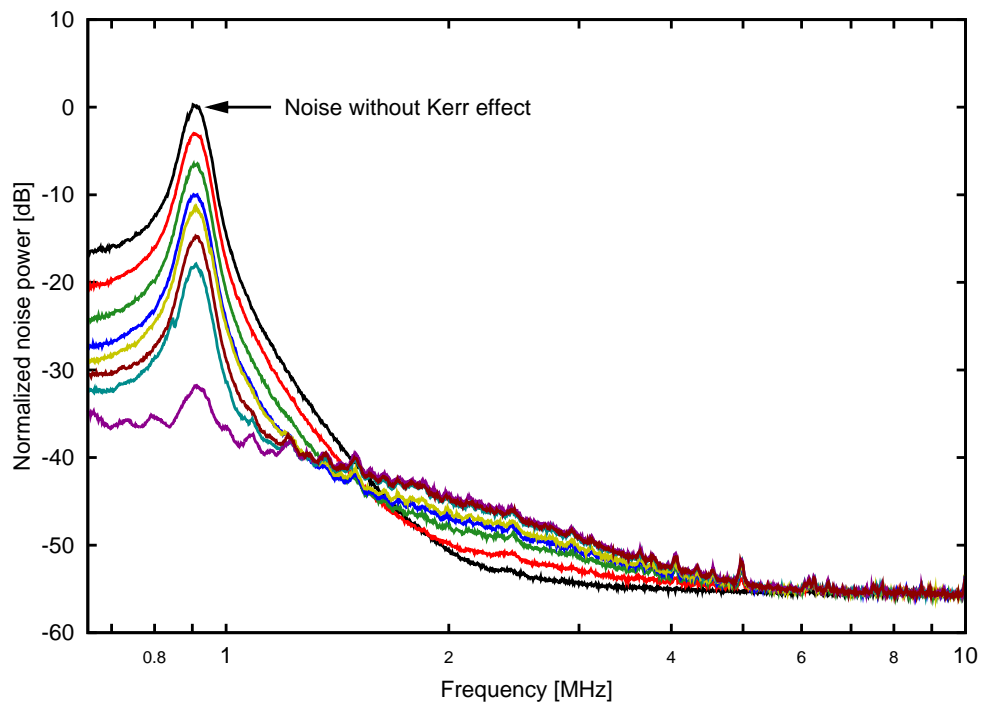


**Figure 6.22** — The figure compares the normalized power noise spectra of the initial laser beam with the laser beam after reflecting off the KNLR. The KNLR was locked on several OPs on the steep resonance slope. The maximum noise reduction was achieved at an OP where the intra cavity power reaches approximately 3/4 of the maximum power obtained at resonance.

## 6.7 Tomographic analysis of the noise transformation

### 6.7.1 Motivation

From the measurements of the laser noise reduction presented in the previous Section the actual (de-)amplification factor of the classical noise level could not be precisely determined for two reasons. First, in the self-homodyning readout scheme only the amplitude quadrature of the incident field is detected. Since the KNLR was operated detuned, a frequency dependent phase-space rotation of the de-amplified quadrature occurs. Second, the investigated laser showed an elliptical noise distribution (i.e. the noise in the amplitude quadrature was much higher than in the phase quadrature). Together with the first argument, the measurement presented in Fig. 6.22 does not allow to distinguish between

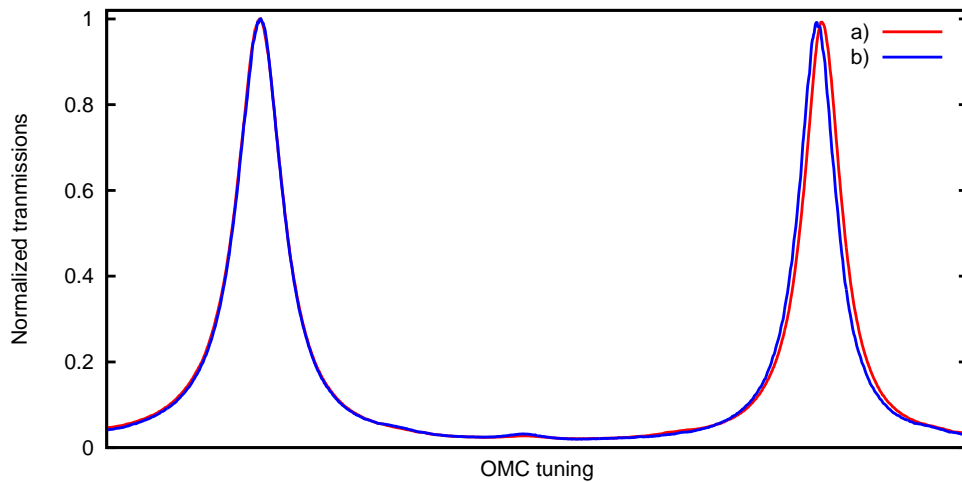


**Figure 6.23** — The figure shows the normalized mode spectrum of the scanned OMC for a) the beam reflected off the reference mirror and b) for the beam reflected off the KNLR. The x-positions are arbitrary.

the actual amount of deamplification and the noise reduction possibly caused by a rotation of the initial amplitude quadrature into the less noisy phase quadrature. Furthermore, in view of an application in gravitational-wave detectors the noise level in the phase quadrature of the laser beam needs to be known as it could limit the detectors sensitivity. These informations can be obtained from a tomographic analysis recovering the noise distribution in phase-space.

### 6.7.2 Measurements

For the tomographic analysis a homodyne readout was performed as illustrated in Fig. 6.9. The local oscillator beam was gained in transmission of a PBS placed in front of the MC. The spatial signal mode of the beam reflected off the KNLR and transmitted through the OMC was matched to the LO beam with a measured visibility of about 97%. During the alignment process of the OMC, the MC was locked strongly detuned whereby the  $TEM_{00}$  mode dominated the power in the signal beam. The mode spectrum of the scanned OMC is shown in Fig. 6.23. Curve a) shows the mode matching of the reference beam and curve b) that of the beam reflected off the KNLR. The KNLR was locked on its steep resonance slope such that an intra cavity power  $P$  of about 50% of the maximum power  $P_{\text{res}}$  was reached. The data of both measurements

were normalized to the respective maximum transmission to allow a direct comparison. This measurement shows, that the mode pattern of the reference beam and the KNLR affected beam have almost the same mode pattern.

In the first instance the tomographic measurements were targeted on the determination of the deamplification and amplification factors of the *classical* noise power. In addition, the phase-space rotation at the investigated sideband frequencies should be deduced. Accordingly, the MC was locked tuned to avoid an additional frequency dependent rotation of the signal field occurring due to the reflection at the back-reflection port.

For the measurement of the KNLR transformed noise distribution a sideband frequency was chosen at which the initial laser beam yields almost the same noise levels in its amplitude and phase quadrature. In this case, the noise transformation of the KNLR – although measured for classical noise – corresponds to the transformation expected for a shot noise limited input beam and the amplification and deamplification levels could be easily determined. The best regime was found at a sideband frequency of 1 MHz whereby the noise eater [98] of the laser was used to reduce the power noise around the relaxation oscillation. For an input power of about 500 mW the classical noise level was about 45 dB above the shot noise level. The input power of 500 mW was chosen because the observed excess noise was expected to be about 20 dB above the shot-noise level at this input power. This has been shown in independent measurements. The excess noise does not originate from the KNLR noise transformation as it was observed even at crystal temperatures where no cascaded Kerr effect occurs. In order to recover the pure noise transformation and the corresponding (de-)amplification factor without being affected by the excess noise, the KNLR resonator was operated not at the critical state. In this case, the achievable deamplification factor is expected to be much smaller. Accordingly, since the noise of the input beam was about 25 dB above the excess noise level, the deamplification was expected to be not limited by this noise.

The homodyne detection angle was swept by actuating on a PZT mounted steering mirror placed in the LO beam path. The AC signals of both homodyne photo-detectors were subtracted and demodulated at 1 MHz. After filtering with a 7-pole Bessel low-pass with a corner frequency of 200 kHz the data were recorded with a NI PCI-6133 card [108]. Additionally, the DC signal of one of the homodyne photodetector was recorded serving as homodyne detection angle reference for the data evaluation. The sampling rate was 1MS/s in both cases. The data acquisition controlled by a LABVIEW interface.

### 6.7.3 Evaluation of the measured data

The data analysis and the evaluation of the measurement were based on MATLAB-scripts developed by Boris Hage. The main focus was on the reconstruction of the *Wigner function* representing a quasi-probability distribution in phase space. On the basis of the Wigner functions obtained from the measured data the phase-space rotation at the investigated sideband frequency could be extracted. For further details on the tomographic reconstruction refer to [109]. In [87] the frequency dependent rotation of a squeezing ellipse reflected off a filter cavity was analyzed similar to the method presented here.

First, the detection angle of each measurement was extracted. Assuming that the PZT motion is well approximated by a third order polynomial function, by fitting the function

$$f(x) = a_0 + a_1 \sin(b_1x + b_2x^2 + b_3x^3 + c_1) \quad (6.6)$$

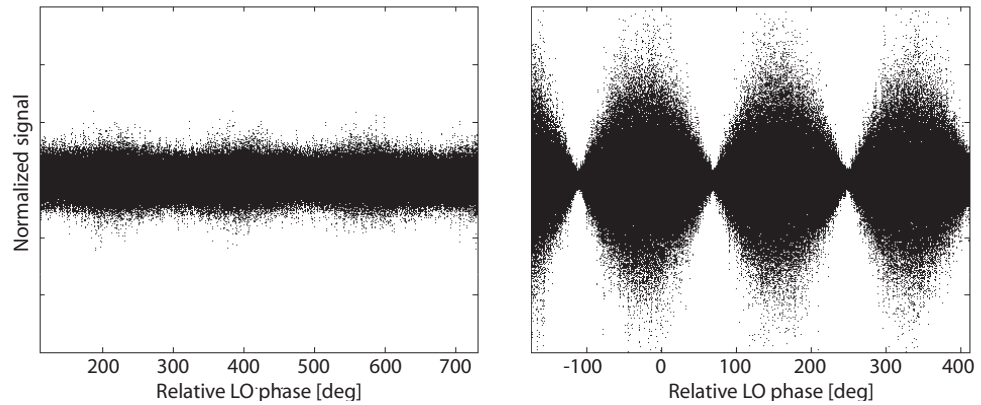
to the recorded DC Signal of one photo-detector it was possible to interpolate the actual detection angle of each data sample. Note, that this detection angle refers to the amplitude quadrature of the pump beams DC part reflected off the KNLR. Second, the sampled demodulated AC-signal was divided into 100 slices attributed to the respective detection angle. For each slice containing 5000 data points a histogram was build from with the Wigner function was reconstructed by means of an inverse Radon transformation. Finally, the phase-space rotation  $\Theta$  was determined by fitting an ellipse

$$e(x) = \frac{ab}{\sqrt{a^2 \sin(x - \Theta)^2 + b^2 \cos(x - \Theta)^2}} \quad (6.7)$$

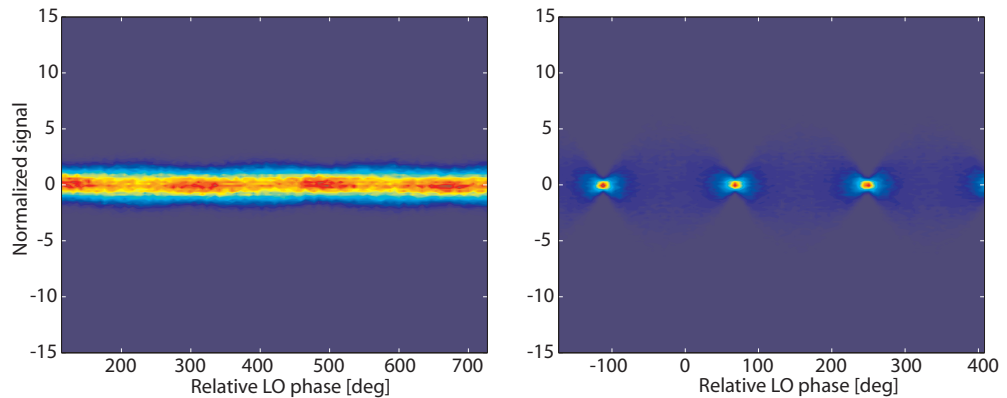
to a contour line of the reconstructed Wigner function.

Figure 6.24 shows the demodulated AC signals obtained for the reference beam (left) and the beam reflected of the KNLR (right). The signals are normalized to the mean standard deviation  $\sigma_{\text{ref}}$  of the reference beams noise distribution. The detection angles were interpolated according to Eq. 6.6. It can be seen that the noise of the reference beam is almost independent of the detected quadrature. In contrast to this, the noise distribution of the Kerr affected beam clearly shows the quadrature dependent deamplification and amplification of the input beam. Figures 6.25 and 6.26 show the corresponding histograms and reconstructed Wigner functions, respectively.

The noise transformation of the KNLR was investigated for several of its OPs on the steep and shallow slope of the Airy peak. In each case, four



**Figure 6.24** — The Figure compares the sampled signals measured for the reference beam (left) and the beam reflected off the KNLR (right). Here the KNLR was locked on its steep slope with  $P/P_{\text{res}} = 0.88$ .



**Figure 6.25** — Histograms corresponding to the measured data shown in Fig. 6.24.

tunings were chosen leading to an intra cavity power  $P$  of approximately 76 %, 82 %, 88 % and 90 % of the maximum power  $P_{\text{res}}$  obtained at resonance. Figure 6.27 compares the reconstructed Wigner functions. It can be seen, that the deamplification and amplification of the classical noise increases with the intra cavity power. Compared to the OPs on the shallow resonance slope, the OPs on the steep slope (top graphs) lead to higher (de-)amplification factors as expected from theory. Furthermore, moving the OP on the steep slope from strong detunings to low detunings (i.e. from  $P/P_{\text{res}} = 0.76$  towards  $P/P_{\text{res}} = 0.88$ ), the noise ellipse rotated counter clockwise . At the OP corresponding to

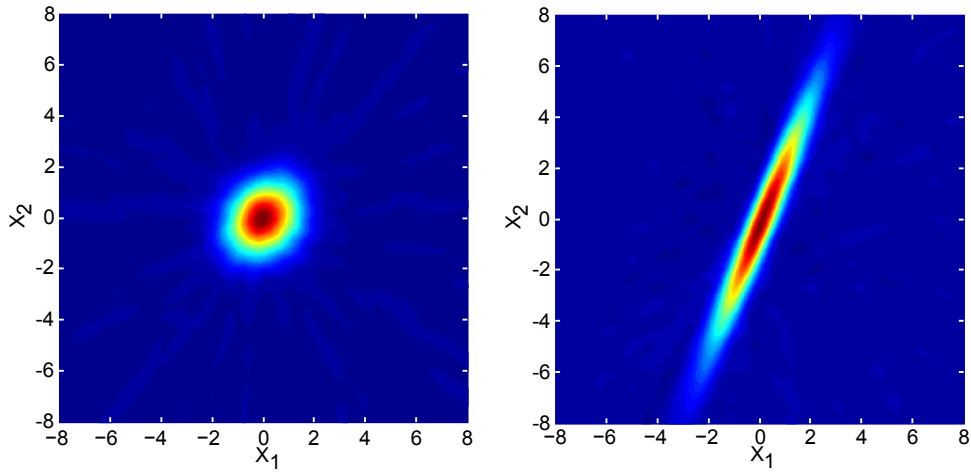


**Figure 6.26** — Reconstructed Wigner function corresponding to the noise distribution of the reference beam (left) and the beam reflected off the KNLR (right). The definition of the quadratures refers to the carrier field reflected off the KNLR, where  $X_1$  is the amplitude quadrature and  $X_2$  the phase quadrature.

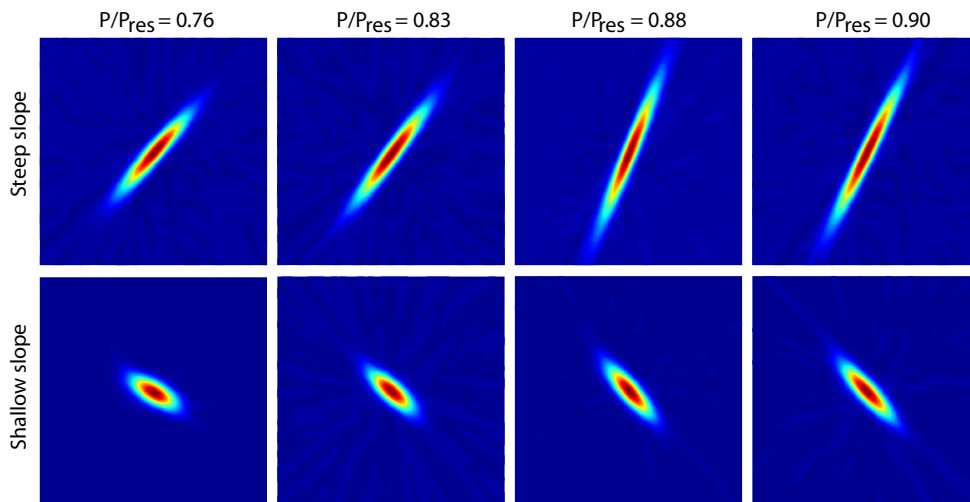


**Figure 6.27** — Comparison of the Wigner functions showing the noise transformation occurring at various OPs on the steep (top) and shallow (bottom) resonance slope.

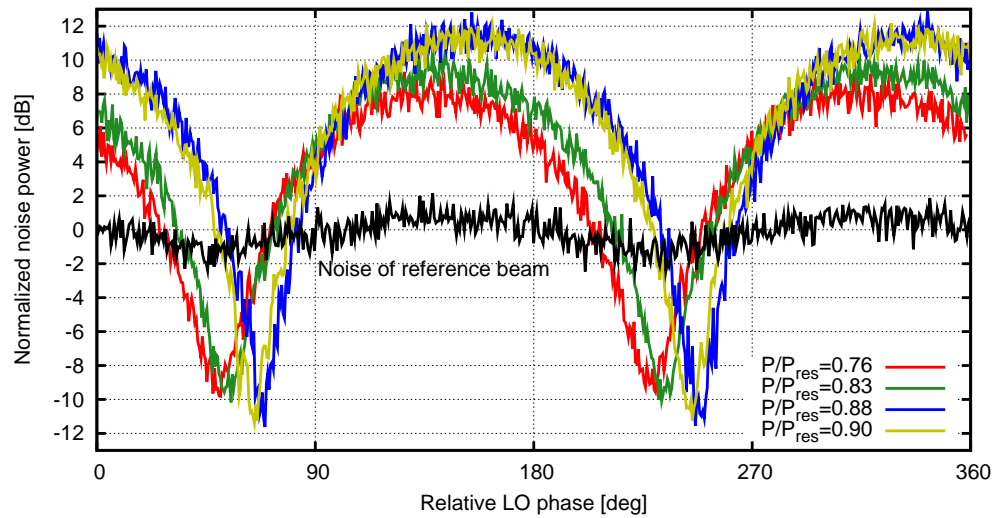


**Figure 6.28** — The figure shows the noise power depending on the relative detection angle (RBW=200 kHz, VBW=500 Hz). The initial beam was reflected off the KNLR that was operated on the steep resonance slope. The readout of the amplitude quadrature corresponds to the angles of  $90^\circ$  and  $270^\circ$ . A deamplification level of about 11 dB was achieved at  $P/P_{\text{res}} = 0.88$  and  $P/P_{\text{res}} = 0.90$ . For all traces the respective (de-)amplification factors are almost equal.

$P/P_{\text{res}} = 0.90$  the ellipse rotated again clockwise. This characteristic can be observed in reversed orientation for the OPs on the shallow resonance slope.

#### 6.7.4 Discussion of the results

As a main result it could be deduced that the (de-)amplification factors obtained at a certain OP are of the same order. Thus, no considerable excess noise is induced due to the noise transformation in the KNLR at the investigated sideband frequency of 1 MHz. For illustration purposes Figure 6.28 shows the quadrature dependent noise power obtained at the OPs on the steep resonance slope. A maximum deamplification of about 11 dB was achieved. Secondly it was shown that the amplitude quadrature (related to the relative LO phase of  $90^\circ$ ) of the reflected carrier field is *amplified* at the investigated OPs. Since the input power was set to 500 mW for these measurements, the critical state at which the amplitude quadrature is optimally squeezed was not reached. However, the measurements presented in Fig. 6.22 clearly show the achievable laser power noise reduction when the KNLR is operated very

close to the critical state (magenta curve). A theoretical investigation adapted to these two different experimental situations revealed, that the obtained (de-)amplification factors as well as the observed phase-space rotation can be qualitatively recovered with a theoretical model [110].

## 6.8 Conclusions

In the proof of principle experiment presented in this Chapter it was shown that a Kerr non-linear resonator can efficiently be used for the spectral power noise reduction of a continuous-wave laser beam *within* the bandwidth of the resonator. A strong power noise reduction of up to 32 dB at a frequency corresponding to about one fifth of the resonators bandwidth and below was demonstrated. Such a high value of noise suppression from the Kerr effect has not been reported before for continuous-wave laser light. The noise reduction technique presented here can be combined with standard techniques like passive filtering through mode cleaner cavities. But in particular for high laser powers and for amplitude noise at rather low Fourier frequencies, say the kHz regime and below, the technique investigated here proves to be rather powerful. It allows for a strong noise reduction at frequencies much smaller than the cavity linewidth, without photo-electric detection of a considerable fraction of the laser beam. In future work, the presented technique can be used for the noise suppression of the new generation of single-mode high-power lasers for advanced gravitational-wave detectors. These lasers provide powers of up to 200 W whereby the noise reduction by means of a KNLR will prove to be even more powerful. Since a smaller enhancement of the input power is required, the finesse can be relaxed and optical loss thus be reduced. Additionally, for these high input powers the intra cavity power will be about two order of magnitudes higher compared to those in the actual experiment. Accordingly, the third-order non-linearity of high quality optical materials like fused silica might be sufficient to reach the critical state and thus the targeted noise suppression.

Although a strong effective third order non-linearity was achieved and a huge noise reduction in the classical regime was observed, the deamplified noise was still far above the shot-noise limit. In order to demonstrate the power noise reduction of the input laser, at first it was necessary to reach the critical state of the KNLR. Accordingly, a comparatively high finesse was required leading to a narrow bandwidth of about 4.5 MHz. This resulted in an escape efficiency  $\eta_{\text{esc}} = T_c / (T_c + L_{\text{rt}})$  of about 0.77, where  $T_c$  is the power

transmittance of the coupling mirror and  $L_{rt}$  the round-trip loss. Accordingly, a maximum squeezing of about 6 dB can be expected assuming that infinite squeezing is generated inside the KNLR. At frequencies above the bandwidth of the KNLR, the squeezing is further reduced. As the laser carries an enormous amount of classical noise around and below its relaxation oscillation, the squeezing possibly generated was masked at frequencies within the bandwidth of the KNLR. At higher frequencies where the laser noise could be reduced, the low pass characteristic of the KNLR limited the achievable squeezing strength. Further loss was introduced in the homodyne read-out scheme due to a imperfect visibility and the imperfect quantum efficiency of the photo diodes. Additionally, the observed excess noise presumably caused by internal Brillouin scattering contributed to the noise of the beam reflected off the KNLR. For these reasons the squeezing of quantum noise could not be observed. In order to beat the shot-noise limit for continuous-wave radiation in future experiments Fourier frequencies far above the lasers relaxation oscillation need to be considered. Thus, the bandwidth of the KNLR needs to be adapted. Additionally, the input power has to be reduced in order to get closer to the shot-noise limit from the very beginning. A reduction of the input power and the finesse then requires materials with stronger non-linearities, for example periodically poled second-order non-linear crystals, and a tighter focusing.

---

## Summary and Outlook

The purpose of this thesis was the theoretical and experimental investigation of advanced interferometric techniques applicable especially for future gravitational-wave detectors. Two aspects that can lead to an improved sensitivity of these detectors were treated: the optimization of the interferometer topology itself with respect to an improved signal transfer function, and second the reduction of noise sources. The former was focused on advanced power- and signal-recycling techniques while the latter considered the quantum noise reduction by squeezed field injection and the pure optical passive laser power noise reduction by means of a Kerr non-linear resonator.

A comprehensive analysis and visualization of the resonance structure of linearly coupled resonators was presented. Analytical expressions were derived which allow systematically parameter studies and the adaptation of the frequency response of coupled optical resonators to the requirements. Based on this investigations the shot noise limited sensitivity of the four-mirror cavity enhanced Michelson interferometer could be analyzed systematically despite a huge 11-dimensional parameter space (see Chapter 3). The study revealed, that in this topology the featured resonance doublet could not be exploited optimally. As the resonance condition of the carrier field and the sideband fields are coupled, the carrier light enhancement and the transfer function for signal sidebands could not be optimized independently. Contrary to expectations, the *tunable* frequency splitting lead to considerable sensitivities only at narrowband resonance frequencies.

In Chapter 4 a novel Twin-Signal-Recycling interferometer technique was proposed and investigated for the use as squeezed light enhanced gravitational-wave detector. It was shown, that this topology has an intrinsic increased

signal to noise ratio compared to signal sideband recycling techniques like SR and RSE. Additionally, the squeezed field injection is less demanding as no additional filter cavities are required for a broadband shot noise reduction. Likewise, the gravitational-wave signal is detected optimally by a frequency independent read-out of the carrier lights phase quadrature. Such a frequency independent DC readout (self-homodyning) is targeted for future gravitational-wave detector because it provides an improved signal to noise ratio compared to the currently established heterodyne readout schemes [72]. Especially in view of squeezed field injection it is favorable [69].

The first experimental demonstration of a broadband shot noise reduction in a Michelson interferometer with TSR was presented in Chapter 5. By means of extensive accompanying simulations it was possible to upgrade an existing experimental infrastructure of a dual-recycled Michelson interferometer [41]. A broadband shot noise reduction by a factor of up to 4 dB was demonstrated whereby the measurements were in good agreement with the numerical simulations.

The TSR technique came already into consideration for the GEO-HF detector [40]. Implementation issues and expected sensitivities were studied in [87] and reviewed in Sec. 4.5 of this thesis. It was shown, that the enhancement achievable with a TSR configuration will be masked by thermal noise in the mid-frequency detection band. Nevertheless, a proper parameter choice allows to adapt the sensitivity curve optimally to the thermal noise as shown in Fig. 4.10. Compared to a tuned SR configuration a slightly improved sensitivity at frequencies up to approximately 5 kHz can be achieved.

In conclusion, under consideration of the thermal noise TSR might find applications where high, narrowband sensitivities are required at even higher frequencies in the detection band which could not be covered with tuned SR. At a point, where the thermal noise can be reduced by the realization of cryogenic test-masses or coating free mirrors as well as an elongation of the interferometer arms, TSR can also lead to considerable sensitivities in the low and mid-frequency detection band. Additionally it was shown, that the sensitivity of a TRSE topology as exemplary shown in Fig. 4.11 yields a considerable improvement around a certain resonance frequency when compared to the RSE topology as targeted for the next generation of gravitational-wave detectors.

In Chapter 6 the capability of a Kerr non-linear resonator for a passive laser power noise reduction was demonstrated in a proof of principle experiment. Several experiments were performed to characterize the resonator whereby suitable settings for a laser power noise reduction could be determined based

on a comparison of the measurements with numerical simulations. A huge noise suppression of up to 32 dB could be achieved for a continuous-wave laser beam for the first time by exploiting the optical Kerr effect. These results implied that a Kerr non-linear resonator is applicable to a pure optical noise reduction in the field of advanced gravitational-wave detectors where stable high-power lasers are required.



---

## Matlab scripts

### A.1 Noise spectral densities for GEO 600 with squeezed input

With the following matlab script the noise spectral densities of GEO 600 was calculated using the input-output formalism. This script was originally developed by Jan Harms and adapted within this thesis for the comparison with the TSR interferometer.

```
1 clear;
2 %physical constants
3 c=299792458;
4 hbar=1.054e-34;
5 %carrier light angular frequency
6 w0=1.77e15;
7
8 %design parameters GEw0600
9 m=5.6; %Mirror mass
10 L=1200; %Interferometer arm length
11 Pin=10; %Input power
12 %Power at beam splitter (PR gain=1000)
13 Pbs=1000*Pin;
14 %Power in each interferometer arm
15 Parm=0.5*Pbs;
16
17 %Interferometer end mirrors
```

```

18 rend=sqrt(0.99995);
19 tend=sqrt(1-rend^2);
20 %SR Mirror
21 rsr=sqrt(0.99);
22 tsr=sqrt(1-rsr^2);
23
24 %Traget frequency [Hz]
25 ftar=2000.0
26 %corresponding SRC detuning
27 phi=(2*pi*ftar*L/c);
28
29 %Frequency range [10^fmin:10^fmax]
30 fmin=1;
31 fmax=4;
32 %calculation steps
33 steps=2000;
34
35 %Identity matrix
36 Ein=[1 0; 0 1];
37
38 %Detection angle of homodyne readout
39 zetaX1=0; %Amplitude Quadrature;
40 zetaX2=pi/2;%Phase Quadrature;
41
42 %Description of Squeezing
43 r=1; %squeezing parameter
44 sphi=pi*1; %Squeezed quadratur
45 %Squeezing matrix
46 SQ=[cosh(r)+sinh(r)*cos(2*sphi), sinh(r)*sin(2*sphi);
47     sinh(r)*sin(2*sphi) cosh(r)-sinh(r)*cos(2*sphi)];
48
49 %Vector for data storage
50 data=[];
51
52 for f=logspace(fmin,fmax,2000)
53
54 %SQL for GEO600
55 h=sqrt(20*hbar/m/L^2/(2*pi*f)^2);

```

```

56 %optomechanical coupling
57 K=4*Parm*w0/(m/5)/c^2/(2*pi*f)^2;
58 KM=[1 0;-K 1];
59
60 %Propagation matrix
61 Psr=[cos(phi) -sin(phi); sin(phi) cos(phi)]*exp(i*2*pi*f*L/c);
62
63
64 %field enhancement in SRC
65 InSRC=tsr*inv(Ein-rsr*Psr*rend*KM*Psr);
66 %Reflexion at SRC
67 RhoSRC=(rsr*Ein-Psr*rend*KM*Psr)*inv(Ein-rsr*Psr*rend*KM*Psr);
68
69 %Reflexion of squeezed input
70 RHOsqz=RhoSRC*SQ;
71 %Loss: Shotnoise couples in at end-mirror
72 LOSS=tend*InSRC*Psr;
73 %Signal TF
74 Sig=2*InSRC*Psr*rend*KM*[0;1]*sqrt(2*K)/h;
75
76 %Spectral Densities
77 %Vacuum noise in reflexion of SRC
78 NSD = 1/2*(RhoSRC*transpose(conj(RhoSRC))+conj(RhoSRC)*(2
79     transpose(RhoSRC)));
80 %Squeezed vacuum noise in reflexion of SRC
81 NSDSQZ=1/2*(RHOsqz*transpose(conj(RHOsqz))+conj(RHOsqz) 2
82     *transpose(RHOsqz)); %Squeezing
83 %Loss (Imperfect end-mirror)
84 LSD = 1/2*(LOSS*transpose(conj(LOSS))+conj(LOSS) 2
85     *transpose(LOSS));
86
87 %Vacuum noise at detection port
88 NSDD = NSD + LSD;
89 NSDSQZD = NSDSQZ + LSD;
90 %Signal at output
91 SSD = 1/2*(Sig*transpose(conj(Sig))+conj(Sig)*transpose( 2
92     Sig))
93

```

```

94 %Homodyne detection
95 %Amplitude Quatrature
96 noutX1=[cos(zetaX1) sin(zetaX1)]*NSDD*[cos(zetaX1);sin(
97     zetaX1)];
98 noutSQZX1=[cos(zetaX1) sin(zetaX1)]*NSDSQZD*[cos(zetaX1)
99     ;sin(zetaX1)];
100 soutX1=[cos(zetaX1) sin(zetaX1)]*SSD*[cos(zetaX1);sin(
101     zetaX1)];
102
103 NtoSX1=sqrt(noutX1/(soutX1));
104 NSQZtoSX1=sqrt(noutSQZX1/(soutX1));
105
106 %Phase Quatrature
107 noutX2=[cos(zetaX2) sin(zetaX2)]*NSDD*[cos(zetaX2);sin(
108     zetaX2)];
109 noutSQZX2=[cos(zetaX2) sin(zetaX2)]*NSDSQZD*[cos(zetaX2)
110     ;sin(zetaX2)];
111 soutX2=[cos(zetaX2) sin(zetaX2)]*SSD*[cos(zetaX2);sin(
112     zetaX2)];
113
114 NtoSX2=sqrt(noutX2/(soutX2));
115 NSQZtoSX2=sqrt(noutSQZX2/(soutX2));
116
117 %Variational Readout according to
118 %Eq.(29) in Harms et.al. PRD 68 (2003)
119
120 Q11 = SSD(1,1)*(NSDD(1,2)+NSDD(2,1)) - NSDD(1,1)*(SSD(1,
121     2)+SSD(2,1));
122 Q12 = SSD(1,1)*NSDD(2,2) - NSDD(1,1)*SSD(2,2);
123 Q22 = NSDD(2,2)*(SSD(1,2)+SSD(2,1)) - SSD(2,2)*(NSDD(1,
124     2)+NSDD(2,1));
125 Q=[Q11 Q12; Q12 Q22];
126 %optimal detection angle (variational readout
127 %according to corrected Eq.(30) in Harms et.al. PRD 68
128     (
129     2003)
129 zetaVar = -acot(1/Q11*(sqrt(-det(Q))+Q12));
130

```

```

131 noutVar=[cos(zetaVar) sin(zetaVar)]*NSDD*[cos(zetaVar);
132         sin(zetaVar)];
133 noutSQZVar=[cos(zetaVar) sin(zetaVar)]*NSDSQZD*[cos(
134         zetaVar);sin(zetaVar)];
135 soutVar=[cos(zetaVar) sin(zetaVar)]*SSD*[cos(zetaVar);
136         sin(zetaVar)];
137
138 NtoSVar=sqrt(noutVar/(soutVar));
139 NSQZtoSVar=sqrt(noutSQZVar/(soutVar));
140
141 %fully frequency dependend squeezing according to
142 %Eq.(16) in Harms et.al. PRD 68 (2003)
143 %For amplitude quadrature
144 lambdaX1=atan(-(RhoSRC(1,1)*cos(zetaX1) + RhoSRC(2,1)
145         *sin(zetaX1))/(RhoSRC(1,2)*cos(zetaX1)+RhoSRC(
146         2,2)*sin(zetaX1)));
147 %For phase quadrature
148 lambdaX2=atan(-(RhoSRC(1,1)*cos(zetaX2) + RhoSRC(2,1)
149         *sin(zetaX2))/(RhoSRC(1,2)*cos(zetaX2)+RhoSRC(
150         2,2)*sin(zetaX2)));
151 %For squeezed-variational readout
152 lambdaVar=atan(-(RhoSRC(1,1)*cos(zetaVar) + RhoSRC(2,1)
153         *sin(zetaVar))/(RhoSRC(1,2)*cos(zetaVar)+
154         RhoSRC(2,2)*sin(zetaVar)));
155
156 %frequency dependent squeezing for detection of X1
157 SQX1fd=RhoSRC*[cosh(r)+sinh(r)*cos(2*lambdaX1), sinh(r)
158         *sin(2*lambdaX1); sinh(r)*sin(2*lambdaX1) cosh(r)
159         -sinh(r)*cos(2*lambdaX1)];
160 %frequency dependent squeezing for detection of X2
161 SQX2fd=RhoSRC*[cosh(r)+sinh(r)*cos(2*lambdaX2), sinh(r)
162         *sin(2*lambdaX2); sinh(r)*sin(2*lambdaX2) cosh(r)
163         -sinh(r)*cos(2*lambdaX2)];
164 %for squeezed-variational readout
165 SQVarfd=RhoSRC*[cosh(r)+sinh(r)*cos(2*lambdaVar), sinh(
166         r)*sin(2*lambdaVar); sinh(r)*sin(2*lambdaVar)
167         cosh(r)-sinh(r)*cos(2*lambdaVar)];
168

```

```

169 %noise spectral densities
170 NSDSQX1fd = 1/2*(SQX1fd*transpose(conj(SQX1fd))+conj(
171     SQX1fd)*transpose(SQX1fd)) + LSD;
172 NSDSQX2fd = 1/2*(SQX2fd*transpose(conj(SQX2fd))+conj(
173     SQX2fd)*transpose(SQX2fd)) + LSD;
174 NSDSQVarfd = 1/2*(SQVarfd*transpose(conj(SQVarfd))+conj(
175     SQVarfd)*transpose(SQVarfd)) + LSD;
176
177
178 noutX1fd = [cos(zetaX1) sin(zetaX1)]*NSDSQX1fd*[cos(
179     zetaX1);sin(zetaX1)];
180 NSQZtoSX1fd =sqrt(noutX1fd/soutX1);
181
182 noutX2fd = [cos(zetaX2) sin(zetaX2)]*NSDSQX2fd*[cos(
183     zetaX2);sin(zetaX2)];
184 NSQZtoSX2fd =sqrt(noutX2fd/soutX2);
185
186 noutVarfd = [cos(zetaVar) sin(zetaVar)]*NSDSQVarfd*[cos(
187     zetaVar);sin(zetaVar)];
188 NSQZtoSVarfd =sqrt(noutVarfd/soutVar);
189
190
191 data=[data; [NtoSX1 NSQZtoSX1 NSQZtoSX1fd NtoSX2
192     NSQZtoSX2 NSQZtoSX2fd NtoSVar NSQZtoSVar
193     NSQZtoSVarfd zetaVar lambdaVar]];
194 end;
195
196 figure(1)
197 x=logspace(fmin,fmax,2000);
198 loglog(x,data(:,1),x,data(:,2));
199 save('E:\aei-work\matlabs\forthesis\data-output\GEO600-
200     2k.dat','data','-ascii');

```

## A.2 Noise spectral densities for TSR

With the following matlab script the noise spectral densities of the TSR topology was calculated using the input-output formalism.

```

1 clear;
2 %physical constants
3 c=299792458;
4 hbar=1.054e-34;
5 %carrier light angular frequency
6 w0=1.77e15;
7
8 %design parameters GEw0600
9 m=5.6; %Mirror mass
10 L1=1200; %Interferometer/TSRC1 length
11 L2=1200; %TSRC2 length
12 Pin=10; %Input power
13 %Power at beam splitter (PR gain=1000)
14 Pbs=1000*Pin;
15 %Power in each interferometer arm
16 Parm=0.5*Pbs;
17
18 %Interferometer end mirrors
19 rend=sqrt(0.99995);
20 tend=sqrt(1-rend^2);
21 %Center mirror determining fsplit
22 fsplit=2*pi*1000;
23
24 rc=sqrt(4*cos(2*fsplit*L1/c)^2*rend^2/(1+rend^2)^2);
25 %rc=sqrt(0.99);
26 tc=sqrt(1-rc^2);
27
28 rtsr=sqrt(0.963);
29 ttsr=sqrt(1-rtsr^2);
30
31 phitsr1=0; %tuning of TSRC1
32 phitsr2=0; %tuning of TSRC2
33
34 %Frequency range [10^fmin:10^fmax]
35 fmin=1;
36 fmax=4;
37 %calculation steps
38 steps=2000;

```

```

39
40 %Identity matrix
41 Ein=[1 0; 0 1];
42
43 %Detection angle of homodyne readout
44 zetaX2=pi/2; %Phase Quadrature;
45
46 %Description of Squeezing
47 r=1; %squeezing parameter
48 sphi=0; %Squeezed quadratur
49 %Squeezing matrix
50 SQ=[cosh(r)+sinh(r)*cos(2*sphi), sinh(r)*sin(2*sphi);
51     sinh(r)*sin(2*sphi) cosh(r)-sinh(r)*cos(2*sphi)];
52
53 %Vector for data storage
54 data=[];
55
56 for f=logspace(fmin,fmax,2000)
57
58 %SQL for GEO600
59 h=sqrt(20*hbar/m/L1^2/(2*pi*f)^2);
60 %optomechanical coupling
61 K=4*Parm*w0/(m/5)/c^2/(2*pi*f)^2;
62 KM=[1 0;-K 1];
63
64 %Propagation matrices
65 Ptsr1=[cos(phitsr1) -sin(phitsr1); sin(phitsr1) cos(
66     phitsr1)]*exp(i*2*pi*f*L1/c);
67 Ptsr2=[cos(phitsr2) -sin(phitsr2); sin(phitsr2) cos(
68     phitsr2)]*exp(i*2*pi*f*L2/c);
69
70 %Reflexion at TSRC1
71 RhoTSR1=(rc*Ein-Ptsr1*rend*KM*Ptsr1)*inv(Ein-
72     rc*Ptsr1*rend*KM*Ptsr1);
73 %field enhancement in TSRC2
74 InTSRC2=ttsr*inv(Ein-rtsr*Ptsr2*RhoTSR1*Ptsr2);
75 %field enhancement in TSRC1
76 InTSRC1=tc*inv(Ein-rc*Ptsr1*rend*KM*Ptsr1)

```

```

77      *InTSRC2*Ptrsr2;
78 %Reflexion at TSRC2
79 RhoTSR=(-rtsr*Ein+Ptrsr2*RhoTSR1*Ptrsr2)*inv(Ein- 2
80      rtsr*Ptrsr2*RhoTSR1*Ptrsr2);
81 %Reflexion of squeezed input
82 RHOSqz=RhoTSR*SQ;
83 %Loss: Shotnoise couples in at end-mirror
84 LOSS=tend*InTSRC1*Ptrsr1;
85 %Signal TF
86 Sig=2*InTSRC1*Ptrsr1*rend*KM*[0;1]*sqrt(2*K)/h;
87
88 %Spectral Densities
89 %Vacuum noise in reflexion of SRC
90 NSD = 1/2*(RhoTSR*transpose(conj(RhoTSR))+conj(RhoTSR)*( 2
91      transpose(RhoTSR)));
92 %Squeezed vacuum noise in reflexion of SRC
93 NSDSQZ=1/2*(RHOSqz*transpose(conj(RHOSqz))+conj(RHOSqz) 2
94      *transpose(RHOSqz)); %Squeezing
95 %Loss (Imperfect end-mirror)
96 LSD = 1/2*(LOSS*transpose(conj(LOSS))+conj(LOSS) 2
97      *transpose(LOSS));
98
99 %Vacuum noise at detection port
100 NSDD = NSD + LSD;
101 NSDSQZD = NSDSQZ + LSD;
102 %Signal at output
103 SSD = 1/2*(Sig*transpose(conj(Sig))+conj(Sig)*transpose( 2
104      Sig))
105
106 %Homodyne detection
107 %Phase Quatrature
108 noutX2=[cos(zetaX2) sin(zetaX2)]*NSDD*[cos(zetaX2);sin( 2
109      zetaX2)];
110 noutSQZX2=[cos(zetaX2) sin(zetaX2)]*NSDSQZD*[cos(zetaX2) 2
111      ;sin(zetaX2)];
112 soutX2=[cos(zetaX2) sin(zetaX2)]*SSD*[cos(zetaX2);sin( 2
113      zetaX2)];
114

```

```

115 NtoSX2=sqrt(noutX2/(soutX2));
116 NSQZtoSX2=sqrt(noutSQZX2/(soutX2));
117
118 %fully frequency dependend squeezing according to
119 %Eq.(16) in Harms et.al. PRD 68 (2003)
120 %For phase quadrature
121 lambdaX2=atan(-(RhoTSR(1,1)*cos(zetaX2) + RhoTSR(2,1)
122             *sin(zetaX2))/(RhoTSR(1,2)*cos(zetaX2)+RhoTSR(
123             2,2)*sin(zetaX2)));
124
125 %frequency dependent squeezing for detection of X2
126 SQX2fd=RhoTSR*[cosh(r)+sinh(r)*cos(2*lambdaX2), sinh(r)
127             *sin(2*lambdaX2); sinh(r)*sin(2*lambdaX2) cosh(r)
128             -sinh(r)*cos(2*lambdaX2)];
129
130 %noise spectral densities
131 NSDSQX2fd = 1/2*(SQX2fd*transpose(conj(SQX2fd))+conj(
132             SQX2fd)*transpose(SQX2fd)) + LSD;
133 noutX2fd = [cos(zetaX2) sin(zetaX2)]*NSDSQX2fd*[cos(
134             zetaX2);sin(zetaX2)];
135 NSQZtoSX2fd =sqrt(noutX2fd/soutX2);
136
137
138 data=[data; [NtoSX2 NSQZtoSX2 NSQZtoSX2fd lambdaX2]];
139 end;
140
141 figure(1)
142 x=logspace(fmin,fmax,2000);
143 loglog(x,data(:,1),x,data(:,2), x,data(:,3));
144
145 figure(2)
146 semilogx(x,data(:,4));
147
148 save('E:\aei-work\matlabs\forthesis\data-output\TSR-OPv. 2
149     dat','data','-ascii');

```

---

## FINESSE simulation for the TSR experiment

The following FINESSE script was written to investigate the control scheme for the table-top TSR interferometer.

```
1 #####
2 # .kat-file for simulating a tabletop experiment #
3 #     investigating properties of #
4 #     DETUNED TWIN-SIGNAL-RECYCLING #
5 # A.Thuering 05.03.0 #
6 #####
7
8
9 ##### HIGHER ORDER MODES #####
10 maxtem 3
11 gauss inputbeam PRM nprm2 499.85666e-6 -314.90741e-3
12
13 ##### Parameter Declaration #####
14
15 #----- Power-Recycling-Mirror PRM -----
16 const RPRM 0.9 #Power Reflexion
17 const TPRM 0.1 #Power Transmission
18 const RCPRM -2 #Radius of Curvature
19 const dxPRM -4e-5 #misalignment of x
20 const dyPRM 4e-5 #misalignment of y
```

```

21
22 #----- Signal-Recycling-Mirror SRM -----
23 const RSRM 0.9          #Power Reflexion
24 const TSRM 0.1          #Power Transmission
25 const RCSR 2            #Radius of Curvature
26 const dxSRM -3e-5      #misalignment of x
27 const dySRM 5e-5       #misalignment of y
28
29 #----- Twin-Signal-Recycling-Mirror TSRM -----
30 const RTSRM 0.95        #Power Reflexion
31 const TTSRM 0.05        #Power Transmission
32 const RCTSRM 1.87       #Radius of Curvature
33 const dxTSRM 3e-5       #misalignment in x
34 const dyTSRM 1e-5       #misalignment in y
35
36 #----- Interferometer End-Mirrors -----
37 const REND1 0.999        #Power Reflexion
38 const TEND1 0.0008       #Power Transmission
39 const REND2 0.9992       #Power Reflexion
40 const TEND2 0.0008       #Power Transmission
41 const RCEND 1.5         #Radius of Curvature
42 const dxEND1 -8e-6       #misalignment in x
43 const dyEND1 8e-6        #misalignment in y
44 const dxEND2 0e-5        #misalignment in x
45 const dyEND2 0e-5        #misalignment in y
46
47 #----- cavity lengths -----
48 const LPRC 0.21          #Distance PRM to BS
49 const LSRC 0.21          #Distance SRM to BS
50 const LTSRC 1.21         #Length of TSRCavity
51
52 const IFOARM1 1.00        #Interferometer Arms
53 const IFOARM2 1.007      #7mm SchnuppAsymetry
54
55 #----- modulation frequencies -----
56 const fmod1 15M
57 const fmod2 123.13121M
58 const fmod3 234.3874M

```

```

59
60 #----- Input Optics -----
61 l laser 1 0 n1
62 mod eom1 $fmod1 0.2 2 pm n1 n2
63 mod eom2 $fmod2 0.2 2 pm n2 n3
64 mod eom3 $fmod3 0.2 2 pm n3 n4
65 bs splitLO 0.00 1 0 0 n4 tohomobs toifo dumpB
66 s toPRM 1 toifo nprm1
67 #-----
68
69 #####
70 #           The TSR-Interferometer           #
71 #####
72
73 m PRM $RPRM $TPRM 180.0 nprm1 nprm2 #PR Mirror
74 attr PRM RC $RCPRM #Radius of Curvature
75 attr PRM xbeta $dxPRM #Misalignment in x
76 attr PRM ybeta $dyPRM #Misalignment in y
77 s PRC $LPRC nprm2 nbs1 #Distance to BS
78
79 #----- Interferometers Beamsplitter -----
80 bs MainBS 0.5 0.5 0 45 nbs1 narm1 narm2 toSRMa
81 #----- AR-Coating of the Beamsplitter -----
82 bs BSAR-darkport 0.003 0.997 0 45
83           toSRMa pickoff toSRM pickoff2
84
85 s ARM1 $IFOARM1 narm1 narm1end #1st Ifo Arm
86 s ARM2 $IFOARM2 narm2 narm2end #2nd Ifo Arm
87 m END1 $REND1 $TEND1 180.0
88           narm1end narm1trans #1st Endmirror
89 m END2 $REND2 $TEND2 270.0
90           narm2end narm2trans #2nd Endmirror
91
92 attr END1 RC $RCEND #Radius of Curvature
93 attr END1 xbeta $dxEND1 #Misalignment in x
94 attr END1 ybeta $dyEND1 #Misalignment in y
95
96 attr END2 RC $RCEND #Radius of Curvature

```

```

97 attr END2 xbeta $dxEND2      #Misalignment in x
98 attr END2 ybeta $dyEND2      #Misalignment in y
99
100
101 s SRC $LSRC toSRM nsrm1      #Distance SRM to BS
102 m SRM $RSRM $TSRM 0 nsrm1 nsrm2 #Signal-Recycling-Mirror
103 attr SRM RC $RCSR           #Radius of Curvature
104 attr SRM xbeta $dxSRM       #Misalignment in x
105 attr SRM ybeta $dySRM       #Misalignemnt in y
106
107 s TSRC $LTSRC nsrm2 ntsrm1    #TSR-Cavity length
108 m TSRM $RTSRM $TTSRM 0 ntsrm1 detectionport #TSR-Mirror
109 attr TSRM RC $RCTSRM        #Radius of Curvature
110 attr TSRM xbeta $dxTSRM     #Misalignment in x
111 attr TSRM ybeta $dyTSRM     #Misalignment in y
112
113 #####
114 #####
115
116 ##### cavity tracing #####
117
118 trace 2
119 cav PRC1 PRM nprm2 END1 narm1end #PRC build with END1
120 cav PRC2 PRM nprm2 END2 narm2end #PRC build with END2
121 cav SRC1 SRM nsrm1 END1 narm1end #SRC build with END1
122 cav SRC2 SRM nsrm1 END2 narm2end #SRC build with END2
123 cav TSRC SRM nsrm2 TSRM ntsrm1   #TSR-Cavity
124
125 retrace off
126
127
128
129 #####
130 #                               ErrorSignals                               #
131 #####
132
133 pd1 PRC-LOCK $fmod1 0 nprm1      #15MHz in refl for PRC
134 pd1 SRC-LOCK $fmod2 90 nprm1     #123.5MHz in Refl for SRC

```

```

135 scale 0.01 PRC-LOCK
136 scale 0.01 SRC-LOCK
137 pd1 TSR-LOCK $fmod2 0 narmitrans
138             #123.5MHz in transmission of
139             #MI-endmirror for TSRC
140
141 #####
142 func negative = $x1 * (-1)+90
143 noplot negative
144 func common = $x1 +90
145 noplot common
146 func sync = $x1 * 2.0 # +2.56
147 noplot sync
148 #####
149
150 #####
151 #             commands             #
152 #####
153
154 #xaxis END1 phi lin 0 360 1000      #sweeps tuning of END1
155 #put END2 phi $common              #sweeps tuning of END2
156 #put PRM phi $x1                  #in common mode with END1
157                                   #-> PRC is scanned
158
159 #put END2 phi $negative            #sweeps tuning of END2
160                                   #in differential mode with END1
161                                   #-> Darkport is scanned
162
163
164 xaxis SRM phi lin -360 -0 400      #sweeps tuning of SRM
165 put TSRM phi $x1                  #sweeps tuning of TSRM in
166 #put TSRM phi $sync              #in common mode with SRM
167                                   #-> SRC is scanned
168
169 #xaxis TSRM phi lin -90 270 1000   #sweeps tuning of TSRM
170                                   #-> TSRC is scanned
171 #x2axis TSRM phi lin -150 250 1000
172 #x2axis eom2 f lin 123.5M 123.6M 100

```

```
173 #put SRC-LOCK f $x2
174
175 #xaxis ccd x lin -6 6 100
176 #x2axis ccd y lin -6 6 100
177 yaxis abs
178
179 #gnuterm NO
180
181 GNUPLOT
182 #set log y
183 #set yrange [-1e-4:1e-4]
184 END
```

---

## Investigation of a scanned 3rd-order non-linear resonator

With the following C-script the dynamics of a 3rd-order non-linear resonator was calculated.

```
1 #include "./headers/header.h"
2
3 main()
4 {
5     //data files
6     FILE *out;
7     FILE *index;
8     FILE *gnu;
9
10    int i,j, di;
11
12    //fields inside and in reflexion of the resonator
13    _Complex double at1, at2, R;
14    _Complex double A;
15
16    //Reflectivities of cavity mirrors
17    extern double rho1, tau1;
18    extern double rho2, tau2;
19    extern double P;
20
```

```

21 //optical and geometric length of the resonator
22 double phit2, phigeo;
23
24 //effective kerr non-linearity
25 double x3;
26
27 int steps;
28 int nos;
29 double sweep;
30 double dt, dT;
31 double phimin, phimax;
32 double dphif, dphib;
33 double prop;
34 double trt;
35
36 double dPdt, dPdt1;
37
38 double f[5];
39 int n;
40
41 /* Scanning one FSR with nu [lamda/s]*/
42 f[0]=100.0;
43 f[1]=200.0;
44 f[2]=500.0;
45 f[3]=1000.0;
46 f[4]=2000.0;
47
48 // Input Power [W]
49 P=1.0;
50
51 // round-trip time of the resonator
52 trt=2.0*L/c;
53 // time step for calculation
54 dt=trt;
55
56 // tuning range
57 phimin=-2/180.0*M_PI;
58 phimax=2.0/180.0*M_PI;

```

```

59     dphif=phimax-phimin;      //forward scan
60     dphib=phimin-phimax;     //backward scan
61
62     // Reflectivities of the non-linear cavity
63     rho1=sqrt(0.983);
64     tau1=sqrt(1.0 - rho1*rho1);
65     // rho2 includes roundtrip loss
66     rho2=sqrt(0.9992-0.004);
67     tau2=sqrt(1.0 - rho2*rho2);
68
69     // dispersion
70     prop=omega*L/c;
71
72     // effective x3 gives theta = Pin/waist^2*x3
73     x3=-5.9e-14; // [W/m^2]
74
75     // calculation of static Airypeak
76     solve_intrafield(x3);
77
78     out=fopen("./data-output/forw.dat","w");
79     index=fopen("./data-output/n-forw.dat","w");
80
81     /***** scanning forward *****/
82     nos = 5;
83     for(j = 0; j < nos; j++)
84     {
85         // scan velocity [rad/s]
86         sweep=f[j]*2*M.PI;
87         // time needed to scan tuning range dphi
88         dT=((phimax-phimin))/sweep;
89         // stepsize needs to be dt=storage time
90         steps=(int)ceil(dT/(trt));
91
92         di=(int)(steps)/(1000);
93
94         // static intra cavity field at t=0
95         at1=I*tau1*sqrt(P)
96             /(1.0-rho2*rho1*cexp(2*I*(phimin)));

```

```

97     A=at1;
98
99     fprintf(out, "\n");
100    fprintf(index, "\n");
101    // index of n-th maximum reset to zero
102    n=0;
103
104    for(i = 1; i < steps+1; i++)
105    {
106        // optical microscopic length at t = dt*i
107        phit2=phimin+dphif/steps*i+x3*cabs(A)*cabs(A)/
108            pow(waist,2);
109        // corresponding geometric length
110        phigeo=phimin+dphif/steps*i;
111
112        dPdt=cabs(A)*cabs(A);
113
114        // Intra cavity field at t = dt*i
115        A=I*tau1*sqrt(P)+rho2*rho1*cexp(2*I*phit2)*A;
116        // Reflected field at t = dt*i
117        R=sqrt(P)*rho1+I*tau1*A;
118        //dP/dt needed for finding n-th extreme value
119        dPdt=(cabs(A)*cabs(A)-dPdt);
120
121        // index of nth-maximum in ringing
122        if(((dPdt <= 0 && dPdt1 >= 0) ||
123            (dPdt >= 0 && dPdt1 <= 0)) &&
124            //avoid numerical ringing
125            i >= steps/3.0)
126        {
127            n+=1;
128            fprintf(index, "\n%e\t%d\t%e\t%e",
129                (dt*i+dt*(i-1))/2.0,
130                n, cabs(A)*cabs(A), 0.0);
131        }
132        // just save each 1000th calculation step
133        // to assure a manageable file size
134        if(i % di == 0)

```

```
135     fprintf(out, "\n%e\t%e\t%e\t%e\t%e",
136             (phigeo)/M_PI*180.0,
137             dt*i, cabs(A)*cabs(A),
138             pow(cabs(R),2.0),
139             dPdt, phit2/M_PI*180.0);
140
141     dPdt1=dPdt;
142 }
143 }
144 fclose(out);
145 fclose(index);
146
147 return 0;
148
149 }
```



# Bibliography

- [1] A. Einstein, "On gravitational waves," *Sitzungsbericht Preuss. Akad. Wiss. Berlin* p. 154 (1918).
- [2] A. Einstein, "Approximative integration of the field equations of gravitation," *Sitzungsbericht Preuss. Akad. Wiss. Berlin* p. 688 (1916).
- [3] R. A. Hulse, "The discovery of the binary pulsar (psr 1913+16)," *Rev. Mod. Phys.* **66**, 699–710 (1994).
- [4] J. H. Taylor, "Binary pulsars and relativistic gravity," *Rev. Mod. Phys.* **66**, 711–719 (1994).
- [5] P. Astone, "Resonant mass detectors: present status," *Classical and Quantum Gravity* **19**, 1227–1235 (2002).
- [6] <http://sci.esa.int/home/lisa/>
- [7] R. W. P. Drever, J. Hough, A. J. Munley, S.-A. Lee, R. Spero, S. E. Whitecomb, H. Ward, G. M. Ford, M. Hereld, N. Robertson, I. Kerr, J. R. Pugh, G. P. Newton, B. Meers, E. D. B. III, and Y. Grüsel, *Quantum Optics, Experimental Gravitation and Measurement Theory* (Plenum Press, New York, 1983). P.321.
- [8] B. J. Meers, "Recycling in laser-interferometric gravitational-wave detectors," *Phys. Rev. D* **38**, 2317–2326 (1988).
- [9] <http://gw.icrr.u-tokyo.ac.jp:8888/lcgt/>
- [10] S. Rowan, J. Hough, and D. R. M. Crooks, "Thermal noise and material issues for gravitational wave detectors," *Phys. Lett. A* (2005).
- [11] Y. T. Liu and K. S. Thorne, "Thermoelastic noise and homogeneous thermal noise in finite sized gravitational-wave test masses," *Phys. Rev. D* **62**, 122002 (2000).

- [12] V. A. Braginsky and S. P. Vyatchanin, "Frequency fluctuations of nonlinear origin in self-sustained optical oscillators," *Phys. Lett. A* (2001).
- [13] V. A. Braginsky, M. L. Gorodetsky, and S. P. Vyatchanin, "Thermodynamical fluctuations and photo-thermal shot noise in gravitational wave antennae," *Phys. Lett. A* (1999).
- [14] S. G. Ier, J. Cumpston, K. McKenzie, C. M. Mow-Lowry, M. B. Gray, and D. E. McClelland, "Coating-free mirrors for high precision interferometric experiments," *Physical Review A (Atomic, Molecular, and Optical Physics)* **76**, 053810 (2007).
- [15] V. B. Braginsky and F. Y. Khalili, *Quantum Measurements* (Cambridge University Press, 1992).
- [16] A. Weinstein, "Advanced ligo optical configuration and prototyping effort," *Class. Quantum Grav.* **19**, 1575–1584 (2002).
- [17] W. Winkler, K. Danzmann, A. Rüdiger, and R. Schilling, "Heating by optical absorption and the performance of interferometric gravitational-wave detectors," *Phys. Rev. A* **44**, 7022–7036 (1991).
- [18] K. A. Strain, K. Danzmann, J. Mizuno, P. G. Nelson, A. Rüdiger, R. Schilling, and W. Winkler, "Thermal lensing in recycling interferometric gravitational wave detectors," *Phys. Lett. A* **194**, 124–132 (1994).
- [19] H. Lück, K.-O. Müller, P. Aufmuth, and K. Danzmann, "Correction of wavefront distortions by means of thermally adaptive optics," *Opt. Comm* **175**, 275–287 (2000).
- [20] R. Lawrence, M. Zucker, P. Fritschel, P. Marfuta, and D. Shoemaker, "Adaptive thermal compensation of test masses in advanced ligo," *Classical and Quantum Gravity* **19**, 1803–1812 (2002).
- [21] R. Lawrence, D. Ottaway, M. Zucker, and P. Fritschel, "Active correction of thermal lensing through external radiative thermal actuation," *Opt. Lett.* **29**, 2635–2637 (2004).
- [22] J. Degallaix, C. Zhao, L. Ju, and D. Blair, "Thermal lensing compensation for aigo high optical power test facility," *Classical and Quantum Gravity* **21**, S903–S908 (2004).

- [23] T. Tomaru, T. Suzuki, S. Miyoki, T. Uchiyama, C. T. Taylor, A. Yamamoto, T. Shintomi, M. Ohashi, and K. Kuroda, "Thermal lensing in cryogenic sapphire substrates," *Classical and Quantum Gravity* **19**, 2045–2049 (2002).
- [24] R. W. P. Drever, *Proceedings of the Seventh Marcel Grossman Meeting on General Relativity* (World Scientific, Singapore, 1995).
- [25] F. Seifert, P. Kwee, M. Heurs, B. Willke, and K. Danzmann, "Laser power stabilization for second-generation gravitational wave detectors," *Opt. Lett.* **31**, 2000–2002 (2006).
- [26] P. Kwee, B. Willke, and K. Danzmann, "Optical ac coupling to overcome limitations in the detection of optical power fluctuations," *Opt. Lett.* **33**, 1509–1511 (2008).
- [27] A. F. Pace, M. J. Collett, and D. F. Walls, "Quantum limits in interferometric detection of gravitational radiation," *Phys. Rev. A* **47**, 3173–3189 (1993).
- [28] H. Rehbein, J. Harms, R. Schnabel, and K. Danzmann, "Optical transfer functions of kerr nonlinear cavities and interferometers," *Physical Review Letters* **95**, 193001 (2005).
- [29] S. Reynaud, C. Fabre, E. Giacobino, and A. Heidmann, "Photon noise reduction by passive optical bistable systems," *Phys. Rev. A* **40**, 1440–1446 (1989).
- [30] M. Kitagawa and Y. Yamamoto, "Number-phase minimum-uncertainty state with reduced number uncertainty in a kerr nonlinear interferometer," *Phys. Rev. A* **34**, 3974–3988 (1986).
- [31] J. Mizuno, K. A. Strain, P. G. Nelson, J. M. Chen, R. Schilling, A. Rüdiger, W. Winkler, and K. Danzmann, "Resonant sideband extraction: a new configuration for interferometric gravitational wave detectors," *Phys. Lett A* **175**, 273–276 (1993).
- [32] C. M. Caves, "Quantum-mechanical noise in an interferometer," *Phys. Rev. D* **23**, 1693–1708 (1981).
- [33] H. Vahlbruch, S. Chelkowski, B. Hage, A. Franzen, K. Danzmann, and R. Schnabel, "Coherent control of vacuum squeezing in the gravitational-wave detection band," *Physical Review Letters* **97**, 011101 (2006).

- [34] H. Vahlbruch, M. Mehmet, S. Chelkowski, B. Hage, A. Franzen, N. Lastzka, S. G. Iyer, K. Danzmann, and R. Schnabel, "Observation of squeezed light with 10-dB quantum-noise reduction," *Physical Review Letters* **100**, 033602 (2008).
- [35] K. Goda, O. Miyakawa, E. E. Mikhailov, S. Saraf, R. Adhikari, K. McKenzie, R. Ward, S. Vass, A. J. Weinstein, and N. Mavalvala, "A quantum-enhanced prototype gravitational-wave detector," *Nat. Phys.* (2008).
- [36] W. G. Unruh, *Quantum Optics, Experimental Gravitation and Measurement Theory* (Plenum, New York, 1982), chap. 6, p. 647.
- [37] H. P. Yuen, "Contractive states and the standard quantum limit for monitoring free-mass positions," *Phys. Rev. Lett.* **51**, 719–722 (1983).
- [38] M. T. Jaekel and S. Reynaud, "Quantum limits in interferometric measurements," *EPL (Europhysics Letters)* **13**, 301–306 (1990).
- [39] H. J. Kimble, Y. Levin, A. B. Matsko, K. S. Thorne, and S. P. Vyatchanin, "Conversion of conventional gravitational-wave interferometers into quantum nondemolition interferometers by modifying their input and/or output optics," *Phys. Rev. D* **65**, 022002 (2001).
- [40] B. Willke *et al.*, "The geo-hf project," *Classical and Quantum Gravity* **23**, S207–S214 (2006).
- [41] H. Vahlbruch, S. Chelkowski, B. Hage, A. Franzen, K. Danzmann, and R. Schnabel, "Demonstration of a squeezed-light-enhanced power- and signal-recycled michelson interferometer," *Phys. Rev. Lett.* **95**, 211102 (2005).
- [42] A. G. White, J. Mlynek, and S. Schiller, "Cascaded second-order nonlinearity in an optical cavity," *EPL (Europhysics Letters)* **35**, 425–430 (1996).
- [43] H. Kogelnik and T. Li, "Laser beams and resonators," *IEEE* (1966).
- [44] J. Poirson, F. Bretenaker, M. Vallet, and A. L. Floch, "Analytical and experimental study of ringing effects in a fabry–perot cavity. application to the measurement of high finesse," *J. Opt. Soc. Am. B* **14**, 2811–2817 (1997).

- [45] M. Malec, "Commissioning of advanced, dual-recycled gravitational-wave detectors: simulations of complex optical systems guided by the phasor picture," Ph.D. thesis, Universität Hannover (2006).
- [46] L. Matone, M. Barsuglia, F. Bondu, F. Cavalier, H. Heitmann, and N. Man, "Finesse and mirror speed measurement for a suspended fabryperot cavity using the ringing effect," *Phys. Lett. A* (2000).
- [47] J. Mizuno, "Comparison of optical configurations for laser-interferometric gravitational-wave detectors," Ph.D. thesis, Universität Hannover (1995).
- [48] S. Hild and A. Freise, "A novel concept for increasing the peak sensitivity of ligo by detuning the arm cavities," *Classical and Quantum Gravity* **24**, 5453–5460 (2007).
- [49] H. van de Stadt and J. M. Muller, "Multimirror fabry-perot interferometers," *J. Opt. Soc. Am. A* **2**, 1363–1370 (1985).
- [50] D. E. McClelland, J. B. Camp, J. Mason, W. Kells, and S. E. Whitcomb, "Arm cavity resonant sideband control for laser interferometric gravitational wave detectors," *Opt. Lett.* **24**, 1014–1016 (1999).
- [51] A. Bunkowski, O. Burmeister, P. Beyersdorf, K. Danzmann, R. Schnabel, T. Clausnitzer, E.-B. Kley, and A. Tünnermann, "Low-loss grating for coupling to a high-finesse cavity," *Opt. Lett.* **29**, 2342–2344 (2004).
- [52] A. Bunkowski, O. Burmeister, K. Danzmann, and R. Schnabel, "Input-output relations for a three-port grating coupled fabry-perot cavity," *Opt. Lett.* **30**, 1183–1185 (2005).
- [53] A. Freise, A. Bunkowski, and R. Schnabel, "Phase and alignment noise in grating interferometers," *New Journal of Physics* **9**, 433 (2007).
- [54] J. Mizuno, A. Rüdiger, R. Schilling, W. Winkler, and K. Danzmann, "Frequency response of michelson- and sagnac-based interferometers," *Opt. Comm.* **138**, 383–393 (1997).
- [55] W. Winkler, *The Detection of gravitational waves* (Cambridge University Press, Cambridge, 1991). P.269.
- [56] This feature has previously been noticed by B. J. Meers and R. W. P. Dr-  
ever in unpublished work.

- [57] C. M. Caves and B. L. Schumaker, "New formalism for two-photon quantum optics. i. quadrature phases and squeezed states," *Phys. Rev. A* **31**, 3068–3092 (1985).
- [58] J. Harms, Y. Chen, S. Chelkowski, A. Franzen, H. Vahlbruch, K. Danzmann, and R. Schnabel, "Squeezed-input, optical-spring, signal-recycled gravitational-wave detectors," *Phys. Rev. D* **68**, 042001 (2003).
- [59] J. Harms, "Quantum noise in the laser-interferometer gravitational-wave detector geo 600," Diploma thesis, Universität Hannover (2002).
- [60] C. C. Garry, P. L. Knight, *Introductory quantum optics* (Cambridge University Press, Cambridge, UK, 2004).
- [61] M. Xiao, L.-A. Wu, and H. J. Kimble, "Precision measurement beyond the shot-noise limit," *Phys. Rev. Lett.* **59**, 278–281 (1987).
- [62] P. Grangier, R. E. Slusher, B. Yurke, and A. LaPorta, "Squeezed-light-enhanced polarization interferometer," *Phys. Rev. Lett.* **59**, 2153–2156 (1987).
- [63] K. McKenzie, D. A. Shaddock, D. E. McClelland, B. C. Buchler, and P. K. Lam, "Experimental demonstration of a squeezing-enhanced power-recycled michelson interferometer for gravitational wave detection," *Phys. Rev. Lett.* **88**, 231102 (2002).
- [64] R. Schnabel, J. Harms, K. A. Strain, and K. Danzmann, "Squeezed light for the interferometric detection of high-frequency gravitational waves," *Classical and Quantum Gravity* **21**, S1045–S1051 (2004).
- [65] S. Chelkowski, H. Vahlbruch, B. Hage, A. Franzen, N. Lastzka, K. Danzmann, and R. Schnabel, "Experimental characterization of frequency-dependent squeezed light," *Phys. Rev. A* **71**, 013806 (2005).
- [66] T. Corbitt, N. Mavalvala, and S. Whitcomb, "Optical cavities as amplitude filters for squeezed fields," *Phys. Rev. D* **70**, 022002 (2004).
- [67] A. Buonanno and Y. Chen, "Signal recycled laser-interferometer gravitational-wave detectors as optical springs," *Phys. Rev. D* **65**, 042001 (2002).

- [68] M. Hewitson, H. Grote, S. Hild, H. Luck, P. Ajith, J. R. Smith, K. A. Strain, B. Willke, and G. Woan, "Optimal time-domain combination of the two calibrated output quadratures of geo 600," *Classical and Quantum Gravity* **22**, 4253–4261 (2005).
- [69] J. Gea-Banacloche and G. Leuchs, "Squeezed states for interferometric gravitational-wave detectors," *Journal of Modern Optics* **34**, 798–811 (1987).
- [70] T. M. Niebauer, R. Schilling, K. Danzmann, A. Rüdiger, and W. Winkler, "Nonstationary shot noise and its effect on the sensitivity of interferometers," *Phys. Rev. A* **43**, 5022–5029 (1991).
- [71] B. J. Meers and K. A. Strain, "Modulation, signal, and quantum noise in interferometers," *Phys. Rev. A* **44**, 4693–4703 (1991).
- [72] A. Buonanno, Y. Chen, and N. Mavalvala, "Quantum noise in laser-interferometer gravitational-wave detectors with a heterodyne readout scheme," *Phys. Rev. D* **67**, 122005 (2003).
- [73] S. Hild, "Beyond the first generation: Extending the science range of the gravitational wave detector geo 600." Ph.D. thesis, Universität Hannover (2007).
- [74] V. Chickarmane, S. V. Dhurandhar, T. C. Ralph, M. Gray, H.-A. Bachor, and D. E. McClelland, "Squeezed light in a frontal-phase-modulated signal-recycled interferometer," *Phys. Rev. A* **57**, 3898–3912 (1998).
- [75] S. Chelkowski, H. Vahlbruch, K. Danzmann, and R. Schnabel, "Coherent control of broadband vacuum squeezing," *Physical Review A (Atomic, Molecular, and Optical Physics)* **75**, 043814 (2007).
- [76] S. Hild, H. Grote, J. Degallaix, S. Chelkowski, K. Danzmann, A. Freise, M. Hewitson, J. Hough, H. Luck, M. Prijatelj, K. A. Strain, J. R. Smith, and B. Willke, "Dc-readout of a signal-recycled gravitational wave detector," *Classical and Quantum Gravity* **26**, 055012 (10pp) (2009).
- [77] R. L. Ward, R. Adhikari, B. Abbott, R. Abbott, D. Barron, R. Bork, T. Fricke, V. Frolov, J. Heefner, A. Ivanov, O. Miyakawa, K. McKenzie, B. Slagmolen, M. Smith, R. Taylor, S. Vass, S. Waldman, and A. Weinstein, "dc readout experiment at the caltech 40m prototype interferometer," *Classical and Quantum Gravity* **25**, 114030 (8pp) (2008).

- [78] <http://www.ligo.caltech.edu/advLIGO/>
- [79] <http://wwwcascina.virgo.infn.it/advirgo/>
- [80] K. A. Strain and J. Hough, "Experimental demonstration of the use of a fabry-perot cavity as a mirror of variable reflectivity," *Review of Scientific Instruments* **65**, 799–802 (1994).
- [81] S. Hild, A. Freise, M. Mantovani, S. Chelkowski, J. Degallaix, and R. Schilling, "Using the etalon effect for in situ balancing of the advanced virgo arm cavities," *Classical and Quantum Gravity* **26**, 025005 (12pp) (2009).
- [82] B. J. Meers, *Proceedings of the 6th Marcel Grossman Meeting on General Relativity* (World Scientific, Singapore, 1992).
- [83] G. de Vine, D. A. Shaddock, and D. E. McClelland, "Variable reflectivity signal mirrors and signal response measurements," *Classical and Quantum Gravity* **19**, 1561–1568 (2002).
- [84] G. de Vine, D. A. Shaddock, and D. E. McClelland, "Experimental demonstration of variable-reflectivity signal recycling for interferometric gravitational-wave detectors," *Opt. Lett.* **27**, 1507–1509 (2002).
- [85] K. Kawabe, W. Winkler, and S. Hild, "Demonstration of thermal tuning of dual-recycled interferometer for gravitational wave detection," .
- [86] S. Hild, "Thermisch durchstimmbares signal-recycling für den gravitationswellendetektor geo 600," Diploma thesis, Universität Hannover (2003).
- [87] S. Chelkowski, "Squeezed light and laser interferometric gravitational wave detectors," Ph.D. thesis, Universität Hannover (2007).
- [88] F. A., "Frequency-domain interferometer simulation with higher-order spatial modes," *Classical and Quantum Gravity* **21**, S1067–S1074(1) (7 March 2004).
- [89] A. Thüring, "Lineare mehrfach spiegel-resonatoren für gravitationswellendetektoren," Diploma thesis, Universität Hannover (2004).
- [90] C. Gräf, "PPKTP-quetschlichtquelle und twin-signal recycling," Diploma thesis, Leibniz Universität Hannover (2008).

- [91] A. Thüring, R. Schnabel, H. Lück, and K. Danzmann, "Detuned twin-signal-recycling for ultrahigh-precision interferometers," *Opt. Lett.* **32**, 985–987 (2007).
- [92] M. J. Collett and D. F. Walls, "Squeezing spectra for nonlinear optical systems," *Phys. Rev. A* **32**, 2887–2892 (1985).
- [93] L. A. Ostrovskii, *ZhETF Pis'ma*, *JETP Lett.*, 5 (1967), 272 (1967).
- [94] A. G. White, P. K. Lam, D. E. McClelland, H.-A. Bachor, and W. J. Munro, "Kerr noise reduction and squeezing," *Journal of Optics B: Quantum and Semiclassical Optics* **2**, 553–561 (2000).
- [95] P. Tombesi, "Enhanced squeezing with mixed two-photon and four-photon processes in two external pump fields," *Phys. Rev. A* **39**, 4288–4290 (1989).
- [96] A. Berzanskis, K. H. Feller, and A. Stabinis, "Squeezed light generation by means of cascaded second-order nonlinearity," *Optics Communications* (1995).
- [97] R. W. Boyd, *Nonlinear Optics* (Academic Press, 2003).
- [98] Innolight GmbH, <http://www.innolight.de/docs/mephisto.html>
- [99] P. Kwee and B. Willke, "Automatic laser beam characterization of monolithic nd:yag nonplanar ring lasers," *Appl. Opt.* **47**, 6022–6032 (2008).
- [100] This method was suggested by Boris Hage.
- [101] H. Vahlbruch, "Squeezed light for gravitational wave astronomy," Ph.D. thesis, Leibniz Universität Hannover (2008).
- [102] N. Lastzka and R. Schnabel, "The gouy phase shift in nonlinear interactions of waves," *Opt. Express* **15**, 7211–7217 (2007).
- [103] H. Rehbein, "On the enhancement of future gravitational wave laser interferometers and the prospects of probing macroscopic quantum mechanics," Ph.D. thesis, Leibniz Universität Hannover (2009).
- [104] N. Imoto, H. A. Haus, and Y. Yamamoto, "Quantum nondemolition measurement of the photon number via the optical kerr effect," *Phys. Rev. A* **32**, 2287–2292 (1985).

- [105] K. Bergman and H. A. Haus, "Squeezing in fibers with optical pulses," *Opt. Lett.* **16**, 663–665 (1991).
- [106] R. Dong, J. Heersink, J. F. Corney, P. D. Drummond, U. L. Andersen, and G. Leuchs, "Experimental evidence for raman-induced limits to efficient squeezing in optical fibers," *Opt. Lett.* **33**, 116–118 (2008).
- [107] K. S. Zhang, T. Coudreau, M. Martinelli, A. Maître, and C. Fabre, "Generation of bright squeezed light at 1.06  $\mu\text{m}$  using cascaded nonlinearities in a triply resonant cw periodically-poled lithium niobate optical parametric oscillator," *Phys. Rev. A* **64**, 033815 (2001).
- [108] National Instruments,  
<http://sine.ni.com/nips/cds/view/p/lang/en/nid/201937>
- [109] B. Hage, "Quantentomographische charakterisierung gequetschter zustände," Diploma thesis, Universität Hannover (2004).
- [110] Within a personal communication this analysis was performed by Hennig Rehbein based on his analytical description of a KNLR presented in [103].

# Acknowledgments

My thanks goes to the many people whose support has a great part in the success of this work.

I would like to thank Karsten Danzmann who gave me the opportunity to accomplish my a Ph.D. studies at the AEI Hannover. It was a great pleasure to work in a friendly atmosphere accompanied by an impressive technical and financial support.

I thank Roman Schnabel for his excellent mentoring. Our continuous discussions were characterized by his overwhelming enthusiasm and always led to new approaches and ideas. Being part of his youngster research team was a great experience.

During the entire time of my Ph.D. studies I was surrounded by many helpful people who made their contribution to the success of my work. Working together with Henning Vahlbruch, Moritz Mehmet, Boris Hage, Nico Lastzka, Oliver Burmeister, Alexander Franzen, Simon Chelkowski, Alexander Khalaidovski, Christian Gräf, Stefan Hild and many others was a great pleasure.

I thank Henning Vahlbruch for being a great companion during the past years.

Boris Hage and Henning Rehbein are acknowledged for their unconditional help in the evaluation and verification of the tomographic measurements.

For proof reading parts of this thesis I thank Nico Lastzka, Henning Vahlbruch, Boris Hage, Oliver Burmeister, Moritz Mehmet, Christian Gräf and Alexander Khalaidovski. All remaining errors are in my own responsibility.

Special thanks goes to my parents for supporting me on my way. I am deeply impressed by the selfless encouragement of my father during his lifetime.

Many thanks goes to Sonja, Jorik and Birla. You are the greatest enrichment in my life.



# Curriculum vitae

André Thüring  
Hoppenstedts Weg 14 A  
29308 Winsen

Born on June 28th, 1978 in Hannover, Germany

## University studies

- |                   |  |
|-------------------|--|
| 05/2004 - present | Scientific Assistant,<br>University of Hannover  |
| 05/2004 - present | Doctoral studies in Physics, University of Hannover  |
| 01/2004           | Diploma thesis, University of Hannover, <i>Lineare mehrfach<br/>Spiegel-Resonatoren für Gravitationswellendetektoren</i> |
| 10/1998 - 01/2004 | Physics studies, University of Hannover  |

## Community service

- |                   |  |
|-------------------|--|
| 08/1997 - 08/1998 | Civil service. Behinderten Zentrum Hannover,<br>Hannoversche Werkstätten |
|-------------------|--|

## Education

- |      |   |
|------|---|
| 1997 | Abitur, Kaiser-Wilhelm- und Rats Gymnasium Hannover |
|------|---|



# Publications

— 2009 —

- 1 | **A. Thüring**, C. Gräf, H. Vahlbruch, M. Mehmet, K. Danzmann, and R. Schnabel,  
*„Broadband squeezing of quantum noise in a Michelson interferometer with Twin-Signal-Recycling“*,  
Opt. Lett. **34**, 824-826 (2009).
- 2 | M. Mehmet, S. Steinlechner, T. Eberle, H. Vahlbruch, **A. Thüring**, K. Danzmann, and R. Schnabel,  
*„Observation of cw squeezed light at 1550 nm“*,  
Opt. Lett. **34**, 1060-1062 (2009).
- 3 | B. Abbott, ..., **A. Thüring**, ..., J. Zweizig,  
*„All-Sky LIGO Search for Periodic Gravitational Waves in the Early Fifth-Science-Run Data“*,  
Phys. Rev. Lett **102**, 111102 (2009).
- 4 | B. Abbott, ..., **A. Thüring**, ..., J. Zweizig,  
*„Einstein@Home search for periodic gravitational waves in LIGO S4 data“*,  
Phys. Rev. D **79**, 022001 (2009).

- 5 | B. Abbott, . . . , **A. Thüring**, . . . , J. Zweizig,  
„Search for Gravitational-Wave Bursts from Soft Gamma Repeaters“,  
Phys. Rev. Lett **101**, 211102 (2008). B. Abbott, . . . , **A. Thüring**, . . . ,  
J. Zweizig,  
„First joint search for gravitational-wave bursts in LIGO and GEO 600 data“,  
Class. Quantum Grav. **25**, 245008 (2008).
- 6 | B. Abbott, . . . , **A. Thüring**, . . . , G. Santostasi,  
„Beating the Spin-Down Limit on Gravitational Wave Emission from the Crab  
Pulsar“,  
ApJ. Lett. **683**, L45-L49 (2008).
- 7 | L. Baggio, . . . , **A. Thüring**, . . . , J. Zweizig,  
„A joint search for gravitational wave bursts with AURIGA and LIGO“,  
Class. Quantum Grav. **25**, 095004 (2008).
- 8 | B. Abbott, . . . , **A. Thüring**, . . . , J. Zweizig,  
„Search of S3 LIGO data for gravitational wave signals from spinning black  
hole and neutron star binary inspirals“,  
Phys. Rev. D **78**, 042002 (2008).
- 9 | B. Abbott, . . . , **A. Thüring**, . . . , J. Zweizig,  
„Search for gravitational waves associated with 39 gamma-ray bursts using  
data from the second, third, and fourth LIGO runs“,  
Phys. Rev. D **77**, 062004 (2008).
- 10 | B. Abbott, . . . , **A. Thüring**, . . . , J. Zweizig,  
„Search for gravitational waves from binary inspirals in S3 and S4 LIGO data“,  
Phys. Rev. D **77**, 062002 (2008).
- 11 | B. Abbott, . . . , **A. Thüring**, . . . , J. Zweizig,  
„All-sky search for periodic gravitational waves in LIGO S4 data“,  
Phys. Rev. D **77**, 022001 (2008).
- 12 | B. Abbott, . . . , **A. Thüring**, . . . , J. Zweizig,  
„Implications for the Origin of GRB 070201 from LIGO Observations“,  
Astrophys. J. **681**, 1419 (2008).

- 13 | **A. Thüring**, R. Schnabel, H. Lück, and K. Danzmann  
„Detuned Twin-Signal-Recycling for ultrahigh-precision interferometers“,  
Opt. Lett. **32**, 985-987 (2007).
- 14 | B. Abbott, . . . , **A. Thüring**, . . . , J. Zweizig,  
„Searches for periodic gravitational waves from unknown isolated sources and  
Scorpius X-1: Results from the second LIGO science run“,  
Phys. Rev. D **76**, 082001 (2007).
- 15 | B. Abbott, . . . , **A. Thüring**, . . . , J. Zweizig,  
„Search for gravitational wave radiation associated with the pulsating tail of  
the SGR 1806-20 hyperflare of 27 December 2004 using LIGO“,  
Phys. Rev. D **76**, 062003 (2007).
- 16 | B. Abbott, . . . , **A. Thüring**, . . . , J. Zweizig,  
„Search for gravitational-wave bursts in LIGO data from the fourth science  
run“,  
Class. Quantum Grav. **24**, 5343-5369.
- 17 | B. Abbott, . . . , **A. Thüring**, . . . , J. Zweizig,  
„Upper limits on gravitational wave emission from 78 radio pulsars“,  
Phys. Rev. D **76**, 042001 (2007).
- 18 | B. Abbott, . . . , **A. Thüring**, . . . , J. Zweizig,  
„Searching for a Stochastic Background of Gravitational Waves with the Laser  
Interferometer Gravitational-Wave Observatory“,  
Astrophysical Journal, **659**, 918 (2007).
- 19 | B. Abbott, . . . , **A. Thüring**, . . . , J. Zweizig,  
„Upper limit map of a background of gravitational waves“,  
Phys. Rev. D **76**, 082003 (2007).
- 20 | B. Abbott, . . . , **A. Thüring**, . . . , J. Zweizig,  
„First cross-correlation analysis of interferometric and resonant-bar gravitational-  
wave data for stochastic backgrounds“,  
Phys. Rev. D **76**, 022001 (2007).

— 2006 —

- 21 | International patent application, PCT/EP 2006/062626, 24 May 2006, „*Laser device*“, Universität Hannover, Max-Planck-Institut für Gravitationsphysik, inventors: R. Schnabel, O. Burmeister, A. Bunkowski, **A. Thüring**, R. Rinkleff, and K. Danzmann.
- 22 | H. Lück, M. Hewitson, . . . , **A. Thüring**, . . . , R. Zhu, „*Status of the GEO 600 detector*“, *Classical Quantum Gravity* **23**, S71–S78 (2006).
- 23 | B. Willke, P. Ajith, . . . , **A. Thüring**, . . . , R. Zhu, „*The GEO-HF project*“, *Classical Quantum Gravity* **23**, S207–S214 (2006).

— 2005 —

- 24 | **A. Thüring**, H. Lück, and K. Danzmann, „*Analysis of a four-mirror-cavity enhanced Michelson interferometer*“, *Phys. Rev. E* **72**, 022001 (2007).
- 25 | H. Grote, B. Allen, . . . , **A. Thüring**, . . . , I. Zawischa, „*The status of GEO 600*“, *Classical Quantum Gravity* **22**, 066615 (2005).

— 2004 —

- 26 | **A. Thüring**, „*Lineare mehrfach Spiegel-Resonatoren für Gravitationswellendetektoren*“, Diplomarbeit, Universität Hannover (2004).
- 27 | J. R. Smith, . . . , **A. Thüring**, . . . , I. Zawischa, „*Commissioning, characterization and operation of the dual-recycled GEO 600*“, *Classical Quantum Gravity* **21**, S1737–1745 (2004).